

**THE FORMATION OF COMPACT OBJECT BINARIES
THROUGH ISOLATED BINARY EVOLUTION**

by

COENRAAD JACOB NEIJSEL

A thesis submitted to the University of Birmingham for the degree of
DOCTOR OF PHILOSOPHY



**UNIVERSITY OF
BIRMINGHAM**

School of Physics and Astronomy
College of Engineering and Physical Sciences

University of Birmingham

March, 2022

UNIVERSITY OF
BIRMINGHAM

University of Birmingham Research Archive

e-theses repository

This unpublished thesis/dissertation is copyright of the author and/or third parties. The intellectual property rights of the author or third parties in respect of this work are as defined by The Copyright Designs and Patents Act 1988 or as modified by any successor legislation.

Any use made of information contained in this thesis/dissertation must be in accordance with that legislation and must be properly acknowledged. Further distribution or reproduction in any format is prohibited without the permission of the copyright holder.

Acknowledgements

First and foremost I want to sincerely thank Ilya Mandel. I have never been a “grade A” student, but nonetheless you were happy enough to take me on as a student. Despite, your impressive skill set in almost all aspects of science, I never felt judged for my misunderstandings or algebraic limitations and truly enjoyed the possibility of speculating about physics freely. I hope we can keep in touch and if you need a place to stay for Kingsday, or any other moment, you have a standing invitation. This has been a life changing experience which in large part I owe to you.

To my grandmother Wilhelmina Maria Pauw-Koole, my mother Tine Francine Pauw, and my sister Margerethe Francine Neijssel. You are the strongest people I know. I might not say it often, but you have been the single greatest examples throughout my life and have always supported me in my sometimes peculiar choices.

Alla famiglia Vinciguerra, grazie mille per tutto...che brutta vita così.

To Serena “SMRA” Vinciguerra: Hot Chocolate, Doe Maar, Jovanotti.

In memoriam:

Jacob Pauw:

“Altijd blijven lachen”

Coenraad Pieter Neijssel:

“Ook al heb ik geen gelijk, ik heb toch gelijk”

Declaration

This thesis is written by Coenraad Jacob Neijssel. Throughout this thesis I use the alpha-version of the population synthesis code COMPAS. The code is developed by Simon Stevenson, Alejandro Vigna-Gómez, Jim W. Barrett, Ilya Mandel and me.

I wrote the introductory chapters 1, 2 and 3.

Chapter 4 provides a manuscript accepted by Monthly Notices of the Royal Astronomical Society (Neijssel et al., 2019). The text and figures in this thesis are slightly altered compared to (Neijssel et al., 2019), but the quantitative results remain the same. I wrote the Python pipelines to calculate the rates of merging systems. Dr. Sebastian Gaebel wrote the code to calculate the selection effects by gravitational-wave detectors. I wrote the first draft of the manuscript including the figures. The co-authors and anonymous referees provided feedback on both text and figures.

Chapter 5 contains a manuscript intended for publication. I altered the alpha-version of the COMPAS code to change the stability of mass transfer. I made the first draft of the manuscript including the figures. The co-authors provided helpful feedback on both text and figures.

Chapter 6 contains a manuscript as accepted by Astrophysical Journal Letters. I wrote the independent Python code, based on the alpha-version of COMPAS, which evolves the stellar tracks and some binary physics backwards in time. Serena Vinciguerra helped with both text and various post-processing routines. Ryosuke Hirai provided helpful and suggestions for some of the derivations. Ryosuke Hirai and Ilya Mandel wrote parts on the abundances in the discussion section. Alejandro Vigna-Gómez, James C. A. Miller-Jones, Arash Bahramian, and Thomas J. Maccarone provided helpful discussions and feedback on the manuscript. The chapter contains an additional appendix (Sec. 6.B) which is not part of the accepted manuscript. The appendix contains a discussion and a figure that I provided for for the work by James C. A. Miller-Jones and collaborators in Miller-Jones et al. (2021).

Contents

I	Introductory Chapters	7
1	Single Stellar Evolution	8
2	Binary Stellar Evolution	31
3	COMPAS	57
II	Papers	73
4	The effect of the metallicity-specific star formation history on double compact object mergers	74
5	Revisiting the stability of mass transfer for the rates and formation channels of binary black hole mergers.	138
6	Wind mass-loss rates of stripped stars inferred from Cygnus X-1	173
7	Summary and Conclusion	205

Introduction

Observations indicate that most stars are in binary or higher multiplicity systems (Preibisch et al., 1999; Sana et al., 2012, 2013; Duchêne and Kraus, 2013; Chini et al., 2013; Sota et al., 2014; Kobulnicky et al., 2014; Dunstall et al., 2015; Moe and Di Stefano, 2017; Sana, 2017). In a binary two stars orbit each other, bound by their mutual gravitational pull. If the orbital separation is short enough the stars interact, drastically altering their evolution. In the past decades, the means to perform complex calculations have drastically improved, giving us the chance to explore the physics of binary evolution in greater detail. This helped explain several observed properties, amongst others, why some stars are more luminous than expected or have peculiar surface abundances. Nonetheless, large uncertainties persist in the field of binary star physics.

In 2015, the gravitational waves from two colliding black holes were detected for the first time (Abbott et al., 2016b). For decades it has been hypothesised that two massive stars in an isolated binary could interact without external influences and form a binary black hole system tight enough to merge in a Hubble time (van den Heuvel and De Loore, 1973; Tutukov and Yungelson, 1973). In this dissertation I follow in the footsteps of many other studies and assume the observed gravitational-wave events come from isolated binary evolution, even though other formation channels for the mergers of neutron stars and black holes are also possible. The aim is to study what constraints, if any, properties of gravitational-wave events can place on the evolution of massive stars in binaries.

The general approach in of this dissertation is to evolve a population of stars under various model assumptions and estimate the rates and properties of gravitational-wave mergers for each model. The predicted distributions enable a quantitative or qualitative assessment of the impact of current uncertainties in binary-star physics on estimates of the rates and masses of gravitational-wave events. Evaluating the effect of uncertainties is crucial to determine whether comparisons between synthetic populations of gravitational-wave sources and observations can place meaningful con-

straints on binary-star physics. If the uncertainties are large and model-dependent features are not predicted, then the detections of gravitational-wave mergers may only provide marginal constraints.

In this dissertation I assess the impact of the following model assumptions. In chapter 4 I investigate the uncertainties in the rate and initial chemical composition with which stars form and the impact of these uncertainties on the predictions of the merger rate of neutron stars and black holes. In chapter 5 I vary the response of stars to mass loss and explore how it alters the interactions that lead to the formation of binary black holes. In chapter 6 I examine whether Cygnus X-1 may evolve into a binary black hole system and if the observed mass of the black hole in Cygnus X-1 provides constraints on the wind mass-loss rates of stars. Chapter 1 and chapter 2 provide introductory material for the reader on stellar evolution and binary interactions. Chapter 3 summarises the theoretical model used in this dissertation to evolve a population of stars. Chapter 7 provides a summary and personal view on the conclusions of this dissertation.

Part I

Introductory Chapters

Chapter 1

Single Stellar Evolution

1.1 Introduction

The theory of stellar evolution involves relativistic physics, thermal physics, nuclear physics, quantum physics and more. There are plenty of textbooks and notes that review the theory of stellar evolution and its history in great detail (e.g. Chandrasekhar, 1939; Maeder, 2009; Kippenhahn et al., 2012). This chapter gives a brief summary of some of the basic concepts of the evolution of single stars. The focus is mostly on the evolution of massive stars with mass $M \gtrsim 8 M_{\odot}$, which are capable of forming neutron stars and black holes.

Sections 1.2 and 1.3 give a basic introduction to stellar physics and nuclear fusion in stars and largely follow the textbooks of Kippenhahn et al. (2012) and Hansen et al. (2012). For more in-depth discussions and derivations I refer the reader to these textbooks. Section 1.4 describes the evolution of a massive star in terms of its temperature, luminosity and radius. Sections 1.5, 1.6 and 1.7 provide a brief introduction to stellar winds, stellar rotation and supernovae. Section 1.8 briefly summarises the differences in stellar models and some of the major uncertainties. The chapter closes with a summary in section 1.9.

1.2 Basic definitions

Stars are gaseous bodies without a “hard” boundary which defines their surface. For this reason, in practice the radius of a star’s photosphere is often used as a proxy for the radius of the star itself. Following this approximation, the radius R of a star is then defined as the distance, from its centre, where the optical depth τ , calculated from infinity,

$$\tau = \int_R^\infty \kappa \rho \, dr, \quad (1.1)$$

equals $2/3$. Here κ and ρ are respectively the opacity and the density of the gas through which photons travel. Under the assumption that a star emits its entire luminosity L as a black body, the effective temperature (T_{eff}) is related to the radius and luminosity by

$$L = 4\pi R^2 \sigma T_{\text{eff}}^4, \quad (1.2)$$

where σ is the Stefan-Boltzmann constant. For an interesting discussion on the different definitions of stellar radii and temperatures, see Baschek et al. (1991).

1.2.1 Hydrostatic equilibrium

Pressure at any point within a star consists of both gas pressure P_{gas} and radiation pressure P_{rad} ,

$$P = P_{\text{gas}} + P_{\text{rad}} = \frac{k}{\mu m_{\text{p}}} \rho T + \frac{1}{3} a T^4, \quad (1.3)$$

where k is the Boltzmann constant, μ the mean molecular weight, m_{p} the proton mass, a the radiation constant, ρ the density and T the temperature. The first term on the right hand side is the ideal gas law and the second term comes from the Stefan-Boltzmann law¹.

¹For a derivation see chapters 1 & 2 of Chandrasekhar (1939).

A spherical star of total mass M and radius R is in hydrostatic equilibrium if everywhere within the star

$$\frac{dP}{dm} = -\frac{Gm}{4\pi r^4}, \quad (1.4)$$

where P is the pressure, G is the gravitational constant and m the mass of the gas within a distance r from the centre. In other words, a star is in hydrostatic equilibrium when its gravitational force, aimed towards the centre, is balanced by the pressure within a star.

1.2.2 Timescales

Different processes of stellar evolution happen on different timescales. For the calculations of interest in this dissertation, it is common practice to refer to three characteristic timescales of a star, namely its dynamical, Kelvin-Helmholtz ² and nuclear timescale.

1.2.2.1 Dynamical timescale

A star which is no longer in hydrostatic equilibrium will expand or contract until hydrostatic equilibrium is recovered. The expansion or contraction proceeds on the dynamical timescale of the star,

$$\tau_{\text{dyn}} = \sqrt{\frac{R^3}{GM}}. \quad (1.5)$$

This timescale is a factor of 2π smaller than the period of a Keplerian orbit grazing the stellar surface, and is thus of the same order of magnitude as the free-fall collapse time of the star in the absence of pressure.

²The Kelvin-Helmholtz timescale is sometimes also referred to as the thermal timescale of a star. However, in later chapters a slightly different definition is introduced for the thermal timescale and therefore equation 1.6 is only referred to as the Kelvin-Helmholtz timescale.

1.2.2.2 Kelvin-Helmholtz timescale

Another commonly used timescale is the Kelvin-Helmholtz timescale,

$$\tau_{\text{KH}} = \frac{GM^2}{2RL}, \quad (1.6)$$

where L is the stellar luminosity. This timescale estimates the time it takes for a star to radiate away all of its gravitational energy with its current luminosity L . For example, this is the timescale that governs the contraction of a star when nuclear fusion within a star ceases and as a result the star contracts while remaining in hydrostatic equilibrium (Kippenhahn et al., 2012).

1.2.2.3 Nuclear timescale

The nuclear timescale estimates the lifetime of a star when undergoing a specific phase of nuclear fusion, such as hydrogen fusion. The nuclear timescale,

$$\tau_{\text{n}} = \frac{E_{\text{n}}}{L}, \quad (1.7)$$

assumes a star fuses its entire reservoir of nuclear energy, E_{n} , while its luminosity remains equal to its current luminosity L .

Typically $\tau_{\text{n}} \gg \tau_{\text{KH}} \gg \tau_{\text{dyn}}$; this is indeed the case for all stars which are burning hydrogen and helium in their cores, or in other words, during most of the lifetime of a star. For the Sun, during its hydrogen-burning phase (see Sec.1.4), the nuclear timescale is ~ 10 Gyr, whereas the thermal and dynamical timescales are ~ 10 Myr and ~ 1 hour respectively (Kippenhahn et al., 2012).

1.2.3 Metallicity

Another crucial property which determines the life of a star is its chemical composition, often expressed in terms of metallicity. In astrophysics we refer to any element with a higher atomic number than helium as a metal. The metallicity Z of a star is

then defined as the mass fraction of metals in the star and it is related to the mass fraction of hydrogen X and helium Y by

$$Z = 1 - X - Y. \quad (1.8)$$

1.2.4 Convective and radiative transport

Energy produced by nuclear fusion or released from gravitational potential energy is transported outwards to the stellar surface. The two main means of energy transport within a star are radiation and convection. The efficiency of these processes depends, amongst others, on the temperature gradient within a star.

If radiation is the only process which transports energy outwards, then the temperature gradient as a function of the distance from the stellar centre r equals:

$$\frac{dT}{dr} = -\frac{3}{4ac} \frac{\kappa\rho}{T^3} F, \quad (1.9)$$

where F is the radiative flux and c the speed of light.

Convection occurs when there is a steep temperature gradient. Consider a small amount of gas which heats up due to absorption of photons and expands adiabatically. The “blob” of gas is less dense compared to its surroundings. Buoyancy forces carry the blob upwards whilst the adiabatic expansion cools the blob of gas. However, if the temperature gradient within a star is steeper than the change in temperature due to the adiabatic expansion, then the blob of gas remains hotter than its surroundings. The process becomes dynamically unstable and convective flows develop within the star which carry the energy outwards³. The momentum of this convective flow allows it to penetrate into the radiative layer, a process known as convective overshoot (Roxburgh, 1965; Shaviv and Salpeter, 1973).

How energy is transported throughout a star is crucial in determining the star’s evolution, and, during hydrogen burning, it mostly depends on the mass of the star. The energy transport within hydrogen-burning stars with masses above $\sim 1.2 M_{\odot}$

³This analogy is attributed to Prandtl (1925) in (Kippenhahn et al., 2012).

is predominantly convective in the core and radiative in the envelope. Stars less massive than $\sim 1.2 M_{\odot}$ have radiative cores and convective envelopes. Stars below $\sim 0.3 M_{\odot}$ are fully convective (Paxton et al., 2011).

1.3 Nuclear Fusion

Nuclear fusion is the process by which atomic nuclei fuse together and form heavier elements (Eddington, 1926). It is a complicated process, which involves many branches of modern physics, including for example quantum tunneling (Gamow, 1928), particle physics and statistical mechanics (e.g. the Pauli exclusion principle). The details of such nuclear fusion are however not crucial for the content of this dissertation. For this reason, what happens in the core of a star is presented in the following, commonly used, simplified picture. The interior of stars can easily reach temperatures of millions of degrees (the exact value of the maximum temperature in the interior of a star depends on its mass and chemical composition). At these high temperatures nuclei are often found in their ionised state. For nuclear fusion, it is therefore necessary to overcome the Coulomb force which repels atomic nuclei from each other, as the attractive strong force only acts at very short nuclei separations. Extreme conditions are therefore needed for initiating nuclear fusion. These requirements can be met in the core of a star. In practice, nuclear fusion only occurs if the reaction is exothermic, i.e. if it is energetically advantageous and the star releases energy during the process. The internal energy of nuclei, which regulates the energy balance of these nuclear reactions, depends on the mass and proton number and reaches its maximum at the formation of iron mass. For heavier elements fusion is therefore no longer an exothermic reaction.

1.3.1 Hydrogen fusion

Hydrogen fusion happens through two different sets of reaction chains. The first is the proton-proton chain or pp chain (Bethe and Critchfield, 1938). The pp chain

fuses hydrogen to form ${}^3\text{He}$ and subsequently ${}^4\text{He}$. The second chain involves carbon, nitrogen and oxygen and is therefore named the CNO cycle (Weizsäcker, 1937; Bethe, 1939).

Nuclear reaction rates of both the pp chain and the CNO cycle depend on several parameters, amongst others, the temperature of the gas. The rate at which energy is released through fusion by the pp chain scales with temperature as $\propto T^\alpha$ with $\alpha \sim 4$, whereas for the CNO cycle the rate of energy released scales with temperature with $\alpha \sim 18$ (Karakas and Lattanzio, 2014). At temperatures above $T \approx 15 \times 10^6$ K (Kippenhahn et al., 2012) the CNO cycle is the dominant process by which hydrogen is fused into helium. This central temperature is achieved in stars with initial masses above $M \approx 1.2 M_\odot$.

When hydrogen is depleted in the core, central hydrogen fusion comes to a halt. At the boundary between the helium core and the hydrogen envelope, hydrogen abundances and temperatures are high enough to sustain hydrogen fusion. Therefore, hydrogen fusion continues in a shell around the core. As shell burning continues the helium core gains in mass. The core is no longer pressure supported by radiation from nuclear fusion and contracts, increasing in temperature and density.

1.3.2 Fusion of heavier elements

Helium fusion proceeds at temperatures $T \gtrsim 10^8$ K (Kippenhahn et al., 2012; Hansen et al., 2012). The helium is fused into carbon through the triple-alpha reaction, whereby two helium nuclei form beryllium which fuses with an additional helium nucleus to form carbon. Additional alpha capture may also occur and generate oxygen from carbon and neon from oxygen. In stellar evolution, however, it is general practice to refer to nuclear-burning phases by the dominant process which is responsible for the luminosity of a star; in the case just described, helium burning.

Temperatures need to exceed $T \gtrsim 5 \times 10^8$ K to fuse carbon, mostly into sodium and neon. Oxygen fusion proceeds at temperatures above $T \gtrsim 10^9$ K, creating elements such as sulfur, phosphorus, silicon and magnesium. At temperatures around

$T \approx 3 \times 10^9$ K, silicon particles are photodisintegrated into smaller elements and free neutrons, protons and alpha particles. These particles react with the remaining silicon nuclei and form iron, which is the final product of nuclear fusion in stellar cores (Kippenhahn et al., 2012).

1.3.3 Stellar-mass thresholds and timescales of nuclear-burning stages

Not all stars are able to fuse elements up till iron. The maximum central temperature a star can reach increases with the stellar mass. The stellar-mass thresholds, which specify whether a star is capable of fusing certain elements, depend on a range of parameters such as its metallicity, the degree of overshooting and rotational velocity. The following thresholds and timescales are derived from detailed simulations of non-rotating stars with initial metallicities of $Z = 0.02$ taken from Paxton et al. (2011).

For simplicity the following mass ranges only consider fusion in stellar cores and not in shells or thermal pulses. Stars with initial masses between $0.9 \lesssim M/M_\odot < 2.0$ ignite helium in a helium flash after the core has become fully degenerate. Stars with masses $M \gtrsim 2.0M_\odot$ start fusing helium inside their core before it is fully degenerate. Stars heavier than $8.0M_\odot$ are massive enough to ignite carbon during their evolution. Stars with masses between $2.0 \lesssim M/M_\odot \lesssim 8.0$ end their lives as white dwarfs whereas more massive stars continue to evolve until their cores explode or collapse into a neutron star or black hole.

As a general rule of thumb stars spend about 90% of their lives fusing hydrogen. The lifetime of a star decreases with mass. A star with an initial mass of $2 M_\odot$ fuses hydrogen for approximately 0.9×10^9 yr, whereas a $15 M_\odot$ star and a $25 M_\odot$ star fuse hydrogen for about 1.1×10^7 yr and 6.4×10^6 yr respectively (Paxton et al., 2011). Each consecutive burning phase of heavier elements proceeds on shorter and shorter timescales. For example, a star with an initial mass of $15 M_\odot$ goes through helium fusion in 1.1×10^6 yr, carbon in 4.2×10^3 yr, neon in 3.5 yr, oxygen in 4.1 yr and silicon in 0.8×10^{-2} yr (Paxton et al., 2011).

Similar to hydrogen fusion, each core burning phase is followed by a shell burn-

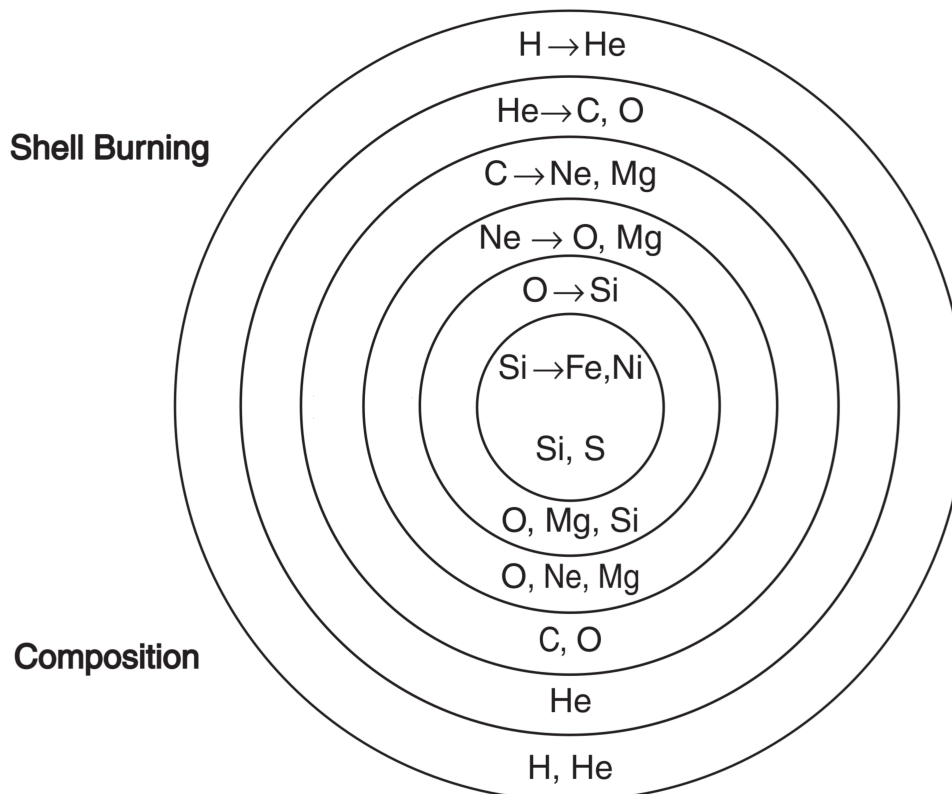


Figure 1.1: Schematic diagram of the internal structure of a massive star in a late stage of its evolution. The bottom half shows the most predominant element in each layer of the star. The top half shows the nuclear reaction in each burning shell between the layers. The figure is adapted from McCracken and Stott (2013).

ing phase (though the next phase of core burning may start concurrently with the previous phase of shell burning). The core is no longer pressure supported and contracts, increasing in temperature and density until, if the star is sufficiently massive, it ignites the next burning phase. By the time a massive star starts to form an iron core, it has developed what is often referred to as an onion-skin structure with multiple shell burning layers, as depicted in Fig.1.1.

1.4 Stellar phases and evolution

This section describes the generic evolution of a non-rotating massive star. The different evolutionary phases are named after their location and features in the Hertzsprung-Russell (HR) diagram, which depicts the luminosity L versus the effective surface temperature of a star T_{eff} . Figure 1.2 is a schematic representation of

the evolution of massive stars in time in the HR diagram.

1.4.1 Main-sequence and Hertzsprung-gap stars

A population of hydrogen-burning stars with different masses form a sequence in the HR-diagram. These main sequence (MS) stars evolve on a nuclear timescale until hydrogen is depleted in their cores. At the end of the MS phase the core is no longer supported by nuclear fusion and contracts. In a massive star the core mass exceeds the Schönberg-Chandrasekhar limit (Schönberg and Chandrasekhar, 1942) and therefore has insufficient support against gravity and collapses. The star is no longer in thermal equilibrium. The released energy from the collapsing core, combined with fusion in the hydrogen-burning shell, results in a rapid expansion of the envelope (see Fig. 1.2). The core contraction and envelope expansion occur on a Kelvin-Helmholtz timescale which is shorter than the prior MS phase and the following helium-burning phase (for a $15 M_{\odot}$ star by about two orders and one order of magnitude, respectively). Due to the short timescale it is not likely to observe a star during this phase, resulting in a gap of observations in the HR-diagram. Therefore, this phase is commonly referred to as the Hertzsprung gap (HG).

1.4.2 Giant branch

Expansion results in the cooling of the outer layers of a star. Core contraction is halted when central temperatures reach $\sim 10^8$ K and the core is supported by nuclear fusion of helium. The evolutionary phase during which helium ignition occurs depends on the mass of the star.

Massive stars with initial masses $M \lesssim 15 M_{\odot}$ reach the first giant branch (FGB) before igniting helium in the core. During the HG the envelope expands and the effective temperature drops. The outermost layers cool until, at around 5000 K, the neutral hydrogen atoms capture free electrons from the partially ionised heavier elements and form hydrogen anions (H^-). The H^- has a high opacity and the outermost part of the envelope starts to develop a thicker convective region. The core

continues to contract, but the envelope cannot cool any further due to the Hayashi limit (Hayashi and Hoshi, 1961). The Hayashi limit describes the edge of a “forbidden region” in the HR diagram. Any star with cooler effective temperatures cannot maintain hydrostatic equilibrium and convective flows quickly readjust the star until its temperature and luminosity again follow the Hayashi limit. Therefore, as the core contracts, the envelope continues to expand at a fixed surface temperature. Radial expansion results in an increase in luminosity and the star ascends the FGB until it ignites helium in the core. A star with an initial mass of $\sim 10 M_{\odot}$ and initial radius of $\sim 10 R_{\odot}$ will have increased its radius to $\sim 200 R_{\odot}$ by the time it ignites helium in the core (see Fig 1.2). After the depletion of helium in the core, helium fusion continues in a shell around the core. Similar to the HG, the core contracts again until it is hot enough to ignite carbon. The star expands again and evolves onto the asymptotic giant branch (AGB).

Stars more massive than $\sim 15 M_{\odot}$ ignite helium in the core before reaching the giant branch (see Fig 1.2). However, the envelope has not yet reached thermal equilibrium and the star keeps expanding, becoming a supergiant.

Stars more massive than $30 - 70 M_{\odot}$ (Smith, 2014) may lose their envelopes through stellar winds either before or during the giant phase. The extent to which mass is lost from the envelope depends on the star’s metallicity and wind mass-loss rate. If the entire envelope is removed, what is left is a hot exposed core also known as a Wolf-Rayet star (for a review see Abbott and Conti, 1987; Crowther, 2007), which are characterised by broad emission lines in their spectra.

In massive stars, nuclear fusion continues until dynamical instabilities in their cores result in core collapse and possibly a supernova.

1.5 Stellar winds

Stars have outflows of matter from their surfaces known as stellar winds. Winds are accelerated from the surface of a star until they reach a terminal velocity, v_{∞} . The

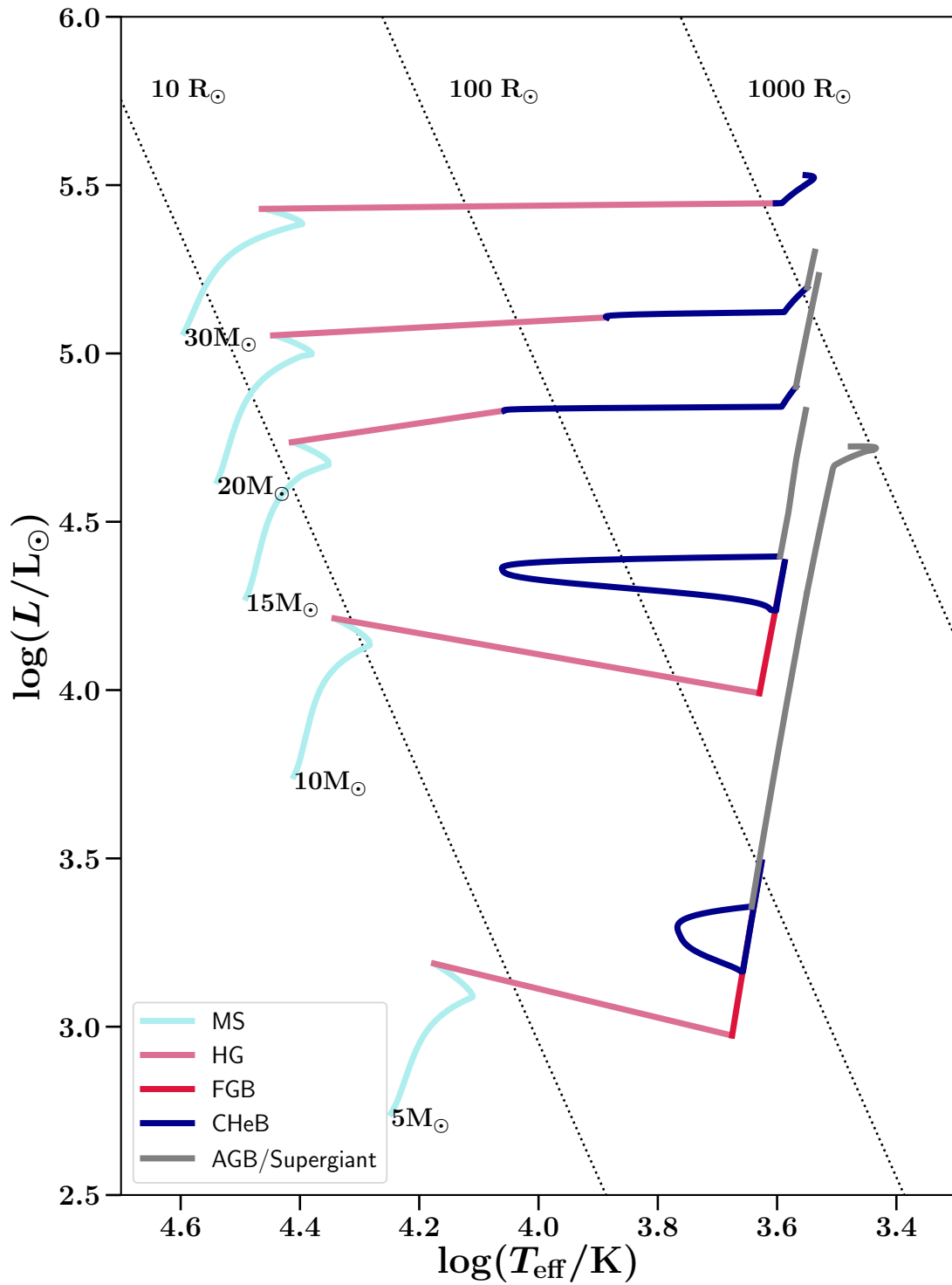


Figure 1.2: Evolutionary tracks of single stars with an initial metallicity of $Z = 0.0142$. The colours relate to the different stellar phases of stars: main sequence (MS), Hertzsprung gap (HG), first giant branch (FGB), core helium burning (CHeB), asymptotic giant branch (AGB) and supergiant phase. All stars were evolved using the analytic fits to stellar tracks by Hurley et al. (2000) as implemented in COMPAS (see chapter 3).

wind mass-loss rate is found by calculating

$$\dot{M} = 4\pi r^2 \rho(r) v_\infty, \quad (1.10)$$

where ρ is the average density and r the distance from the centre of the star. The distance r can be recovered from radio and infrared spectra of the star while the terminal velocity can be inferred from P-Cygni profiles⁴ in the ultra-violet spectrum (see e.g. Smith, 2014, and references therein). The terminal wind velocity is typically a few times the escape velocity of the star (Castor et al., 1975), where the escape velocity is defined as

$$v_{\text{esc}} = \sqrt{\frac{2GM}{R}}. \quad (1.11)$$

Stellar winds are driven by radiation pressure and pulsations from the interior of a star (for reviews on stellar winds and pulsations of massive stars see e.g. Wood and Sebo, 1996; Lamers and Cassinelli, 1999; Puls et al., 2008; Smith, 2014). The mechanism responsible for radiation pressure in stellar winds is commonly divided into two types: line- and dust-driven winds.

1.5.1 Line-driven winds

Atoms absorb photons at specific frequencies. Photon absorption accelerates the atoms, which are coupled to a stellar atmosphere by Coulomb interactions. Absorption of photons in a stellar atmosphere therefore results in a line-driven stellar wind (Lucy and Solomon, 1970; Castor et al., 1975). The number of line transitions in an atom depends on the size of the nucleus and the level of ionization of the atom. The mass-loss rate, therefore, depends on the luminosity, surface temperature and metallicity of the star.

Wind mass-loss rates of non-interacting massive stars on the MS, early on the HG

⁴P-Cygni profiles are spectral lines, named after the variable star P Cygni, characterised by the presence of both absorption and emission.

before the envelope cools during the giant phase and Wolf-Rayet stars are dominated by line-driven winds. Theoretical and observational estimates of mass-loss rates from massive stars typically range from $10^{-7} M_{\odot} \text{ yr}^{-1}$ up to a few times $10^{-5} M_{\odot} \text{ yr}^{-1}$ (Lamers and Cassinelli, 1999). Nieuwenhuijzen and de Jager (1990) derive, from detailed stellar tracks, a generic prescription of the wind mass-loss rates for all massive stars with surface temperatures above 5000 K and hydrogen-rich envelopes (thus excluding Wolf-Rayet stars),

$$-\dot{M} = 9.6 \times 10^{-15} (L/L_{\odot})^{1.42} (M/M_{\odot})^{0.16} (R/R_{\odot})^{0.81} M_{\odot} \text{ yr}^{-1}. \quad (1.12)$$

Here the mass-loss rate increases with increasing luminosity, mass and radius of a star. Given that line-driven winds rely on the presence of metals, stars with a higher metallicity on average experience higher wind mass-loss rates (see e.g. Kudritzki and Puls, 2000; Vink et al., 2001).

1.5.2 Dust-driven winds

When the stellar envelope expands during the HG, its radius increases and the surface temperatures drop. During the AGB, the outer layers of a star becomes cool enough, 1000–1500 K, for dust grains to form. Since dust grains absorb from the continuum, their contribution to the opacity of the gas is far greater than the effect of atomic lines. Observations of AGB stars show that wind velocities range from 3–30 km s⁻¹ (Höfner and Olofsson, 2018). Furthermore, these stars pulsate resulting in additional shedding of the outer parts of the envelope. The expelled gas cools further and is blown away by dust-driven winds (Vassiliadis and Wood, 1993; Yoon and Cantiello, 2010; Smith, 2014).

There are still large uncertainties regarding mass-loss rates of AGB or supergiant stars. Moreover, studies only rarely include giant stars with masses above $\sim 10 M_{\odot}$ (for reviews see Willson, 2000; Smith, 2014; Höfner and Olofsson, 2018). Some estimates from observations of red supergiants indicate mass-loss rates as high as

$10^{-3} M_{\odot} \text{ yr}^{-1}$ (Smith, 2014).

1.5.3 Luminous blue variable winds

Some stars with masses above $50 M_{\odot}$, named luminous blue variables (LBVs), show luminous irregular mass-loss events (Humphreys and Davidson, 1994). Part of the variability in LBV winds is attributed to changes in the efficiency of line-driven winds, which can explain mass-loss rates ranging from 10^{-6} to $10^{-4} M_{\odot} \text{ yr}^{-1}$ (Vink and de Koter, 2002). However, stars can also have eruptive events. This is the case, for example, of η Carinae, which shed about $10 M_{\odot}$ on a timescale of 20 years (Owocki and Shaviv, 2012, and references therein). The driving mechanism behind these outbursts is still unclear and possible explanations range from super-Eddington winds, to instabilities in the envelope (when the stellar luminosity is close to the Eddington limit) or eruptions triggered by a pulsational pair-instability supernova (Smith, 2014, and references therein).

1.5.4 Wind mass-loss rates: complexity and uncertainties

Estimates of wind mass-loss rates rely, amongst others, on estimates of wind densities and terminal velocities (see Eq. 1.10), which are either uncertain or show irregular behaviour. For example, Lamers et al. (1995) infer terminal wind velocities of observed MS stars and find that terminal velocities range from $\sim 500 \text{ km s}^{-1}$ for stars of $\sim 15 M_{\odot}$ to $\sim 3000 \text{ km s}^{-1}$ for stars of $\sim 50 M_{\odot}$. However, terminal wind velocities are not a continuous function of stellar mass and temperature. Lamers et al. (1995) and Vink et al. (1999, 2001) find that there are “bi-stability” jumps. The terminal velocity sharply increases, as a function of surface temperature, due to a change in opacities, such as at temperatures of $\sim 25000 \text{ K}$ due to the ionisation of Fe IV (Vink et al., 1999, 2001). Mass-loss rates are predicted to increase by a factor of five at this bi-stability jump (Vink et al., 1999, 2001). Therefore, instead of a single prescription such as Eq. 1.12, simulations of stars often rely on a patchwork of different prescriptions which apply to different ranges of stellar masses, metallicities,

temperatures and luminosities.

Results by Mokiem et al. (2007) and Bestenlehner et al. (2014) show that mass-loss rates as inferred from observations are in reasonable agreement with theoretical predictions, such as the mass-loss rates of massive stars such as those presented by Vink et al. (2001). However, as noted in Bestenlehner et al. (2014), the empirical estimates are still subject to theoretical uncertainties, in particular clumping of the wind. Clumping is expected to occur in line-driven winds due to radiative instabilities (Owocki et al., 1988; Sundqvist et al., 2018). Uncertainties in clumping could mean that we overestimate wind mass-loss rates by as much as a factor of 10 (Puls et al., 2008). Section 6.A in chapter 6 provides an example of the impact of uncertainties of stellar winds, due to clumping, on the evolution of massive stars and the formation of compact objects.

1.6 Rotation

Observations of massive stars show that the majority of massive stars rotate with rotational velocities in the range of 10 km s^{-1} to 600 km s^{-1} (Fukuda, 1982; Ramírez-Agudelo et al., 2013, 2015). Stellar rotation has an impact on the evolution of stars such as brightness, size of the nuclear-burning core and size of the star (for reviews see e.g. Maeder and Meynet, 2000; Maeder and Meynet, 2010).

Stars with initial masses of $15 M_{\odot}$, experience rotation-induced mixing when rotation rates exceed $\sim 200 \text{ km s}^{-1}$. In these cases some of the processed material in the stellar core can reach the stellar surface. The surface then shows abundance patterns that non-rotating models cannot explain (Heger and Langer, 2000). Stellar rotation also results in additional mixing of gas of the envelope into the stellar core enhancing the MS lifetime possibly up to 30 per cent (Maeder and Meynet, 2000).

The maximum rotational velocity of a stellar surface, such that it is still bound to the star, is often referred to as the Keplerian velocity or critical rotation rate,

$$v = \sqrt{\frac{GM}{R}}, \quad (1.13)$$

where R is the stellar radius, assuming spherical symmetry or the equatorial radius, if deformation is accounted for (the equatorial radius can be up to 1.5 times the polar radius (Maeder, 2009)). If the stellar rotation is close to the Keplerian rotation rate of the star, then evolution of the star will completely differ from the picture presented in Sec. 1.4. Instead the entirety of the star is mixed through the core resulting in a homogeneous evolving star. Such a star directly contracts towards the Wolf-Rayet phase instead of expanding during and after the MS phase (see e.g. Maeder, 1987).

1.7 Final core collapse and supernovae

Massive stars end their lives when their cores collapse due dynamical instabilities. In some cases the collapse is followed by a (partial) explosion of the star during a supernova (SN). However, not all SNe are alike. What follows is a brief description of some of the different SN types, based on explosion mechanism, originating from the collapse of massive stars⁵.

1.7.1 Electron-capture supernovae

Electron-capture supernova (ECSN) progenitors are not massive enough to form a degenerate iron core, instead fusion stops when the stellar core mostly consists of oxygen and neon. In the absence of fusion the oxygen-neon core contracts until a degenerate core is formed. In ECSN progenitors the oxygen-neon core is more massive than the oxygen-neon Chandrasekhar mass and therefore the magnesium and neon atoms within the core capture electrons. Heat from the electron-capture process results in the ignition of oxygen, but nonetheless the dense core continues to contract and collapse until the formation of a proto-neutron star and subsequent SN (Miyaji et al., 1980; Nomoto, 1984). Calculations by Nomoto (1987) and Takahashi et al. (2013) indicate a mass threshold of oxygen-neon core, above which ECSNe

⁵Other types of SNe exist; these include, for example, type Ia SNe coming from the explosions of accreting, colliding or merging white dwarfs (see e.g. Hillebrandt and Niemeyer, 2000, for a review).

are possible, of $1.376 M_{\odot}$ and $1.367 M_{\odot} \pm 0.01 M_{\odot}$ respectively. Initial estimates by Miyaji et al. (1980) and Nomoto (1984) indicate that stars with initial masses between $8 \leq M \leq 12 M_{\odot}$ experience ECSNe. However, mass ranges of initial stellar masses that produce ECSNe are uncertain and theoretical estimates may differ by a few solar masses, because the relation between the initial mass of a star and the final oxygen-neon core mass is sensitive to parameters such as the initial metallicity of a star or the treatment of convection in the core (Takahashi et al., 2013).

1.7.2 Iron core-collapse supernovae

Stars which are massive enough to ignite neon and therefore avoid an ECSN continue fusion until an iron core is formed. Once an iron core exceeds the Chandrasekhar mass, $1.44 M_{\odot}$, it collapses in what is commonly referred to as a core-collapse supernova (CCSN). In the case of CCSNe, the shock may be energetic enough to explode the entire star. However, if enough energy is lost during the propagation of the shock, e.g. by disintegrating nuclei along its path (see Janka et al., 2007; Burrows, 2013, for a review), and carried away by non-interacting neutrinos (Janka et al., 2007), the shock may not be energetic enough to unbind material from a star (see e.g. Shigeyama et al., 1988; Woosley, 1989; Fryer et al., 2012).

Mass which does not escape from the star falls back onto the remnant. The final remnant mass is then mostly determined by the initial mass of the core at the onset of the SN, the amount of accretion during the collapse and the final mass that falls back onto the remnant. Fryer et al. (2012) estimate that the fraction of the total mass of the star that falls back onto the remnant is negligible in stars with initial masses below $\sim 11 M_{\odot}$, but is close to unity in stars with initial masses $\gtrsim 40 M_{\odot}$ (depending on the initial metallicity of the star). Chapter 3 shows an example of the remnant mass as a function of the initial mass of the star based on the models of Fryer et al. (2012).

1.7.3 Pair-instability supernovae

Massive stars, capable of creating helium cores with masses between $30 - 133 M_{\odot}$, are expected to end their lives in pulsational pair-instability supernovae (PPISNe) or pair-instability supernovae (PISNe) (Woosley, 2017). Woosley (2017) estimates this is the case in non-rotating stars with initial masses ranging from 70 to $250 M_{\odot}$. Photons with energies above 1.022 MeV can create an electron-positron pair. When this process occurs within a star, the loss of photons leads to a reduction in radiation pressure. The high temperature of helium cores with mass above $\sim 64 M_{\odot}$ (Woosley, 2017) allows for a significant loss of radiation pressure through pair creation and a subsequent contraction of the core. This contraction results in hotter temperatures which increase the rate of pair creation resulting in a runaway collapse. The collapse and subsequent explosion, which is powered by oxygen and sometimes silicon burning (Heger and Woosley, 2002), is what constitutes a PISN. The entire star disintegrates without leaving a compact remnant.

Helium cores with masses $30 - 64 M_{\odot}$ also experience a loss of radiation pressure due to pair instability. However, the following rapid nuclear fusion of oxygen and silicon is not energetic enough to disintegrate the star. Instead, the core expands until fusion ceases. Then the core contracts again on dynamical or thermal timescales (Woosley, 2017). This process repeats until the core collapses in a CCSN and forms a black hole (BH). Each rapid expansion of the core results in a pulse which injects energy into the envelope. The star increases in luminosity and loses part of its mass during the PPISN. Each pulse, with its mass loss, reduces the mass that is capable of falling back onto the remnant during the SN. Some pulses (but not all of them) may be seen as luminous SNe and the duration of the pair-instability period could span many orders of magnitude from hours to thousands of years (Woosley, 2017). Stars with helium cores more massive than $\sim 133 M_{\odot}$ are too massive to experience PISNe and form BHs through direct collapse.

1.7.4 Observations of supernovae

There are multiple observations that seem to support the existence of the different aforementioned types of SNe. Light curves and spectra of SNe inform us on the properties of the explosion and the progenitor star (see Smartt, 2009, for a review). Continuous large scale observational surveys play a crucial role in monitoring the sky to find the progenitor stars of SNe (Kochanek et al., 2008). Based on SNe for which the progenitor are found, the observed minimum mass of these progenitors confirms that the minimum mass to explode in a CCSN is $\sim 8M_{\odot}$ (Smartt, 2009). Here are some examples of possible links between observations and supernova types and mechanisms. The variability in the brightness of the supernova iPTF14hls might be explained by pulsations of a PPISNe (Arcavi et al., 2017; Woosley, 2018). Observations of a super-luminous SN have been linked to PISN (Kozyreva et al., 2014). Some massive stars have been observed to disappear without a bright SN, suggesting that they have collapsed and the envelope fell back onto the remnant (Adams et al., 2017; Allan et al., 2020).

1.7.5 Supernova natal kicks

A SN ejects part of the mass of the star. Asymmetric ejection of the envelope or neutrinos imparts momentum on the remnant. The amount of momentum depends on the energetics of the explosion and the asymmetry of the ejecta.

Observational surveys of isolated pulsars indicate that their velocity distribution is reasonably well approximated by a Maxwellian distribution with a root-mean-squared speed of 265 km/s (Hobbs et al., 2005) or a combination of two different Maxwellian distributions with average speeds of 120 km/s and 540 km/s (Verbunt et al., 2017). Detailed three-dimensional supernova simulations indicate a possible connection between the progenitor mass and the final explosion and natal kick (Müller et al., 2016; Mandel and Müller, 2020). However, there are still uncertainties considering the relation between the supernova progenitor and the supernova kick. The studies in this dissertation therefore rely on the simplified approach where the

kick velocity is drawn from a Maxwellian distribution and the direction is isotropic in the frame of reference of the remnant. If the remnant experiences fall back during its formation, the kicks are often assumed to be reduced by an amount proportional to the fall back fraction (see e.g. Fryer et al., 2012).

1.8 Uncertainties in single stellar evolution and the formation of black holes

Understanding of the evolution of stars heavily relies on computational methods, in particular one-dimensional stellar evolutionary codes such as **Geneva** (Eggenberger et al., 2008), **KEPLER** (Weaver et al., 1978, 1985; Woosley and Weaver, 1988), **MESA** (Paxton et al., 2011, 2015), **PARSEC** (Bressan et al., 2012) and **STARS** (Eggleton, 1971, 1972; Eggleton et al., 2011). Differences in the results of simulations may arise due to different numerical procedures (e.g. solving integrals or coupled stellar-structure equations) or different physical assumptions (e.g. amount of convective overshooting or wind mass-loss rates).

Reiter et al. (1995) show that different methods to solve the stellar structure equations only result in differences of $\sim 10^{-3}L_{\odot}$ in simulations of the luminosity of the Sun. Stancliffe (2006) investigates the difference between simultaneously and non-simultaneously solving the stellar-structure equations for stars with initial masses of $3 M_{\odot}$ and $5 M_{\odot}$ at $Z = 0.02$. He finds that the results of the two schemes only start to differ at the final stages of stellar evolution, during the thermal pulsations of a star. The impact of different numerical procedures is therefore expected to be minor compared to differences due to physical assumptions, although more studies into numerical uncertainties of massive stellar evolution are needed.

Differences in physical assumptions greatly impact the evolution of stars changing their luminosities, radii, surface temperatures, stellar lifetimes and abundances (see e.g. Chiosi, 1986; Kippenhahn et al., 2012; Weiss, 2002; Ekström et al., 2020). Those same uncertainties also affect models of the formation of neutron stars and black

holes, one of the main focuses of this dissertation.

Convective overshooting, the convective mixing between the core and stellar envelope, results in an enhanced mixing of fuel into the core. Kaiser et al. (2020) find that within the stellar-evolution code `MESA` differences in the amount of convective overshooting lead to changes of up to 70 per cent in the helium-burning lifetime and carbon-oxygen core mass. It is this carbon-oxygen core mass which plays an important role in determining the final remnant mass (see e.g. Sec. 3.2.2).

Wind mass-loss rates remain highly uncertain (see Sec. 1.5). Renzo et al. (2017) show how different wind mass-loss rates affect the final core structure and the star's ability to explode and form a neutron star or black hole. Renzo et al. (2017) estimate that uncertainties in stellar winds result in about a 50 per cent uncertainty in the mapping between the initial and final mass of the star, where the initial masses range from $15 M_{\odot}$ to $35 M_{\odot}$ and the stars are evolved with solar metallicities. Furthermore, in chapter 6 we show that differences in assumed wind mass-loss rates, in even more massive stars, could result in changes in the remnant mass by more than a factor of 2.

The effects of stellar rotation are still uncertain (see e.g. Maeder and Meynet, 2000). Stars which rotate near their Keplerian velocity (see Sec. 1.5) may avoid expansion altogether and evolve as chemically-homogeneous stars (Maeder, 1987). Stellar expansion plays an important role in this dissertation, since it is one of the main drivers of mass transfer between stars in a tight stellar binary. Chemically-homogeneous stars are not included in the stellar models considered in this dissertation. They evolve through entirely different pathways and may also form merging binary black holes (Marchant et al., 2016; Mandel and de Mink, 2016; Riley et al., 2021). Estimates by Riley et al. (2021) indicate that up to 70 per cent of the detected binary black hole mergers coming from isolated binary evolution may have evolved through chemically-homogeneous evolution.

1.9 Summary

This chapter briefly described some of the physics of single stellar evolution, in particular the evolution of massive stars. As massive stars fuse elements in their cores, they expand and lose mass through winds. After the final stage of nuclear burning they end their lives in a SN, possibly leaving behind a neutron star or black hole.

It is clear that the evolution of massive stars, despite all the advances in the field, remains uncertain. The uncertainties due to stellar evolution are largely outside the scope of this dissertation, except for a limited discussion of Wolf-Rayet winds in chapter 6. The main scope of this dissertation is constraining binary-star physics using observations of gravitational waves and the COMPAS code (see chapter 3). The COMPAS code relies on a single set of stellar models and the uncertainties quoted in chapters 4, 5 and 6 therefore do not account for the uncertainties coming from single-stellar evolution. Newer versions of COMPAS do allow for estimates of the contributions of chemically-homogeneous stars (Riley et al., 2021). Future efforts will simultaneously explore uncertainties coming from both single- as well as binary-star physics using the COMPAS code by implementing METISSE (Agrawal et al., 2020), which enables interpolation between different sets of single stellar models.

Chapter 2

Binary Stellar Evolution

This chapter reviews some of the basic concepts of binary stellar evolution. The focus is mostly on mass transfer through Roche-lobe overflow. The technical details of the models used to study the evolution of massive stellar binaries in this thesis are found in chapter 3.

Section 2.1 provides a brief introduction followed by section 2.2 which describes the gravitational potential field of two stars in a binary. Sections 2.3 and 2.4 describe the effects of tides and wind mass loss on the orbital separation and eccentricity of a binary system. Section 2.5 presents a summary of the physics involved in mass transfer through Roche-lobe overflow. Section 2.6 describes the effect of gravitational waves on the orbit of the binary. Section 2.6 presents the main formation channel for merging binary black holes and neutron stars through isolated binary evolution.

The following terminology is used in this chapter to refer to the stars. The primary star (subscript 1) is the more massive star in the binary at zero-age main sequence (ZAMS). The secondary star (subscript 2) is the less massive star at ZAMS. Mass transfer could be initiated by either the primary or secondary star (or in some cases even both) and invert the mass ratio of the system. Here it is more important to indicate which star initiated the mass transfer. The subscript D refers to the star which loses mass, the donor, whereas the subscript A refers to the accreting companion star, the accretor.

Contents

2.1	Introduction	33
2.2	Roche potential	34
2.3	Tides	36
2.4	Wind mass loss and wind mass transfer	37
2.5	Roche-lobe overflow	39
2.5.1	Mass-transfer rate from the donor star	40
2.5.2	Response of the accreting companion	43
2.5.3	Non-conservative mass transfer	44
2.5.4	Common-envelope evolution	48
2.6	Gravitational-wave radiation	52
2.6.1	Binary-star physics that lead to binary black-hole mergers	53
2.7	Summary	55

2.1 Introduction

Observational studies¹ of young stellar populations suggest most of the massive stars are born in binaries or higher multiplicity systems. Massive stars are found with companions in both the field and in clusters (Duchêne and Kraus, 2013; Preibisch et al., 1999; Kobulnicky et al., 2014) and at different metallicities (Sana et al., 2013, 2012; Chini et al., 2013; Sota et al., 2014). The average number of companions per massive primary star ranges between 0.5 and 1.5 (Preibisch et al., 1999; Sana et al., 2013; Kobulnicky et al., 2014; Dunstall et al., 2015; Moe and Di Stefano, 2017; Sana, 2017). The probability density of the orbital separation a of observed massive stellar binaries appears to be roughly proportional to a^{-1} (Opik:1924,Sana:2013,Kobulnicky:2014). However deviations have been observed: particularly at periods of less than a thousand days, where massive stellar binaries appear to favour shorter separations compared an to Öpik law (a^{-1}) (Sana et al., 2013). About 70% of massive stars in binaries are expected to interact with their stellar companion (Sana et al., 2013).

Binary interactions can change the mass of both stars, remove the envelope of the donor, enrich the surface of the accretor, change the apparent age of the star, affect the rotation rates of stars and result in the merger of the two stars. Stars in binary systems evolve through various evolutionary channels which in turn are associated with different observations². Binary interactions in massive stars are linked to astrophysical phenomena such as blue stragglers (McCrea, 1964; van den Heuvel, 1967; Stryker, 1993), Algol systems (Crawford, 1955; Morton, 1960; Hjellming, 1989; Pustyl'nik, 1998), runaway stars (Blaauw, 1961, 1993; van Rensbergen et al., 1996), X-ray binaries (Davidson and Ostriker, 1973; Hutchings et al., 1973; van den Heuvel and De Loore, 1973), peculiar surface helium abundances on main sequence (MS) stars (Tuchman and Wheeler, 1990), ultra-luminous X-ray sources (King et al., 2001;

¹See e.g. Moe and Di Stefano (2017) and Sana (2017) for schematic figures that relate the observational technique to the orbital properties of the binary.

²See Fig. 1 of Han et al., 2020 for a nice schematic overview of evolutionary channels and observations.

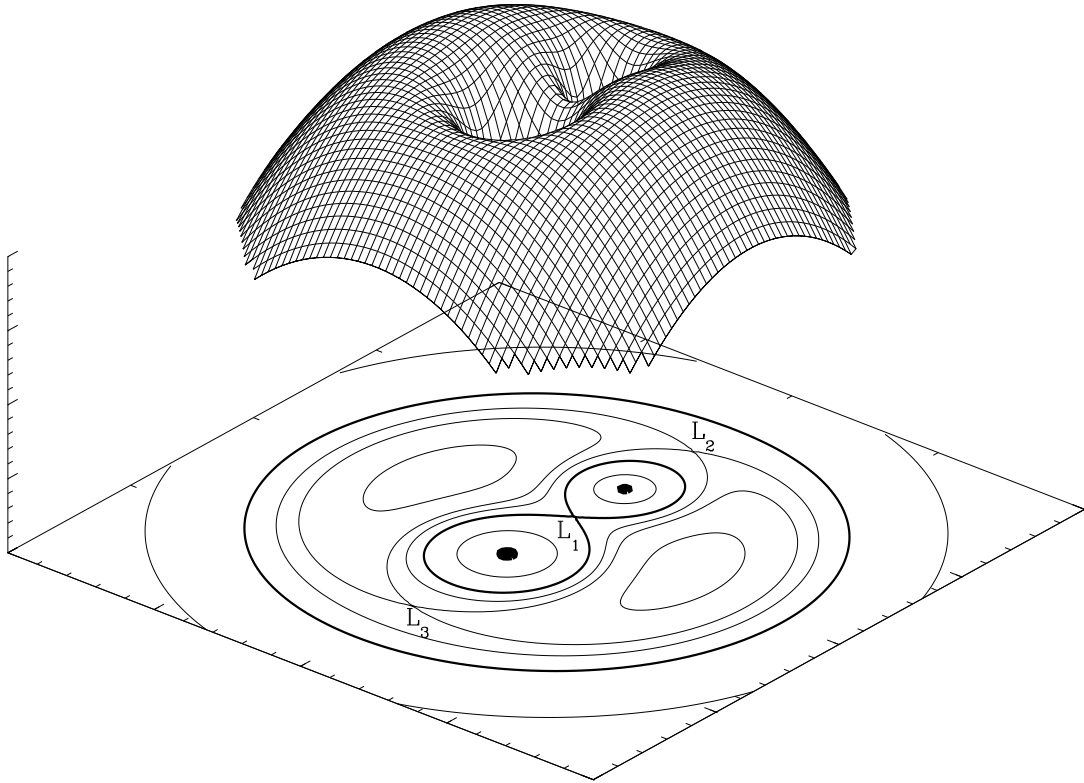


Figure 2.1: A three-dimensional representation of the Roche potential of a binary, where the mass ratio of the point masses is 2. The figure is taken from the lecture notes of van der Sluys (2019). The surface below shows the equipotential lines. The bold equipotential connecting to L_1 depicts the Roche lobes of the two stars. If a star expands and overflows its Roche lobe, then mass is transferred onto the companion through L_1 .

Rappaport et al., 2005), the origin of magnetic fields in massive stars (de Mink et al., 2014; Schneider et al., 2016), luminous red novae (Ivanova et al., 2013a) and the formation of binary neutron stars and black holes (van den Heuvel and Heise, 1972; Tutukov and Yungelson, 1973). Aside from astrophysical events, binary interactions also affect the large scale evolutionary processes such as the enrichment of the interstellar medium (De Donder and Vanbeveren, 1999; de Mink et al., 2009; Izzard et al., 2013) and the ionization of the early universe (Stanway et al., 2016; Götberg et al., 2017).

2.2 Roche potential

In a binary system two stars orbit each other bound by their reciprocal gravitational pull. The total angular momentum of two stars in a binary is the sum of the orbital angular momentum and the rotational angular momentum of each star,

$$J = M_1 M_2 \sqrt{\frac{Ga(1 - e^2)}{M_{\text{tot}}}} + I_1 \omega_1 + I_2 \omega_2, \quad (2.1)$$

where G is the gravitational constant, a the orbital separation, e the eccentricity, $M_{\text{tot}} = M_1 + M_2$ is the total mass of both the stars, I the moment of inertia of a star and ω the angular frequency of a star.

Figure 2.1 depicts two point masses orbiting in a circular binary system and the gravitational potential field in a co-rotating reference frame. The lines in the square plane show the equipotential surfaces. Such a gravitational potential field is known as the Roche potential, as discussed and calculated in great detail by, amongst others, Kopal (1954) and Plavec and Kratochvil (1964). A test mass in the rotating reference frame experiences centrifugal and gravitational forces. At a Lagrangian point L , such as L_2 in Fig. 2.1, a test mass does not experience a net force. A test mass which is initially at rest at L_2 remains in orbit around the stars at L_2 .

Close to a point mass, the equipotential surface describes approximately a sphere centred on the point mass. Further away from the point mass the equipotential starts to become non-spherical. At the inner Lagrangian point L_1 the two equipotential surfaces around each point mass intersect for the first time (see the bold line in Fig. 2.1). The equipotential surface around a point mass, which connects to L_1 , is referred to as a Roche lobe.

The Roche radius is the radius of a sphere with the same volume as the Roche lobe (Kopal, 1954). Eggleton (1983) provides a fitting formula for the Roche radius,

$$R_{\text{RL}} = \frac{0.49q^{2/3}}{0.6q^{2/3} + \ln(1 + q^{1/3})} a, \quad (2.2)$$

where R_{RL} is the Roche radius, a the separation of the binary and q the mass ratio of the system. The Roche radius of the primary is found by using $q = M_1/M_2$ and the Roche radius of the secondary by $q = M_2/M_1$. The above fit to the Roche radius is accurate to within one percent over the entire range of q (Eggleton, 1983).

2.3 Tides

The closer the stellar surface is to the boundary of the Roche lobe, the more the surface deforms and the star becomes approximately an oblate spheroid. The part of the stellar surface which is further away from the centre of the star is darker (von Zeipel, 1924). The effect, called gravitational darkening, depends on the energy transport within the envelope of a star (Lucy, 1967). Gravitational darkening due to the Roche potential is observed for multiple sources such as stars in X-ray binaries (see e.g. Orosz et al., 2011; Ratti et al., 2013).

The bulge on the stellar surface faces the companion star as the stars circle around the centre of mass. The bulge exerts a torque onto the star through tidal effects. The torque comes from either a misalignment between the rotational angular momentum of the star and the orbital angular momentum, an eccentric orbit or a difference between the rotational frequency of the star and the orbital frequency. Tides are commonly divided into equilibrium tides and dynamical tides. A star under the exclusive effect of equilibrium tides would roughly assume the shape of its Roche potential, while remaining in hydrostatic equilibrium. The tides essentially subject the star to drag forces. In the case of a convective envelope these drag forces are dissipated into the envelope by convective eddies (Zahn, 1977). A star under the exclusive effect of dynamical tides can be approximated by an oscillator, excited by the gravitational pull of the companion. When these oscillations are damped, energy is dissipated (Eggleton et al., 1998, and references therein). Equilibrium tides are more effective in stars with convective envelopes whereas dynamical tides dominate in stars with radiative envelopes (Zahn, 1977; Lai, 1997).

The equilibrium tide tends to align the rotational angular momentum of the star

and orbital angular momentum of the binary, synchronize the orbital period and rotational period of the star and circularize the orbit (Darwin, 1879; Hut, 1980, 1981; Eggleton et al., 1998). The same is true for the dynamical tides (Zahn, 1977; Lai, 1997) although in some instances the continuous excitation of the oscillations might result in an increased eccentricity (Eggleton et al., 1998).

The theory of tides successfully explains the orbital properties of giant stars and in turn helps to constrain uncertainties in stellar evolution such as the depth of the convective surface layer (Verbunt and Phinney, 1995). Tidal effects further help to explain the orbits of planets and pre-main-sequence stars (Mazeh, 2008). However, in some cases, such as barium stars, tidal effects seem too efficient in circularizing the orbits (Pols et al., 2003), unless other binary-star physics is responsible for reintroducing the eccentricity of the orbit (see e.g. Izzard et al., 2010, and references therein).

2.4 Wind mass loss and wind mass transfer

Stars lose mass through stellar winds (see Sec. 1.5). Part of the mass lost through winds leaves the binary, draining some angular momentum. A fraction of the wind material can potentially interact with the companion star.

A common assumption to estimate the effect of wind mass loss on the orbital parameters of a binary is that matter leaves isotropically from the surface of the star. Under this assumption, this matter instantaneously leaves the system taking away the orbital angular momentum it had at the surface of the star. In this scenario the orbital separation widens by

$$\frac{\dot{a}}{a} = -\frac{\dot{M}_{\text{tot}}}{M_{\text{tot}}}, \quad (2.3)$$

where wind mass loss is defined as $\dot{M}_{\text{tot}} < 0$.

A star in a binary can interact with the wind of the other star, depending on the orbital properties, peculiar velocity of the system and the velocity of the wind. A

star accretes from the stellar wind of a companion through Bondi-Hoyle-Lyttleton accretion (Hoyle and Lyttleton, 1939; Bondi and Hoyle, 1944). The accretion is less efficient when the velocity of the wind is much faster than the orbital velocity of the accreting star. Winds accelerate outwards from the surface of the star. Therefore, for wide binaries there is little accretion and the winds are fast enough such that equation 2.3 is valid.

In the regime where the orbital velocity is comparable to the velocity of the wind (slow winds), for example if the star is close to filling its Roche lobe, part of the mass beyond the Roche lobe is transferred onto the companion through wind Roche-lobe overflow (RLOF). The mass-accretion rate of wind RLOF possibly results in anisotropic outflows (Theuns et al., 1996; Mohamed and Podsiadlowski, 2007; Chen et al., 2020). Since the wind is no longer isotropically ejected from the original star, the orbital evolution of the system differs from equation 2.3. If the wind velocity is comparable to the orbital velocity and the companion is heavier than the mass-losing star, then the wind mass loss and wind mass transfer results in additional loss of angular momentum and the orbital separation reduces instead of widening (see e.g. Schröder et al., 2021).

When a binary system is tidally locked the orbital frequency is the same as the rotational frequency of the star. Wind mass loss increases the orbital separation and hence decreases the orbital frequency. Thus, the combination of wind mass loss and tidal locking decreases the rotation rate of stars in binaries. However, additional angular momentum loss due to magnetic braking, combined with the tidal locking, shortens the orbital separation (Verbunt and Zwaan, 1981; Ivanova and Taam, 2003; Justham et al., 2006).

Bondi-Hoyle-Lyttleton accretion and wind RLOF are important for the period distribution and surface abundances of lower mass asymptotic giant branch stars in symbiotic binaries (Mohamed and Podsiadlowski, 2007; Izzard et al., 2010; Abate et al., 2013; Saladino et al., 2018; Abate, 2019). Wind RLOF in high-mass X-ray binaries is also linked to detections of ultra-luminous X-ray sources (El Mellah et al.,

2019).

2.5 Roche-lobe overflow

If a star expands and the stellar surface reaches L_1 , the gas at the stellar surface is not uniquely bound to the star. Further expansion results in RLOF and gas flows to the companion star in the form of mass transfer. Here, it is assumed for simplicity that tidal effects have circularized the orbit and synchronized the rotational frequencies of the binary system at the onset of mass transfer (Zahn, 1977; Verbunt and Phinney, 1995), although this may not be valid in very eccentric systems (Sepinsky et al., 2007) or stars where the radial expansion timescale is shorter than the timescale of circularization (Vigna-Gómez et al., 2020). The total angular momentum of the binary is then equal to the orbital angular momentum of the system as given in equation 2.1, with e , ω_1 and ω_2 equal to zero. The change in the separation due to mass transfer is given by

$$\frac{\dot{a}}{a} = 2 \frac{\dot{J}_{\text{orb}}}{J_{\text{orb}}} - 2 \frac{\dot{M}_1}{M_1} - 2 \frac{\dot{M}_2}{M_2} + \frac{\dot{M}_{\text{tot}}}{M_{\text{tot}}}, \quad (2.4)$$

where other forms of mass and angular momentum loss such as magnetic braking are ignored.

Solving for the effects of the mass-transfer phase, such as the change in separation in Eq. 2.4, is a complex problem even in the absence of other mechanisms such as magnetic braking, tides and wind mass transfer that happen before and during the mass-transfer phase. The changes in orbit, angular-momentum loss, mass-transfer rate, mass-accretion rate (and so stellar masses) and Roche radii are all coupled to each other (see Eq. 2.2 and Eq. 2.4). As mentioned in chapter 1, the evolution of a single star is computationally challenging. Furthermore a star is sometimes also driven out of thermal or hydrostatic equilibrium during mass transfer and a binary system possibly has non-symmetric outflows. Therefore a full scale evolution of two stars during mass transfer, accounting for the details of all these phenomena, is

currently not computationally feasible, especially if expanded to entire populations of stars.

Studies often investigate one or a few aspects of mass transfer, while making simplifying approximations for the others. For example, three-dimensional simulations, which focus on the mass-transfer rates and mass loss of stars, may simplify the stars as fully convective polytropes (Regós et al., 2005; D’Souza et al., 2006; Lajoie and Sills, 2010). Hence these results are only valid for a limited number of systems such as low mass stars or white dwarfs. On the other hand, one dimensional stellar evolutionary codes are capable of investigating the response of the stellar structure to mass loss or mass accretion (Kippenhahn and Meyer-Hofmeister, 1977; Ge et al., 2015; Pavlovskii and Ivanova, 2015). However, they rely on assumptions on the amount of mass and angular momentum lost from the system.

The physics of mass transfer can be roughly divided into the following topics: the mass-transfer rate, the efficiency of mass accretion, the amount of angular momentum lost from the system and the stability of mass transfer. What follows is a (crude) description of each of these four topics. This description mostly relies on results presented in papers between 1960 - 1990. The models and assumptions are often more simplistic compared to current simulations but they provide a more intuitive insight into the different physics and their influence on mass transfer in stellar binaries. Furthermore, they provide the foundation of commonly used simplifying approximations for the physics of mass transfer as currently implemented in population-synthesis codes.

2.5.1 Mass-transfer rate from the donor star

Mass transfer changes both the orbital separation and the mass ratio of a binary system and therefore the Roche lobes of the binary (see Eq. 2.2). At the same time, the donor star adjusts its radius in response to mass loss. The more the stellar radius exceeds the Roche lobe, the higher the mass-transfer rate. Here we follow the notation of Hjellming and Webbink (1987) to quantify the response of the stellar

radius to mass loss by using the dimensionless ζ parameter,

$$\zeta = \frac{\dot{R}_D/R_D}{\dot{M}_D/M_D} = \frac{d \ln(R_D)}{d \ln(M_D)}, \quad (2.5)$$

where R_D and M_D are the radius and mass of a mass-donating star. The response of the Roche radius to mass loss is denoted by ζ_{RL} , in which case the stellar radius R_D in Eq. 2.5 is substituted by the star's Roche radius $R_{\text{RL},D}$. In our notation mass loss from the donor corresponds to a negative \dot{M}_D and therefore, if the (Roche) radius of the donor shrinks, the ζ (ζ_{RL}) is positive.

The response of the stellar radius to mass loss depends on the rate of mass loss. The adiabatic response of the donor star to mass loss is denoted by ζ_{ad} and the thermal response of the donor to mass loss is given by ζ_{th} . If $(\zeta_{\text{ad}}, \zeta_{\text{th}}) > \zeta_{\text{RL}}$ then the stellar radius remains inside the Roche radius after mass loss and the mass transfer stops until the donor expands to once again fill its Roche lobe. When $\zeta_{\text{ad}} > \zeta_{\text{RL}} > \zeta_{\text{th}}$, the donor star cannot adjust its radius to the Roche radius while remaining in thermal equilibrium but it does adjust to the Roche radius on adiabatic timescales. The mass-transfer rate is then comparable to the rate if the donor would lose its entire envelope on its thermal timescale (see e.g Morton, 1960; Kippenhahn and Weigert, 1967; Kippenhahn et al., 1967). When $\zeta_{\text{RL}} > \zeta_{\text{ad}}$ the star cannot adjust adiabatically to stay within the Roche lobe and the mass-transfer rate is comparable to the donor star losing its entire mass on its dynamical timescale. This is referred to as dynamically-unstable mass transfer.

To understand the implication of these considerations, let us focus on the specific example of MS donors. Morton (1960) finds that mass transfer from a MS donor consists of two phases, a fast thermal phase and a slow phase driven by the nuclear evolution of the donor. During the first phase the Roche lobe shrinks ($\zeta_{\text{RL}} > 0$) due to mass transfer. The Morton (1960) models of stars in thermal equilibrium are not capable of readjusting to the shrinking Roche lobe ($\zeta_{\text{RL}} > \zeta_{\text{th}}$). The star is driven out of thermal equilibrium and mass transfer proceeds on a thermal timescale. Once the secondary becomes more massive, the Roche lobe of the donor expands as

a result of mass transfer. The MS star regains thermal equilibrium ($\zeta_{\text{th}} > \zeta_{\text{RL}}$). The star expands to fill its Roche lobe due to the nuclear evolution of the core and the second mass-transfer phase proceeds on the nuclear timescale of the donor (Morton, 1960).

According to the works of Morton (1960); Kippenhahn and Weigert (1967); Kippenhahn et al. (1967); Lauterborn (1970) and Paczyński and Sienkiewicz (1972), mass transfer from massive stars is commonly divided into three cases: A, B and C. Case A applies to mass transfer from massive MS stars, similarly to the just mentioned results of Morton (1960). Therefore, case A mass transfer can have a fast phase and a slow phase, the details of which depend on the mass ratio of the system and the assumed physics of mass transfer. Case B considers mass transfer from Hertzsprung gap (HG) stars. The HG star evolves on a thermal timescale as the core contracts and the envelope expands. Thus, regardless of the mass ratio, mass transfer proceeds on thermal timescales and the star loses almost its entire envelope, leaving an exposed helium core (Kippenhahn and Weigert, 1967; Kippenhahn et al., 1967). Case C assumes mass transfer is started by a giant star with a convective envelope after the exhaustion of core helium burning (Lauterborn, 1970). Paczyński and Sienkiewicz (1972) show that in the case of red giant stars, with fully convective envelopes, the envelope expands as a result of mass loss. Therefore, the response of the envelope drives further mass transfer and the donor star loses its entire envelope on timescales comparable to its dynamical timescale.

This section outlines the crucial role of the star and Roche radius responses to mass loss in determining the mass-loss rates and timescales of mass transfer. Of course, the picture presented here is an oversimplification of the complex and changing processes which actually occur during mass transfer. Paczyński and Sienkiewicz (1972) already mention that comparing the values of ζ is indeed not enough to understand the entire mass-transfer phase. They show that, by assuming polytropes for the structure of the star, the timescales of mass transfer from a fully convective donor varies from nuclear timescales to dynamical timescales during a single

mass-transfer phase.

2.5.2 Response of the accreting companion

Suppose a star accretes mass from a companion star. The mass falls from the inner-Lagrangian point L_1 , which is at a distance R_{L1} from the centre of the accreting star, and all the gravitational potential energy is radiated away in the form of luminosity. During a mass-transfer episode the accreting star needs to radiate away the gravitational potential energy at a rate

$$L_{\text{acc}} = \frac{GM_A \dot{M}_A}{R_A} - \frac{GM_A \dot{M}_A}{R_{L1}}, \quad (2.6)$$

where M_A and R_A are the mass and radius of the accreting star. If the energy is not sufficiently radiated away, then the star is driven out of hydrostatic equilibrium. The Eddington luminosity, L_{Edd} , is the maximum luminosity that can be carried by radiation. Hence the critical accretion rate at the stellar surface, assuming spherical symmetry, equals

$$\dot{M}_{\text{crit}} = L_{\text{Edd}} \left(\frac{GM_A}{R_A} \right)^{-1}. \quad (2.7)$$

This critical accretion rate is a theoretical upper limit, assuming spherically symmetric accretion.

The aforementioned accretion rate does not take into account the response of a star to mass accretion. For example, numerical models of main-sequence stars by Kippenhahn and Meyer-Hofmeister (1977) and Neo et al. (1977) show that a main-sequence star increases in both radius and luminosity during accretion if the mass-transfer rate is high enough. Kippenhahn and Meyer-Hofmeister (1977) consider the simplistic picture where the accreted gas has a similar composition to the accretor and the gas accreted spherically symmetrically at a constant rate onto the surface without having any velocity. The accreting star increases in radius and luminosity when the mass-accretion rate is comparable to the thermal timescale of

the star. Neo et al. (1977) show the radius and luminosity of a $20 M_{\odot}$ star starts to increase when the accretion rate is about 60 per cent of the critical accretion rate. A $1.5 M_{\odot}$ star only has to accrete at 1 per cent of its critical accretion rate to increase in size and luminosity. Webbink (1976); Ulrich and Burger (1976); Neo et al. (1977); Flannery and Ulrich (1977) and Kippenhahn and Meyer-Hofmeister (1977) find that the thermal and dynamical mass-transfer rates during case B and case C mass transfer result in an increase in the size of the accreting companion. The radius of an accreting main-sequence star increases in size by a factor $\sim 2 - 10$ (Webbink, 1976; Ulrich and Burger, 1976; Neo et al., 1977; Flannery and Ulrich, 1977; Kippenhahn and Meyer-Hofmeister, 1977).

2.5.3 Non-conservative mass transfer

In this dissertation the mass-accretion rate of a star \dot{M}_A is defined as

$$\dot{M}_A = -\beta\dot{M}_D, \quad (2.8)$$

where β is the mass-accretion efficiency which can take on the values $0 \leq \beta \leq 1$. When the mass-transfer efficiency β is lower than 1, mass is lost from the system and the mass-transfer phase is non-conservative.

Expansion of an accreting companion potentially results in the accreting companion filling its own Roche lobe, depending on the orbital separation of the stars and the mass-transfer rate from the donor star. If both stars fill their Roche lobes then the binary becomes a contact binary. Such a contact binary phase does not necessarily result in the merger of the two stars if the system rotates as a rigid body (Lucy, 1968). However, any additional mass transfer results in an overflow through the outer Lagrangian points and the mass-transfer phase becomes non-conservative.

An alternative mechanism for non-conservative mass transfer is a rotationally-limited mass-transfer phase. Packet (1981) calculates the effects of mass accretion on the rotation rate of a star, assuming the star is uniformly rotating and the absence

of tidal forces. Furthermore, it is assumed that matter is accreted from a disk in the star's equatorial plane and this matter moves at the Keplerian velocity (see also Eq. 1.13). The accreted matter has specific angular momentum,

$$j = \sqrt{GM_A R_A}, \quad (2.9)$$

and mass accretion spins up the star. Packet (1981) find that a star rotates at break-up velocity after accreting about 5 to 10 per cent of its initial mass. The star is no longer capable to accrete from the accretion disk. If mass transfer continues, the disk increases in size. If the mass transfer ceases before the disk fills the Roche lobe, then the disk may gradually be accreted by the star (Packet, 1981). If instead the disk overflows the Roche lobe during the mass-transfer phase, then mass transfer is non-conservative ($\beta < 1$) and mass is lost through one of the Lagrangian points (Packet, 1981). However, Popham and Narayan (1991) find that there exists an accretion-disk configuration for accreting stars where the star and the accretion disk reach an equilibrium rotation rate. Such a configuration allows the star to continue to accrete without spinning up any further. They are unable to confidently state if this equilibrium rotation rate is below the break-up velocity of a star. If a star could reach this equilibrium rotation rate, then the accretion of angular momentum does not reduce the mass-transfer efficiency β .

2.5.3.1 Mass-transfer efficiency β

The mass-accretion efficiency β is often estimated through simplified parameterisations. As mentioned in the previous paragraphs the mass transfer rate from a donor star and the response of an accreting companion relate to the timescales of both stars. Therefore a common approach is to compare the timescale of mass transfer from the donor τ_D and the thermal timescale of the accretor $\tau_{\text{th},A}$ as done in Pols and Marinus (1994); Portegies Zwart and Verbunt (1996); Hurley et al. (2002).

Additional physics can be included to account, for example, for the expansion of an accreting companion. Here an example is given following Hurley et al. (2002),

the companion accretes a fraction β of the mass lost by the donor,

$$\beta = \min \left(1, C \times \frac{\tau_{\text{D}}}{\tau_{\text{th,A}}} \right). \quad (2.10)$$

The mass transfer becomes non-conservative ($\beta < 1$) if the thermal timescale of the accretor exceeds the mass-transfer timescale of the donor by a factor larger than C . If the accretor increases in size, the thermal timescale changes due to the change in R and L (see also Eq. 1.6). Assuming the accreting star keeps a constant luminosity, a value of $C > 1$ represents the factor by which the radius of the accretor increases. However, the interpretation of C can be broadened to incorporate the uncertainty in the timescale of mass transfer from the donor, where a value of $C > 1$ represents an increase in the timescale.

Several studies have looked into constraining the efficiency of mass transfer by comparing modelled populations to populations of semi-detached binaries and Algol systems which form through case A or early case B mass transfer (see e.g. Nelson and Eggleton, 2001; Ibañoğlu et al., 2006; Chen et al., 2006; de Mink et al., 2007; van Rensbergen et al., 2011). Nelson and Eggleton (2001) show that a subgroup of Algol systems is consistent with their models of conservative case A mass transfer. However no single assumption is capable of reproducing all Algol systems (Nelson and Eggleton, 2001; Ibañoğlu et al., 2006; de Mink et al., 2007; van Rensbergen et al., 2011). Furthermore, these findings might not be directly applicable to the evolution of massive stars since only 22 Algol systems contain a massive star with a mass $M > 10 M_{\odot}$ of which 4 are more massive than $20 M_{\odot}$ (Skowron et al., 2017).

Simulations of Wolf-Rayet + O-star binaries indicate that the observed population must have formed through non-conservative mass transfer (Wellstein et al., 2001; Petrovic et al., 2005a; Shao and Li, 2016). This is consistent with case B mass transfer onto a companion star which leaves behind a Wolf-Rayet star. The results appear consistent with the approximation of Eq. 2.10, since the post-MS donor evolves on rapid timescales and corroborates the findings of de Mink et al. (2007) that mass transfer from initially wider systems is non-conservative. However, recent

studies into the formation and distribution of Be X-ray binaries indicate that mass transfer from HG stars could be more conservative ($\beta > 0.3$, Shao and Li, 2014; Vinciguerra et al., 2020).

Population-synthesis studies commonly adopt one of two possibilities: they either assume a fixed mass transfer efficiency of $\beta = 0.5$ (see e.g. Belczynski et al., 2007) or they follow a prescription similar to Eq. 2.10 (see e.g. Hurley et al., 2002; Schneider et al., 2015; Stevenson et al., 2017). Studies using the approximation of Eq. 2.10 recover, in almost all cases, conservative case A mass transfer and non-conservative case B and case C mass transfer (see for example the appendix in Schneider et al., 2015).

2.5.3.2 Loss of angular momentum

Mass leaving a binary system has some angular momentum. In what follows only the orbital angular momentum is considered and the rotational angular momentum is ignored for simplicity. The change in orbital angular momentum is defined as

$$\dot{J}_{\text{orb}} = \dot{M}_{\text{loss}} \gamma \frac{J_{\text{orb}}}{M_{\text{tot}}}, \quad (2.11)$$

where γ determines the specific angular momentum of the mass leaving the system h_{loss} in units of the specific orbital angular momentum. The value of γ depends on the location or mode by which the mass leaves the binary system.

The three most common “mass-loss modes” that are considered are Jeans’s mode, isotropic re-emission and the formation of a circumbinary ring (see e.g. Huang, 1963, for an introduction into these idealized mass-loss modes). Both Jeans’s mode and isotropic re-emission assume that the velocity of the mass leaving a binary system is fast and therefore the mass leaving the binary system does not interact with the binary system itself. In Jeans’s mode mass is ejected spherically symmetrically from the surface of a donor star with the specific angular momentum of the donor star, $\gamma = \frac{M_{\text{A}}}{M_{\text{D}}}$. During isotropic re-emission mass leaves, spherically symmetrically, from the surface of the accreting companion with $\gamma = \frac{M_{\text{D}}}{M_{\text{A}}}$ (see e.g. Pols, 2012,

for a derivation). Mass loss through a circumbinary ring is an idealized scenario where mass leaving a binary system forms a ring around the centre of mass of the binary. The ring rotates with the binary system and the mass leaves through the circumbinary ring. It carries specific angular momentum given by

$$\gamma = \frac{(M_A + M_D)^2}{M_A M_D} \sqrt{\frac{a_{\text{ring}}}{a}}, \quad (2.12)$$

where a_{ring} is the radius of the circumbinary ring (Huang, 1963).

2.5.4 Common-envelope evolution

So far one of the main underlying assumptions for (non-)conservative mass transfer has been that during the mass-transfer phase any mass surrounding the stars is either co-rotating with the binary or leaves without interacting with the binary system. An alternative possibility is the formation of a common envelope (Paczynski, 1976). In this scenario the mass-transfer rate is fast enough (for example during dynamically-unstable mass transfer) such that the envelope of the donor star engulfs the binary system. If the size of a common envelope is larger than several times the orbital separation of the binary, then there is insufficient angular momentum in the system to maintain co-rotation of both the common envelope and the binary (Meyer and Meyer-Hofmeister, 1979; Rasio and Shapiro, 1995).

The loss of co-rotation results in friction between the binary system and parts of the common envelope. Friction allows transfer of angular momentum and gravitational potential energy of the binary orbit into the envelope. The envelope gains angular momentum and is heated up by the transfer of energy from the binary orbit. The loss of gravitational potential energy and orbital angular momentum reduces the orbital separation of the binary (Paczynski, 1976; Meyer and Meyer-Hofmeister, 1979).

Initially common envelopes were studied in the context of the formation of binary pulsars (Taam et al., 1978) or cataclysmic variables (see e.g. Paczynski, 1976; Meyer

and Meyer-Hofmeister, 1979). It is suggested that common-envelope events are responsible for the observed planetary nebulae which host a tight binary (Livio and Soker, 1988; de Kool, 1990). This is especially true for those planetary nebulae which have a bipolar morphology (De Marco, 2009; Passy et al., 2011; Hillwig et al., 2016; Jones and Boffin, 2017, and references therein). Mass ejection during a common-envelope phase might be responsible for luminous red novae (Ivanova et al., 2013b; Pastorello et al., 2019; Howitt et al., 2020). Furthermore, recent population-synthesis studies suggest their importance for the creation of binary neutron stars and binary black holes (amongst others, Smarr and Blandford, 1976; Bethe and Brown, 1998; Voss and Tauris, 2003; Pfahl et al., 2005; Belczynski et al., 2008; Dominik et al., 2012; Kruckow et al., 2018; Giacobbo et al., 2018; Vigna-Gómez et al., 2018; Spera et al., 2019).

Meyer and Meyer-Hofmeister (1979) discuss the multiple effects that need to be taken into account when estimating the effect of a common-envelope event on a binary system such as the orbital parameters of the binary, the geometry of the envelope, the density of the stars, the viscosity of the envelope and the efficiency with which orbital energy of the binary is deposited into the envelope. Nowadays several methods are available to evaluate the common-envelope phase. They explore different physical assumptions and timescales, as a comprehensive study would still be too computationally expensive (for reviews see e.g. Izzard et al., 2011; Ivanova et al., 2013a). Hydro-dynamical simulations, such as those performed by Rasio and Shapiro (1995); Taam and Ricker (2006); Passy et al. (2011), are able to investigate the geometry of the common envelope. However, these simulations typically cover only a few orbital periods of the common-envelope phase (Izzard et al., 2011). One-dimensional simulations are capable to include physics such as explosive nuclear burning (Podsiadlowski et al., 2010) or recombination energy (Ivanova, 2018) which may add to the energy budget of the common-envelope phase, however these simulations rely on simplified assumptions for the geometry of the common envelope.

2.5.4.1 The onset of a common-envelope event and the “ α - λ ” formalism

In some studies, such as the population-synthesis studies in this dissertation, the main questions of interest are to estimate when a common-envelope event starts and if it results in a stellar merger. A stellar merger happens when the binary system does not have enough orbital energy and orbital angular momentum to eject the common envelope. The onset and outcome of a common-envelope event can be estimated by evaluating the dynamical stability of mass transfer and the energy budget of the binary system. Assuming a common-envelope event starts during dynamically-unstable mass transfer, the threshold for a common-envelope event is

$$\zeta_{\text{RL}} > \zeta_{\text{ad}}, \quad (2.13)$$

which approximates when a donor star is unable to stay within its Roche lobe on its dynamical timescale (see e.g. Paczyński, 1976; Hjellming, 1989).

At the onset of the mass-transfer phase, the envelope of the donor is initially bound to the core of the star with a binding energy (Paczyński, 1976; Webbink, 1984),

$$E_{\text{bind}} = -\frac{GM_{\text{D}}M_{\text{env,D}}}{\lambda R_{\text{D}}}, \quad (2.14)$$

where $M_{\text{env,D}}$ is the envelope mass of the donor and λ a fitting parameter describing the density distribution of the envelope (de Kool, 1990). The amount of orbital energy released when a binary spirals in, from an initial orbital separation of a_i to a final orbital separation of a_f is

$$\Delta E_{\text{orb}} = -\frac{GM_{\text{D}}M_{\text{A}}}{2a_i} + \frac{GM_{\text{core,D}}M_{\text{A}}}{2a_f}, \quad (2.15)$$

where $M_{\text{core,D}}$ is the mass of the core of the donor.

To estimate if a common-envelope event results in a stellar merger, the binding energy of the envelope of the donor star is compared to the orbital energy of the

binary system. The binary system is able to expel the envelope if there is enough orbital energy,

$$E_{\text{bind}} < \alpha \Delta E_{\text{orb}}, \quad (2.16)$$

where α determines the efficiency with which the orbital energy is injected into the envelope (Livio and Soker, 1988). Note that the above approximation does not take into account parameters and processes such as the timescales of the spiral-in, the transfer of angular momentum and subsequent spin up of the envelope and the three dimensional configuration of the common envelope (for a discussion and references see e.g. Livio, 1989; Iben and Livio, 1993; Izzard et al., 2011 and Ivanova et al., 2013a). Alternative methods for evaluating the outcomes of common-envelope events include comparing the orbital angular momentum before and after a common-envelope event (see e.g. Nelemans et al., 2000).

de Kool (1990) finds that the number of binaries in nebulae with orbital periods less than a day is reasonably explained by a value $\alpha = 1$, whereas Livio and Soker (1988) quote $\alpha = 0.3$ as a crude average. More recent studies of a population of post common-envelope binaries, where a white-dwarf orbits a main-sequence star, also indicate that the average value of α ranges from 0.25 to 0.3 (Zorotovic et al., 2010; Toonen and Nelemans, 2013), although the value of α might differ for individual systems (Zorotovic et al., 2010; De Marco et al., 2011). Furthermore, these results are mostly relevant for low-mass stars and to date only about 5% of the observed post common-envelope binaries host a massive star (Kruckow et al., 2021).

The value of α during common-envelope evolution of massive stars remains uncertain. Moreover, some studies suggest additional energy sources such as recombination of helium in the common envelope (Livio, 1989; Ivanova, 2018) or explosive nuclear reactions (Podsiadlowski et al., 2010) help the ejection of the envelope. In some cases this could result in $\alpha > 1$. Passy et al. (2011) perform hydrodynamical simulations of the common-envelope phase and similarly conclude that recombination energy is needed to eject the envelope. Therefore, the value of α could be larger

than 1, if the recombination energy is not included in λ .

The aforementioned studies do not necessarily contradict each other. Aside from α the binding energy parameter λ is also uncertain. Stellar-evolution codes indicate that the binding energy λ of massive stars range from 0 to 5 depending on the mass and evolutionary phase of the star (Tauris and Dewi, 2001; Xu and Li, 2010a,b; Loveridge et al., 2011), whereas for low-mass AGB stars ($M < M_\odot$) λ could be as high as 100 (Dewi and Tauris, 2000). Therefore, differences in estimates of the value of α might actually be due to a difference in the binding energy of the envelope.

Studies (see e.g. Dominik et al., 2012; Kruckow et al., 2018; Giacobbo et al., 2018; Vigna-Gómez et al., 2018; Spera et al., 2019) show that the choice of α and λ has a considerable effect on rate estimates of binary black hole mergers. For some models the rate of binary black hole mergers differs by an order of magnitude solely due to different choices for α .

2.6 Gravitational-wave radiation

A consequence of the theory of general relativity by Einstein is that two point masses in a binary emit gravitational waves. The emission of gravitational waves drains gravitational potential energy and orbital angular momentum. Consequently the orbital separation of two point masses m_1 and m_2 , or average orbital separation in case of a non-circular orbit, in a binary decreases over time,

$$\left\langle \frac{da}{dt} \right\rangle = -\frac{64}{5} \frac{G^3 m_1 m_2 M}{c^5 a^3 (1-e^2)^{7/2}} \left(1 + \frac{73}{24} e^2 + \frac{36}{96} e^4 \right), \quad (2.17)$$

where G is the gravitational constant, c the speed of light, a the semimajor axis of the orbit, e the eccentricity and M the total mass of the binary system (Peters, 1964). In addition the orbit also circularises (Peters, 1964),

$$\left\langle \frac{de}{dt} \right\rangle = -\frac{304}{15} e \frac{G^3 m_1 m_2 M}{c^5 a^4 (1-e^2)^{5/2}} \left(1 + \frac{121}{304} e^2 \right). \quad (2.18)$$

Equations 2.17 and 2.18 can be used to calculate the time it takes for a binary with initial separation a_0 and initial eccentricity e_0 to spiral in and merge due to the emission of gravitational waves,

$$t(a_0, e_0) = \frac{15}{304} \frac{c^5}{G^3 m_1 m_2 M} \left[\frac{a_0(1 - e_0^2)}{e_0^{12/19}} \left(1 + \frac{121}{304} e_0^2 \right)^{-870/2299} \right]^4 \quad (2.19)$$

$$\times \int_0^{e_0} \frac{e^{29/19} [1 + (121/304)e^2]^{1181/2299}}{(1 - e^2)^{3/2}} de.$$

The time for two solar-mass stars in a circular binary with an orbital separation of $2 R_\odot$ to spiral in and collide due to gravitational waves is $\sim 10^9$ yr. The effect of gravitational-wave emission on the evolution of two low-mass stars in a binary is already discussed in Paczyński (1967b), even before observations of the orbital decay of two neutron stars in the Hulse-Taylor binary (Hulse and Taylor, 1975; Weisberg and Taylor, 2005). The loss of angular momentum drives mass transfer between low-mass stars and explains double white-dwarf binaries with periods of less than a day (Paczynski, 1967a). However, for two stars of $10 M_\odot$ with an orbital separation of $20 R_\odot$ the inspiral time is $\sim 10^{10}$ yr. The evolutionary timescale of such a star is 10^7 yr and hence the influence of gravitational waves is negligible during its lifetime. However, gravitational waves are important after both massive stars have collapsed and formed a double compact-object binary. In isolated binary evolution, the double compact object binary does not experience interactions with other stars which harden the binary. It is the emission of orbital angular momentum through gravitational waves that hardens the double compact object binary until it merges.

2.6.1 Binary-star physics that lead to binary black-hole mergers

One method to constrain uncertainties in the physics of binary stellar evolution is by simulating large populations of stellar binaries to predict various observable parameters such as stellar masses and separations (see e.g. Yungelson, 2005; Eldridge, 2017 and Han et al., 2020 for a general introduction to binary population synthesis).

In addition the simulations predict which binary interactions, such as mass-transfer phases and common envelopes, lead to different astrophysical phenomena. Interactions leading to the formation and eventual merger of a binary black hole are a particularly timely example in view of recent gravitational-wave observations (Abbott et al., 2016b, 2018a, 2019; Abbott et al., 2021). In turn a statistical comparison between the observed and simulated population of binary black-hole mergers may help to constrain the formation channels of these phenomena and the binary-star physics involved.

Despite all the uncertainties in binary-star physics, studies report a similar series of events that lead to the formation and merger of binary black holes coming from isolated binary evolution. This series of events is commonly referred to as a formation channel. What follows is a brief description of the “classic” formation channel of binary black holes as described in e.g. Tutukov and Yungelson (1993); Lipunov et al. (1997); Belczynski et al. (2002a); Belczynski et al. (2016) and Stevenson et al. (2017). Fig. 2.2 shows a diagram³ of the evolutionary channel, where in this case the black hole masses are similar to the gravitational-wave event GW151226 (Abbott et al., 2016a). The formation channel shows that the formation of binary black holes relies on all of the aforementioned physics of mass transfer and its uncertainties (not to mention uncertainties that come from single stellar evolution). A binary system starts with two massive stars on the MS. The more massive primary star evolves faster and expands first. Expansion results in the primary overflowing its Roche lobe, most likely during the HG or core-helium-burning (CHeB) phase. The following mass-transfer phase is dynamically stable and, depending on the thermal timescale of the accretor, the companion accretes a fraction of the envelope of the primary. The primary is stripped of its envelope and becomes a helium main sequence (HeMS) star, which can be observed as a Wolf-Rayet star. The primary continues to evolve and finally collapses into a black hole (BH). The binary consists of a MS star in

³Diagrams like Fig. 2.2 are a long-standing tradition in binary evolution; see e.g. Paczyński (1966); Kippenhahn et al. (1967) for a mass-transferring binary and Tutukov and Yungelson (1973) and van den Heuvel and De Loore (1973) for diagrams of the formation of double neutron stars.

orbit with a BH. The MS secondary continues to fuse hydrogen in its core until it too evolves away from the MS and expands. The secondary star fills its Roche lobe during the HG or CHeB phase and starts a mass transfer episode. The mass transfer episode is dynamically unstable and results in a common-envelope (CE) event. After expelling the envelope the secondary, a HeMS star, orbits the black-hole primary at a short orbital separation of several solar radii. The secondary collapses into a BH and the final binary black-hole spirals in and merges due to the emission of gravitational waves. The assumed formation channel of binary black holes makes them interesting candidates to use as constraints on binary-star physics such as the physics of mass transfer.

2.7 Summary

This chapter briefly described some of the physics involved in binary stellar evolution, in particular mass transfer. Binary stellar evolution has already been extensively studied. The concepts and approximations made during the 1960s and 1970s are still very much in use today. Binary interactions alter the properties of stars and their orbits and are linked to multiple astronomical phenomena. However, there still are uncertainties in the physics involved in binary interactions. Those same uncertainties also affect the estimates for the formation and merger rates of binary black holes, which is the topic of this dissertation. This is particularly true for the physics of mass transfer and common-envelope evolution, which is predicted to play a dominant role (see Fig. 2.2) in the formation of binary black-hole mergers.

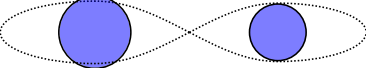
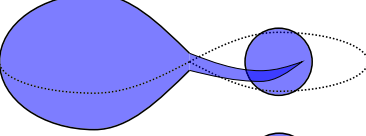
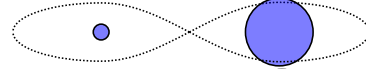
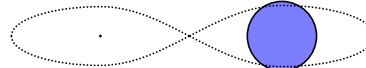
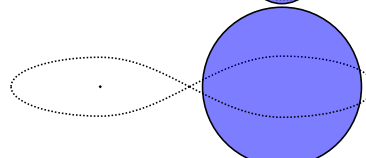
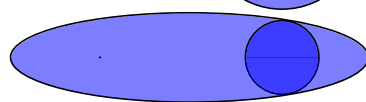


Time (Myr)	M_1 (M_\odot)	ST ₁ –		ST ₂ –	M_2 (M_\odot)	a (R_\odot)
0.0	63.6	MS		MS	27.8	729.93
4.1	60.4	HG		MS	27.7	757.5
4.12	24.6	HeMS		MS	30.6	622.07
4.49	19.1	BH		MS	30.6	692.7
7.21	19.1	BH		CHeB	30.3	697.48
7.42	19.1	BH		CHeB	29.7	706.33
7.42	19.1	BH		HeMS	10.6	5.18
7.88	19.1	BH		BH	5.7	8.82

Figure 2.2: Assumed evolutionary channel of the gravitational-wave event GW151226 (Abbott et al., 2016a) as published in Stevenson et al. (2017). The binary initially starts with two massive MS stars. The primary star (left) expands during the HG and overflows its Roche lobe, transferring mass onto the companion star. The secondary star accretes a few solar mass and the remainder of the mass is isotropically re-emitted from its stellar surface through fast winds. The primary star is left as an exposed HeMS star which continues to evolve and collapses into a BH. The secondary star evolves until it too fills its Roche lobe during the CHeB phase. The mass transfer phase is determined to be dynamically unstable and starts a common-envelope event. After the envelope is expelled the exposed HeMS star orbits the primary BH at a tight separation of $\sim 5 R_\odot$. The secondary collapses into a BH and the BH binary tightens through the emission of gravitational-waves until it merges. The stars are simulated at a metallicity of $Z = 0.002$ using the alpha-version of the COMPAS population-synthesis code (for more information see Stevenson et al., 2017).

Chapter 3

COMPAS

The previous chapters provided a brief introduction into the physics of single and binary stellar evolution and their uncertainties. One approach to constraining these uncertainties, as undertaken in this dissertation, is by simulating large populations of stars using different assumptions to statistically compare the simulated populations to observations. In some cases such population-synthesis studies require the evolution of thousands to millions of binary systems (see e.g. chapter 4). In detailed one-dimensional stellar-evolutionary codes evolving a single binary could take a few hours or more. Rapid population-synthesis codes often use pre-calculated grids or analytic fits of a population of stars combined with methods to interpolate between results, for example at different initial masses or metallicities. It takes as little as 10 milliseconds to evolve a single binary, enabling the creation of large populations of stars using rapid population-synthesis codes.

This chapter describes the assumptions and physics used in this thesis to estimate the rate of black-hole and neutron-star mergers forming through isolated binary evolution. The rapid population-synthesis code, used to solve the evolution of massive stellar binaries, is called **COMPAS**, acronym for Compact Object Mergers: Population Astrophysics and Statistics. **COMPAS** is a rapid population-synthesis code similar to codes such as **BSE** (Hurley et al., 2000, 2002), **STARTRACK** (Belczynski et al., 2002b, 2008), **SeBa** (Portegies Zwart and Verbunt, 1996; Nelemans and van den Heuvel, 2001; Toonen et al., 2012), **binary_c** (Izzard et al., 2004b, 2006, 2009; Izzard et al.,

2017) and MOBSE (Giacobbo et al., 2018).

This thesis relies on the alpha-version of COMPAS (Stevenson et al., 2017; Vignagómez et al., 2018), which predates the public version found on <https://compas.science/> as published in Team COMPAS: J. Riley et al. (2021). Section 3.1 discusses the assumed initial distributions of massive stars used in this dissertation. Section 3.2 describes the single stellar models. Section 3.3 explains the approximations used to model the physics of mass transfer. Section 3.4 mentions some of the uncertainties coming from the assumptions in our models.

Hereafter, the most and least massive star in a binary at zero-age main sequence (ZAMS) are referred to as the primary and the secondary respectively. During mass transfer, the stellar parameters of the mass-losing star are indicated by the subscript D (donor), whereas the stellar parameters of the accreting star are indicated by the subscript A (accretor). The mass ratio is defined as $q = M_D/M_A$ unless written otherwise.

Contents

3.1	Initial distributions	60
3.2	Stellar evolution	60
3.2.1	Single stellar models	60
3.2.2	Supernovae	61
3.3	Binary physics	64
3.3.1	Onset and stability of mass transfer	64
3.3.2	Dynamically-stable mass transfer	65
3.3.3	Dynamically-unstable mass transfer: common-envelope evolution	70
3.4	Uncertainties on our assumption on the merger rates of black holes and neutron stars	71

3.1 Initial distributions

The massive stellar binaries are evolved from ZAMS. Their initial orbital properties are sampled from a set of distributions, whose details are based on observations. We assume that 70 per cent of all stars are born in binaries (Sana et al., 2012). Both the masses of single stars, and the mass of the primary follow the initial mass function of Kroupa (2001). The companion mass is drawn from a uniform distribution of $q = M_{\text{secondary}}/M_{\text{primary}}$ ranging from 0 to 1. The initial orbital separation a is distributed as a^{-1} between $-1 \leq \log_{10}(a/\text{AU}) \leq 3$ (Öpik, 1924; Kobulnicky et al., 2014). All systems are initially assumed circular. For simplicity, we consider the distributions to be uncorrelated to each other and independent of metallicity and age of the Universe. The distributions and uncertainties related to the initial metallicities of stars are discussed in chapter 4.

3.2 Stellar evolution

3.2.1 Single stellar models

COMPAS uses the analytic fits to single stellar models of Hurley et al. (2000, 2002) which include the earlier works of Tout et al. (1996, 1997). The fits are made to a grid of stellar models computed by Pols et al. (1998). The grid of evolutionary tracks consists of 25 masses ranging from 0.5 to $50M_{\odot}$ at metallicities of $Z = 0.0001, 0.0003, 0.001, 0.004, 0.01, 0.02$ and 0.03. The models are computed using the Eggleton code (Eggleton, 1971, 1972; Pols et al., 1995). The fits of Hurley et al. (2000) are made to a set of tracks of Pols et al. (1998) which include enhanced mixing in the core due to overshooting (denoted as OVS in Pols et al., 1998). The analytic fits describe the luminosities and radii of stars as a function of the age of a star. The accuracy of the fits is reported to have root-mean-square errors of three to five percent (Tout et al., 1996; Hurley et al., 2000) compared to the original stellar tracks. The effective surface temperature T_{eff} is recovered by the Stefan–Boltzmann law. Core masses for giant stars are recovered by a core mass–luminosity relation

(Tout et al., 1997; Hurley et al., 2000). The stellar tracks do not include effects of wind mass loss. The effect of wind mass loss is modelled by ‘ageing’ the star (see Sec 7.1 in Hurley et al. 2000). Wind mass-loss rates are calculated using the prescriptions of Hurley et al. (2000) with the updated recipes of Belczynski et al. (2010, and references therein). Chapter 6 explores some of the uncertainties regarding the wind mass-loss rates from Wolf-Rayet stars.

3.2.2 Supernovae

The condition for core collapse, possibly followed by a SN, is based on the total mass of the star, its helium core, and its carbon-oxygen core (see also the discussion of Pols et al. 1998; Hurley et al. 2000). The SN is treated as an instantaneous event which leaves a massive compact remnant (except pair-instability SNe). A fraction of the envelope which is expelled during the SN could fall back onto the remnant. The dependence of fall-back fraction and the remnant mass on the mass of the carbon-oxygen core at the moment of the SN is based on the prescription by Fryer et al. (2012), where in this dissertation the “delayed model” is used. The “delayed model” does not assume a mass gap for remnant masses in the range of $\sim 2\text{--}5M_{\odot}$. By not assuming this mass gap, we can explore whether other physics or selection effects can explain the lack of observed remnants with masses between $\sim 2\text{--}5M_{\odot}$. A mass gap is also not consistent with observations of microlensing, unless black holes (BHs) receive substantial kicks during the supernova (Wyrzykowski and Mandel, 2019).

Chapter 4 does not yet account for possible pair-instability supernovae (PISNe) or pulsational pair-instability supernovae (PPISNe), since these were not yet implemented in the COMPAS code. Chapters 5 and 6 do account for these types of supernovae, by adopting the model based on Marchant et al. (2019) as implemented and described in Stevenson et al. (2019).

The direction of a kick is isotropically distributed in the frame of reference of the exploding star. Kicks of core-collapse supernovae are drawn from a Maxwellian distribution with a one-dimensional root-mean-squared speed of $\sigma = 265 \text{ km s}^{-1}$

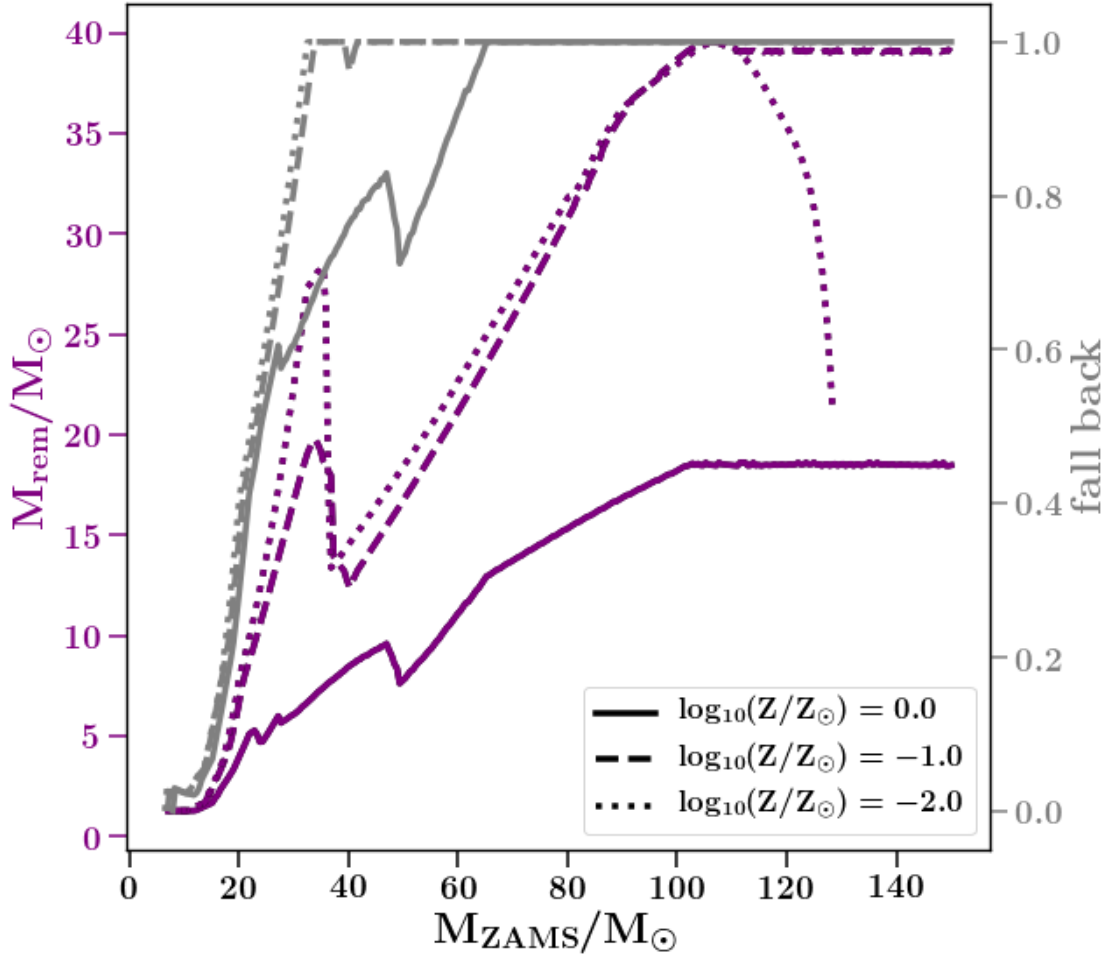


Figure 3.1: Purple: Remnant mass distribution of the “delayed” model by Fryer et al. (2012) for single stellar models from COMPAS (including fall back). Grey: The fall-back fraction of the envelope. The remnants are more massive at lower metallicities, predominantly due to reduced wind mass-loss rates. Note that the remnant mass and fall back by Fryer et al. (2012) are monotonically increasing functions for increasing core and envelope masses. The variations come from the final envelope masses at the onset of the supernova (SN), which vary because different initial masses experience wind mass-loss rates through different discontinuous prescriptions (see e.g. Fig. 6.5).

based on observations of isolated pulsars (Hobbs et al., 2005). Natal kicks of electron-capture supernovae, or supernovae whose progenitors are ultra stripped by a neutron star companion, are drawn from a Maxwellian distribution with one-dimensional root-mean-square kick of 30 km s^{-1} (Pfahl et al., 2002; Podsiadlowski et al., 2004; Tauris et al., 2015, 2017; Vigna-Gómez et al., 2018). In the case where a fraction of the envelope falls back onto the remnant, the kick is linearly reduced by the fall-back fraction f_b (Fryer et al., 2012),

$$V_{\text{kick}} = (1 - f_b)V_{\text{kick,drawn}}, \quad (3.1)$$

where $V_{\text{kick,drawn}}$ is the velocity of the kick drawn from the Maxwellian distribution and V_{kick} is the velocity applied to the remnant.

Figure 3.1 shows the remnant mass and fall-back fraction f_b as a function of the initial mass of a star at several metallicities. On average wind mass-loss rates decrease at lower metallicities. A star at a lower metallicity therefore retains more mass during its lifetime, resulting in a more massive core and remnant compared to a star of similar mass at a higher metallicity (see also Belczynski et al., 2010; Spera et al., 2015; Stevenson et al., 2017).

In this dissertation, the stellar models are extrapolated beyond the grid of initial masses of modelled by Pols et al. (1998), which extended to $M_{\text{ZAMS}} \leq 50 M_{\odot}$. Spera et al. (2015) compare the remnant masses calculated using the population-synthesis code **SSE**, on which **COMPAS** is based, to those calculated using the population-synthesis code **SEVN**, which relies on stellar tracks computed with **PARSEC** (Bressan et al., 2012) with initial masses ranging between $0.1 M_{\odot} - 350 M_{\odot}$. Spera et al. (2015) show that the remnant masses estimated by **SEVN** are close to identical to those coming from **SSE** for masses below $M_{\text{ZAMS}} = 60 M_{\odot}$. Remnant masses coming from more massive stars differ at most by 20 per cent.

3.3 Binary physics

In COMPAS we currently do not account for the change in orbital separation through tidal effects, magnetic braking and gravitational-wave radiation. It is, however, assumed that tides are efficient in circularizing the orbit before the onset of a mass-transfer episode (Portegies Zwart and Verbunt, 1996; Hurley et al., 2002). The strength of tides and their capability to rapidly circularise the binary of massive stars before mass transfer is debatable (see e.g. Zahn, 1977; Hut, 1980; Sepinsky et al., 2007; Vigna-Gómez et al., 2020). Few O-stars show magnetic fields (Ramírez-Agudelo et al., 2013). Moreover magnetic fields are mostly found in single massive stars and not in massive stellar binaries (Schneider et al., 2016, and references therein). Therefore, magnetic braking is currently not taken into consideration. As mentioned in Sec. 2.6, the short lifetimes of massive stars imply that gravitational waves have a negligible impact during their evolution. Therefore, the alpha-version of COMPAS does not include the effect of gravitational-wave emission during the lifetime of the stars, only after the formation of a double compact object. The alpha-version of COMPAS does not include Bondi-Hoyle-Lyttleton accretion (Hoyle and Lyttleton, 1939; Bondi and Hoyle, 1944) nor does it take into account stellar rotation.

This last paragraph implies that, in COMPAS, the orbit of massive stellar binaries only changes due to wind mass-loss (see Eq. 2.3), supernovae and mass transfer. What follows is a brief summary of the physics of mass transfer, as implemented in COMPAS.

3.3.1 Onset and stability of mass transfer

Mass transfer between two stellar companions is initiated when at least one of the stars fills its Roche lobe (see also Sec. 2.2). We check for this condition by comparing the radius of each star R_* to its Roche radius R_{RL} ; if for at least one of the stars $R_* > R_{\text{RL}}$, we assume that the binary system is experiencing a mass-transfer episode. To estimate the Roche radius, we use the fit by Eggleton (1983):

$$R_{\text{RL}} = a \frac{0.49q^{2/3}}{0.6q^{2/3} + \ln(1 + q^{1/3})}, \quad (3.2)$$

where a is the orbital separation and q is the mass ratio between the stars. The Roche radius of the donor star is then found by $q = M_{\text{D}}/M_{\text{A}}$, where subscript D refers to the donor star and subscript A to the accreting companion.

Mass transfer is determined to be dynamically stable (see also chapter 2) if

$$\zeta_{\text{ad}} > \zeta_{\text{RL}}. \quad (3.3)$$

For massive main sequence (MS)/Hertzsprung gap (HG) stars we adopt simple estimates, based on detailed calculations by Ge et al. (2015), and set their correspondent ζ_{ad} respectively to $\zeta_{\text{ad}} = 2$ and $\zeta_{\text{ad}} = 6.5$. For more evolved stars, ζ_{ad} is given by Soberman et al. (1997). In chapter 5 we show the impact of our assumptions on ζ_{ad} for post-MS stars, on the rates and formation channels of binary black holes. Mass transfer from helium main sequence (HeMS) and post-HeMS stars is always assumed to be stable in COMPAS. This assumption differs substantially from other population-synthesis codes and is adopted based on its ability to recover the orbital periods and eccentricities for double neutron stars in the Galaxy (Vigna-Gómez et al., 2018). COMPAS currently does not differentiate between prompt and delayed dynamical instability of mass transfer. In the latter, a thermally stable mass-transfer phase precedes a dynamical instability. In other words, if at the onset of a mass-transfer episode $\zeta_{\text{ad}} > \zeta_{\text{RL}}$, then the entire mass-transfer episode is considered dynamically stable in COMPAS.

3.3.2 Dynamically-stable mass transfer

Solving a dynamically-stable mass-transfer phase requires knowledge of the mass-transfer rate, mass-accretion-rate and angular momentum lost from the binary system. Each of these is solved for at the onset of a mass-transfer episode after which

the stellar and orbital parameters are adjusted for the effects of mass transfer.

3.3.2.1 Mass-transfer rate

The mass-transfer rate is determined by the timescale of the expansion and the change in the size of the Roche radius of a donor star. Mass transfer stops once the radius of a donor star fits inside its Roche lobe, $R_D < R_{RL}$.

The fits to stellar models by Hurley et al. (2000) describe stars which are in thermal and hydrostatic equilibrium. Therefore, we cannot self-consistently determine when $R_D < R_{RL}$ if the mass transfer proceeds on thermal or dynamical timescales. Instead we choose to strip the entire envelope of a donor star, $M_{D,env}$ in a single timestep. However, to calculate the mass-transfer rate and mass-accretion efficiency, β , we use the thermal or dynamical timescale of a donor star and not the single timestep to avoid unrealistically high mass-transfer rates.

Mass transfer from a MS donor star could consist of both a fast mass-transfer phase on the thermal timescale of the donor and a slower mass-transfer phase on the nuclear timescale of the donor. During conservative mass transfer the transition from the fast to the slow mass-transfer phase happens when the mass-ratio of the system is approximately unity¹. In COMPAS, during the fast mass-transfer phase, a MS donor star is stripped of its mass, in a single timestep, until the donor star fits inside its Roche radius whilst in thermal equilibrium. To evaluate if a donor star fits inside its Roche radius we simultaneously evaluate the radius of the donor star after losing an amount of ΔM and the Roche radius of the donor star after having transferred an amount of ΔM . The mass-transfer rate is found by dividing ΔM by the thermal timescale of the donor star. A similar procedure is used to evaluate the slow nuclear-timescale mass-transfer phase, however in this case the mass-transfer

¹The threshold of $q = 1$ between thermal- and nuclear-timescale conservative Case A mass transfer is based on the change in the sign of the derivative of the orbital separation, \dot{a} , in Eq. 2.4. At $q \leq 1$ the orbit widens in response to mass transfer. However, assuming the donor star is initially more massive than the accretor, the Roche radius of a donor already widens at $q \approx 1.16$ during conservative mass transfer, where $q = M_D/M_A$. The value of q at the transition from the fast to the slow mass-transfer phase differs during non-conservative mass transfer and depends on the amount of angular momentum lost from the binary system.

rate is found by dividing ΔM by the nuclear timescale of the donor star.

Our approach for MS mass transfer differs from other population-synthesis codes such as the ones presented by Hurley et al. (2002); Belczynski et al. (2008); Toonen et al. (2012) and Spera et al. (2019). A comparison of our results to **STARTRACK** showed that we recovered similar values for β . Therefore, the orbital evolution is also relatively similar, aside from the timescale of mass transfer and the amount of widening due to wind mass loss.

A HG star expands on a thermal timescale, driven by the contraction of the stellar core. Therefore, the mass-transfer rate proceeds on a thermal timescale (Kippenhahn and Weigert, 1967; Kippenhahn et al., 1967) and is calculated by dividing the mass of the envelope of a donor star by its thermal timescale, where in **COMPAS** the thermal timescale is defined as

$$\tau_{D,\text{th}} = \frac{GM_{\text{D}}M_{\text{D,env}}}{R_{\text{D}}L_{\text{D}}}, \quad (3.4)$$

and therefore the mass-transfer rate equals

$$\dot{M}_{\text{D}} = \frac{M_{\text{D,env}}}{\tau_{D,\text{th}}}. \quad (3.5)$$

In **COMPAS** it is assumed that stars on the first giant branch (FGB) and stars which have ignited helium in their cores have fully-convective envelopes. It is commonly assumed that mass loss from a star with a convective envelope results in the expansion of the envelope (see e.g. Paczyński and Sienkiewicz, 1972). Therefore, it is assumed in **COMPAS** that mass transfer from stars with convective envelopes proceeds on the dynamical timescale of the donor star, where we define the dynamical timescale as

$$\tau_{\text{dyn}} = \sqrt{\frac{2R_{\text{D}}^3}{GM_{\text{D}}}}. \quad (3.6)$$

Considering an envelope as fully convective based on the stellar type of a star has

been used in the models in Stevenson et al. (2017); Vigna-Gómez et al. (2018) and in chapter 4. In chapter 5 this assumption is reconsidered and compared against a prescription which determines if a stellar envelope is fully convective based on the effective surface temperature, T_{eff} , of a star.

For HeMS stars, we calculate the mass-transfer rate using the same procedure as for MS stars. The mass-transfer rates of helium Hertzsprung gap (HeHG) and helium giant branch (HeGB) stars are estimated similarly to HG and stars with fully convective envelopes respectively.

3.3.2.2 Mass-accretion rate

To define the maximum accretion rate of an accreting, non-degenerate star $\dot{M}_{\text{A,max}}$, we firstly assume that the star does not significantly change its radius or luminosity during mass transfer. For this condition to hold we require that the gravitational potential energy introduced by the accreted matter is balanced by the outflowing energy,

$$\frac{G M_{\text{A}} \dot{M}_{\text{A,max}}}{R_{\text{A}}} = L_{\text{A}} \implies \dot{M}_{\text{A,max}} \sim \frac{R_{\text{A}} L_{\text{A}}}{G M_{\text{A}}} \approx \frac{M_{\text{A,env}}}{\tau_{\text{th}}}, \quad (3.7)$$

where, for MS accreting stars, the $M_{\text{A,env}}$ in the last expression is substituted with M_{A} . The fraction of the mass gained by a non-degenerate accretor can then be described by the β parameter,

$$\beta = \min \left(1, C \times \frac{\dot{M}_{\text{A,max}}}{\dot{M}_{\text{D}}} \right), \quad (3.8)$$

where the multiplicative factor C is set to 10, following Tout et al. (1997) and Hurley et al. (2002). With this factor we effectively relax our previous assumption in Eq. 3.7, where an accreting star does not change in radius or luminosity (see also Sec 2.5.3.1). The actual mass accretion rate is then found by

$$\dot{M}_{\text{A}} = \beta \dot{M}_{\text{D}}, \quad (3.9)$$

and the consequent rate of mass lost from the system equals

$$\dot{M}_{\text{loss}} = (1 - \beta)\dot{M}_{\text{D}}. \quad (3.10)$$

If instead the accretor is a compact object, i.e. a white dwarf, a neutron star or a black hole, the accretion flow is assumed to be Eddington limited. In this case $\dot{M}_{\text{A,max}}$ is defined as:

$$\dot{M}_{\text{A,max}} = \frac{4\pi G m_{\text{p}} M_{\text{A}}}{\varepsilon c \sigma_{\text{t}}}, \quad (3.11)$$

where m_{p} is the mass of the proton, ε is the fraction of energy that is radiated away, c the speed of light and σ_{t} the Thomson cross section. Mass transfer onto a neutron star or a black hole is almost always completely non-conservative, $\beta \approx 0$, due to the rapid mass-transfer rate compared to the Eddington-limited mass-accretion rate.

3.3.2.3 Angular-momentum loss

During dynamically-stable mass transfer, we assume gas flows from the donor star through the inner Lagrangian point and reaches the surface of the companion star. Any mass not accreted by the companion star leaves the binary system draining an amount of the orbital angular momentum estimated from,

$$\dot{J}_{\text{orb}} = \dot{M}_{\text{loss}} \gamma \frac{J_{\text{orb}}}{M_{\text{tot}}}, \quad (3.12)$$

where γ determines the specific angular momentum of the mass leaving the system h_{loss} . Throughout this study we assume that mass is lost by isotropic re-emission from the surface of the accretor and γ is given by (Pols, 2012),

$$\gamma = h_{\text{loss}} \left(\frac{J_{\text{orb}}}{M_{\text{tot}}} \right)^{-1} = q. \quad (3.13)$$

Stars are assumed to be spherically symmetric and therefore, since we ignore stellar rotation, the total angular momentum is simply

$$J_{\text{orb}} = M_{\text{D}}M_{\text{A}}\sqrt{\frac{Ga}{M_{\text{tot}}(1-e^2)}}, \quad (3.14)$$

where $M_{\text{tot}} = M_{\text{D}} + M_{\text{A}}$ and e is the eccentricity of the system (assumed to be zero before the first SN or circularized during a mass-transfer episode).

3.3.2.4 The orbital separation after mass transfer

As mentioned in the introduction of this section, we assume that mass transfer circularises the orbit. The change in orbital separation, after the orbit is already circularized, due to mass transfer is

$$\frac{\dot{a}}{a} = 2\frac{\dot{J}_{\text{orb}}}{J_{\text{orb}}} - 2\frac{\dot{M}_{\text{D}}}{M_{\text{D}}} - 2\frac{\dot{M}_{\text{A}}}{M_{\text{A}}} + \frac{\dot{M}_{\text{tot}}}{M_{\text{tot}}}. \quad (3.15)$$

Combining equations 3.5, 3.9, 3.12 and 3.15 the change in orbital separation during mass transfer is

$$\dot{a} = -2a\frac{\dot{M}_{\text{D}}}{M_{\text{D}}}\left[1 - \beta q - (1 - \beta)(\gamma + 1/2)\frac{1}{1 + 1/q}\right]. \quad (3.16)$$

Given an amount of mass, ΔM , being transferred (see Sec. 2.5.1) in a single timestep, Δt , the change in orbital separation is then recovered by integrating Eq. 3.16 in a thousand steps. A constant mass-transfer rate is assumed such that $\dot{M}_{\text{D}} = \Delta M/(1000 \times \Delta t)$, keeping the value of β fixed.

3.3.3 Dynamically-unstable mass transfer: common-envelope evolution

Dynamically-unstable mass transfer is assumed to lead to a common-envelope event. We apply the “ α - λ ” formalism (see Sec. 2.5.4) to solve for the final separation of the stars after the common-envelope event. Here the orbital energy is used to heat up

and expel the envelope with an efficiency α , which is set to 1. The binding energy of the envelope is approximated as its binding energy to the donor star. The binding energy of the common envelope to the donor star is described by the fitting parameter λ , for which we use the fitting formulae by Xu and Li (2010a,b) as implemented in Dominik et al. (2012). We assume that the timescale of common-envelope phase is too short for either of the stars to accrete any mass.

3.4 Uncertainties on our assumption on the merger rates of black holes and neutron stars

Each of the aforementioned assumptions has some uncertainties. de Mink and Belczynski (2015) and Klencki et al. (2018) show that uncertainties in the initial distributions of stars affect rate estimates of the mergers of black holes and neutron stars by a factor of $\lesssim 2$. Many studies (see e.g. Tutukov and Yungelson, 1993; Lipunov et al., 1997; Belczynski et al., 2002a; Marassi et al., 2011; Dominik et al., 2012; Kruckow et al., 2018; Giacobbo and Mapelli, 2018; Chruslinska et al., 2018; Vigna-Gómez et al., 2018) show that different prescriptions for binary physics affect the rates and distributions of black hole and neutron star mergers by a few orders of magnitude. For example, Dominik et al. (2012) find that the difference in their rates vary by a factor 2–6 between the assumption of $\beta = 0$ and $\beta = 1$, where the rate of binary neutron stars and black hole neutron stars increase with efficient mass transfer and the rates of black hole neutron stars decrease with more efficient mass transfer. Chruslinska et al. (2018) calculated the merger rates of double neutron stars depending on, amongst others, the amount of angular momentum lost during mass transfer at metallicities of $Z = 0.02, 0.002$ and 0.0003 and show that the Galactic merger rates vary from 10^{-1} Myr^{-1} to 10^2 Myr^{-1} . Similar uncertainties are reported for the physics of natal kicks and common-envelope efficiencies (Dominik et al., 2012; Kruckow et al., 2018; Giacobbo and Mapelli, 2018; Chruslinska et al., 2018; Vigna-Gómez et al., 2018). The model assumptions presented here are,

overall, similar to the ones adopted in various other population-synthesis codes. It is, however, clear that, despite many available observations in both classical and gravitational-wave astronomy, the physics of binary evolution remains poorly constrained and, therefore, our inferred merger rates of neutron stars and black holes have large uncertainties.

Part II

Papers

Chapter 4

The effect of the metallicity-specific star formation history on double compact object mergers

Coenraad J. Neijssel, Alejandro Vigna-Gómez, Simon Stevenson, Jim W. Barrett, Sebastian M. Gaebel, Floor S. Broekgaarden, Selma E. de Mink, Dorottya Szécsi, Serena Vinciguerra and Ilya Mandel

Abstract We investigate the impact of uncertainty in the metallicity-specific star formation rate over cosmic time on predictions of the rates and masses of double compact object mergers observable through gravitational waves. We find that this uncertainty can change the predicted detectable merger rate by more than an order of magnitude, comparable to contributions from uncertain physical assumptions regarding binary evolution, such as mass-transfer efficiency or supernova kicks. We statistically compare the results produced by the COMPAS population synthesis suite against a catalog of gravitational-wave detections from the first two Advanced LIGO and Virgo observing runs. We find that the rate and chirp mass of observed binary black hole mergers can be well matched under our default evolutionary model with a star formation metallicity spread of 0.39 dex around a mean metallicity $\langle Z \rangle$ that scales with redshift z as $\langle Z \rangle = 0.035 \times 10^{-0.23z}$, assuming a star formation rate of $0.01 \times (1+z)^{2.77} / (1 + ((1+z)/2.9)^{4.7}) M_{\odot} \text{ Mpc}^{-3} \text{ yr}^{-1}$. Intriguingly, this default model predicts that 80% of the approximately one binary black hole merger per day that will be detectable at design sensitivity will have formed through isolated binary evolution with only dynamically stable mass transfer, i.e., without experiencing a common-envelope event.

Contents

4.1	Introduction	77
4.2	Aim and overall method	78
4.3	COMPAS population-synthesis code	81
4.3.1	Initial distributions	81
4.3.2	Single stellar models	83
4.3.3	Mass-transfer stability	83
4.4	DCO population	86
4.4.1	BBH formation channels	87
4.4.2	Yield per metallicity	91
4.4.3	Total-mass distribution	94
4.4.4	Delay-time distribution	94
4.4.5	Mass-ratio distribution	96
4.5	Metallicity-specific star formation rate	98
4.6	Distribution of DCO mergers	102
4.6.1	Rate and redshift of cosmic DCO mergers	102
4.6.2	Mass distribution and redshift of cosmic DCO mergers	103
4.6.3	Priors and rate estimates	107
4.7	Gravitational-wave detections	108
4.7.1	Selection effects	108
4.7.2	Rate and redshift of gravitational-wave detections	108
4.7.3	Mass distribution of detectable binary black hole (BBH) mergers	111
4.7.4	Bayesian comparison of metallicity-specific star formation rate (MSSFR) models	113
4.8	Conclusion and discussion	115

4.9 Acknowledgements	119
4.A Metallicity-specific star formation rate	119
4.A.1 Cosmological star formation rate - SFR	119
4.A.2 Galaxy stellar mass to metallicity - MZ-relation	121
4.A.3 Galaxy stellar mass density function - GSMF	125
4.A.4 Metallicity-specific star formation rate - MSSFR	126
4.A.5 Definition of solar values	127
4.B Remnant masses of single stars	129
4.C Statistics	131
4.C.1 Evaluating model likelihoods	131
4.C.2 Bootstrapping	133

4.1 Introduction

There were 10 binary black hole (BBH) detections and a binary neutron star (BNS) in the first and second observing runs of the advanced Laser Interferometer Gravitational-wave Observatory (aLIGO) and Virgo gravitational-wave detectors (Abbott et al., 2016; Abbott et al., 2018b; Abbott et al., 2017). The intrinsic rate of BBH mergers is currently estimated by the LIGO-Virgo collaboration to be $24\text{--}112 \text{ Gpc}^{-3}\text{yr}^{-1}$, whereas for BNSs it is $110\text{--}3840 \text{ Gpc}^{-3}\text{yr}^{-1}$ (Abbott et al., 2018a). These intrinsic rate estimates depend on the assumed shape of the mass and rate distribution of the double compact object (DCO) mergers, which remains uncertain. Multiple possible stellar origins exist for DCOs such as dynamical capture in open/globular/nuclear clusters, Lidov-Kozai resonances in hierarchical triples, chemically-homogeneous evolution in compact stellar binaries and mergers of primordial black holes (see Miller, 2016; Mandel and Farmer, 2018; Giacobbo and Mapelli, 2018, for reviews). We focus on the merger rate of DCOs that come from isolated binary evolution. It appears that most of the massive stars ($M > 8 M_{\odot}$) in the field are born in binaries (Kiminki and Kobulnicky, 2012; Sana et al., 2012; Moe and Di Stefano, 2017). Once formed, these isolated binaries evolve without external influences and a fraction becomes DCOs. However, the exact physics of stellar and binary evolution and the resulting rates of DCO mergers are still uncertain (e.g., Dominik et al., 2015; Eldridge and Stanway, 2016; Kruckow et al., 2018; Chruslinska et al., 2018).

The evolution of massive stars takes a few million years, but their inspiral as DCOs can span years to billions of years (e.g., Portegies Zwart and Yungelson, 1998a; Belczynski et al., 2002b; Eldridge and Stanway, 2016; Mapelli et al., 2017). The detected mergers could therefore have formed at very high redshifts. Observations show that the star formation rate (SFR) changes significantly as a function of redshift (Madau and Dickinson, 2014). At redshifts $z \gtrsim 2$ the SFR estimates become increasingly more sensitive to the assumed extinction, which is uncertain (Madau and Dickinson, 2014; Strolger et al., 2004). The SFR determines the number of stellar binaries formed and hence introduces an uncertainty on the rate of

DCO formation.

Metallicity, and particularly the fraction of iron in the star at birth, significantly impacts the rate of mass loss through line-driven winds. Consequently, it has a significant effect on the DCO mass distribution and merger rate (Belczynski et al., 2010; Stevenson et al., 2017; Giacobbo et al., 2018). The metallicity of star-forming gas depends on redshift, as subsequent generations of stars enrich the interstellar medium through winds and explosions with metals formed during their evolution. Galaxy catalogs, such as the Sloan Digital Sky Survey (Tremonti et al., 2004), show that there is an empirical correlation between the galaxy stellar mass and the mean metallicity of the galaxy. Furthermore, the galaxy stellar-mass function (GSMF) and the galaxy stellar mass – metallicity (MZ)-relation evolve with redshift. Different calibrations or galaxy samples lead to different results (Savaglio et al., 2005; Kewley and Ellison, 2008; Furlong et al., 2015). Thus there is not only uncertainty in the overall SFR but also in the distribution of the metallicities in the star forming gas. Combined, these result in an uncertainty in the metallicity-specific star formation rate (MSSFR), which affects estimates of the rates and properties of DCO mergers.

4.2 Aim and overall method

Our aim is to assess how the uncertainty in the MSSFR affects predictions for the rate and distributions of DCO mergers. In this section, we introduce the key steps in the calculation of the redshift-dependent DCO merger distribution and the rate of detectable DCO mergers.

The time it takes for a binary to evolve its stars and then merge at t_m as a DCO due to the emission of gravitational waves is called the delay time (t_{delay}). The formation time t_f is related to the merger time t_m by $t_f = t_m - t_{\text{delay}}$. We calculate

the rate of mergers at any given time as a function of chirp mass as,

$$\frac{d^3 N_{\text{merge}}}{dt_s dV_c dM_{\text{chirp}}}(t_m) = \int dZ \int dt_{\text{delay}} \times \frac{d^3 N_{\text{form}}}{dt_{\text{delay}} dM_{\text{SFR}} dM_{\text{chirp}}}(Z) \frac{d^3 M_{\text{SFR}}}{dt_s dV_c dZ}(t_f = t_m - t_{\text{delay}}), \quad (4.1)$$

where Z is the metallicity, z is the redshift, t_s is the time in the source frame of the merger, and V_c is the comoving volume. The first term in the integrand is the number of DCOs per unit star-forming mass M_{SFR} per unit delay time and per unit chirp mass $M_{\text{chirp}} = M_1^{3/5} M_2^{3/5} (M_1 + M_2)^{-1/5}$, where M_1 and M_2 are the individual compact object masses. We compute this first term over a grid of metallicities by running the COMPAS population-synthesis code. The second term is the amount of mass going into the formation of stars, M_{SFR} (from hereon referred to as star-forming mass), at the birth of the binary per unit time, volume, and metallicity (MSSFR), which we model analytically.

The second step is to calculate the distribution of observable DCO mergers. We do this by converting t_m to a redshift z and integrating the entire visible volume in shells of thickness dz . At each redshift we calculate the probability of detecting a binary (P_{det}) given its chirp-mass (M_{chirp}) and luminosity distance ($D_L(z)$). The total number of observable mergers (N_{obs}) per unit chirp mass per unit observing time (t_{obs}) is then,

$$\frac{d^2 N_{\text{obs}}}{dt_{\text{obs}} dM_{\text{chirp}}} = \int_0^{z_{\text{max}}} dz \frac{dt_s}{dt_{\text{obs}}} \frac{dV_c}{dz} \times \frac{d^3 N_{\text{merge}}}{dt_s dV_c dM_{\text{chirp}}}(z) P_{\text{det}}(M_{\text{chirp}}, D_L(z)), \quad (4.2)$$

where dV_c/dz is the differential comoving volume as a function of redshift and $dt_s/dt_{\text{obs}} = 1/(1+z)$ translates the rate to the observer frame (e.g. Hogg, 1999). We assume a flat cosmology with $\Omega_M = 0.308$ and a Hubble constant of $H_0 = 67.8 \text{ km s}^{-1} \text{ Mpc}^{-1}$ (Ade et al., 2016). Altogether this general method is similar to works such as Langer and Norman (2006), Dominik et al. (2013), Mandel and de Mink (2016), Eldridge and Stanway (2016), Madau and Fragos (2017) and Chruslinska

and Nelemans (2019).

We sequentially solve the aforementioned equations, providing results for each intermediate step. The paper is therefore structured as follows:

- Section 4.3: COMPAS population-synthesis code

We create a large sample of DCOs from a broad range of metallicities using the rapid population-synthesis element of the COMPAS suite. We briefly describe the model assumptions used to evolve our massive stellar binaries.

- Section 4.4: $\frac{d^3 N_{\text{form}}}{dt_{\text{delay}} dM_{\text{SFR}} dM_{\text{chirp}}}$ - DCO population

We show the results of our population synthesis of DCOs. We describe some of the key features such as their mass distribution at different formation metallicities in our simulation. We describe the three main formation channels for BBHs. At a tenth of solar metallicity, ignoring selection effects, we find that a third of the BBHs merge without experiencing a common-envelope event.

- Section 4.5: $\frac{d^3 M_{\text{SFR}}}{dt_s dV_c dZ}$ - MSSFR

We combine observations and simulations of galaxy stellar mass distributions with mass – metallicity relations to construct a MSSFR. These different prescriptions introduce an uncertainty into our DCO merger rate distributions. We propose a parametrised, smooth metallicity distribution, which facilitates the exploration of the MSSFR parameter-space

- Section 4.6: $\frac{d^3 N_{\text{merge}}}{dt_s dV_c dM_{\text{chirp}}}$ - DCO Merger Distributions

We calculate the redshift-dependent DCO distribution by convolving the MSSFR with our DCO population. We find that variation in MSSFR prescriptions significantly affects both the total rate and mass distributions of DCOs mergers.

- Section 4.7: $\frac{d^2 N}{dt_{\text{obs}} dM_{\text{chirp}}}$ - Gravitational-Wave Detections

We apply selection effects of gravitational-wave detectors to our cosmic DCO populations. From this we get both rate and mass distributions of detectable BBH mergers for different MSSFR prescriptions. We use a Bayesian approach to compare the predictions of different MSSFR models against the observed

sample of gravitational waves from BBH mergers. We find that the MSSFR could change the predicted rate of gravitational-wave events from BBH mergers by almost an order in magnitude.

– Section 4.8: Discussion and Conclusion

We review our findings and discuss future prospects.

4.3 COMPAS population-synthesis code

We generate our population of DCOs by modelling isolated binary evolution with the population-synthesis code COMPAS (Stevenson et al., 2017; Barrett et al., 2018a; Vigna-Gómez et al., 2018; Stevenson et al., 2019). We use Monte Carlo simulations to empirically estimate the rate density of DCOs per unit star-forming mass in delay time and chirp mass at each simulation metallicity:

$$\frac{d^3 N_{\text{form}}}{dt_{\text{delay}} dM_{\text{SFR}} dM_{\text{chirp}}}(Z, t_{\text{delay}}, M_{\text{chirp}}).$$

In this section we briefly describe the parameter space of our simulation and our model assumptions for isolated binary evolution. The data will be made publicly available at <http://compas.science>.

4.3.1 Initial distributions

The five main initial parameters that describe a stellar binary are the primary m_1 and secondary m_2 masses, the orbital separation a , the orbital eccentricity e , and the metallicity of the stars Z at the zero-age main sequence (ZAMS). The mass of the initially more massive star, the primary, is drawn from an initial mass function (IMF) according to Kroupa (2001). The mass of the initially less massive secondary star is given by,

$$m_2 = m_1 \times q, \tag{4.3}$$

where q is the initial mass ratio ($0 < q < 1$). We draw the mass ratio q from a flat distribution (Sana et al., 2012). We assume that the distribution of separations is $\propto a^{-1}$ (Öpik, 1924), where initial separations range from $0.1 < a/\text{AU} < 1000$, and the orbits are all circular at birth. We assume that these distributions are both independent of each other as well as independent of metallicity. Recent studies such as Moe and Di Stefano (2017) suggest that the initial distributions might be correlated. Varying the distributions of the initial parameters affects the merger rates by a factor of $\lesssim 2$ (de Mink and Belczynski, 2015; Klencki et al., 2018).

For the metallicities Z of the binaries we use 30 grid points spread uniformly in $\log(Z)$ over a broad range of metal mass fractions $0.0001 \leq Z \leq 0.03$. We evolve three million binaries with a total star-forming mass of the order of $6.5 \times 10^7 M_{\odot}$ per grid-point.

To optimise the number of binaries containing a neutron star (NS) or black hole (BH) per binary simulated, whilst still leaving enough room in the parameter space to make sure we simulate all possible NSs and BHs, we draw primaries with masses equal to or larger than $5 M_{\odot}$ (this represents a very naive version of importance sampling introduced by Broekgaarden et al. 2019). Our upper mass limit is 150 solar masses. In this mass range the power index of the IMF is -2.3. Due to this sampling, our simulation does not represent the rate of BBHs per unit star-forming mass evolved in all stars. Hence, we need to correct for the ‘true’ amount of mass evolved in all stars (both single and binary). We calculate this by assuming a binary fraction of 70 per cent and a flat mass ratio for all stellar masses (Sana et al., 2012). This results in a total star-forming mass per metallicity grid point of $\sim 3.1 \times 10^8 M_{\odot}$. It is this star-forming mass that we use as our normalisation dM_{SFR} . Exact binary fractions and hence our normalisation are still uncertain (Sana, 2017; Moe and Di Stefano, 2017). For example, adopting a 50 per cent binary fraction would increase the ratio of single stars to binary stars, increasing our normalisation by 30 per cent.

4.3.2 Single stellar models

Stellar evolution in COMPAS is based on the stellar models by Pols et al. (1998). We use analytical fits to these models by Hurley et al. (2000, 2002) to rapidly evolve binaries. Our wind mass-loss rates for stars with temperatures below 12500 K are prescribed by Hurley et al. (2000) and references therein. For hot massive stars ($T > 12500\text{K}$) we use the wind mass-loss rates by Vink et al. (2001) as implemented in Belczynski et al. (2010). There is a region in the Hertzsprung-Russell diagram at low effective temperatures and high luminosities in which no stars are observed. The boundary of this region is called the Humphreys-Davidson limit (Humphreys and Davidson, 1994). If a star enters this region we apply an overall wind mass-loss rate of $1.5 \times 10^{-4} M_{\odot} \text{ yr}^{-1}$ (Belczynski et al., 2010). From here onwards we refer to these winds as luminous blue variable (LBV) winds.

4.3.3 Mass-transfer stability

The Roche lobe of a star defines the volume within which the self-gravity of the star exceeds the tidal pull of its companion. We use the approximation of Eggleton (1983) for the Roche-lobe radius. When a star expands, its radius may exceed its Roche lobe. At this moment, the star commences mass transfer onto the companion, this phase is commonly referred to as Roche-lobe overflow (RLOF). If mass transfer results in the star further exceeding its Roche lobe then we assume the RLOF is unstable. We evaluate if a mass-transfer episode is dynamically unstable by comparing the radial response of the Roche lobe to mass transfer $d \log(R_L)/d \log(m)$ against the response of the stellar radius to mass transfer $d \log(R_*)/d \log(m)$ (Paczynski and Sienkiewicz, 1972; Hjellming and Webbink, 1987; Soberman et al., 1997). We approximate the radial response of the star as a function of its stellar type. The stellar types are as defined in Hurley et al. (2000).

- Main sequence (MS):

We use $d \log(R_*)/d \log(m) = 2.0$ for core-hydrogen-burning stars.

- Hertzsprung gap (HG):

We use $d \log(R_*)/d \log(m) = 6.5$ for HG stars. Both MS and HG approximations follow our models in Vigna-Gómez et al. (2018), based on the work by Ge et al. (2015). More detailed models based on the evolutionary phase of the star and the amount of mass loss have been explored by Ge et al. (2015), Woods and Ivanova (2011) and Pavlovskii et al. (2017).

- Massive stars with convective envelopes:

We use fits from Hjellming and Webbink (1987) and Soberman et al. (1997) for the radial response to adiabatic mass loss of all evolved stars beyond HG. These fits are based on condensed polytropes for deeply convective stars and depend on the mass fraction of the core compared to the total mass of the star (Hjellming and Webbink, 1987). We will investigate the applicability of these approximations in future work (Neijssel, 2022).

- Stripped stars:

We make a special exception for mass transfer from exposed helium cores. The mass transfer from exposed helium stars might be more stable than previously expected, yielding ultra-stripped stars Tauris et al. (2015, 2017). Currently we assume all mass-transfer episodes from helium stars are stable. This assumption is not based on a physical model but is instead found to be necessary to recreate the orbital periods and eccentricities of the observed sample of Galactic double neutron stars in our models (Vigna-Gómez et al., 2018).

4.3.3.1 Stable mass transfer

If a mass-transfer episode is dynamically stable, the companion star accretes a fraction β of the mass lost by the donor. In our model, this mass-transfer efficiency β depends on the ratio of the thermal timescales t_{th} of the stars $\beta = \min(1, C \times t_{\text{th}_1}/t_{\text{th}_2})$, where $0 \leq \beta \leq 1$, and $C = 10$ to allow for accretor radial expansion while adjusting to mass transfer (Paczynski and Sienkiewicz, 1972; Hurley et al., 2002; Schneider et al., 2015). Any mass that is not accreted leaves the system instantaneously, tak-

ing away the specific angular momentum of the accretor (Hurley et al., 2002). For NS and BH accretors we assume the accretion is Eddington-limited, which results in a highly non-conservative mass-transfer phase with $\beta \approx 0$.

4.3.3.2 Unstable mass transfer

If a mass-transfer episode is dynamically unstable the envelope of the donor enfolds the entire binary in a common-envelope event (Paczynski, 1976). This is a complex phase and we parametrise it in the so-called ‘ α - λ ’ formalism (see Ivanova et al. (2013a) for a review). During a common-envelope event the two stars spiral in due to friction with the envelope and lose orbital energy and angular momentum. This loss of orbital energy can heat up and expel the envelope. To see if a binary is able to expel the common envelope, we compare the orbital energy against the binding energy of the envelope of the star (Webbink, 1984). The efficiency, α , defines the efficiency by which orbital energy is capable of heating up the envelope (Livio and Soker, 1988). We assume that all of the orbital energy goes into expelling the envelope (i.e. $\alpha = 1$). The binding energy of the envelope depends on the stellar structure of the star and is parametrised by λ (de Kool, 1990). Our choices of λ are based on the binding energy fits by Xu and Li (2010b) as implemented by Dominik et al. (2012).

Within the common envelope we define two scenarios for donor stars which are on the Hertzsprung-gap, following Belczynski et al. (2007). In the ‘optimistic’ scenario we evaluate the common-envelope evolution for Hertzsprung-gap stars using the ‘ α - λ ’ prescription. In the ‘pessimistic’ scenario we assume that unstable mass transfer from Hertzsprung-gap donors always results in a merger. The latter will therefore decrease the number of DCOs compared to the optimistic assumption. Common-envelope events with MS donors are assumed to lead to a prompt merger in all variations.

4.3.3.3 Supernovae

We use the ‘delayed’ model of Fryer et al. (2012) to determine the remnant mass from the pre-supernova (SN) mass of the star and its carbon-oxygen core. This model avoids an enforced lower mass gap between NSs and BHs. A lower mass gap is also not consistent with microlensing observations unless BHs are assumed to receive substantial natal kicks (Wyrzykowski and Mandel, 2019). The explosion can be asymmetric and as a result impart a kick on the formed remnant. The kicks are drawn from a Maxwellian distribution with a one-dimensional standard deviation $\sigma = 265 \text{ km s}^{-1}$ based on the observations of isolated pulsars (Hobbs et al., 2005). If the progenitor either experiences an electron-capture supernova or is ultra stripped by a NS companion, we lower the one-dimensional root-mean-square kick to 30 km s^{-1} (Pfahl et al., 2002; Podsiadlowski et al., 2004; Tauris et al., 2015, 2017; Vigna-Gómez et al., 2018). The fraction f_b of mass that falls back onto the newly born compact object is prescribed by Fryer et al. (2012). All of the ejecta falls back ($f_b=1$) for carbon-oxygen core masses above $11 M_\odot$. The natal kick is proportionally reduced based on the fallback fraction according to

$$V_{\text{kick}} = (1 - f_b)V_{\text{kick,drawn}}. \quad (4.4)$$

The direction of the kick is assumed to be isotropically distributed in the frame of reference of the exploding star.

4.4 DCO population

In this section we describe the three main BBH formation channels. We focus on BBHs because they are the most common DCOs among already observed gravitational-wave events. More information on BNSs can be found in Vigna-Gómez et al. (2018) and the channels for black hole – neutron star binaries (BHNSs) are left for another study. In this section we also present the metallicity, mass, mass-ratio, and delay-time distributions for our model DCO population.

The necessity of binary interactions to form close binary systems, which host compact objects, has already been extensively studied in contexts such as the formation of cataclysmic variables (Paczynski, 1967b) or X-ray binaries and double neutron stars (van den Heuvel and De Loore, 1973; Tutukov and Yungelson, 1973). A $30 M_{\odot} + 30 M_{\odot}$ circular BBH needs a separation of $\lesssim 45 R_{\odot}$ to merge in the age of the Universe, whereas the progenitor stars can expand up to hundreds of solar radii. Therefore, progenitors of DCOs are expected to interact (for a review on the formation of BBHs see e.g. Mandel and Farmer, 2018).

Observations indicate ~ 50 percent of massive stars in binaries will interact (Kiminki and Kobulnicky, 2012; Sana et al., 2012). Only a small fraction of interacting massive binaries will form merging DCOs. This requires stars to avoid merger during mass transfer; to have sufficient mass to form compact objects; the binary, must remain bound during and after SNe and, after the formation of a DCO, the binary must be tight enough to merge within the age of the Universe. Our main goal is to determine which DCOs we can detect as gravitational-wave sources hence we are only interested in the systems that merge within the age of the Universe. The results shown below assume the pessimistic common-envelope assumption. The optimistic assumption currently over-predicts the rates of BBHs (e.g. Dominik et al., 2012; Belczynski et al., 2016) and we show results using the optimistic assumption in Appendix 4.C.

4.4.1 BBH formation channels

In our simulations 97% of all BBHs that merge within a Hubble time form through one of three distinct channels. Here we briefly summarise the evolutionary phases of the three main formation channels. The fractions in parentheses indicate the fraction of all systems that reach a certain event or phase in that specific formation channel. The fraction of binaries forming BBHs and the ratios between formation channels depends slightly on metallicity (see also Fig. 4.1). We focus on the systems

that evolved at a metallicity of $Z = 0.1Z_{\odot}$ ¹, and therefore the fraction refers to the percentage of systems remaining compared to all of the systems evolved at this metallicity.

1. – Channel I –

This is the dominant, ‘classical’ channel of BBH formation as described in, e.g., van den Heuvel and De Loore (1973); Tutukov and Yungelson (1993); Lipunov et al. (1997); Belczynski et al. (2002a); Belczynski et al. (2016) and Stevenson et al. (2017).

- 1.1. **-Stable mass transfer-** The primary star expands sufficiently to engage in an episode of mass transfer (51.71%). For the majority of these systems, the first mass-transfer episode will happen between a post-MS primary star and a MS companion (49.26%). The mass-transfer episode is dynamically stable and strips the hydrogen envelope from the primary, leaving an exposed helium core with a main-sequence companion star (23.06%).
- 1.2. **-First supernova-** The exposed core is massive enough to collapse into a BH. The binary survives the supernova (2.66%).
- 1.3. **-Unstable mass transfer-** The secondary star evolves and starts an episode of dynamically-unstable mass transfer resulting in a common envelope (0.87%). The system is able to expel the envelope leaving a tighter binary (0.50%).
- 1.4. **-Second supernova-** The secondary also collapses into a BH and the binary system survives the second supernova (0.43%).
- 1.5. **-DCO merger-** The resulting BBH is then able to merge within the age of the Universe due to the emission of gravitational waves, which leaves

¹In this study, we define the Solar metallicity mass fraction as $Z_{\odot} = 0.0142$ and the Solar oxygen abundance as $\log_{10}[\text{O}/\text{H}]_{\odot} + 12 = 8.69$ based on Asplund et al. (2009); see appendix 4.A.5 for details.

0.24% of all our evolved binaries merging as BBHs. Allowing for the optimistic common-envelope assumption, which allows for HG donors to survive a dynamically-unstable mass-transfer episode, increases the number of BBHs in this channel (0.39%).

2. – Channel II –

The second channel is similar to the ‘classical’ channel and goes through the same steps until the episode of mass transfer initiated by the secondary, which is dynamically stable in channel II.

2.1. **-Stable mass transfer-** see channel I.

2.2. **-First supernova-** see channel I.

2.3. **-Stable mass transfer-** The secondary starts mass transfer as a post-MS star. The mass-transfer episode is now dynamically stable and *does not result in a common-envelope phase* (1.35%).

2.4. **-Second supernova-** The secondary collapses into a BH without disrupting the binary (1.02%).

2.5. **-DCO merger-** Even without the common-envelope phase the BBH hardens (reduces orbital separation) sufficiently during the second mass-transfer episode to spiral in and merge within the age of the Universe (0.15%).

Compared to Stevenson et al. (2017) we changed our prescription for computing $d \log(R_*)/d \log(m)$ of HG donors (see Sec. 4.3.3). In combination with our prescription for angular momentum loss during non-conservative mass transfer onto a compact-object primary (see Sec. 4.3.3.1), the mass-transfer episode is on average now stable at mass ratios up to $m_{\text{donor}}/m_{\text{accretor}} \approx 4.5$. A mass-transfer episode with a donor star that is significantly more massive than the accretor can substantially harden the binary (van den Heuvel et al., 2017). With the increased stability these mass ratios are sufficiently extreme such that a BBH is able to merge within the age of the Universe.

The stability of the second episode of mass transfer acts as a bifurcation point between channel I and channel II. Currently, channel II only happens for HG donors in our models, since we treat core-helium-burning donors as fully convective, making mass-transfer episodes involving core-helium-burning donors less dynamically stable.

Pavlovskii et al. (2017) find that increasing the stability of mass transfer with a giant donor star reduces their rates of BBHs mergers and could possibly explain the formation rate of ultra-luminous X-ray binaries. Furthermore, van den Heuvel et al. (2017) show that the increased stability of mass transfer could explain the formation of short period X-ray binaries consisting of a Wolf-Rayet star orbiting a BH. The X-ray binary could possibly continue to evolve into a close BBH (van den Heuvel et al., 2017).

3. – Channel III –

The third channel for forming BBHs is similar to the double-core common-envelope channel introduced by (Brown, 1995; Dewi et al., 2006).

3.1. **-Unstable mass transfer-** In this scenario both stars evolved beyond the HG before engaging in an episode of mass transfer (1.40%). This mass-transfer episode is dynamically unstable (1.27%) and the binary survives the common-envelope ejection (0.71%). However, unlike the similar formation channel for BNSs (Vigna-Gómez et al., 2018), there is no further episode of mass transfer.

3.2. **-Two supernovae-** Both stars collapse in supernovae (non-simultaneously); 0.04% of binaries remain bound as a BBH.

3.3. **-DCO merger-** The DCO spirals in due to the emission of gravitational waves. In the end 0.03% of all binaries evolved go through this channel and merge within the age of the Universe.

The remaining three per cent of BBHs form through alternative channels. These

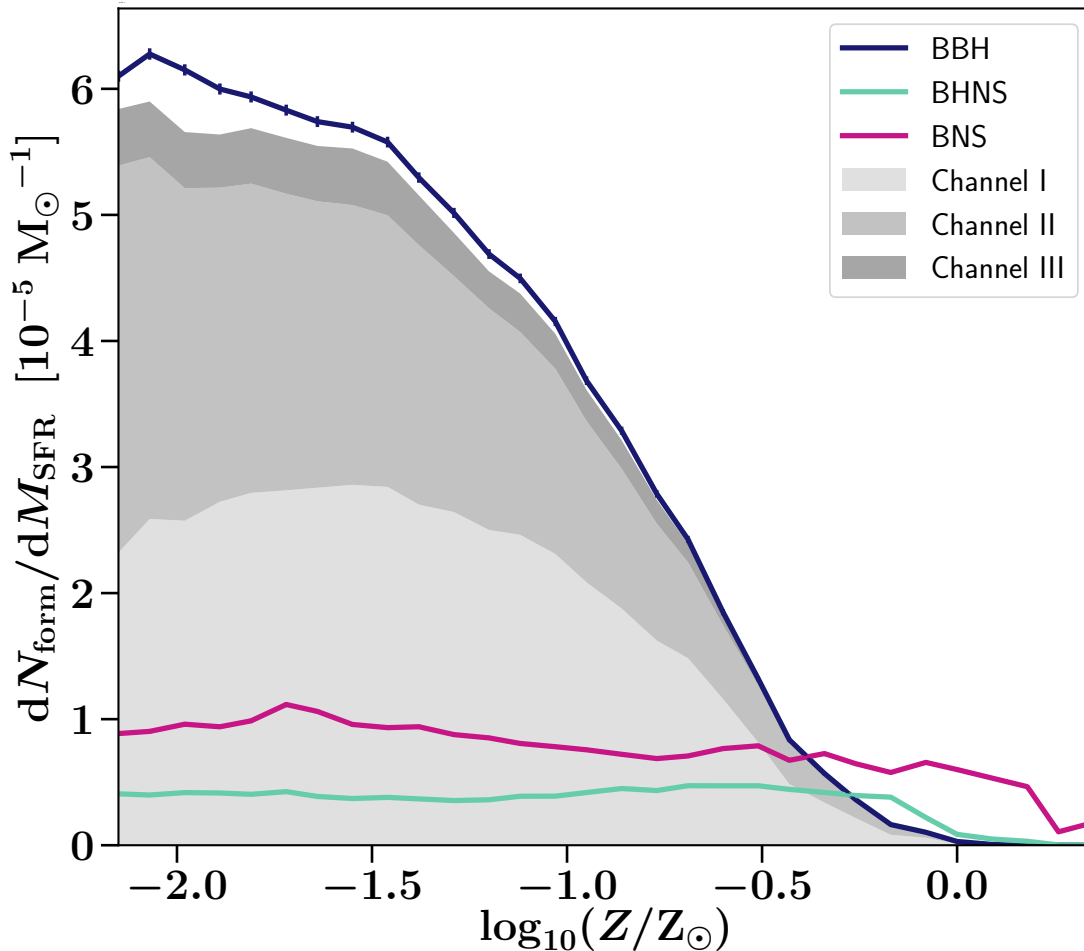


Figure 4.1: Yield of double compact objects with $t_{\text{delay}} < 14$ Gyr per unit star-forming mass from COMPAS population synthesis. BBHs are in blue, BHNSs in mint and BNSs in red. The curve under the BBH yield is shaded by the contribution of each channel (the white residual is due to rare alternative channels). The error bars show the sampling uncertainty of each simulation.

include systems which have an additional moment of mass transfer after a common-envelope phase, or systems where the first moment of mass transfer is started by the secondary after the primary’s supernova kick fortuitously tightened the binary.

4.4.2 Yield per metallicity

The yield of merging DCOs per unit star-forming mass depends on the metallicity at which stars form, as shown in figure 4.1. As previously pointed out by Belczynski et al. (2010), Giacobbo et al. (2018) and Spera et al. (2019), the rate of BBH formation is particularly sensitive to metallicity with a steep decline in BBH production at

higher metallicities. Therefore, while BBHs are the dominant type of merging DCOs at sub-solar metallicities, they are rarer than BNSs and BHNSs at solar metallicity.

At higher metallicities, higher wind mass-loss rates prevent the growth of the carbon-oxygen core (Belczynski et al., 2010; Spera et al., 2015; Stevenson et al., 2017), leaving a less massive remnant. This affects the natal kicks imparted on the BHs. In the prescription of Fryer et al. (2012), stars with carbon-oxygen cores above $11 M_{\odot}$ do not receive any natal kick due to the complete fall back (see Eq. 4.4). In our models, stars with metallicities of $Z = 0.1 Z_{\odot}$ and initial masses of $M \gtrsim 35 M_{\odot}$ experience complete fall back. At Solar metallicity the initial mass needs to be above $\sim 60 M_{\odot}$ to form a carbon-oxygen core massive enough to experience complete fall back. Therefore, we expect more potential BBH progenitors to be disrupted at higher metallicities.

Even when assuming that BBHs form without natal kicks, our simulations show that the yield of BBHs still remains sensitive to the initial metallicity of stars. Further inspection showed that this is due to the sensitivity of the wind-driven mass loss to metallicity. Wind-driven mass loss increases at higher metallicities. Therefore, at higher metallicities, the binary widens more due to wind mass loss and is left with reduced envelope masses which limit the amount of orbital hardening during common-envelope ejection or stable mass transfer. Note that here we focus on the possible progenitors of gravitational-wave events and thus on BBHs which merge within the age of the Universe. When considering all BBHs and the BH natal kicks are set to zero, the BBH yield becomes almost independent of metallicity.

The NS progenitors have lower mass-loss rates compared to BBHs and the envelope mass is less sensitive to metallicity; moreover, their natal kicks are generally uncorrelated with metallicity. Hence it is not surprising that the yield of BNSs per unit solar mass evolved is less sensitive to metallicity, as also found by Giacobbo and Mapelli (2019).

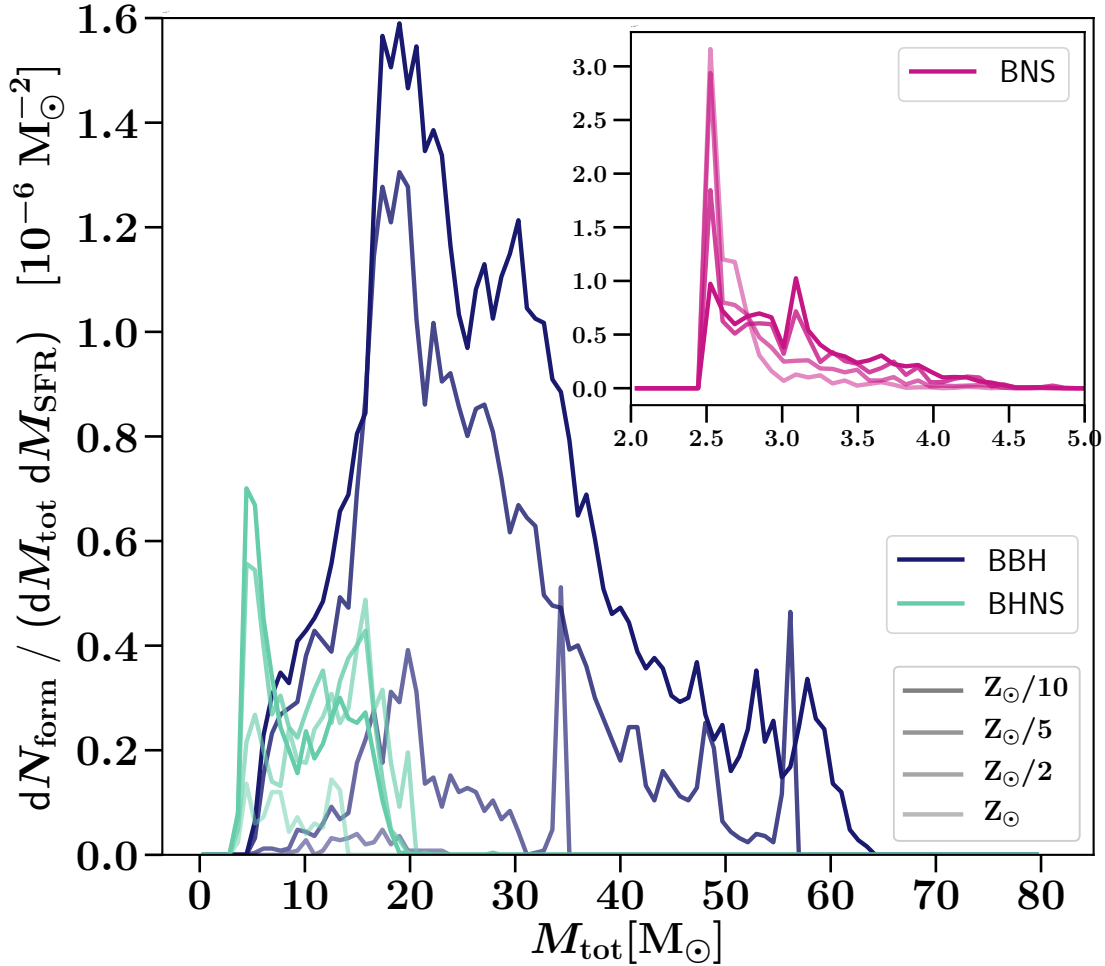


Figure 4.2: Total-mass distributions for BBHs are in blue, BHNSs in mint from COMPAS simulations for a tenth, a fifth, a half, and solar metallicity (dark to light shade), for DCOs merging in $t_{\text{delay}} < 14$ Gyr. The embedded figure presents the total-mass distribution of BNSs in red with the same information on the x and y axis as the overall figure except the unit on the y-axis is $[10^{-5}M_{\odot}^{-2}]$. The integral under the curve is the yield plotted in Fig. 4.1. Higher metallicities yield lower total DCO masses, particularly for BBHs.

4.4.3 Total-mass distribution

Figure 4.2 shows the total-mass distributions of DCOs merging within the age of the Universe for several metallicities. As discussed in the previous section, lower-metallicity stars with reduced wind-driven mass-loss rates leave more massive remnants. For all metallicities the bulk of the total BBH masses lie between 15 & 35 M_{\odot} . More massive BBHs are suppressed by the IMF and wind-driven mass loss. The most massive binary black hole formed at a given metallicity is a function of both our assumptions about wind mass loss in massive stars, and our remnant prescription (these simulations do not include (pulsational) pair-instability supernova (PISN) – see Stevenson et al., 2019). Meanwhile, BHs with low masses get large kicks in the Fryer et al. (2012) prescription, and are therefore less likely to remain bound and form a BBH, explaining a dearth of BBHs with total masses below 15 M_{\odot} . The ‘delayed’ Fryer et al. (2012) remnant prescription does not enforce a lower mass gap between NSs and BHs, so we find some BBHs with total masses below 10 M_{\odot} in our simulations, although these are relatively rare.

The presence of spikes in BBH masses, particularly in the highest mass bin at $Z = 0.5Z_{\odot}$ and $Z = 0.2Z_{\odot}$, are due to mass loss prescriptions, particularly LBV winds, that map a range of ZAMS masses to a single remnant mass (see Appendix. 4.B). Similar features are found in Dominik et al. (2015).

For BNSs we recover a similar total-mass distribution to Vigna-Gómez et al. (2018). As discussed in Vigna-Gómez et al. (2018), this distribution, driven by the Fryer et al. (2012) prescription, does not match the observed distribution of Galactic BNSs. For example, in our model, BNSs have total masses in the range 2.5–5.0 M_{\odot} , while observed Galactic BNSs with precise mass measurements have total masses in the narrower range 2.5–3.0 M_{\odot} (Farrow et al., 2019).

4.4.4 Delay-time distribution

The delay time is the time from the formation of two stars in a binary to their merger as a DCO. We follow Peters (1964) to estimate the time from DCO formation to

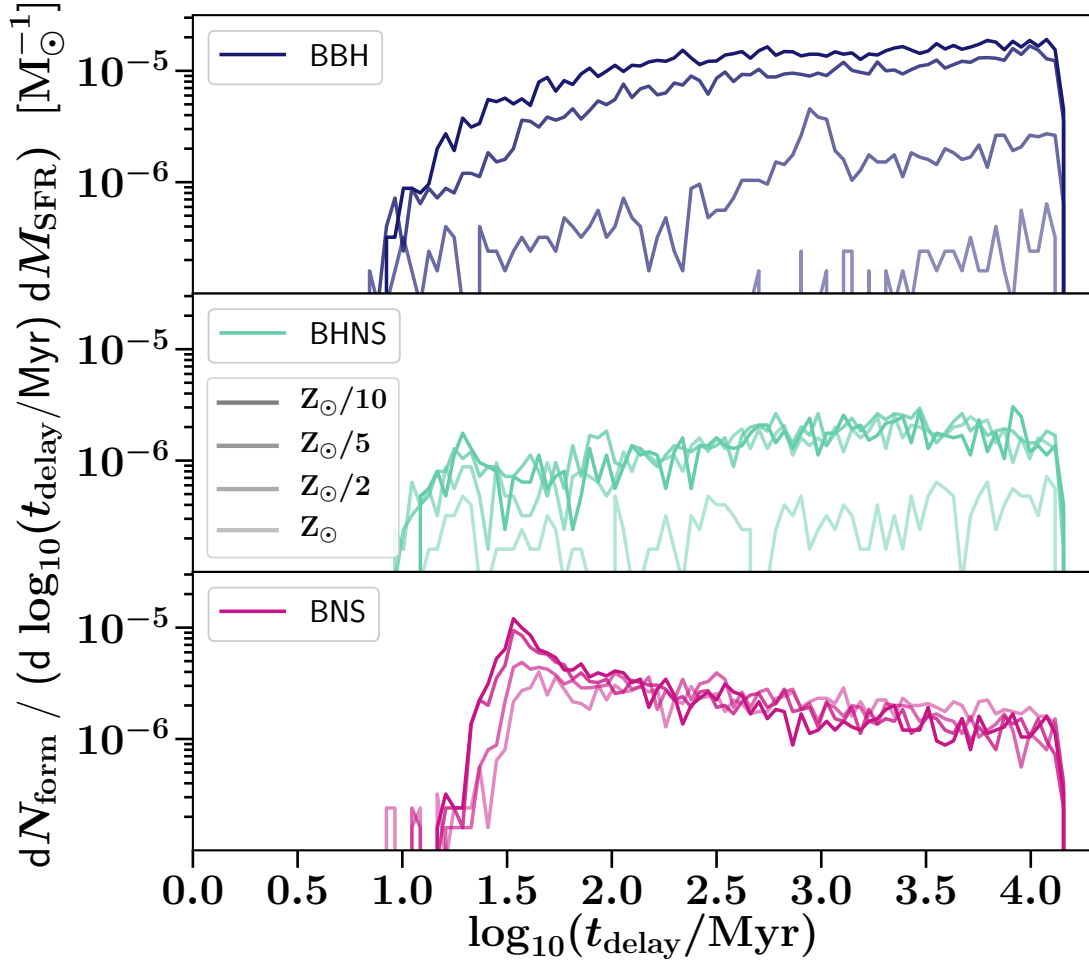


Figure 4.3: Delay-time distributions up to $t_{\text{delay}} = 14$ Gyr for BBHs are in blue, BHNSs in mint and BNSs in red from COMPAS simulations for a tenth, a fifth, a half, and solar metallicity (dark to light shade).

merger through the emission of gravitational waves, where the change in orbital angular momentum due to gravitational waves equals,

$$\frac{dJ_{\text{gr}}}{dt} = -\frac{32}{5} \frac{G^{7/2} M_1^2 M_2^2 \sqrt{M_1 + M_2}}{c^5 a^{7/2} (1 - e^2)^2}. \quad (4.5)$$

The delay-time distribution is roughly uniform in $\log_{10}(t_{\text{delay}})$ for all DCOs (see Fig. 4.3). Furthermore, for the pessimistic assumption it is not very sensitive to metallicity. These findings are similar to Dominik et al. (2012) and Mapelli et al. (2017).

4.4.5 Mass-ratio distribution

Figure 4.4 shows the mass-ratio distributions of DCOs merging within the age of the Universe at several metallicities. It is clear that the distributions differ between different types of DCOs and depend on metallicity.

Most BNSs in our model form through either iron-core collapse from the lowest mass stars, or through electron-capture supernovae (to which we associate a fixed remnant mass of $1.26 M_{\odot}$, Vigna-Gómez et al., 2018). This results in a peak at equal mass ratios for BNSs. There is some spread in mass ratios at higher NS masses, but we do not expect extreme mass ratios given the limited range of possible NS masses.

The BHNSs favour more extreme mass ratios. The average NS mass is $1.2 M_{\odot}$ and the threshold between NS and BH is $2.5 M_{\odot}$ in our models. This already results in a mass ratio of 0.5, but most of the BHs are heavier. Further details are outside the scope of this study.

The mass-ratio distribution of BBHs depends on the formation channel. The classical channel I with a common-envelope phase occurs over a broad range of mass ratios between the donor star and the accreting BH. This channel yields a relatively flat mass-ratio distribution. Meanwhile, channel II, in which the mass transfer onto the BH is dynamically stable, has an upper limit of 4.5 for the mass ratio between the donor and the BH accretor. Mass ratios close to, but less than, 4.5 are preferred

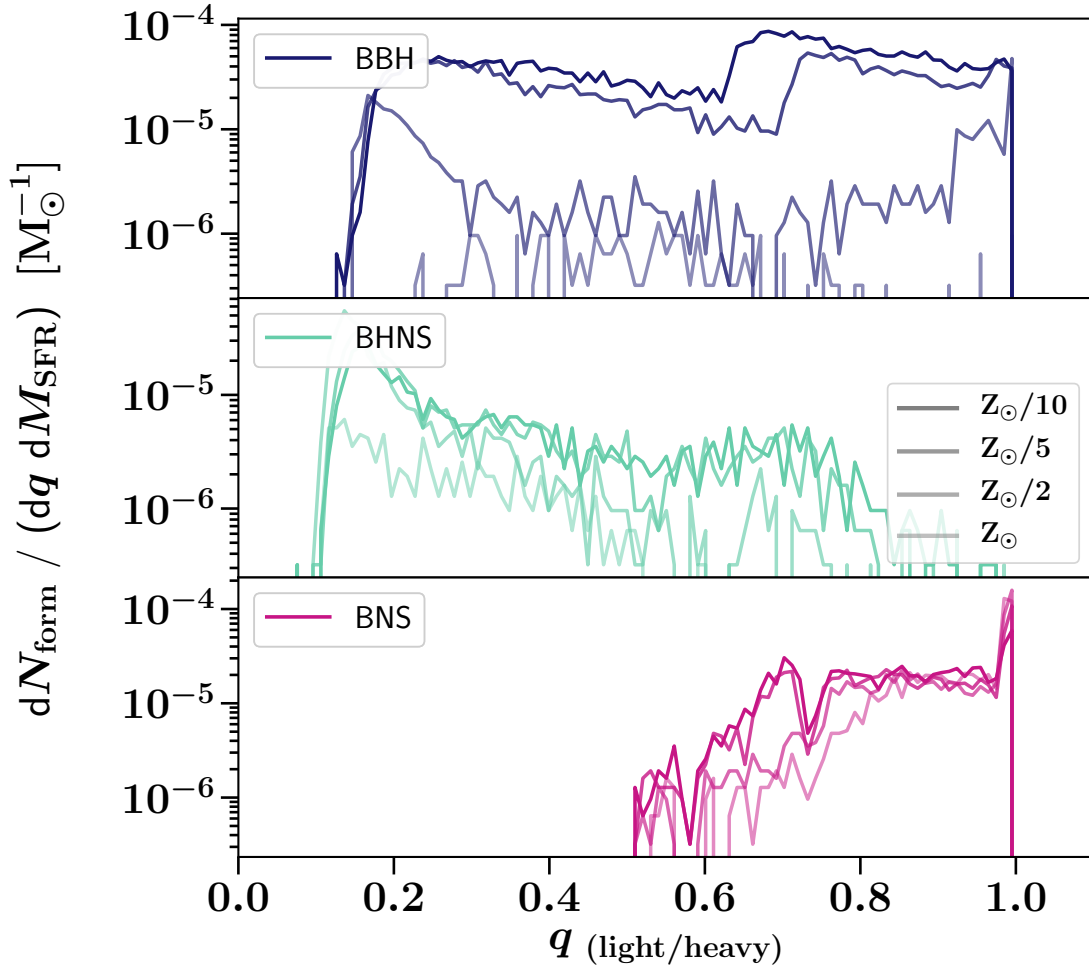


Figure 4.4: Mass-ratio distributions of BBHs (blue), BHNSs (mint) and BNSs (red) merging in $t_{\text{delay}} < 14$ Gyr from COMPAS simulations for a tenth, a fifth, a half, and solar metallicity (dark to light shade). For BBHs channel II contributes more at lower metallicities and therefore the mass-ratio distribution at $0.1Z_{\odot}$ has a prominent feature around $q \approx 0.65$.

as they provide the most orbital hardening. After this mass transfer, the stripped donor star collapses into a BH. This results in a BBH mass ratio around $q \gtrsim 0.6$. If such an additional peak is observed in the mass-ratio distribution of gravitational-wave events, its prominence and location could constrain the ratio of formation channels and hence the stability of mass transfer.

4.5 Metallicity-specific star formation rate

We split the calculation of the MSSFR into two independent factors, the SFR and the metallicity density function dP/dZ :

$$\frac{d^3 M_{\text{SFR}}}{dt_s dV_c dZ}(z) = \frac{d^2 M_{\text{SFR}}}{dt_s dV_c}(z) \times \frac{dP}{dZ}(z). \quad (4.6)$$

In practice, the SFR and the metallicity distribution may be correlated (see for example Furlong et al. 2015). However, decoupling the SFR and the metallicity distribution is a convenient simplifying assumption that yields sufficient degrees of freedom given current observational constraints.

We discuss detailed models of the SFR and metallicity distribution in Appendix 4.A. Here, we summarise the key approach to justify the shape of a phenomenological model that can be used for future inference. We highlight a particular choice of the model parameters that, coupled with our default binary evolution model, well matches the data from the first two observing runs of the advanced detector network (see section 4.7).

Figure 4.5 illustrates our SFR model. All models in Fig. 4.5 agree well at low redshift, $z \lesssim 2$, other than differences in calibration due to the assumed initial mass function (Madau and Fragos, 2017). At higher redshift, Strolger et al. (2004) assume greater extinction and find a higher rate of star formation than Madau and Dickinson (2014). We follow the functional form of Madau and Dickinson (2014) in

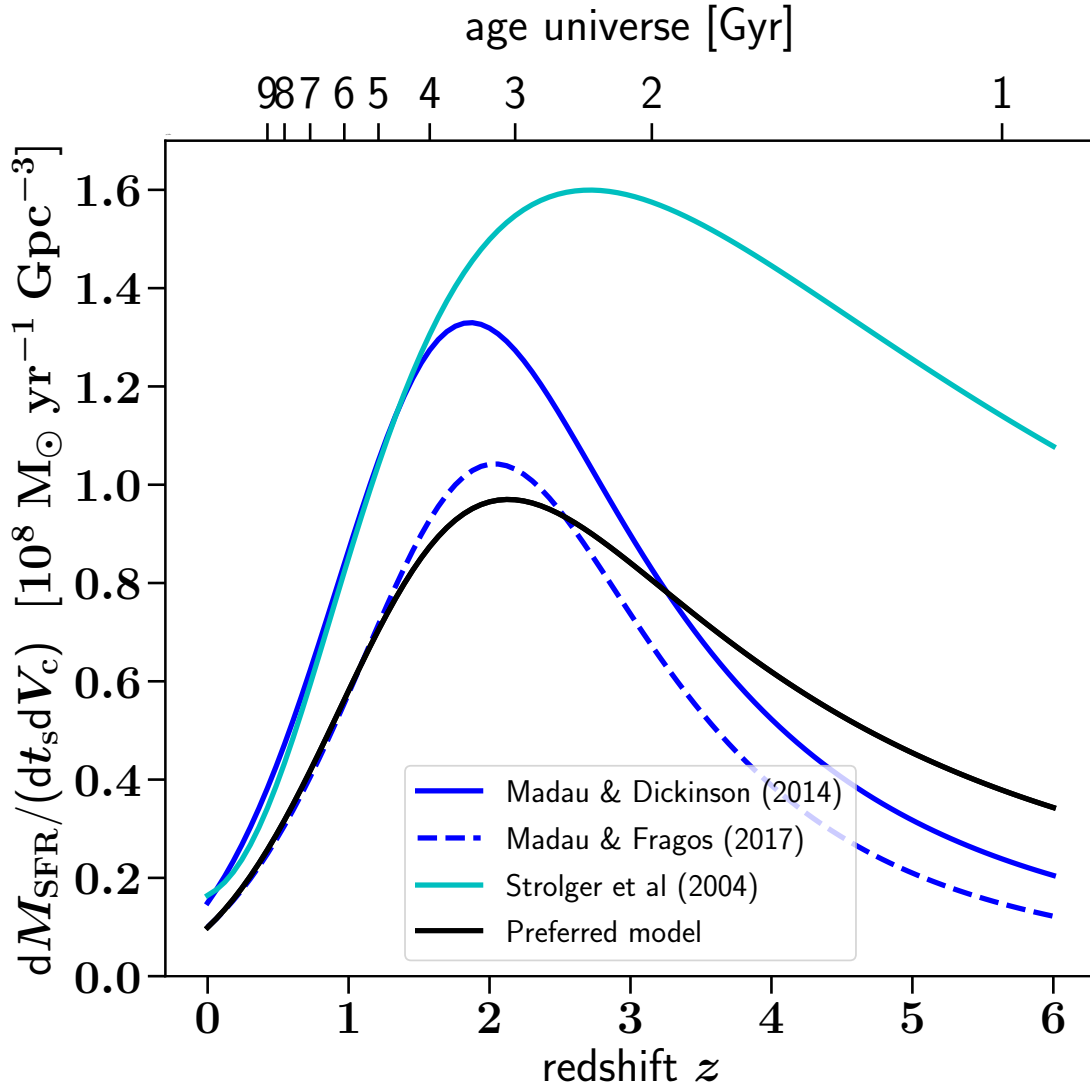


Figure 4.5: The star formation rate: mass per unit comoving volume per unit time as a function of redshift. The shapes of the distributions are similar up to a redshift of 1.5. The star formation rate estimate of Madau and Dickinson (2014) peaks slightly earlier, at a redshift of two, and then decreases steeply. Stolger et al. (2004) used an additional extinction correction and recover a higher star formation rate at higher redshifts. Madau and Fragos (2017) assume a slightly different IMF resulting in a lower normalisation. We also include our preferred phenomenological model for the star formation rate history.

our phenomenological model,

$$\frac{d^2 M_{\text{SFR}}}{dt_s dV_c} = a \frac{(1+z)^b}{1 + [(1+z)/c]^d} \text{ M}_\odot \text{ year}^{-1} \text{ Mpc}^{-3}. \quad (4.7)$$

The entire parameter space would be 4-dimensional, but we find that all of these SFR prescriptions are reasonably reproduced by setting $b = 2.77$, $c = 2.9$ and letting a and d vary in the intervals $[0.01\text{--}0.015]$ and $[3.6\text{--}5.6]$, respectively. In section 4.7, we show that $a = 0.01$ and $d = 4.7$ yield a good match to gravitational-wave observations when coupled with the metallicity distribution model discussed below and our default binary evolution model.

The metallicity density function at each redshift is typically obtained by convolving a GSMF with a MZ relation. Both of these are subject to significant uncertainties, and we describe several GSMF fits (Panter et al., 2004; Furlong et al., 2015) and MZ relations (Savaglio et al., 2005; Langer and Norman, 2006; Ma et al., 2015) in Appendix 4.A. We show the metallicity distribution at several redshifts from a combination of some of these predictions in figure 4.6. This figure also shows our fiducial model – a log-normal distribution in metallicity,

$$\frac{dP}{dZ}(z) = \frac{1}{Z\sigma\sqrt{2\pi}} e^{-\frac{(\ln(Z) - \mu(z))^2}{2\sigma^2}}, \quad (4.8)$$

with redshift-independent standard deviation σ in $\ln(Z)$ space around a redshift-dependent mean μ of $\ln(Z)$ given by,

$$\langle Z \rangle = e^{(\mu + \frac{\sigma^2}{2})}. \quad (4.9)$$

We follow Langer and Norman (2006) in parametrising mean metallicity as

$$\langle Z(z) \rangle = Z_0 10^{\alpha z}, \quad (4.10)$$

where Z_0 is the mean metallicity at $z = 0$ and the parameter α has negative values, yielding lower mean metallicity at higher redshifts. The free parameters of the

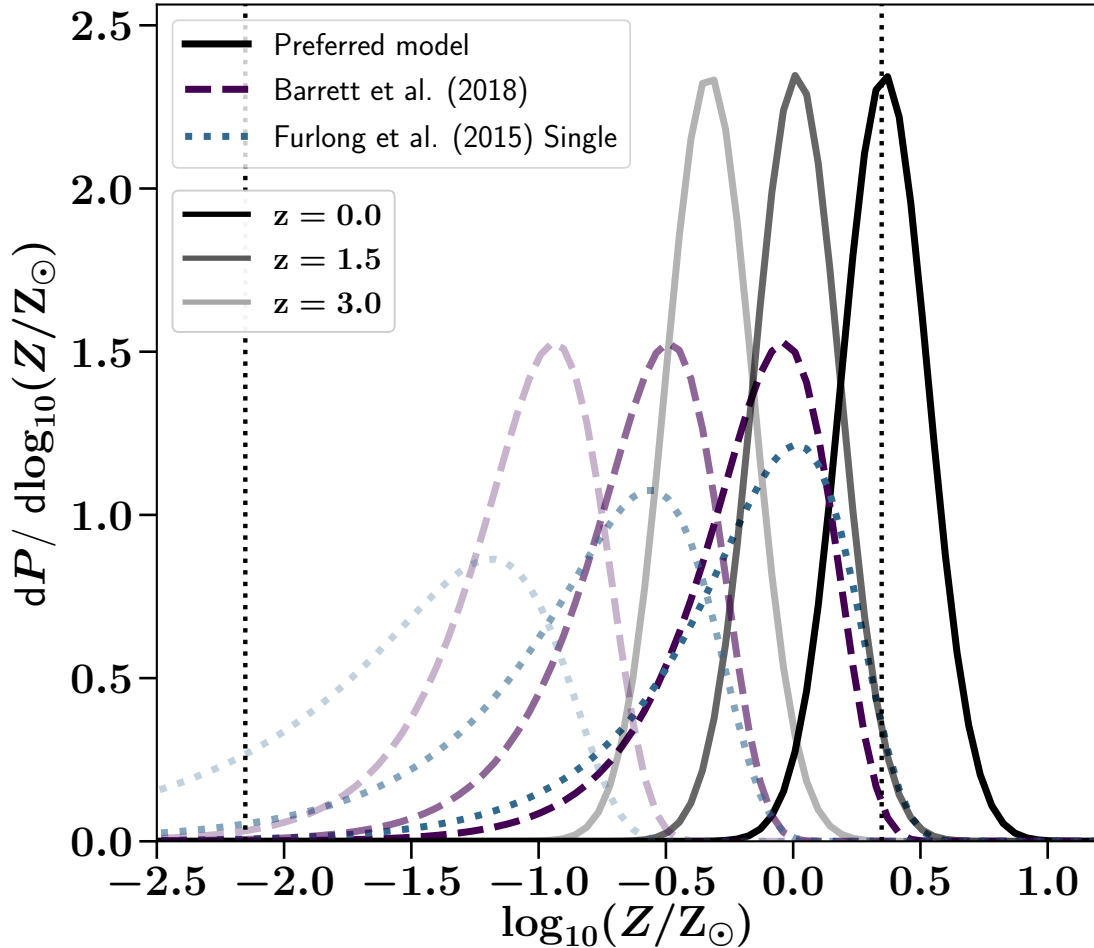


Figure 4.6: The star formation metallicity distribution. The shades (dark to light) denote the redshifts 0, 1.5, and 3. Our previous model of Barrett et al. (2018a) convolves the MZ-relation of Langer and Norman (2006) with a redshift-independent GSMF of Panter et al. (2004) (purple dashed line). The blue dotted line instead uses the GSMF described by a single Schechter function based on Furlong et al. (2015). We also include our preferred model for the metallicity distribution of star formation (black solid). The vertical dotted lines denote the limits of our metallicity grid. Portions of the distribution extending beyond these limits are included in the edge bins when integrating over metallicity.

metallicity distribution are therefore Z_0 , α and σ . We show in section 4.7 that $Z_0 = 0.035$, $\alpha = -0.23$ and $\sigma = 0.39$ yield a good match to gravitational-wave observations when coupled with our other assumptions. This preferred distribution has a similar shape to the metallicity distribution inferred by Rafelski et al. (2012) from measurements of damped Lyman α galaxies.

4.6 Distribution of DCO mergers

In this section we focus on the rate and mass distribution of DCO mergers as a function of redshift. We convolve the DCO population formed at each redshift (section 4.4) with the MSSFR (section 4.5), incorporating the delay-time distribution according to equation 4.1. We do not yet take into account selection effects. We find that the choice of MSSFR affects the total merger rate as a function of redshift, the relative rate of different types of DCO, and the mass distribution. Additionally we show that our predicted distributions do not match the priors used by Abbott et al. (2016) and Abbott et al. (2018b,a) to infer gravitational-wave signals.

4.6.1 Rate and redshift of cosmic DCO mergers

Figure 4.7 shows the intrinsic rate of DCO mergers as a function of redshift over a few MSSFR combinations. In our preferred MSSFR model, the merger rate at redshift $z = 0$ is 49, 57, 20 $\text{Gpc}^{-3} \text{yr}^{-1}$ for BBHs, BNSs, and BHNSs, respectively. These rates are the lowest compared to other models considered in section 4.5. The rate at redshift $z = 0$ is an order of magnitude less compared to our previous MSSFR model (Barrett et al., 2018a). The main reason is that our new preferred model favours extra-solar metallicities at redshifts close to zero (see Fig. 4.6). This suppresses the yield of BBHs and shifts their peak merger rate to higher redshifts which is in principle measurable with future gravitational-wave observations (Fishbach et al., 2018; Vitale and Farr, 2018). The presence of extra-solar metallicities at $z = 0$ in our preferred model is consistent with results of some other MSSFR models such as

the MZ relation found by Ma et al. (2015). Using their MZ relation to estimate the BBH merger rate also yields lower rates. Indeed, when we assume the MZ relation by Langer and Norman (2006), which has a mean solar metallicity at a redshift of $z = 0$, we find that the BBH merger rate increases compared to our preferred model. The slope of the power-law in the redshift-dependent GSMF of Furlong et al. (2015) ranges from -1.43 at $z = 0$ to -1.99 at $z > 4$, whereas the redshift-independent Schechter function by Panter et al. (2004) has a slope of -1.16 . Therefore the distribution of Furlong et al. (2015) has a lower average galaxy stellar mass with correspondingly lower metallicities, yielding higher DCO merger rates compared to the GSMF of Panter et al. (2004) assumed in Barrett et al. (2018a).

The rates of BNS and BHNS mergers differ only by a factor of few at redshifts $z > 2$ for the MSSFR combinations considered here. At these redshifts the mean metallicity is sub-solar for all of our MSSFR combinations. In our models the yield of BNSs and BHNSs is roughly constant as a function of metallicity and therefore varying the distribution of metallicities by changing the MZ relation does not greatly affect the results. Only once the mean metallicity is about solar or extra-solar, for example at $z = 0$, does the yield of BNSs and BHNSs become sensitive to metallicity and therefore to a change in MZ relations. The different estimates for the rates of BHNS mergers span an order of magnitude ($10\text{--}100 \text{ yr}^{-1} \text{ Gpc}^{-3}$) at $z = 0$. We note that the change in the MSSFR affects not only the overall DCO merger rate, but also the ratio between merger rates of different DCO types.

4.6.2 Mass distribution and redshift of cosmic DCO mergers

Figure 4.8 shows the normalised total-mass distribution of BBH mergers at several redshifts in our preferred MSSFR model. The merger rates of the systems are the result of the convolution of the redshift dependence of the MSSFR with the delay-time distribution. There is a significant contribution to low-redshift mergers from DCOs that formed at low metallicity and high redshift, with long delay times (see Fig.4.3). These low-metallicity systems give rise to high-mass BBH mergers (see

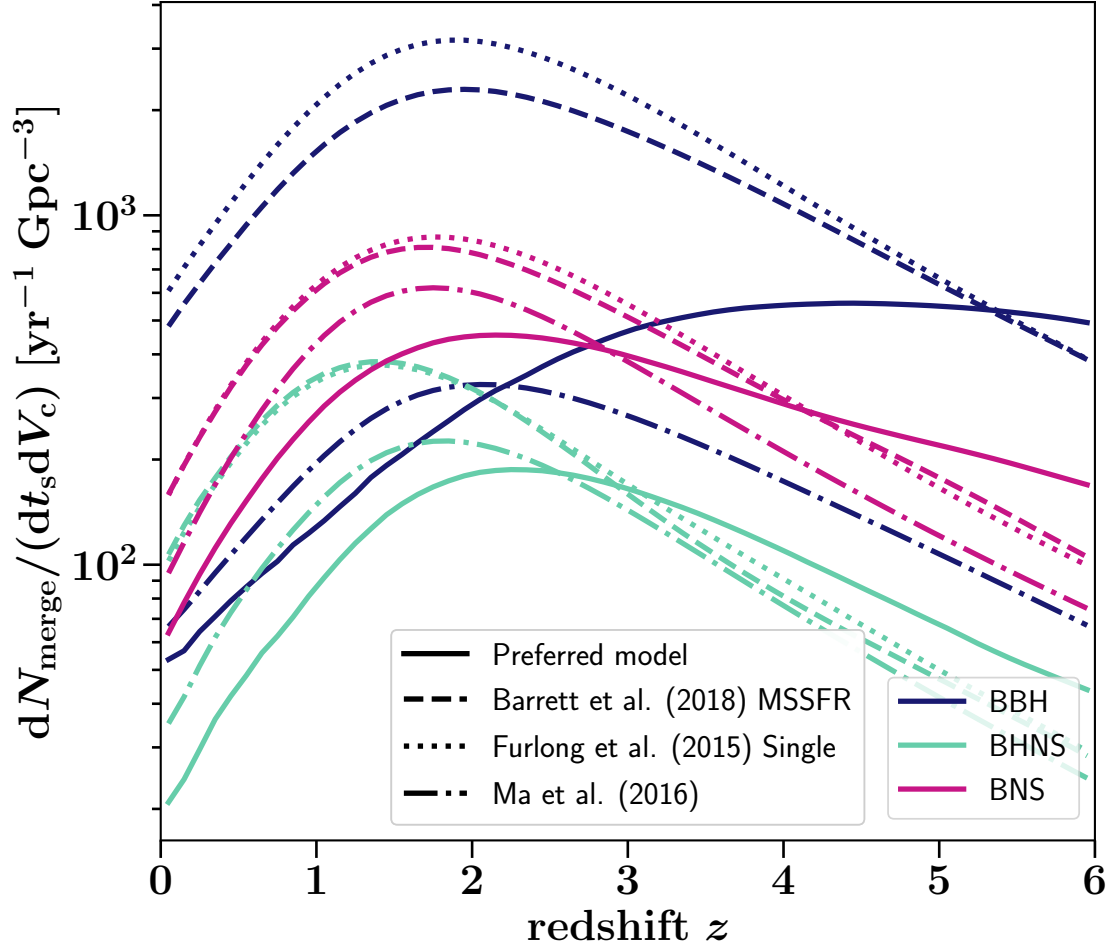


Figure 4.7: The intrinsic rate of DCO mergers per cubic Gpc per year. The colours denote different DCO types: BBHs in dark blue, BHNSs in mint, and BNSs in red. The solid line is our preferred phenomenological model. The dashed line is the default model of Barrett et al. (2018a), which combines the SFR of Madau and Dickinson (2014), the MZ-relation of Langer and Norman (2006), and the redshift-independent GSMF of Panter et al. (2004). The dotted line replaces the latter with the redshift-dependent single Schechter GSMF of Furlong et al. (2015).

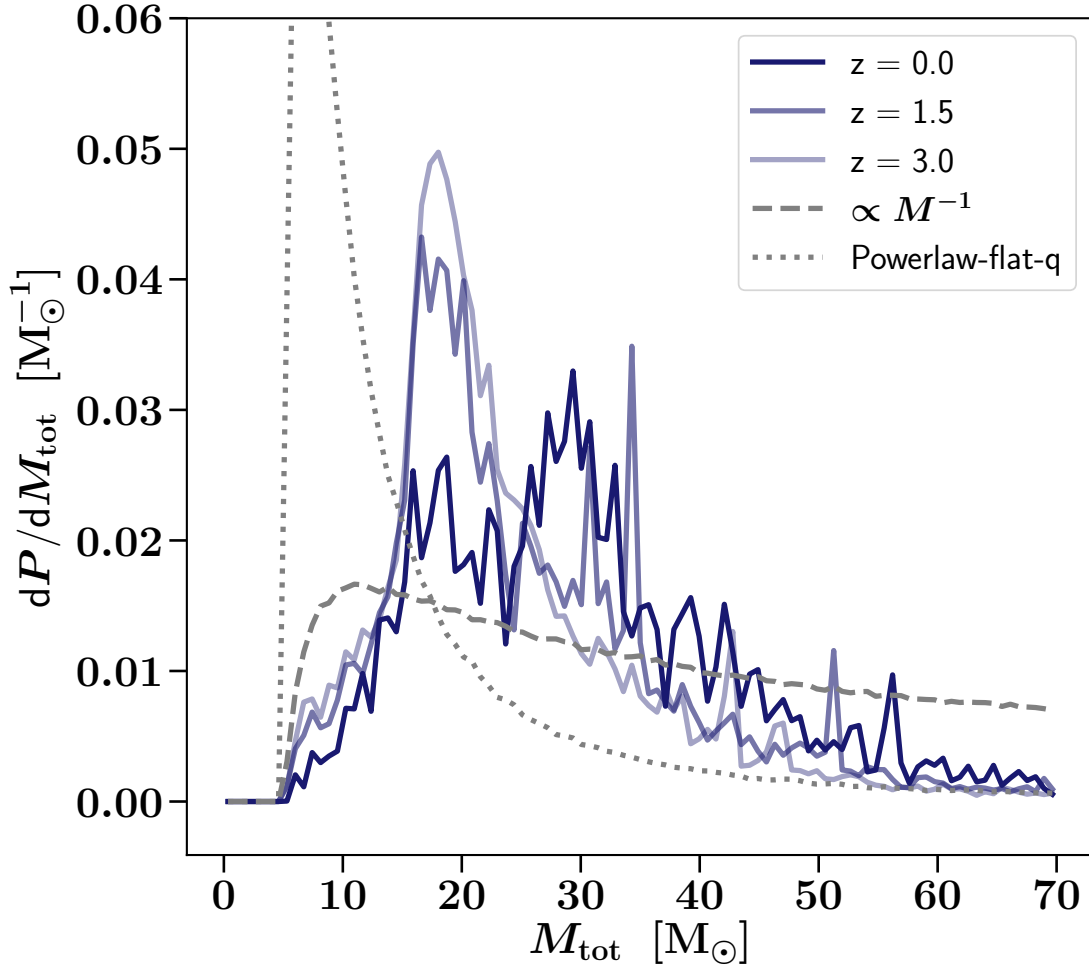


Figure 4.8: The normalised total-mass distribution of BBH mergers at redshifts 0, 1.5, and 3 (shaded dark to light) for our preferred MSSFR model. The narrow spikes above $30 M_{\odot}$ relate to the LBV systems (for more details see appendix 4.B). The dotted and dashed curve emulate the priors by Abbott et al. (2016) and Abbott et al. (2018a). The dotted curve indicates the total-mass distribution assuming that the more massive BH is sampled from a power law with an index of -2.3 paired with a companion drawn from a flat mass-ratio distribution. The dashed curve is a total-mass distribution where both BH masses are sampled from M^{-1} density distribution. For the minimum BH remnant mass we assumed $2.5 M_{\odot}$ given that we have not a lower remnant-mass gap in any of our models.

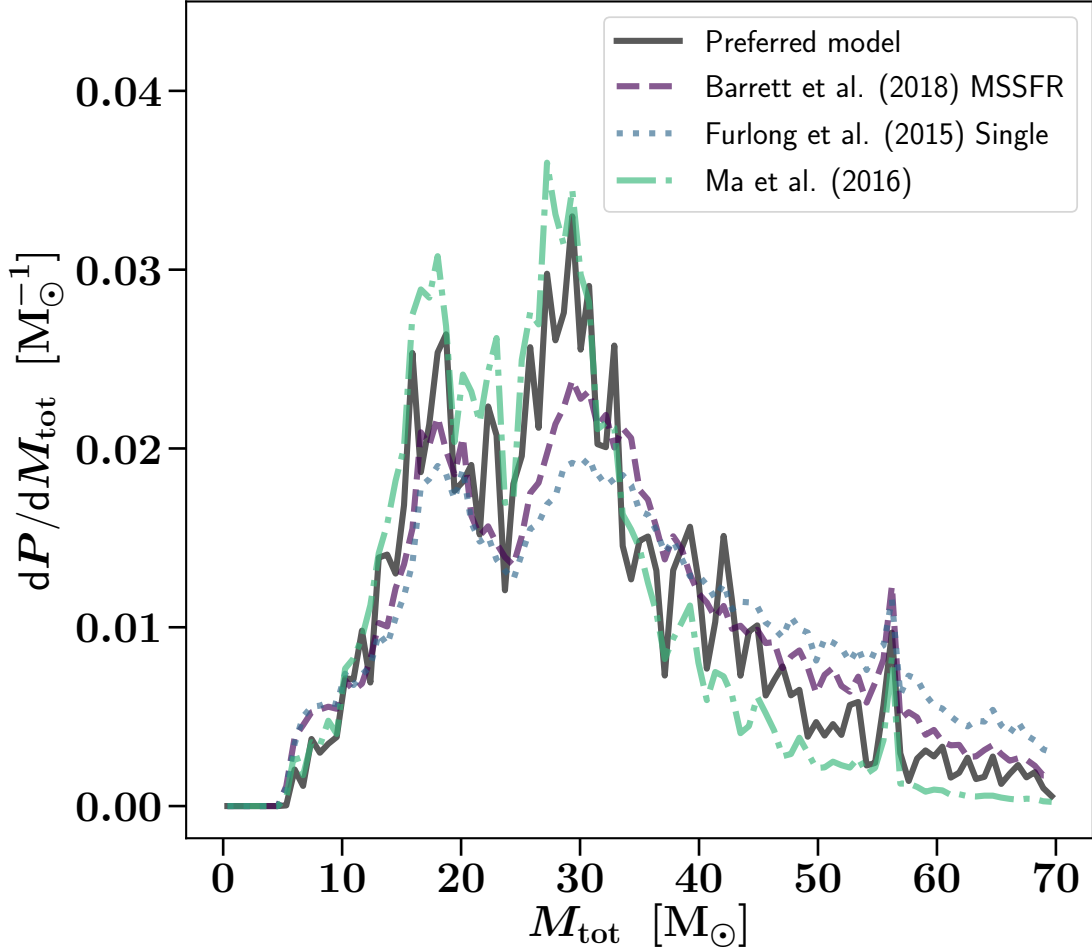


Figure 4.9: The normalised total-mass distribution of BBH mergers at redshift $z = 0$. The MSSFR models are the same as in Fig. 4.7.

Fig. 4.2). There is a greater tail of high-mass DCOs merging at redshift $z = 0$ compared to higher redshifts. Fig. 4.8 shows that the rate of systems with total masses $M_{\text{tot}} > 50 M_{\odot}$ is about three times higher at $z = 0$ compared to $z = 3$ (see also Dominik et al. 2015 and Belczynski et al. 2016).

The normalised total-mass distribution is sensitive to the metallicity at which stars form, and therefore depends on the assumed MSSFR prescription. We show the impact of the MSSFR on the mass distribution of DCOs merging at redshift $z = 0$ in figure 4.9. As with the BBH merger rate discussed in section 4.6.1, MSSFR models which have relatively more star formation at lower metallicities (our previous model in Barrett et al. 2018a, especially with the Furlong et al. 2015 GSMF variation) show enhanced high-mass tails relative to MSSFR models with higher metallicity

(our preferred model) or reduced high-redshift, low-metallicity SFR (the Ma et al. 2015 MZ relation combined with the SFR of Madau and Dickinson 2014 and the redshift-independent GSMF of Panter et al. 2004). The peaks at high masses, such as at $M_{\text{tot}} \approx 51 M_{\odot}$ and $M_{\text{tot}} \approx 56 M_{\odot}$, in figures 4.8 and 4.9 are due to mass loss prescriptions, particularly LBV winds (for more details see Appendix 4.B). These depend on metallicity, hence the prominence of the peaks varies depending on the MSSFR prescription.

4.6.3 Priors and rate estimates

The DCO merger rate inferred from gravitational-wave observations is sensitive to the assumed mass distribution of the DCOs (Abbott et al., 2018b,a). We show the mass priors assumed by Abbott et al. (2016) and Abbott et al. (2018a) in figure 4.8; it is clear that these are inconsistent with our predicted mass distribution. Abbott et al. (2018a) account for uncertainties in the shape of the BBH mass distribution by varying the slope of a power law distribution. However, as we show in Fig. 4.8, the mass distribution of BBHs might be more complex than a simple power law, and is furthermore a function of redshift, along with the merger rate itself. Therefore, DCO merger rates and mass distributions inferred from simple priors or phenomenological models should be treated with caution.

The complex dependence of the mass distribution of merging DCOs on both the binary evolution model (e.g. Dominik et al., 2013; Mapelli et al., 2017; Stevenson et al., 2017) and the MSSFR (this study), and the variation in the mass distribution and merger rate with redshift, makes it challenging to propose alternative priors. Therefore, it is preferable to apply selection effects to the model population to compare model predictions against observations. This is the approach we take in the next section.

4.7 Gravitational-wave detections

This section focuses on the effect of the MSSFR on the predicted rates and mass distributions of detectable DCO mergers. We evaluate these using Eq. 4.2. We predict the total rate of detectable DCO mergers as a function of redshift and describe the mass distribution of BBH mergers. We carry out a Bayesian model comparison of different MSSFR prescriptions, taking into account both the number and the mass estimates of the 10 BBH mergers detected during the first and second observing runs of aLIGO (Abbott et al., 2016; Abbott et al., 2018b). We do not include in our analysis the 6 additional BBH candidates found in the same data set by Venumadhav et al. (2019) with an independent search pipeline and somewhat different data quality choices.

4.7.1 Selection effects

For the selection effects we use the same method as described in Barrett et al. (2018a). We use a single detector signal to noise ratio (SNR) threshold of 8 (Aasi et al., 2016), above which we assume that gravitational waves from the merger are detectable. To evaluate the SNR for a given DCO system, we compute the waveforms for the appropriate masses using a combination of IMRPhenomPv2 (Hannam et al., 2014; Husa et al., 2016; Khan et al., 2016) and SEOBNRv3 (Pan et al., 2014; Babak et al., 2017). We approximate the sensitivity of the second observing run (Abbott et al., 2018b) to be similar to the first observing run (Abbott et al., 2016). The fraction of systems with SNR above the threshold of 8 at a given distance (redshift), after sampling over the sky location and orientation of the binary (Finn and Chernoff, 1993), yields the detection probability $P_{\text{det}}(M_{\text{chirp}}, D_L)$.

4.7.2 Rate and redshift of gravitational-wave detections

The rate of detectable DCO mergers depends on the underlying merger rate, which increases up to redshift $z \sim 2$ (Fig. 4.7). However, the detection probability drops

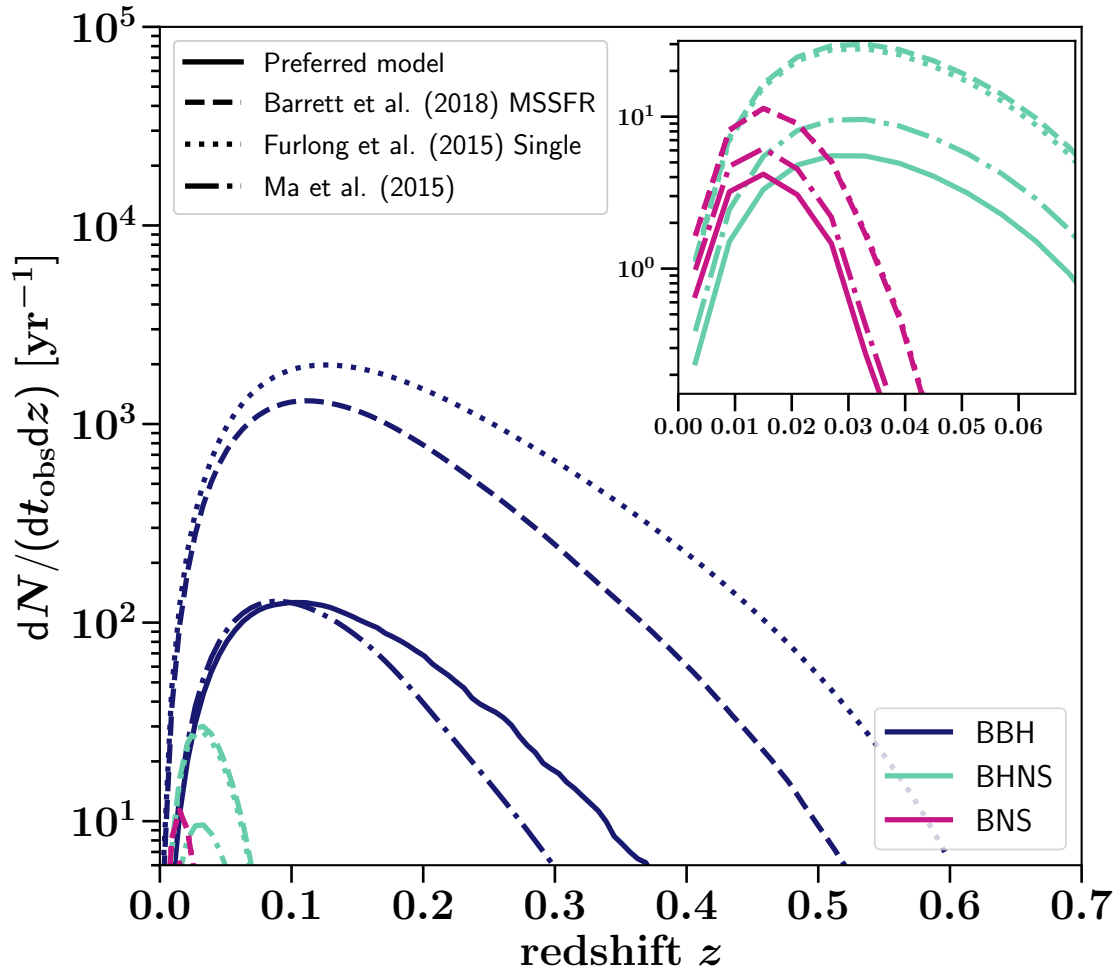


Figure 4.10: The rate of detected DCO mergers per unit redshift at the sensitivity of the first two advanced detector observing runs. The top-right panel is an enlargement with the same axes to focus in on the merger rates of BHNSs and BNSs. The MSSFR models are the same as in Fig. 4.7.

SFR	Variation MSSFR		Detection rate [yr ⁻¹]			Likelihoods (log ₁₀)		
	MZ	GSMF	BBH	BHNS	BNS	$\mathcal{L}_{\text{Mchirp}}$	\mathcal{L}_{R}	\mathcal{L}_{tot}
	Preferred model		22.15	0.23	0.08	-32.32	-0.90	-33.22
Madau et al.	Ma et al. (2004)	1	18.43	0.4	0.11	-33.9	-0.97	-34.87
		2	94.35	0.51	0.12	-32.42	-8.86	-41.28
		3	113.92	0.52	0.13	-32.48	-11.9	-44.38
	Langer et al.	1	247.22	1.28	0.22	-32.24	-34.85	-67.09
		2	441.08	1.19	0.22	-32.61	-70.6	-103.21
		3	492.27	1.25	0.23	-32.77	-80.23	-113.0
	Langer et al., offset	1	28.72	0.23	0.09	-32.3	-1.07	-33.38
		2	120.3	0.35	0.11	-32.68	-12.93	-45.61
		3	148.74	0.35	0.11	-32.87	-17.62	-50.49
Strolger et al.	Ma et al. (2004)	1	32.93	0.52	0.12	-33.82	-1.31	-35.13
		2	203.93	0.6	0.14	-32.81	-27.14	-59.95
		3	208.21	0.61	0.14	-32.65	-27.9	-60.54
	Langer et al.	1	406.39	1.28	0.23	-32.44	-64.11	-96.55
		2	659.25	1.19	0.24	-32.98	-111.92	-144.9
		3	710.91	1.25	0.24	-33.09	-121.79	-154.87
	Langer et al., offset	1	89.79	0.33	0.11	-32.46	-8.18	-40.63
		2	267.34	0.43	0.12	-33.2	-38.48	-71.68
		3	292.76	0.43	0.12	-33.22	-43.1	-76.33

Table 4.1: Rate estimates and likelihoods per MSSFR variation. The numbers in the column GSMF refer to 1=Panter et al. (2004), 2=Furlong et al. (2015) using a single Schechter function, 3=Furlong et al. (2015) using a double Schechter function. The detection rates are estimated for a year of coincident observing with the sensitivity of the first observing run of aLIGO. The likelihoods account for BBH detections during the first and second observing runs, assuming the same sensitivity (Abbott et al., 2016; Abbott et al., 2018b). The total log likelihood \mathcal{L}_{tot} is the sum of the log likelihoods of the chirp-mass distribution $\mathcal{L}_{\text{Mchirp}}$ and the rate \mathcal{L}_{R} .

off at higher redshift. These competing effects mean that the detection rate of BBH mergers peaks at a redshift between 0.1–0.15 depending on the MSSFR model at the sensitivity of the first two observing runs. This is shown in Fig. 4.10. Note that this figure displays the number of detections per unit redshift per unit observer time, rather than per unit volume per unit source time as in Fig. 4.7 (see Eq. 4.2 for the additional factors of $dV_c/dz/(1+z)$). Because NSs are less massive than BHs, mergers involving NSs cannot be observed as far as BBH mergers. The detection rates of BHNS and BNS mergers per unit redshift peak at $z \approx 0.03$ and $z \approx 0.015$, respectively. As discussed in Sec. 4.6.1, the sensitivity of the detection rate to MSSFR variations tracks the sensitivity of the DCO formation rate to metallicity (see Fig. 4.1).

Table 4.1 shows the observed rate per DCO type per year. The combined observing time of the first two observing runs is about 166 days: 48 days of coincident

data for the first and 118 days for the second observing run (Abbott et al., 2016; Abbott et al., 2018b). Thus, 10 detections translate to an observed detection rate of 22 BBH mergers per year. Most of our variations significantly overestimate the observed rate. As previously mentioned, variations that favour a higher SFR (Strolger et al., 2004), lower metallicities (Langer and Norman, 2006) or lower galaxy stellar masses (Furlong et al., 2015) predict a higher detection rate. We find that by changing the MSSFR alone we can vary the predicted rate of detectable BBH mergers by more than an order of magnitude.

All of our predictions for detectable BNS mergers are fewer than one every four years of observing time, suggesting that GW170817 was a fortuitous event if we believe our models. MSSFR models with the highest star-formation rates predict more than one detectable BHNS merger in one year observing time, however, these are generally inconsistent with observations in their BBH merger rate predictions.

4.7.3 Mass distribution of detectable BBH mergers

The top panel of Fig. 4.11 shows the predicted chirp-mass distributions of detectable BBH mergers for several MSSFR variations. We use the chirp masses of the BBHs mergers here since these are typically better observationally constrained than the total masses.

Mergers of more massive DCOs emit louder gravitational-wave signals that can be detected to greater distances. Therefore, the mass distribution of detectable BBHs is biased to higher masses relative to the intrinsic mass distribution of Fig. 4.9. The impact of MSSFR variations on the shape of the distribution follows the discussion in Sec. 4.6.2. However, the selection effects emphasise the peak due to the LBV winds at chirp masses around $25 M_{\odot}$ (see also appendix 4.B). Although the ‘delayed’ remnant mass model of Fryer et al. (2012) used in our simulations does not enforce a lower mass gap between NS and BH masses, we find that low-mass merging BBHs are very rare, especially after selection effects are applied. We do not expect significant numbers of detections in the lower mass gap for any of the MSSFR variations.

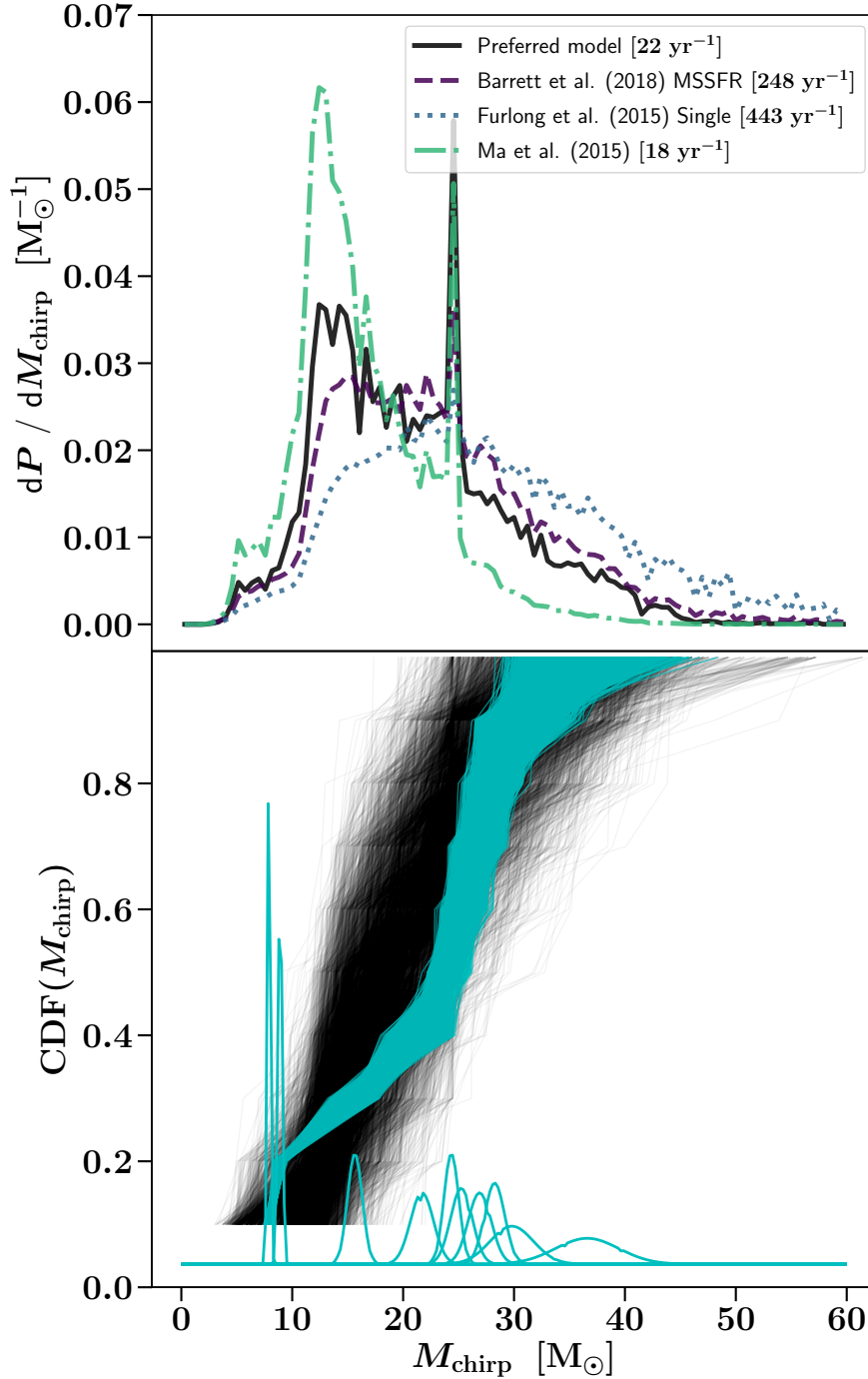


Figure 4.11: Top panel: The normalised chirp-mass distribution of BBH mergers detectable at the sensitivity of the first two observing runs. The masses are in the source reference frame. The MSSFR models are the same as in Fig. 4.7. The numbers in the label are the predicted annual detection rate. Bottom panel: Approximate Gaussian posteriors (see appendix 4.C) of BBH mergers detected during the first and second observing runs (Abbott et al., 2018b), from left to right: GW170608, GW151226, GW151012, GW170104, GW170814, GW170809, GW170818, GW150914, GW170823, GW170729. The cyan area shows randomly sampled cumulative density functions from the posteriors, indicating the spread due to the measurement uncertainty. The black lines are cumulative density functions when 10 events are randomly drawn from the preferred model.

The bottom panel of Fig. 4.11 shows that our preferred MSSFR model predicts a chirp-mass distribution of detectable BBH mergers that is consistent with the detection from the first two advanced detector observing runs. Approximate Gaussian posteriors (see appendix 4.C) for the ten detections are shown in cyan at the bottom of the plot. We construct observed CDFs by taking a random sample from each of these ten posteriors. The set of cyan curves indicates the range of observed CDFs consistent with measurement uncertainty. Meanwhile, each black curve represents a CDF constructed by sampling from the predicted distribution of detectable BBH events under the preferred MSSFR model. The visual overlap between the black and cyan regions indicates that the observations are consistent with the model within the statistical uncertainty of this limited data set, although the CDF of the data does not perfectly match the model prediction.

4.7.4 Bayesian comparison of MSSFR models

We showed that the choice of the MSSFR affects both the detectable rates and mass distributions of DCO mergers. Here we quantitatively compare these models against observations during the first and second observing run (Abbott et al., 2018b). We consider the total rate of events and the relatively well-measured chirp masses. We do not consider other properties such as relatively poorly measured mass ratios or source redshifts given the narrow range of redshifts reached to date. Bavera et al. (2019) compare a possible model for BBH spins evolving through channel I (see section 4.4.1) using the COMPAS data presented here against observations. In this analysis (as in Barrett et al. 2018a), the total log likelihood \mathcal{L}_{tot} is the sum of the rate log likelihood \mathcal{L}_{R} and the likelihood of the normalised chirp-mass distribution $\mathcal{L}_{\text{Mchirp}}$,

$$\mathcal{L}_{\text{tot}} = \mathcal{L}_{\text{Mchirp}} + \mathcal{L}_{\text{R}}. \quad (4.11)$$

The rate likelihood assumes a Poisson distribution for the detection of gravitational-wave events, where the MSSFR model gives the expected number of detections over the duration of the first two observing runs. The chirp-mass likelihood is the product over the ten events of the probabilities of making individual detections given the predicted chirp-mass distribution (see appendix 4.C). A difference of 1 in log likelihoods, corresponding to a factor of 10 in the likelihoods, implies that the higher-likelihood model is preferred over the lower-likelihood model by a factor of 10 (i.e., has an odds ratio of 10 : 1, assuming both models are equally probable a priori). Table 4.1 shows the total likelihoods for the pessimistic common-envelope assumptions. A longer list of variations, including the optimistic common-envelope assumption, can be found in tables 4.3 and 4.2.

The rate likelihoods differ significantly given our range in rate estimates. Many of the MSSFR models greatly overestimate the rates and are strongly disfavoured under the assumed model of binary evolution. Meanwhile, despite the visual difference in the shape of the chirp-mass distribution (see Fig. 4.11), the difference in the chirp-mass likelihoods is small. More detections will make it possible to jointly explore MSSFR and evolutionary models using the observed chirp-mass distributions (Barrett et al., 2018a). Given our binary evolution model, the log-likelihoods indicate a preference for higher star-formation metallicities at low redshifts to match the observed BBH rate and chirp-mass distribution.

In section 4.5 we introduced a 5-parameter phenomenological model of the MSSFR. With suitable parameter choices this generic model can match all of the detailed models considered here, while providing the convenience of a continuous, smooth parametrisation that is useful for inference. We also introduced a particular choice of these 5 parameters – our preferred model – that yields a good match to both the number of BBH mergers detected during the first two observing runs (10.06 predicted vs. 10 observed) and their chirp mass distribution (section 4.7.3 and the bottom panel of Fig. 4.11). As table 4.1 shows, this preferred model also yields the highest likelihood among all considered models. This preferred model favours a SFR

similar to Madau and Fragos (2017), which includes the contribution from stars in binaries. However, we do favour a higher SFR at high redshifts, where metallicity is lower, to enhance the fraction of massive BBH merger events. We caution, however, that the MSSFR parameters in the preferred model are chosen ad hoc, with some ‘Fingerspitzengefühl’. We refrain from further optimising the MSSFR parameters since the uncertainty in binary evolution should be taken into account. Future analyses should jointly infer the parameters of the MSSFR and parameters describing the binary evolution model, using gravitational waves and other observational constraints.

4.8 Conclusion and discussion

We showed that assuming different MSSFR within observational constraints can vary the rate of BBH mergers by more than an order of magnitude within a fixed stellar and binary evolution model² and affect the ratio between BBH, BHNS, and BNS detection rates. This is comparable to the impact of uncertainties on evolutionary physics such as wind mass-loss rates, conservativeness of mass transfer, the efficiency of common-envelope evolution and BH natal kicks (Dominik et al., 2012; Kruckow et al., 2018; Giacobbo and Mapelli, 2018).

The sensitivity to MSSFR is predominantly driven by the impact of metallicity on the yield of BBHs per unit star-forming mass. This is consistent with earlier findings (e.g., Dominik et al., 2015; Chruslinska et al., 2018). In particular, Chruslinska et al. (2018) also find that a higher average metallicity is required in order to not over-predict the BBH merger rate.

Here, we explored the impact of the MSSFR while keeping the binary evolution model unchanged. In practice, joint inference on stellar and binary physics and the MSSFR is required to fully interpret observations (e.g., Chruslinska et al., 2018). For example, (pulsational) PISNe (see for example Woosley (2017) and references therein) can prevent the formation of BHs with masses between around 50 and 130

²There is a further uncertainty from the definition of solar metallicity, see appendix 4.A.5.

M_{\odot} , i.e., with chirp masses between 45 and 115 M_{\odot} for equal-mass binaries. Abbott et al. (2018a) find that existing gravitational-wave detections show evidence for a maximum black hole mass of around $\sim 45 M_{\odot}$, consistent with population synthesis studies such as Belczynski et al. (2016); Spera and Mapelli (2017) and Stevenson et al. (2019). However in Fig. 4.11, we show that it is possible to reproduce such a limit within the evolutionary model of this paper, which does not include pulsation PISNe, by choosing a suitable MSSFR alone (Madau and Dickinson (2014); Ma et al. (2015); Langer and Norman (2006)). A similar argument can be made for the presence or absence of a mass gap between NSs and BHs. Beyond gravitational-wave observations, other observational constraints such as the epoch of reionisation (Stanway et al., 2016), SNe (Chruslinska and Nelemans, 2019; Eldridge et al., 2019), and X-ray binaries (Madau and Fragos, 2017) can further help to lift the degeneracy between binary physics and the MSSFR.

We introduced a phenomenological description of the MSSFR with 5 continuous parameters (section 4.5) to facilitate the joint exploration of the MSSFR and parametrised evolutionary assumptions. We also proposed a particular choice of the MSSFR model parameters that represents a good match to the BBH gravitational-wave detections made during the first two observing runs of advanced LIGO and Virgo. We use constraints from BBH observations rather than BNS or BHNS because the precision of the latter observational constraints is limited by the small number of detections. Assuming our preferred model, the observed BNS detection GW170817 appears to be fortuitous, however our models are consistent with other observational constraints on BNS merger rates, such as observations of Galactic binary pulsars (Vigna-Gómez et al., 2018). Future detections will enable joint inference of both the MSSFR and the parametrised evolutionary model uncertainties and may shift the preferred model presented in this study. In the meantime, we used this model in other population studies, such as Stevenson et al. (2019). Looking ahead, we can apply this preferred MSSFR model to make predictions for the detection rate and chirp mass distribution at the expected design sensitivity of LIGO gravitational-

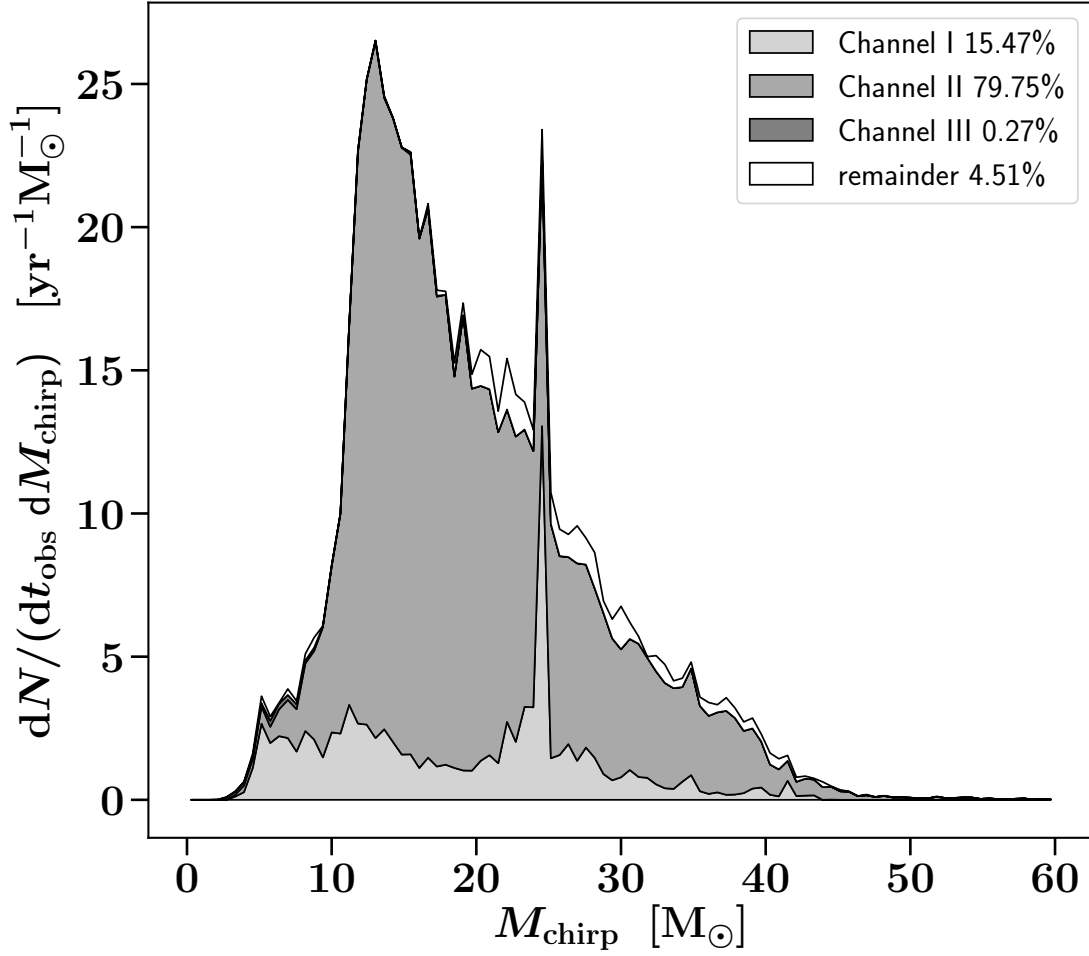


Figure 4.12: The predicted chirp mass distribution of detectable BBH mergers at advanced detector design sensitivity within our preferred MSSFR model, coloured by the BBH formation channels. Almost 80% of the expected 380 detectable BBHs per year are formed through channel II (dynamically stable mass transfer) within our evolutionary model.

wave observatory, shown in figure 4.12. We predict 380 BBH detections per year, or approximately one detection per day, within our default evolutionary model.

Our phenomenological model of the redshift-dependent MSSFR is adequate for exploring cosmologically averaged merger rates. Studies of specific galaxy hosts or host types (e.g., in the context of electromagnetic counterpart observations) require more detailed models, such as those considered by Lamberts et al. (2016); Chruslinska and Nelemans (2019); Boco et al. (2019).

Figure 4.12 also highlights the importance of the dynamically stable mass transfer channel without a common-envelope phase to form of detectable merging BBHs. We find that channel II may be responsible for 80% of all detected BBH mergers. This highlights the importance of mass transfer stability criteria, which merit further investigation. Meanwhile, the narrow chirp mass spike at around $25 M_{\odot}$ is due to the operation of LBV mass loss at a particular metallicity (cf. Dominik et al., 2015). The peaks do not have a great impact on the overall rates and likelihood distributions, but possibly complicate efforts to emulate the results of population-synthesis codes using techniques such Gaussian process regression (Barrett et al., 2017). While we expect that a finer metallicity grid or interpolation between metallicities would lead to a smoother chirp mass distribution, this again highlights the importance of highly uncertain LBV winds for these predictions (Mennekens and Vanbeveren, 2014). Finally, the sampling accuracy of predictions (e.g., the time-delay distribution for BHNS in Figure 4.3) could be improved with more efficient importance sampling techniques (Broekgaarden et al., 2019).

Our predictions suggest that approximately one thousand detections could be reached within a couple of years of operation of advanced detectors operating at design sensitivity. Barrett et al. (2018a) showed that this will be sufficient to constrain the binary evolutionary parameters to a fractional accuracy of a few percent. Our phenomenological MSSFR model can be incorporated into this hierarchical modelling framework to be enable joint inference on binary evolution and the cosmic history of star formation.

4.9 Acknowledgements

We thank the anonymous referee for helpful suggestions. C. J. N. thanks the University of Birmingham for financial support, C. P. L. Berry, S. Bavera and A. Vecchio for helpful discussions, D. J. Stops for technical support, and of course above all T. F. Pauw for everything. A. V. G. acknowledges support from Consejo Nacional de Ciencia y Tecnologia (CONACYT). S. S. is supported by the Australian Research Council Centre of Excellence for Gravitational Wave Discovery (OzGrav), through project number CE170100004. S. M. G. is supported by STFC grant ST/M004090/1. S. dM. acknowledges funding by the European Union’s Horizon 2020 research and innovation programme from the European Research Council (ERC), Grant agreement No. 715063), and by the Netherlands Organisation for Scientific Research (NWO) as part of the Vidi research program BinWaves with project number 639.042.728. D. Sz. accepts funding from the Alexander von Humboldt Foundation. This paper used the `Astropy` library (Astropy Collaboration et al., 2013, 2018), `matplotlib` (Hunter, 2007), and `numpy` (Oliphant, 2006).

4.A Metallicity-specific star formation rate

4.A.1 Cosmological star formation rate - SFR

We consider several prescriptions for the cosmological SFR as a function of redshift z . The first is from Madau and Dickinson (2014):

$$\frac{d^2 M_{\text{SFR}}}{dt_s dV_c}(z) = 0.015 \frac{(1+z)^{2.7}}{1 + [(1+z)/2.9]^{5.6}} \text{ M}_\odot \text{ yr}^{-1} \text{ Mpc}^{-3}. \quad (4.12)$$

At higher redshifts the observations become more sensitive to extinction which remains uncertain. Strolger et al. (2004) construct a fit for the SFR using a different

extinction correction, as

$$\frac{d^2 M_{\text{SFR}}}{dt_s dV_c}(t) = 0.182 \times \left(t^{1.26} e^{-t/1.865} + 0.071 e^{0.071(t-t_0)/1.865} \right) \text{M}_{\odot} \text{yr}^{-1} \text{Mpc}^{-3}, \quad (4.13)$$

where $t(z)$ is the age of the Universe at redshift z in Gyrs, and t_0 is the current age of the Universe, which they set to 13.47 Gyrs. These two SFR models agree at low redshifts, $z \lesssim 2$, where both models peak; however, the model of Strolger et al. (2004) has a shallower drop off at higher redshifts (see Fig. 4.5). Simulations so far have not independently constrained the SFR at high redshifts. There are, for example, additional uncertainties such as the role of active galactic nuclei and feedback on the interstellar medium (Taylor and Kobayashi, 2015).

Madau and Fragos (2017) use an updated SFR compared to Madau and Dickinson (2014). A key difference is assuming a broken power-law IMF by Kroupa (2001) instead of the classic power-law by Salpeter (1955). This increases the relative number of massive stars and therefore lowers the overall SFR normalisation by a factor of 0.66. The shape of the Madau and Fragos (2017) and Madau and Dickinson (2014) SFR models is similar, and we generally use the Madau and Dickinson (2014) prescription in our analysis. However, we adjust the low-redshift normalisation of our preferred model to approximately match the more recent estimate of Madau and Fragos (2017).

Estimates of the SFR at high redshifts rely on proxy observations, such as UV luminosities or gamma-ray bursts. For UV luminosities dust attenuation is an issue. Correlations between UV continuum slopes, redshift and dust obscuration witnessed in lower-redshift galaxies can be extrapolated to higher-redshift observations (Bouwens et al., 2009). The sensitivity to the assumed IMF introduces additional uncertainties (Hopkins and Beacom, 2006). These combined uncertainties lead to a broad range of high-redshift SFR estimates (Hopkins and Beacom, 2006), between 10^7 and $10^8 \text{M}_{\odot} \text{Gpc}^{-3} \text{yr}^{-1}$ at $z = 6$ (cf. Fig. 4.5). Gamma-ray bursts are not sensitive to dust, but the connection between their rate and the underlying SFR is itself

model-dependent. Yüksel et al. (2008) recover an SFR drop-off at higher redshifts from gamma-ray burst observations that is less steep than the drop-off recovered from UV observations. The various SFR models used in this study are generally consistent within uncertainties in the literature, despite being based on different observational evidence and different assumptions.

4.A.2 Galaxy stellar mass to metallicity - MZ-relation

As described in section 4.5, we can construct star-forming metallicity density functions by convolving the galaxy stellar mass distribution with the MZ relation, which connects the galaxy stellar mass (M_*) and metallicity. We describe the MZ relations considered in this work in this subsection, and the GSMFs in the next one.

Stellar metallicities are assumed to match the metallicity of the interstellar gas of their surroundings at birth. Observations are typically given in terms of the ratio of the number density of oxygen and hydrogen in the gas, generally written as $\log_{10}[\text{O}/\text{H}] + 12$. Conversions to metallicity depend on the assumed solar abundances. In this study we define the solar metallicity mass fraction as $Z_{\odot} = 0.0142$ and the solar oxygen abundance of $\log_{10}[\text{O}/\text{H}]_{\odot} + 12 = 8.69$ based on Asplund et al. (2009). Ma et al. (2015) discuss some of the uncertainties in the slopes and offsets in the MZ relation, including the use of different observational samples or metallicity diagnostics, or the use of different simulation resolutions and feedback mechanisms in theoretical models (e.g., Taylor and Kobayashi, 2015).

In Barrett et al. (2018a) we used the prescriptions of Langer and Norman (2006), who in turn use a MZ relation from Savaglio et al. (2005). This MZ relation is derived from a fit of 56 galaxies in the Gemini Deep Deep Survey with a mean redshift of around 0.7. Savaglio et al. (2005) provide a quadratic and linear bisector fit, the latter being

$$\log_{10}[\text{O}/\text{H}] + 12 = 0.478 \log_{10} \left(\frac{M_*}{M_{\odot}} \right) + 4.062. \quad (4.14)$$

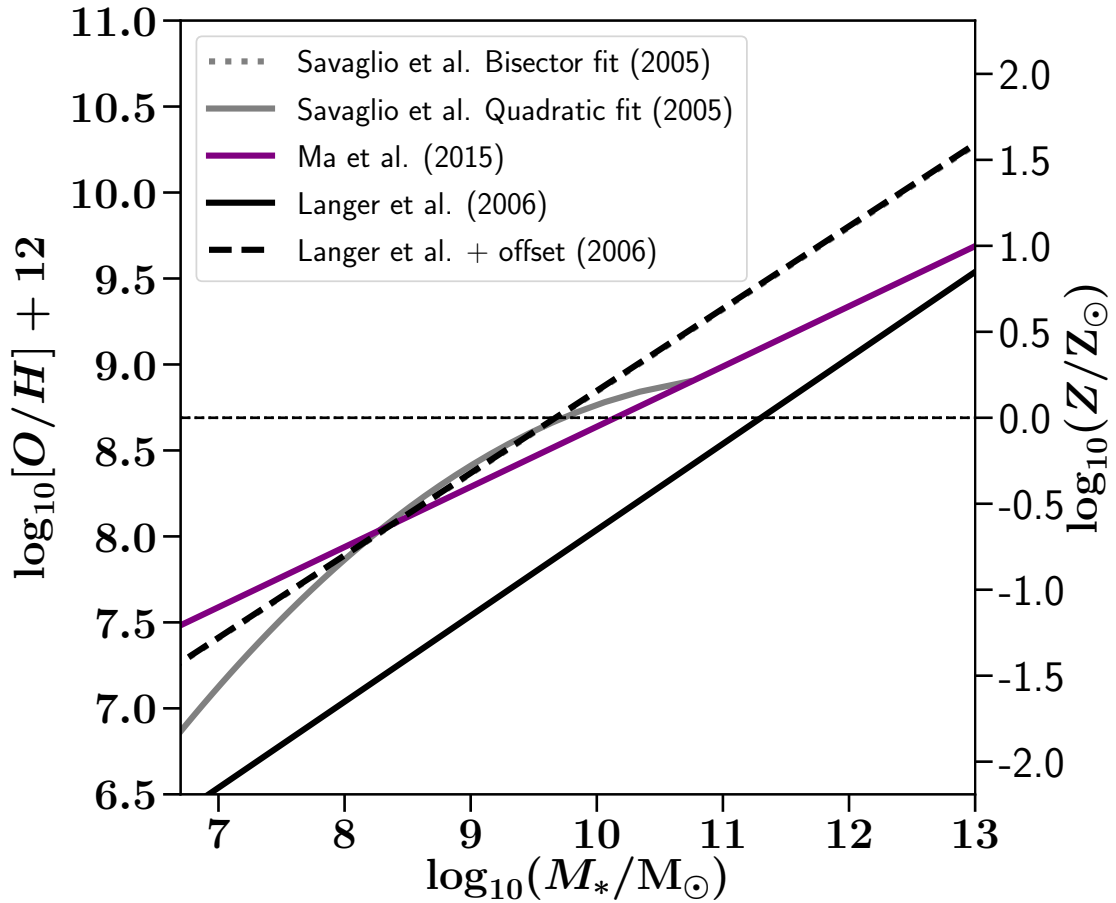


Figure 4.13: Comparison between different MZ relations at a redshift of 0.7, at which the relation of Savaglio et al. (2005) was determined. We also show our introduced offset to Langer and Norman (2006) which overlaps with the bisector fit of Savaglio et al. (2005). Note that the extrapolation of the quadratic fit of Savaglio et al. (2005) beyond their upper limit of $\log_{10}(M_*) = 11$ results in a turnover. The dot-dashed horizontal line is our definition of the relation between solar metallicity and solar oxygen number density (Asplund et al., 2009).

We use the bisector fit because it is a monotonically increasing function of galaxy mass. The large differences at higher masses between the fits are largely due to the inclusion or exclusion of just four high-mass galaxies (Savaglio et al., 2005), illustrating the uncertainty at the extreme ends of MZ relations. Langer and Norman (2006) approximate this fit with a simplified MZ relation:

$$\frac{M_*}{M_x} = \left(\frac{Z}{Z_\odot} \right)^2, \quad (4.15)$$

where $M_x = 7.64 \times 10^{10} M_\odot$ (Panter et al., 2004). Langer and Norman (2006) assume that the mean metallicity decreases exponentially with redshift as,

$$\langle Z \rangle = Z_\odot 10^{-0.3z}. \quad (4.16)$$

When we translate this back into a MZ relation we find that there is difference between the approximate Langer and Norman (2006) MZ relation and the fit of Savaglio et al. (2005) (see Fig. 4.13). We introduce an offset to the model of Langer and Norman (2006) in order to recover the relation by Savaglio et al. (2005). This offset together with the original redshift scaling results in a high mean metallicity at redshift zero, but we keep this as an alternative model to look at its effects.

The second MZ-relation we consider is a theoretical model due to Ma et al. (2015). They combine cosmological simulations with stellar population synthesis models and a variety of feedback mechanisms to trace the evolution of the interstellar gas, for galaxy stellar masses ranging between $4 \leq \log_{10}(M_*/M_\odot) \leq 11$ and redshifts between 0–6. Ma et al. (2015) give the MZ-relationship as

$$\begin{aligned} \log_{10} \left(\frac{Z_{\text{gas}}}{Z_\odot} \right) &= 0.35 \left[\log_{10} \left(\frac{M_*}{M_\odot} \right) - 10 \right] \\ &+ 0.93e^{-0.43z} - 1.05. \end{aligned} \quad (4.17)$$

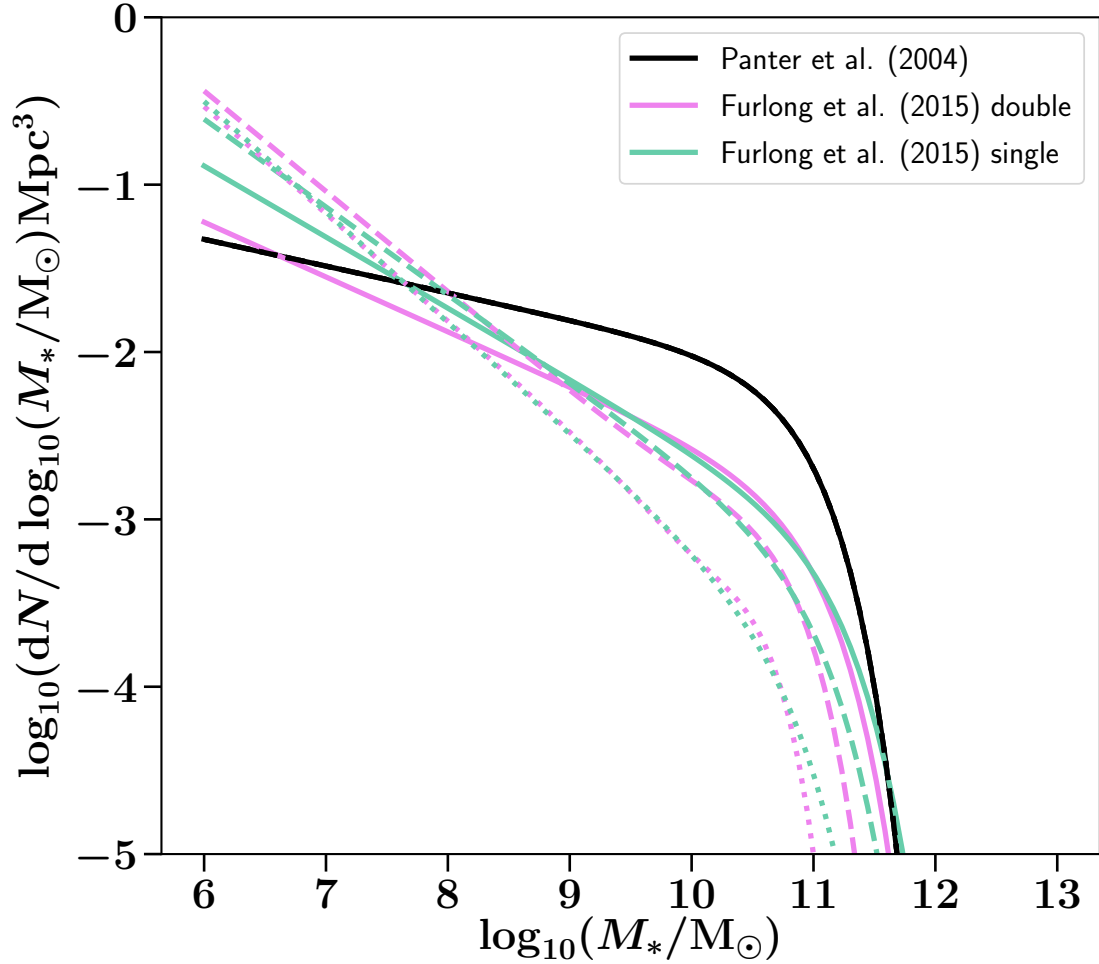


Figure 4.14: Comparison between the galaxy stellar mass density functions at redshifts $z = 0$ (solid), $z = 1.5$ (dashed), and $z = 3$ (dotted). The relation by Panter et al. (2004) is independent of redshift, therefore there is only a single curve (black). The double Schechter function by Furlong et al. (2015) (pink) has a steeper drop off at higher galaxy stellar masses compared to their single Schechter function (mint). Both power-law slopes of Furlong et al. (2015) are steeper than the Schechter function of Panter et al. (2004). This shifts the former distribution towards lower galaxy stellar masses, which translates to lower metallicities.

4.A.3 Galaxy stellar mass density function - GSMF

The GSMF is empirically constructed by converting the luminosity of a sample of galaxies into a stellar mass, assuming a mass-to-light ratio. Although samples and methods differ between compilations, Baldry et al. (2008) show that for galaxies within the mass range of $8.5 \leq \log_{10}(M_*/M_\odot) \leq 12$ at redshift $z < 0.1$, there is good agreement on the shape of the GSMF.

The general shape is that of a Schechter function (Schechter, 1976):

$$\Phi_{M_*}(z)dM = \phi_1(z) \left(\frac{M_*}{M_c(z)} \right)^{-\alpha(z)} e^{-\frac{M_*}{M_c(z)}} dM, \quad (4.18)$$

where α determines the slope of the GSMF at the low-mass end, M_c is the turnover mass, and ϕ_1 the overall normalisation. However, a double Schechter function appears to better fit the extreme mass ends of the GSMF (Baldry et al., 2008; Furlong et al., 2015):

$$\Phi_{M_*}(z)dM = e^{-\frac{M_*}{M_c(z)}} \times \left[\phi_1(z) \left(\frac{M_*}{M_c(z)} \right)^{-\alpha_1(z)} + \phi_2(z) \left(\frac{M_*}{M_c(z)} \right)^{-\alpha_2(z)} \right] dM. \quad (4.19)$$

The double Schechter function fit determined from the EAGLE simulations by Furlong et al. (2015) is able to reproduce the empirical observations of Duncan et al. (2014). We performed a linear fit to the tabulated coefficient values in the appendix of Furlong et al. (2015) (see their table A1) to recover both a single and double Schechter GSMF. Their results are for redshifts in the range $0.1 < z < 4$ and we linearly interpolate the coefficients within that range. We also extrapolate for lower and higher redshifts. In order to avoid unphysical behaviour, we set ϕ_2 , which is zero at $z = 0.1$ to also be zero at all redshifts below 0.1; fix $\alpha_2 = -1.79$ at $z \leq 0.5$; and enforce $\alpha \geq -1.99$ everywhere. This allows us to extrapolate the Furlong et al. (2015) GSMF over the full range $z \in [0, 6.5]$.

The GSMFs has an overall normalisation which in principle carries information

on the star formation history, although Furlong et al. (2015) note that the normalisation of their fits is imperfect at the highest redshifts, while the slope remains well fitted. However, we use a simplified model in which the SFR is independent of the GSMF, allowing us to independently parametrise and test the SFR and the metallicity distribution. Consequently, the normalisation coefficients ϕ are relevant only for describing the ratio between the two Schechter functions in Eq.4.19.

Figure 4.14 shows the different GSMF relations at a few redshifts. For comparison we also use a *redshift-independent* single Schechter function of Panter et al. (2004) as used in Langer and Norman (2006) and our previous work (Barrett et al., 2018a).

Even though the Panter et al. (2004) GSMF is redshift-independent, the metallicity distribution still changes due to the redshift dependence in the MZ relation. Meanwhile, the Furlong et al. (2015) GSMF is redshift-dependent: as galaxies grow over time, the mass distribution shifts toward higher masses at lower redshifts (Duncan et al., 2014). Conversely, the masses are lower at higher redshifts, favouring lower metallicity. Coupled with a redshift-dependent MZ relation, this further reduces mean metallicity at higher redshifts.

4.A.4 Metallicity-specific star formation rate - MSSFR

The MZ relation allows us to convert the GSMF into a metallicity distribution dP/dZ (the last term of Eq. 4.6). In practice, when integrating over metallicity, we sum over discrete bins. We convert the edges of those bins into limits on galaxy stellar masses in order to determine the fraction of star formation that happens in a given metallicity bin as the fraction of the GSMF that falls into the appropriate mass range at a given redshift.

We convert the number density of Eq. 4.19 into a mass density by multiplying by M_* . The form of this equation makes it possible to carry out the mass integral analytically, with the amount of mass at $M_* \leq M_x$ given through the incomplete

gamma functions $\hat{\Gamma}$:

$$\int_0^{M_x} M_* \Phi_{M_*} dM_* = \Phi_1 \hat{\Gamma}(\alpha_1 + 2, \frac{M_x}{M_c}) + \Phi_2 \hat{\Gamma}(\alpha_2 + 2, \frac{M_x}{M_c}) \quad (4.20)$$

The fraction of mass in the range between $M_x \leq M_* \leq M_y$ can be obtained from the above equation after normalisation with the complete gamma function Γ . Figure 4.6 shows several of the resulting star formation metallicity distributions at a few redshifts.

We compute the MSSFR by multiplying the metallicity distribution at a given redshift by the SFR at that redshift (Eq.4.6). Altogether we test the effect of 18 variations (2 SFR \times 3 MZ \times 3 GSMF), as well as our preferred MSSFR model. The two SFR variations differ mostly at redshifts above 2. The MZ relations span the range between extra-solar and sub-solar metallicities at $z = 0$. The GSMFs variants include a static redshift-independent fit and two redshift-dependent fits, which evolve toward higher galaxy stellar masses at lower redshifts (see tables 4.2, 4.3).

4.A.5 Definition of solar values

In this study we defined the solar metallicity mass fraction as $Z_{\odot} = 0.0142$ and the solar oxygen abundance as $\log_{10}[\text{O}/\text{H}]_{\odot} + 12 = 8.69$ based on Asplund et al. (2009). However, the assumed solar values differ between papers, so our choice is not always consistent with the fits used.

In particular, Ma et al. (2015) assume a mass fraction of $Z_{\odot} = 0.02$ and a specific iron mass fraction of 0.00173 to obtain an oxygen abundance of $\log_{10}[\text{O}/\text{H}]_{\odot} + 12 = 9.0$. Savaglio et al. (2005) assume an oxygen abundance of 8.69, but mention that systematics can lead to uncertainties in the range between 8.7 and 9.1. Meanwhile, their single stellar models for their galaxy models assume a mass fraction of $Z_{\odot} = 0.02$ (Leitherer et al., 1999). On the other hand, Furlong et al. (2015) use a solar mass fraction of $Z_{\odot} = 0.0127$.

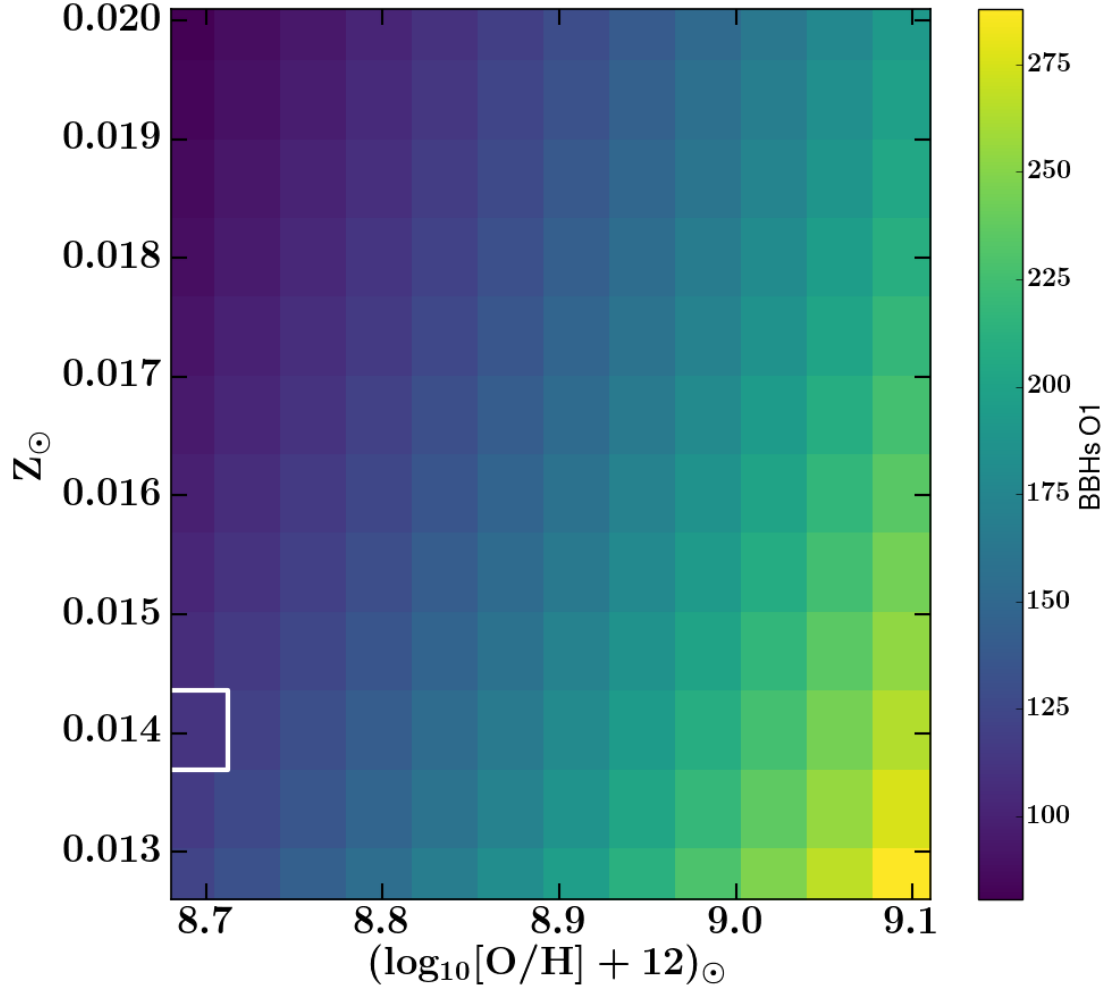


Figure 4.15: The predicted number of BBH detections per year at the sensitivity of the first observing run for different choices of the solar mass fraction Z_{\odot} and oxygen abundance $(\log_{10}[\text{O}/\text{H}] + 12)_{\odot}$. The MSSFR model is based on the SFR of Madau and Dickinson (2014), with the MZ relation of Ma et al. (2015) and the double Schechter GSMF of Furlong et al. (2015). The same (pessimistic) evolutionary model is assumed. The white square denotes the point in parameter space we assumed for this study.

We evaluate the impact of the assumed solar metallicity and oxygen abundances on our predictions by varying these within a single MSSFR model. Figure 4.15 shows the predicted number of BBH detections per year at the sensitivity of the first observing run over a two-dimensional grid of solar metallicities and oxygen abundances, while keeping all other model parameters fixed. We see that these uncertainties alone could change the predicted values by up to a factor of 3.

4.B Remnant masses of single stars

In COMPAS models, metallicity impacts the masses of compact remnants by influencing stellar evolutionary tracks and the rates of wind-driven mass loss. The Fryer et al. (2012) recipes for calculating the remnant mass are based on the mass of the carbon-oxygen core and the total stellar mass at the moment of the supernova. If the carbon-oxygen core mass exceeds $11 M_{\odot}$, there is assumed to be no explosion. In that case, the entire mass of the star, other than the 10 per cent of the mass assumed to be lost through neutrino emission, collapses into the remnant.

However, within our models, all single stars above a certain initial mass yield the same remnant mass at a given metallicity.³ This is driven by our implementation of LBV-wind mass loss (see Sec. 4.3).

Figure 4.16 shows three tracks of very massive single stars. The shaded region is where we apply the LBV-wind mass-loss rates (Belczynski et al., 2010). When stars are on the main sequence (core-hydrogen-burning phase), they evolve on a nuclear timescale, which is not sufficiently fast to overcome the LBV winds and pass through the Humphreys-Davidson limit (Humphreys and Davidson, 1994) into the shaded region. At point 1 the stars start to turn off the main sequence. By this time stars with initial masses of 100 and 110 solar masses have the same mass. At point 2 they begin to evolve onto the Hertzsprung gap. It is at this point that the analytical fits of Hurley et al. (2000) define a core mass. This core mass only depends on the

³These simulations do not include PISNe or pulsational PISNe. Future COMPAS analyses will incorporate them (Stevenson et al., 2019).

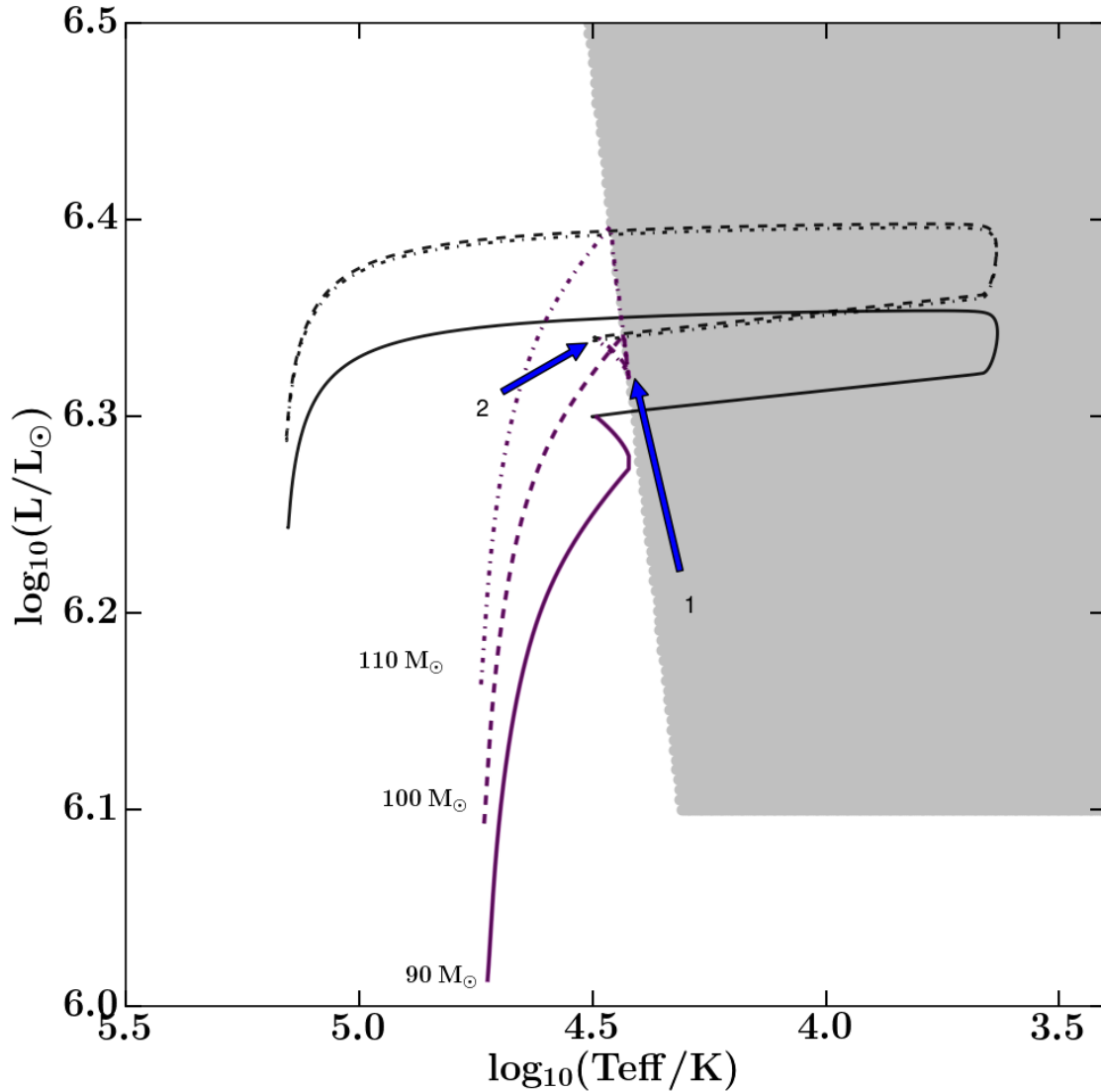


Figure 4.16: Single stellar tracks of stars with initial masses of 90 M_{\odot} , 100 M_{\odot} , and 110 M_{\odot} . The metallicity of the stars is $Z = Z_{\odot}/3$. The purple portions of the tracks indicate the core-hydrogen-burning phase (main sequence), while subsequent evolution is shown in black. The region in which we apply the LBV-wind-mass-loss rate is shaded. At point 1 the 100 M_{\odot} and 110 M_{\odot} stars turn off the main sequence. At point 2 they start evolving onto the Hertzsprung gap. The two tracks evolve identically from point 1, resulting in the same remnant mass.

current properties of the stars, so the two stars continue evolving identically. Their faster, thermal-timescale evolution now allows them to pass through the Humphreys-Davidson limit and enter the shaded region. The stars end up having the same remnant mass.

The process described above can yield sharp peaks in the BBH mass distribution. Every BBH progenitor in which both stars go through this LBV phase on the main sequence will end up with the same total BBH mass. This is the maximum total mass for a given metallicity. The lower the initial mass for this LBV-wind mass loss, i.e., the higher the metallicity, the more binaries will have degenerate remnant masses. The lowest initial mass for LBV-wind mass loss is around a third to a half solar, which explains the sharp peaks for the total BBH mass distribution at half solar (see Fig. 4.2). This feature of the COMPAS and StarTrack implementation of LBV winds also explains the asymptote of the maximal remnant mass in figure 1 of Belczynski et al. (2010) and the peaks in the highest mass bins of Dominik et al. (2012).

4.C Statistics

In this appendix, we describe our procedures for computing the likelihood of a given MSSFR model given the observed number of detections and their chirp masses, and describe the use of bootstrapping to estimate the Monte Carlo simulation uncertainty.

4.C.1 Evaluating model likelihoods

We can write the total likelihood $\mathcal{L}_{\text{tot}}(d|M)$ of observing the data set d , which consists of N_{obs} detections with individual data d_i , given a model M that predicts N_M expected detections with a probability distribution of source properties P_M , as

(e.g., Mandel et al., 2019)

$$\mathcal{L}_{\text{tot}}(d|M) = \frac{N_M^{N_{\text{obs}}}}{N_{\text{obs}}!} e^{-N_M} \prod_{i=1}^{N_{\text{obs}}} p(d_i|P_M). \quad (4.21)$$

Here, we focus on the chirp mass \mathcal{M}_c , as the parameter which is best constrained by gravitational wave observations and is directly predicted by COMPAS simulations. Writing the preceding equation in logarithmic form, the log-likelihood of a particular MSSFR model is

$$\begin{aligned} \log_{10}(\mathcal{L}_{\text{tot}}(d|M)) &= \log_{10}(\mathcal{L}(N_{\text{obs}}|N_M)) + \\ &\quad \sum_{i=1}^{N_{\text{obs}}} \log_{10}(\mathcal{L}(\mathcal{M}_{c,i}|p_M(\mathcal{M}_c))), \end{aligned} \quad (4.22)$$

where $\mathcal{M}_{c,i}$ is the measured chirp-mass of the i 'th gravitational wave observation and $p_M(\mathcal{M}_c)$ is chirp-mass distribution characterising the MSSFR model M . The first term is abbreviated as \mathcal{L}_R in table 4.3. The second term, $\mathcal{L}_{\text{Mchirp}} \equiv \mathcal{L}(\mathcal{M}_{c,i}|p_M(\mathcal{M}_c))$ is the probability of detecting a chirp mass $\mathcal{M}_{c,i}$ given the chirp-mass distribution predicted from the MSSFR model M .

COMPAS Monte Carlo simulations yield a discrete set of chirp masses and their respective rates. A kernel density estimator is used to turn this set of discrete data points into an approximated continuous function. We do this by approximating each of N_{sim} chirp masses produced by the COMPAS simulation as a 1-dimensional Gaussian centred on the simulated chirp-mass value \mathcal{M}_j . All Gaussians have the same bandwidth σ , determined using the default ‘Scott’s rule’ (Scott, 2015) of the Gaussian kernel density estimator in the `scipy` package (Oliphant, 2007; Perez et al., 2011). Each simulated data point j contributes to the overall probability density function proportionally to its observing rate R_j , estimated in Eq. 4.2. Therefore we re-weigh each data point by R_j and normalise by the total rate R_{tot} ,

$$p_M(\mathcal{M}_c) = \frac{1}{R_{\text{tot}}} \sum_{j=1}^{N_{\text{sim}}} R_j \frac{1}{\sqrt{2\pi\sigma^2}} e^{-\frac{(\mathcal{M}_c - \mathcal{M}_j)^2}{2\sigma^2}}. \quad (4.23)$$

For a single perfect detection, the likelihood of observing a chirp-mass \mathcal{M}_c would be given by Eq. 4.23. In practice, gravitational-wave measurements suffer from observational uncertainty, although these are typically small for chirp masses. Chirp-mass posteriors of individual detections were not yet available when this work started; therefore, we reconstruct them as symmetric Gaussian distributions with 90 per cent confidence intervals matching those reported in Abbott et al. (2016); Abbott et al. (2018b). The reported error-bars are asymmetric, so the median of our reconstructed posterior is slightly shifted compared to the original. Given the accuracy of chirp mass measurement, we make two further simplifications. We ignore the impact of the priors used in Abbott et al. (2018b) (which is reasonable inasmuch as the posterior is determined by the sharply peaked likelihood function), and do not reweigh by those priors; and we ignore the selection effects on the chirp mass for the purpose of population analysis, since the selection function does not vary significantly over the range of likelihood support (see Mandel et al. (2019) for a discussion of both issues). With these simplifications, the likelihood of observing a particular gravitational wave event i , characterised by the approximated Gaussian posterior of the chirp mass $p_i(\mathcal{M}_c)$, given a MSSFR model M , becomes

$$\mathcal{L}(\mathcal{M}_{c,i}|p_M(\mathcal{M}_c)) = \int_0^\infty p_i(\mathcal{M}_c) p_M(\mathcal{M}_c) d\mathcal{M}_c. \quad (4.24)$$

Figure 4.17 shows our constructed posterior for GW150914 (red); part of the chirp-mass distribution estimated from the MSSFR model which combines the SFR of Madau and Dickinson (2014), the MZ relation of Ma et al. (2015) and the GSMF of Furlong et al. (2015) (blue); and the convolution between the two (black). The unnormalised integral of this convolution is our estimate of the likelihood $\mathcal{L}(\mathcal{M}_{c,i}|p_M(\mathcal{M}_c))$.

4.C.2 Bootstrapping

Our simulation is based on a Monte Carlo sampling of binaries. We estimate the sampling uncertainty on all derived quantities via bootstrapping: we uniformly re-

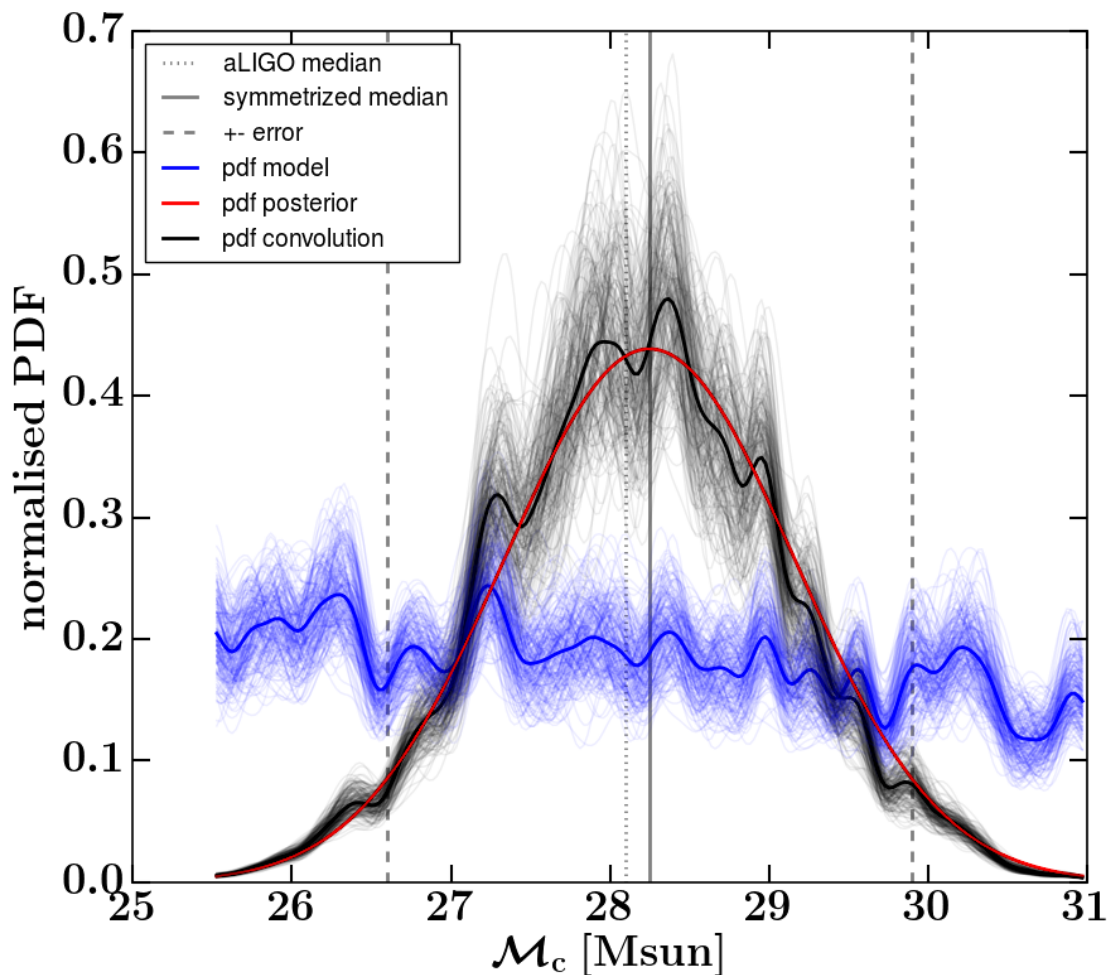


Figure 4.17: An example of the likelihood calculation for GW150914. The dashed vertical lines show the 90 per cent confidence interval from Abbott et al. (2016). The dotted vertical line is the median from Abbott et al. (2016) and the solid vertical line is the median after symmetrising. The red curve is a mock gaussian posterior. The blue curve is part of the normalised chirp mass distribution obtained by applying a one dimensional KDE to the results of the COMPAS simulation. The black curve shows the Gaussian likelihood convolved with the model. The fainter lines show scatter in the chirp-mass distribution and the convolution as estimated with bootstrapping.

sample a set with the same total number of binaries from our already evolved initial set of binaries (with replacement), including systems which did not form a DCO. The central value in tables 4.2, 4.3 corresponds to the original sample, while the error bars correspond to the 5th and 95th percentile rates and likelihoods from bootstrapping.

SFR	MSSFR Variation		BBH Rates		BHNS Rates		BNS Rates	
	MZ	GSMF	$z = 0$ merg. Gpc ⁻³ yr ⁻¹	O1 det. yr ⁻¹	$z = 0$ merg. Gpc ⁻³ yr ⁻¹	O1 det. yr ⁻¹	$z = 0$ merg. Gpc ⁻³ yr ⁻¹	O1 det. yr ⁻¹
Pessimistic								
Preferred model			49.00 ^{+1.93} _{-1.68}	21.80 ^{+0.47} _{-0.50}	56.87 ^{+1.80} _{-1.89}	0.07 ^{+0.00} _{-0.00}	20.00 ^{+1.34} _{-1.03}	0.23 ^{+0.02} _{-0.015}
Madau et al.	Ma et al. (2004)	1	63.07 ^{+1.86} _{-1.76}	18.43 ^{+0.42} _{-0.4}	32.22 ^{+1.7} _{-1.43}	0.4 ^{+0.02} _{-0.02}	85.97 ^{+2.47} _{-2.41}	0.11 ^{+0.0} _{-0.0}
		2	158.56 ^{+2.07} _{-2.48}	94.35 ^{+1.37} _{-1.39}	40.73 ^{+1.37} _{-1.13}	0.51 ^{+0.02} _{-0.02}	90.87 ^{+2.39} _{-2.15}	0.12 ^{+0.0} _{-0.0}
		3	174.71 ^{+2.28} _{-2.7}	113.92 ^{+1.12} _{-1.22}	42.14 ^{+1.43} _{-1.22}	0.52 ^{+0.02} _{-0.02}	91.42 ^{+2.37} _{-2.24}	0.13 ^{+0.0} _{-0.0}
	Langer et al.	1	448.84 ^{+4.28} _{-5.24}	247.22 ^{+2.63} _{-2.78}	95.47 ^{+1.85} _{-2.12}	1.28 ^{+0.03} _{-0.03}	144.57 ^{+2.08} _{-2.3}	0.22 ^{+0.0} _{-0.0}
		2	563.44 ^{+4.1} _{-5.9}	441.08 ^{+5.72} _{-6.24}	91.76 ^{+1.73} _{-1.8}	1.19 ^{+0.03} _{-0.03}	143.81 ^{+1.93} _{-2.1}	0.22 ^{+0.0} _{-0.0}
		3	589.13 ^{+4.27} _{-6.05}	492.27 ^{+5.85} _{-6.63}	96.32 ^{+1.9} _{-1.9}	1.25 ^{+0.03} _{-0.03}	147.1 ^{+1.92} _{-2.3}	0.23 ^{+0.0} _{-0.0}
	Langer et al., offset	1	59.17 ^{+1.27} _{-1.34}	28.72 ^{+0.46} _{-0.45}	18.98 ^{+1.01} _{-0.77}	0.23 ^{+0.01} _{-0.01}	72.09 ^{+3.21} _{-3.01}	0.09 ^{+0.0} _{-0.0}
		2	151.84 ^{+1.88} _{-2.23}	120.3 ^{+2.12} _{-2.23}	28.67 ^{+0.92} _{-0.88}	0.35 ^{+0.01} _{-0.01}	79.27 ^{+2.67} _{-2.52}	0.11 ^{+0.0} _{-0.0}
		3	167.64 ^{+1.92} _{-2.29}	148.74 ^{+2.0} _{-2.05}	29.4 ^{+0.97} _{-0.98}	0.35 ^{+0.01} _{-0.01}	79.32 ^{+2.57} _{-2.51}	0.11 ^{+0.0} _{-0.0}
Strolger et al.	Ma et al. (2004)	1	101.98 ^{+3.01} _{-3.99}	32.93 ^{+0.83} _{-0.84}	42.11 ^{+2.4} _{-1.81}	0.52 ^{+0.03} _{-0.02}	91.66 ^{+2.71} _{-2.49}	0.12 ^{+0.0} _{-0.0}
		2	255.46 ^{+4.49} _{-5.7}	203.93 ^{+5.17} _{-4.76}	49.05 ^{+2.1} _{-1.68}	0.6 ^{+0.02} _{-0.02}	98.87 ^{+2.59} _{-2.72}	0.14 ^{+0.0} _{-0.0}
		3	271.91 ^{+4.09} _{-4.67}	208.21 ^{+3.29} _{-3.38}	50.49 ^{+1.98} _{-1.66}	0.61 ^{+0.03} _{-0.02}	98.72 ^{+2.4} _{-2.72}	0.14 ^{+0.0} _{-0.0}
	Langer et al.	1	574.91 ^{+6.58} _{-8.19}	406.39 ^{+5.25} _{-5.66}	99.35 ^{+2.32} _{-2.43}	1.28 ^{+0.03} _{-0.04}	153.78 ^{+2.74} _{-2.9}	0.23 ^{+0.0} _{-0.0}
		2	688.91 ^{+9.03} _{-10.42}	659.25 ^{+15.27} _{-14.58}	95.9 ^{+2.65} _{-2.62}	1.19 ^{+0.03} _{-0.03}	153.93 ^{+3.49} _{-3.4}	0.24 ^{+0.01} _{-0.01}
		3	714.15 ^{+8.77} _{-11.17}	710.91 ^{+15.17} _{-14.29}	100.12 ^{+2.67} _{-2.69}	1.25 ^{+0.03} _{-0.03}	157.4 ^{+3.8} _{-3.43}	0.24 ^{+0.01} _{-0.01}
	Langer et al., offset	1	132.55 ^{+3.38} _{-3.54}	89.79 ^{+1.42} _{-1.42}	27.88 ^{+1.96} _{-1.27}	0.33 ^{+0.02} _{-0.01}	79.81 ^{+3.16} _{-3.29}	0.11 ^{+0.0} _{-0.0}
		2	259.14 ^{+4.65} _{-6.53}	267.34 ^{+5.58} _{-7.55}	36.67 ^{+1.57} _{-1.57}	0.43 ^{+0.02} _{-0.02}	88.47 ^{+3.02} _{-3.58}	0.12 ^{+0.01} _{-0.0}
		3	276.57 ^{+5.32} _{-6.48}	292.70 ^{+7.71} _{-6.55}	37.36 ^{+1.64} _{-1.56}	0.43 ^{+0.02} _{-0.02}	88.34 ^{+2.88} _{-3.29}	0.12 ^{+0.0} _{-0.0}
Optimistic								
Preferred model			190.85 ^{+3.94} _{-3.99}	36.80 ^{+0.65} _{-0.65}	158.8 ^{+3.13} _{-3.49}	0.23 ^{+0.00} _{-0.01}	56.68 _{-1.87} +2.21	0.51 ^{+0.02} _{-0.02}
Madau et al.	Ma et al. (2004)	1	291.23 ^{+4.93} _{-5.28}	46.27 ^{+0.7} _{-0.72}	89.32 ^{+3.19} _{-2.47}	0.85 ^{+0.03} _{-0.02}	231.08 ^{+4.36} _{-4.8}	0.33 ^{+0.01} _{-0.01}
		2	408.74 ^{+4.03} _{-5.52}	128.37 ^{+1.44} _{-1.48}	102.22 ^{+2.67} _{-2.07}	1.04 ^{+0.03} _{-0.02}	227.38 ^{+4.13} _{-4.46}	0.33 ^{+0.01} _{-0.01}
		3	431.55 ^{+4.5} _{-5.58}	148.55 ^{+1.26} _{-1.38}	104.83 ^{+2.71} _{-2.18}	1.06 ^{+0.03} _{-0.02}	226.34 ^{+3.71} _{-4.21}	0.33 ^{+0.01} _{-0.01}
	Langer et al.	1	938.86 ^{+6.16} _{-7.01}	332.4 ^{+2.92} _{-2.77}	201.14 ^{+3.44} _{-3.1}	2.33 ^{+0.04} _{-0.04}	209.7 ^{+2.85} _{-2.73}	0.33 ^{+0.0} _{-0.0}
		2	1002.87 ^{+5.33} _{-6.55}	517.59 ^{+5.41} _{-6.39}	187.17 ^{+2.79} _{-2.49}	2.16 ^{+0.04} _{-0.03}	210.0 ^{+2.47} _{-2.48}	0.33 ^{+0.0} _{-0.0}
		3	1042.93 ^{+5.27} _{-6.97}	572.54 ^{+5.69} _{-6.41}	193.78 ^{+2.98} _{-2.65}	2.25 ^{+0.04} _{-0.03}	208.21 ^{+2.55} _{-2.49}	0.33 ^{+0.0} _{-0.0}
	Langer et al., offset	1	190.7 ^{+3.5} _{-3.65}	43.44 ^{+0.52} _{-0.52}	59.21 ^{+2.89} _{-2.15}	0.52 ^{+0.01} _{-0.01}	236.54 ^{+4.8} _{-6.59}	0.34 ^{+0.01} _{-0.01}
		2	317.64 ^{+3.16} _{-4.02}	141.94 ^{+2.28} _{-2.08}	74.72 ^{+2.18} _{-1.91}	0.73 ^{+0.02} _{-0.02}	232.11 ^{+5.66} _{-5.96}	0.34 ^{+0.01} _{-0.01}
		3	335.02 ^{+3.3} _{-4.01}	170.2 ^{+2.17} _{-2.02}	75.38 ^{+2.2} _{-1.9}	0.73 ^{+0.02} _{-0.02}	231.52 ^{+5.68} _{-5.52}	0.33 ^{+0.01} _{-0.01}
Strolger et al.	Ma et al. (2004)	1	361.59 ^{+5.79} _{-7.1}	64.2 ^{+1.08} _{-1.12}	111.51 ^{+4.29} _{-3.31}	1.09 ^{+0.04} _{-0.03}	238.44 ^{+4.5} _{-4.66}	0.34 ^{+0.01} _{-0.01}
		2	523.11 ^{+5.83} _{-8.21}	239.42 ^{+5.7} _{-4.94}	116.48 ^{+3.27} _{-2.7}	1.18 ^{+0.03} _{-0.03}	235.98 ^{+4.6} _{-4.62}	0.34 ^{+0.01} _{-0.01}
		3	547.87 ^{+6.08} _{-7.09}	244.58 ^{+3.4} _{-3.41}	119.46 ^{+3.05} _{-2.75}	1.22 ^{+0.03} _{-0.03}	234.53 ^{+3.89} _{-4.63}	0.34 ^{+0.01} _{-0.01}
	Langer et al.	1	1061.19 ^{+8.04} _{-9.88}	486.78 ^{+3.82} _{-5.84}	204.37 ^{+3.37} _{-3.35}	2.33 ^{+0.05} _{-0.04}	220.3 ^{+3.44} _{-3.03}	0.34 ^{+0.01} _{-0.01}
		2	1118.71 ^{+8.74} _{-10.66}	730.55 ^{+14.82} _{-14.5}	189.09 ^{+2.96} _{-3.06}	2.14 ^{+0.04} _{-0.04}	221.11 ^{+4.03} _{-3.54}	0.34 ^{+0.01} _{-0.01}
		3	1157.22 ^{+9.06} _{-11.19}	785.44 ^{+14.83} _{-14.23}	194.98 ^{+3.02} _{-3.31}	2.22 ^{+0.04} _{-0.04}	219.59 ^{+3.93} _{-3.66}	0.34 ^{+0.01} _{-0.01}
	Langer et al., offset	1	291.8 ^{+5.57} _{-5.44}	107.66 ^{+1.37} _{-1.53}	76.78 ^{+3.4} _{-2.67}	0.7 ^{+0.02} _{-0.02}	244.96 ^{+6.31} _{-6.62}	0.35 ^{+0.01} _{-0.01}
		2	440.74 ^{+6.82} _{-7.95}	290.5 ^{+8.53} _{-7.21}	87.17 ^{+2.78} _{-2.77}	0.86 ^{+0.03} _{-0.02}	240.95 ^{+6.21} _{-6.05}	0.35 ^{+0.01} _{-0.01}
		3	460.27 ^{+6.42} _{-7.84}	315.88 ^{+7.94} _{-6.5}	87.82 ^{+2.79} _{-2.54}	0.86 ^{+0.02} _{-0.03}	240.19 ^{+6.13} _{-5.99}	0.34 ^{+0.01} _{-0.01}

Table 4.2: Table showing the merger and detection rates per DCO type. The columns labeled ‘ $z = 0$ merg.’ are the merger rate per year per cubic gigaparsec at zero redshift without selection effects; columns labeled ‘O1 det.’ are the expected rate of detections per year at the sensitivity of the first observing run. The error bars show the 90 per cent confidence interval due to Monte Carlo sampling evaluated via bootstrapping. The numbers in the column GSMF refer to 1=Panter et al. (2004), 2=Furlong et al. (2015) (single Schechter function), 3=Furlong et al. (2015) (double Schechter function). Optimistic and pessimistic variants relate to the ability to eject the common envelope when the donor is a Hertzsprung-gap star.

SFR	MSSFR Variation		GSMF	Likelihoods (\log_{10})		
	MZ			\mathcal{L}_{M_c}	\mathcal{L}_R	\mathcal{L}_{tot}
				Pessimistic		
	Preferred model			$-32.32^{+0.16}_{-0.18}$	$-0.90^{+0.00}_{-0.00}$	$-33.22^{+0.16}_{-0.18}$
Madau et al.	Ma et al. (2004)	1	$-33.9^{+0.14}_{-0.16}$	$-0.97^{+0.01}_{-0.02}$	$-34.87^{+0.14}_{-0.16}$	
		2	$-32.42^{+0.07}_{-0.08}$	$-8.86^{+0.21}_{-0.21}$	$-41.28^{+0.24}_{-0.26}$	
		3	$-32.48^{+0.07}_{-0.07}$	$-11.9^{+0.19}_{-0.18}$	$-44.38^{+0.23}_{-0.22}$	
	Langer et al.	1	$-32.24^{+0.05}_{-0.05}$	$-34.85^{+0.5}_{-0.47}$	$-67.09^{+0.49}_{-0.47}$	
		2	$-32.61^{+0.06}_{-0.06}$	$-70.6^{+1.23}_{-1.05}$	$-103.21^{+1.22}_{-1.05}$	
		3	$-32.77^{+0.06}_{-0.07}$	$-80.23^{+1.32}_{-1.04}$	$-113.0^{+1.3}_{-1.09}$	
	Langer et al., offset	1	$-32.3^{+0.09}_{-0.1}$	$-1.07^{+0.02}_{-0.02}$	$-33.38^{+0.09}_{-0.1}$	
		2	$-32.68^{+0.08}_{-0.08}$	$-12.93^{+0.38}_{-0.33}$	$-45.61^{+0.42}_{-0.38}$	
		3	$-32.87^{+0.07}_{-0.07}$	$-17.62^{+0.35}_{-0.33}$	$-50.49^{+0.38}_{-0.36}$	
Strolger et al.	Ma et al. (2004)	1	$-33.82^{+0.14}_{-0.17}$	$-1.31^{+0.06}_{-0.05}$	$-35.13^{+0.18}_{-0.17}$	
		2	$-32.81^{+0.11}_{-0.1}$	$-27.14^{+0.87}_{-0.91}$	$-59.95^{+0.93}_{-0.97}$	
		3	$-32.65^{+0.08}_{-0.08}$	$-27.9^{+0.61}_{-0.58}$	$-60.54^{+0.63}_{-0.61}$	
	Langer et al.	1	$-32.44^{+0.06}_{-0.06}$	$-64.11^{+1.08}_{-0.97}$	$-96.55^{+1.08}_{-1.02}$	
		2	$-32.98^{+0.1}_{-0.1}$	$-111.92^{+2.83}_{-2.81}$	$-144.9^{+2.9}_{-2.83}$	
		3	$-33.09^{+0.09}_{-0.1}$	$-121.79^{+2.8}_{-2.83}$	$-154.87^{+2.86}_{-2.9}$	
	Langer et al., offset	1	$-32.46^{+0.08}_{-0.1}$	$-8.18^{+0.21}_{-0.21}$	$-40.63^{+0.23}_{-0.26}$	
		2	$-33.2^{+0.12}_{-0.12}$	$-38.48^{+1.44}_{-1.48}$	$-71.68^{+1.51}_{-1.51}$	
		3	$-33.22^{+0.11}_{-0.11}$	$-43.1^{+1.29}_{-1.27}$	$-76.33^{+1.35}_{-1.34}$	
				Optimistic		
	Preferred model			$-33.1^{+0.08}_{-0.11}$	$-1.58^{+0.05}_{-0.05}$	$-34.73^{+0.12}_{-0.11}$
Madau et al.	Ma et al. (2004)	1	$-36.37^{+0.11}_{-0.1}$	$-2.46^{+0.07}_{-0.07}$	$-38.84^{+0.16}_{-0.14}$	
		2	$-32.61^{+0.05}_{-0.06}$	$-14.24^{+0.25}_{-0.23}$	$-46.85^{+0.27}_{-0.26}$	
		3	$-32.52^{+0.04}_{-0.05}$	$-17.59^{+0.24}_{-0.21}$	$-50.1^{+0.24}_{-0.22}$	
	Langer et al.	1	$-32.55^{+0.05}_{-0.04}$	$-50.38^{+0.52}_{-0.52}$	$-82.93^{+0.5}_{-0.53}$	
		2	$-32.55^{+0.04}_{-0.05}$	$-85.01^{+1.21}_{-0.98}$	$-117.56^{+1.23}_{-1.02}$	
		3	$-32.67^{+0.04}_{-0.05}$	$-95.41^{+1.28}_{-1.07}$	$-128.08^{+1.29}_{-1.11}$	
	Langer et al., offset	1	$-32.85^{+0.07}_{-0.06}$	$-2.18^{+0.05}_{-0.05}$	$-35.03^{+0.09}_{-0.08}$	
		2	$-32.49^{+0.06}_{-0.06}$	$-16.48^{+0.39}_{-0.37}$	$-48.97^{+0.43}_{-0.39}$	
		3	$-32.59^{+0.05}_{-0.06}$	$-21.27^{+0.35}_{-0.36}$	$-53.85^{+0.38}_{-0.36}$	
Strolger et al.	Ma et al. (2004)	1	$-35.37^{+0.11}_{-0.12}$	$-4.58^{+0.15}_{-0.14}$	$-39.95^{+0.21}_{-0.19}$	
		2	$-32.54^{+0.08}_{-0.08}$	$-33.45^{+0.89}_{-0.99}$	$-65.99^{+0.95}_{-0.98}$	
		3	$-32.39^{+0.05}_{-0.05}$	$-34.37^{+0.62}_{-0.6}$	$-66.77^{+0.65}_{-0.62}$	
	Langer et al.	1	$-32.38^{+0.05}_{-0.05}$	$-79.19^{+1.11}_{-1.08}$	$-111.57^{+1.14}_{-1.11}$	
		2	$-32.78^{+0.08}_{-0.09}$	$-125.54^{+2.79}_{-2.83}$	$-158.32^{+2.82}_{-2.86}$	
		3	$-32.86^{+0.08}_{-0.08}$	$-136.06^{+2.78}_{-2.82}$	$-168.92^{+2.79}_{-2.88}$	
	Langer et al., offset	1	$-32.24^{+0.06}_{-0.07}$	$-10.91^{+0.24}_{-0.21}$	$-43.15^{+0.23}_{-0.24}$	
		2	$-32.83^{+0.1}_{-0.1}$	$-42.69^{+1.46}_{-1.51}$	$-75.52^{+1.53}_{-1.51}$	
		3	$-32.84^{+0.09}_{-0.08}$	$-47.34^{+1.31}_{-1.35}$	$-80.18^{+1.31}_{-1.36}$	

Table 4.3: Table showing the log likelihoods of observing the rate and chirp mass distribution of BBH mergers detected during the first two observing runs, within our default binary evolution model and for a range of MSSFR variations. \mathcal{L}_{tot} is the total likelihood, \mathcal{L}_R is the Poisson likelihood of observing 10 BBH events over 166 days of coincident observation, and \mathcal{L}_{M_c} is the likelihood of observing the chirp-mass distribution. The error bars show the 90 per cent confidence interval due to Monte Carlo sampling evaluated via bootstrapping. The numbers in the column GSMF refer to 1=Panter et al. (2004), 2=Furlong et al. (2015) (single Schechter function), 3=Furlong et al. (2015) (double Schechter function). Optimistic and pessimistic variants relate to the ability to eject the common envelope when the donor is a Hertzsprung-gap star.

Chapter 5

Revisiting the stability of mass transfer for the rates and formation channels of binary black hole mergers.

Coenraad J. Neijssel, Alejandro Vigna-Gómez, Simon Stevenson, Serena Vinciguerra, and Ilya Mandel

Abstract:

Rapid population synthesis is a useful tool for estimating the formation and merger rates of binary black hole mergers. We assess the impact of our description of the adiabatic response of the stellar radius to mass loss on the rate and mass distribution of binary black hole mergers forming through isolated binary evolution. Our updated prescription, based on detailed models, predicts that the majority of gravitational-wave events of merging binary black holes formed without the need of a common envelope event.

Contents

5.1	Introduction	140
5.2	Formation of merging DCOs	143
5.2.1	Three main formation channels of merging DCOs	143
5.2.2	ζ_{ad} and the formation of DCOs through channel I	147
5.2.3	Channel I forms massive equal-mass binary black holes (BBHs)	150
5.3	Recipes for the adiabatic response to mass loss	150
5.3.1	Radiative vs. convective envelopes	151
5.3.2	Adiabatic response to mass loss of stars without deep convective envelopes	152
5.4	Results	153
5.4.1	Convective envelopes: Stellar type vs. effective temperature threshold	154
5.4.2	Varying the single values of ζ_{ad} and T_{conv}	157
5.4.3	A mass- and radius-dependent value of ζ_{ad}	163
5.5	Discussion	165
5.5.1	Quasi-chemically-homogeneous evolution	165
5.5.2	Avoiding contact	166
5.5.3	ζ_{ad} and gravitational-wave detections	167
5.5.4	Constraints from other observations	169
5.6	Conclusion	169
5.A	Implementation Models and Illustrations	171

5.1 Introduction

Gravitational-wave observatories detect the coalescence of double compact objects (DCOs). Several catalogues (Abbott et al., 2016b, 2018a, 2019; Abbott et al., 2021) are now published detailing the observed mergers of binary black holes (BBHs), binary neutron stars (BNSs) and the perhaps-detected coalescences of black hole – neutron star binaries (BHNSs) such as GW190425 and GW190814 (Abbott et al., 2020a,b). One of the possible origins of these coalescing compact systems is the evolution of isolated binaries. In this scenario the two compact objects are born as a pair of massive stars in a binary and evolve without external influences (where a massive star is defined as having an initial zero-age main sequence (ZAMS) mass $M_{\text{ZAMS}} \gtrsim 8 M_{\odot}$). Many aspects of the physics of massive stars and binary evolution, such as wind mass-loss rates, mass transfer and supernovae, remain highly uncertain. However, assuming that the merging compact binaries, detected with gravitational-wave observations, formed through isolated binary evolution, their inferred properties, such as the component masses and spins, may provide constraints on these aspects.

One possible method for constraining binary-star physics with gravitational-wave events is by statistically comparing the properties of a simulated population of DCOs with the properties inferred from observations. Because detailed modelling of massive stellar binaries is computationally expensive, their evolution is often modelled using simplifying approximations in “stellar population-synthesis” codes. Several studies modelling the population of DCOs already highlight the impact of various uncertainties in e.g. the velocity and direction of the kick imparted during a supernova (SN) event (Tutukov and Yungelson, 1993; Lipunov et al., 1997; Portegies Zwart and Yungelson, 1998b; Belczynski et al., 2006; Dominik et al., 2012; Giacobbo and Mapelli, 2018; Chruslinska et al., 2018; Vigna-Gómez et al., 2018) or the binding energy of the stellar envelope and efficiency of ejecting a common envelope during dynamically-unstable mass transfer (e.g. Dominik et al., 2012; Giacobbo and Mapelli, 2018; Vigna-Gómez et al., 2018).

Currently observed gravitational-wave events must have been generated by binaries that formed and merged within the lifetime of the universe. For two $25 M_{\odot}$ black holes (BHs) to merge within a Hubble time (~ 14 Gyr), their separation should be no more than ~ 0.2 AU (Peters, 1964); for two neutron stars (NSs) of $2 M_{\odot}$ the upper limit in separation lowers to ~ 0.03 AU. However, massive stars have a radius of several solar radii ($1 R_{\odot} \approx 5 \cdot 10^{-3}$ AU) already at the beginning of their life and may expand up to hundreds of solar radii during their evolution. Therefore, some events must tighten the orbital separation of the binary at or after the formation of at least one compact star, to form a DCO which merges within a Hubble time. Hereafter we refer to compact binaries merging within a Hubble time as *merging DCOs*.

Two of the possible mechanisms which can reduce the orbital separation are fortuitous natal kicks, imparted on the remnant of a star during a SN, and mass-transfer events, when at least one of the stars overflows its Roche lobe. During a SN the core collapses and the released energy ejects (part of) the envelope, imparting a kick to the remnant if the ejection is asymmetric. However, in some cases, the shock produced during the collapse might not be energetic enough to unbind material from the star (Shigeyama et al., 1988; Woosley, 1989; Fryer et al., 2012). The star collapses without a SN, since the envelope falls back onto the remnant, and the remnant does not receive a natal kick. Fryer et al. (2012) already noted that the effect of fallback is negligible for stars with initial masses below $11 M_{\odot}$ but increases towards higher initial masses. Therefore, SNe likely play an important role in the formation of merging BNSs but not in the creation of merging BHs with remnant masses above $\sim 15 M_{\odot}$. This implies that, to explain the observed mergers of massive DCOs in the context of isolated binary evolution, it is necessary to invoke mass-transfer episodes between the two binary components. Multiple studies (amongst others, Smarr and Blandford, 1976; Bethe and Brown, 1998; Voss and Tauris, 2003; Pfahl et al., 2005; Belczynski et al., 2008; Dominik et al., 2012; Kruckow et al., 2018; Giacobbo et al., 2018; Vigna-Gómez et al., 2018; Spera et al.,

2019) suggest that a common-envelope (CE) resulting from dynamically-unstable mass transfer (Paczynski, 1976, see e.g. Ivanova et al. 2013a for a review) plays a crucial role in the mergers of BBHs, BHNSs and BNSs.

Neijssel et al. (2019) estimate that the majority of the detectable BBH mergers did not experience a CE event. This differs from other studies, including the earlier predictions by Stevenson et al. (2017) which relies on the same population-synthesis code COMPAS. In COMPAS mass transfer is considered dynamically stable if,

$$\zeta_{\text{ad}} < \zeta_{\text{RL}}, \quad (5.1)$$

at the onset of mass transfer, where ζ_{ad} is the adiabatic response of the stellar radius of the donor to mass loss and ζ_{RL} is the response of the Roche lobe of the donor to mass loss. The difference between the results of Stevenson et al. (2017) and Neijssel et al. (2019) is attributed to changes in the adiabatic response of the donor star to mass loss. In this paper, we study the impact on our rate estimates of merging DCOs of various recipes for ζ_{ad} . We focus in particular on the formation of merging BBHs.

The structure of the paper is as follows. In Sec. 5.2 we describe the formation of merging BBH through dynamically-stable and dynamically-unstable mass transfer. In Sec. 5.3 we introduce different prescriptions for modelling the adiabatic response of the stellar radius of the donor at the onset of mass transfer, aimed at determining the dynamical stability of the mass-transfer episode. In Sec.5.4 we show the impact of these models on our estimates of the merger rates of BBHs, for a population simulated with a single initial metallicity. In Sec. 5.5 we discuss possible caveats and additional uncertainties. In this study we use the alpha-version of the COMPAS population-synthesis code (Stevenson et al., 2017; Vigna-Gómez et al., 2018). The COMPAS population-synthesis code and the modelling assumptions are described in chapter 3.

At this preliminary stage we only study the impact for stars with initial metallicities of $Z = 0.0045$. At this metallicity, adopting the radial response of the donor

star to mass loss proposed by (Ge et al., 2015) (for donor stars which have not yet developed a deep convective envelope) increases the rate of merging BBHs by a factor of 2, compared to the approach of (Neijssel et al., 2019). More importantly the peak of the distribution of the total BBH mass shifts from $M_{\text{tot}} \approx 15 M_{\odot}$ to $M_{\text{tot}} \approx 35 M_{\odot}$. This shift is almost entirely due to merging BBHs which formed without a dynamically-unstable mass-transfer episode. Although tentative, this result suggests that the more massive DCO mergers provide a different set of constraints on the physics of massive stellar binaries than the constraints provided by their less massive counterparts; indeed, according to our results, the rate of mergers from massive compact binaries no longer relies on the uncertain physics of CE evolution.

5.2 Formation of merging DCOs

This section describes the three main formation channels of merging DCOs and provides an example which highlights how different choices of ζ_{ad} impact the formation of merging DCOs. In particular we focus on systems forming without a dynamically-unstable mass-transfer episode.

5.2.1 Three main formation channels of merging DCOs

Within the framework of isolated binary evolution, the merging DCOs, which contribute to the detectable gravitational-wave population, are commonly assumed to form through two main classes of formation channels (Belczynski et al. 2002a; Dewi et al. 2005; Kruckow et al. 2018; Giacobbo and Mapelli 2018; Spera et al. 2019 and references therein). Most of the merging DCO objects form through formation channels which require at least two mass-transfer episodes. First the binary system experiences a dynamically-stable mass-transfer episode from the primary onto the stellar companion. The donor star continues to evolve until it collapses into a NS or a BH. The second mass-transfer episode starts when the companion expands overflows its Roche lobe; at this point some mass is transferred back onto the com-

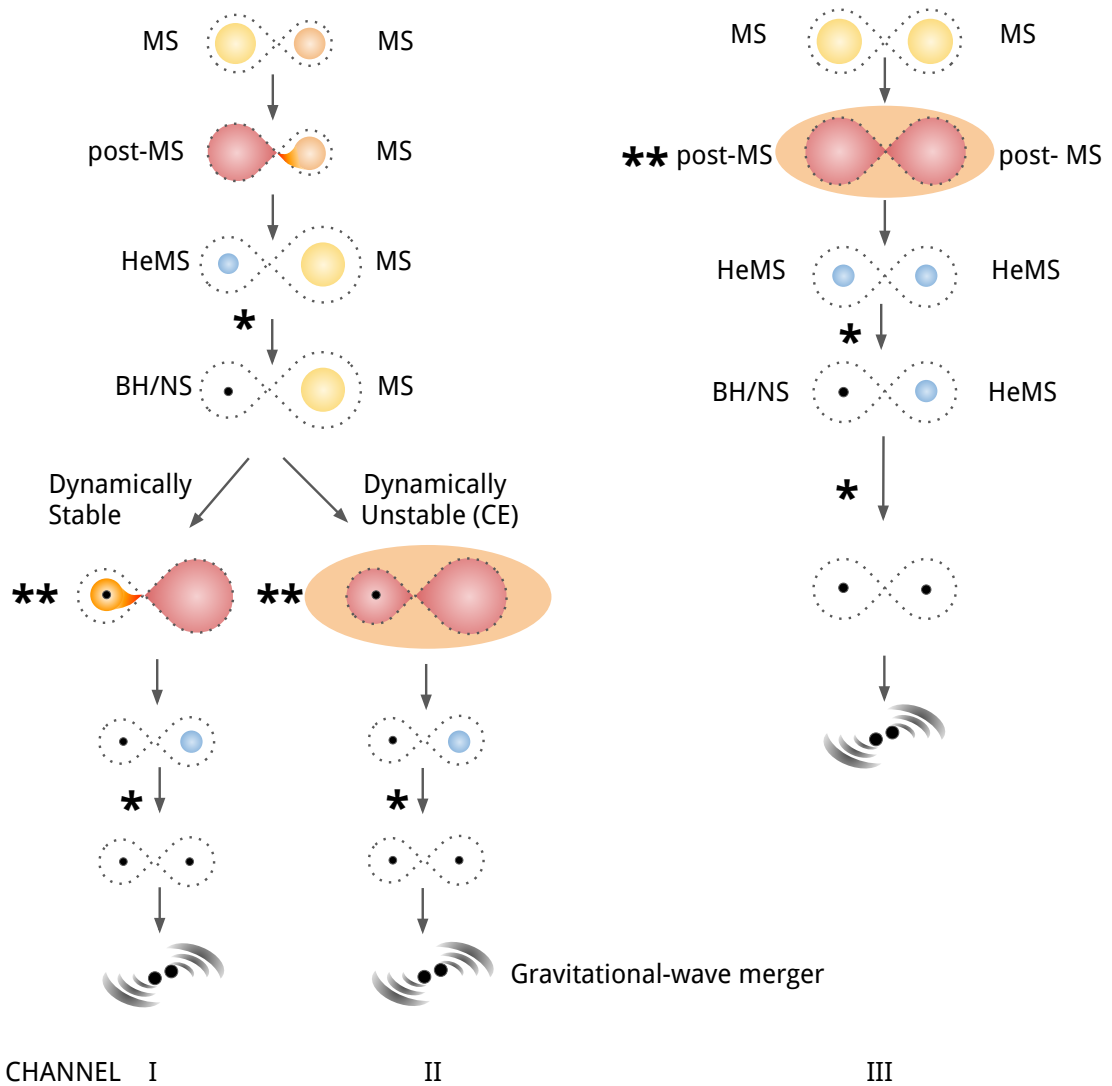


Figure 5.1: The three main formation channels of DCOs merging within a Hubble time. A mass-transfer episode initiated by a post-main sequence (MS) star leaves behind a helium main sequence (HeMS) or helium Hertzsprung gap (HeHG) star. The * indicates a phase where additional ultra stripping of the HeMS/HeHG star might occur leaving behind a carbon-oxygen or oxygen-neon core instead of a HeMS/HeHG star. This is mostly relevant for NSs and low mass BHs. The ** indicates the most crucial mass-transfer phase to tighten the orbit. Fig. 5.3 focuses on the luminosities and temperatures of donor stars at the onset of the mass-transfer phase indicated by **. For BHNSs we find that a fraction of systems could instead experience the first mass-transfer episode during the MS stage of the donor (Broekgaarden et al., 2021).

pact object. The mass-transfer episode dynamically unstable and results in a CE phase, leaving a tight DCO (see channel II in Fig. 5.1). In the second most common family of formation channels of merging DCOs, the first mass-transfer episode involves two core-helium-burning or helium-shell-burning stars, which drive the mass transfer to a CE event. The CE strips both stars of their envelopes while shrinking their orbital separation. Both cores continue to evolve to form a DCO (see channel III in Fig. 5.1). As described below, the two formation paths just described can be enriched by additional mass-transfer stages. This is the reason why we are presenting them as classes and not as single formation channels. However, for simplicity hereafter we will refer to these two families simply as channel II and channel III, respectively. Other channels of merging BBHs forming through isolated binary evolution exist such as those evolving through chemically-homogeneous evolution (see e.g. Mandel and de Mink, 2016; Marchant et al., 2016), but they are currently not taken into consideration in this work.

Both in channel II and channel III the donor star could experience an additional mass-transfer phase after it has been stripped of its envelope (see the single asterisk symbol in Fig. 5.1). When the donor star is stripped for the first time, it indeed leaves a stripped HeMS or post-HeMS star, depending on the burning phase of the core. During the HeHG, a star can significantly expand and therefore overflow its Roche lobe, if the system is tight enough. In this case, the helium envelope is removed leaving behind an ultra-stripped carbon-oxygen or oxygen-neon core. Earlier simulations, using the COMPAS population-synthesis codes and similar model assumptions, show that ultra-stripping is only relevant during the formation of BNSs (Vigna-Gómez et al., 2018) and not for the progenitors of merging BBHs (Stevenson et al., 2017; Neijssel et al., 2019).

As mentioned, Stevenson et al. (2017); Vigna-Gómez et al. (2018) find that merging DCOs mostly form through either channel II or III. However, Neijssel et al. (2019) report that 35 per cent of the merging BBHs simulated at a metallicity of $Z = 0.1Z_{\odot}$ ¹

¹ $Z_{\odot} = 0.142$ based on Asplund et al. (2009).

did not form through either of them. These merging BBHs form through a family of formation channels hereafter referred to as channel I. Channel I is similar to channel II, however the mass-transfer episode onto the compact object is dynamically stable and does not result in a CE (see also Fig. 5.1). This channel is reminiscent of the earlier works for BNSs by Tutukov and Yungelson (1973) and De Loore et al. (1975) and has recently been mentioned by Pavlovskii et al. (2017) and van den Heuvel et al. (2017). Neijssel et al. (2019) estimate that channel I could be responsible for 80 per cent of the BBH mergers detectable by the LIGO gravitational-wave detectors at design sensitivity depending on, amongst others, the model for the metallicity-specific star-formation rate. The prevalence of channel I in Neijssel et al. (2019) significantly differs from the results by Stevenson et al. (2017). Neijssel et al. (2019) conclude that channel I becomes dominant, compared to Stevenson et al. (2017), due to the different value of ζ_{ad} assumed for Hertzsprung gap (HG) stars. Other studies mention a similar channel, but, according to them, only few per cent of the merging systems form through it (Kruckow et al., 2018; Giacobbo et al., 2018).

5.2.1.1 Optimistic vs. pessimistic assumption

Whether a CE event started by a HG donor results in the merger of the two stars is uncertain. Calculations focused on lower-mass stars, in the context of formation of double white dwarfs, indicate that a common-envelope event initiated by a HG donor always leads to a stellar merger (Ivanova and Taam, 2004). This seems to be due to the lack of a clear core-envelope separation (Dominik et al., 2012). This argument however remains uncertain for stars more massive than white-dwarf progenitors.

In the optimistic scenario of our COMPAS code the binary system may avoid a stellar merger during a CE event initiated by a HG donor, if there is enough gravitational potential energy in the orbit to expel the envelope of the donor star. In our pessimistic scenario the stars always merge when a mass-transfer episode started by a HG star results in a CE event (Dominik et al., 2012); the main results of Neijssel et al. (2019) assume this last scenario. Assuming the optimistic scenario results in

an increased merger rate of DCOs by a factor of a few compared to the pessimistic scenario (Dominik et al., 2012; Chruslinska et al., 2018; Neijssel et al., 2019). The systems that form through the optimistic scenario, and not through the pessimistic scenario, evolve through channel II. Neijssel et al. (2019) find that in the optimistic scenario 17 per cent of the BBHs simulated at a metallicity of $Z = 0.1Z_{\odot}$ form through channel I, but do not report the percentage of detectable BBH mergers forming through channel I (see chapter 4).

5.2.2 ζ_{ad} and the formation of DCOs through channel I

Here we focus on the mass-transfer phase in channel I and II where a star transfers mass onto a compact companion. The change in orbital separation a is given by,

$$\frac{\dot{a}}{a} = -2\frac{\dot{M}_{\text{D}}}{M_{\text{D}}} \left[1 - \beta q - (1 - \beta)(\gamma + 1/2)\frac{1}{1 + 1/q} \right], \quad (5.2)$$

where M_{D} is the mass of the donor, β is the fraction of the mass accreted by the companion, $q = M_{\text{D}}/M_{\text{A}}$ is the mass ratio of the system and γ is the specific angular momentum of the mass leaving the system in units of the specific orbital angular momentum of the binary. Here we consider that any mass which is not accreted by the compact companion is isotropically re-emitted from the surface of the accretor such that $\gamma = q$.

Figure 5.2 shows the logarithm of the ratio between the initial separation at the onset of such a mass-transfer phase and the final separation after the mass-transfer phase. Here we assume, for simplicity, that the core of the donor star is half of the total mass of the star. The final separation after the mass-transfer phase is shorter if more mass is lost from the system or if the system initially has a higher the mass-ratio.

As mentioned, the dynamical stability of a mass-transfer episode is determined at the onset of a mass-transfer phase. The Roche lobe of the donor shrinks faster if the initial mass ratio is larger. The hatched region in figure 5.2 indicates where

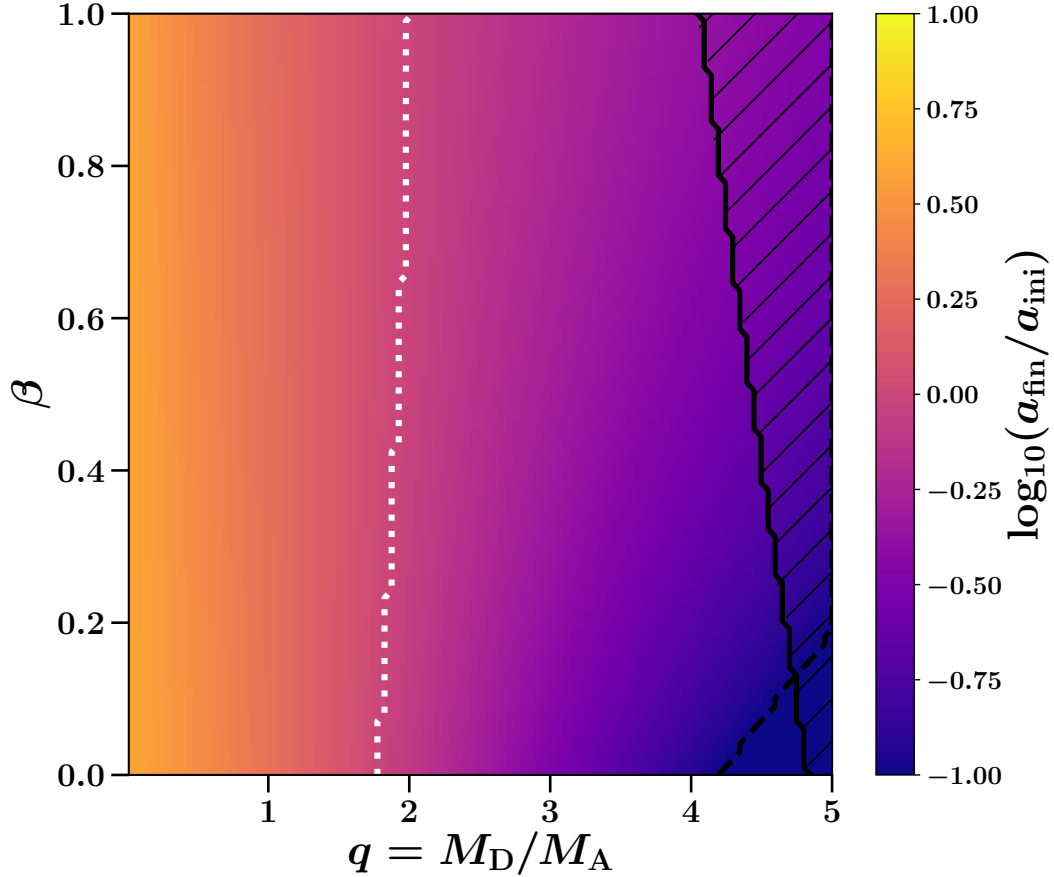


Figure 5.2: The logarithm of the ratio between the final separation (a_{fn}) and the initial separation (a_{ini}) during a dynamically-stable mass-transfer episode. The donor is assumed to lose half its mass, where the mass leaving the systems carries with it the specific angular momentum it had at the surface of the accretor. The white-dotted line indicates where $a_{\text{ini}} = a_{\text{fn}}$. The hatched region indicates where $\zeta_{RL} > 6.5$ and a mass-transfer episode started by HG donor stars is considered dynamically unstable. The black-dashed line indicates where $a_{\text{ini}} = 10 a_{\text{fn}}$.

$\zeta_{\text{RL}} > 6.5$, i.e. where a mass-transfer phase started by a HG donor is considered dynamically unstable.

Let us consider for example a scenario where a $50 M_{\odot}$ HG star with a $25 M_{\odot}$ helium core transfers mass onto a $25 M_{\odot}$ BH companion at a distance of 2 AU (the giant is about 1AU in radius). The HG star loses its entire envelope leaving behind a $25 M_{\odot}$ core which, after the HeMS and HeHG phase, completely collapses into a BH without experiencing a kick. If the mass-transfer phase is dynamically unstable a CE event with $\lambda = 0.1$ (as adopted in Stevenson et al. 2017) results in a final separation after the mass-transfer phase of $a \approx 0.02$ AU. If instead the mass-transfer phase is dynamically stable and highly non-conservative ($\beta \approx 0$), then the final separation is approximately 0.8 AU. In the latter case, the BBH system is too wide to merge in a Hubble time through the emission of gravitational waves.

The black-dashed line in figure 5.2 indicates the minimum required mass ratio of a system at the onset of dynamically-stable mass transfer which allows the orbital separation to shrink by at least a factor of ten. Hence, our choice for $\zeta_{\text{ad}} = 6.5$ enables systems with initial mass ratios $4.2 \leq q = M_{\text{D}}/M_{\text{A}} \leq 4.5$ to experience non-conservative dynamically-stable mass transfer and shrink their orbital separation by at least an order of magnitude. To shrink the separation by at least factor of five the initial mass ratio needs to be above 3.5. For non-conservative mass transfer in the absence of magnetic braking, tides and gravitational-wave radiation, a mass ratio threshold of 3.5 corresponds to $\zeta_{\text{ad}} > 4.5$. Stevenson et al. (2017) applied the prescription by Soberman et al. (1997) to calculate ζ_{ad} to all giant stars including those on the HG. Here $\zeta_{\text{ad}} > 3$ only if the core mass constitutes more than 80 per cent of the total mass of the star, which does not happen for HG stars based on the fits by Hurley et al. (2000). Therefore, Neijssel et al. (2019) find that it is possible to form merging BBHs through dynamically-stable mass transfer whereas Stevenson et al. (2017) do not.

5.2.3 Channel I forms massive equal-mass BBHs

The more massive the donor star is, compared to the compact companion at the onset of mass transfer, the more efficiently the orbit shrinks through dynamically-stable mass transfer. One might therefore expect this channel to produce merging BBHs with extreme mass ratios. However, the remnant-mass distribution (Fryer et al., 2012) flattens for the most massive stars, partly due to our implementation of stellar winds (Belczynski et al., 2010). Therefore, a system with an extreme mass ratio at the onset of a mass-transfer episode still results in a relatively equal-mass BBH. Furthermore, the in-spiral through gravitational-wave emission is more efficient for binaries with more massive and equal-mass remnants. Altogether, this introduces a selection effect on the merging BBHs which form through the dynamically-stable channel, favouring the detection of massive and nearly equal-mass BBHs ($q \gtrsim 0.6$).

5.3 Recipes for the adiabatic response to mass loss

The difference between the results of Stevenson et al. (2017) and Neijssel et al. (2019) show that the assumed adiabatic response of the stellar radius to mass loss, ζ_{ad} , affects the estimates for the rates and masses of merging BBHs. In particular it impacts the fraction of merging BBHs which form through channel I (see Fig. 5.1). As mentioned this formation channel does not involve a dynamically-unstable mass-transfer episode and results in more massive equal-mass systems compared to other channels. However, our current approximations for ζ_{ad} for post-MS stars are oversimplified at best.

This section describes updated recipes for estimating ζ_{ad} in the COMPAS population-synthesis code based on results of detailed models. The recipes determine the ζ_{ad} of a star depending on a temperature threshold, which indicates if a star is assumed to have a radiative envelope or a deep convective envelope. Moreover they adopt an updated prescription for estimating the ζ_{ad} of massive stars with radiative envelopes.

5.3.1 Radiative vs. convective envelopes

Massive stars on the MS have radiative envelopes. As they expand and move away from the MS a convective layer develops at the surface which grows in size. By the time the star ascends the asymptotic giant-branch almost the entire envelope is convective such that it dredges up helium from the core (Iben, 1974; Kippenhahn et al., 2012). The response of a star to mass loss can be estimated by approximating its structure with a polytrope. If we are describing a fully radiative sphere, this approximation predicts that the star will shrink ($\zeta_{\text{ad}} > 0$); whereas if we are describing a fully convective sphere, this approximation predicts that the star will expand ($\zeta_{\text{ad}} < 0$). The distinction between stars with convective and radiative envelope is therefore crucial for the dynamical stability of mass transfer.

In Stevenson et al. (2017); Vigna-Gómez et al. (2018) and Neijssel et al. (2019) the models do not differentiate between radiative or convective envelopes in massive stars. For massive stars, the fits to stellar models by Hurley et al. (2000) only suggest a growing convective envelope from the HG stage and consider fully convective envelopes for stars beyond the HG (see text after Eq. 111 Hurley et al. 2000). The adiabatic response to mass loss of MS and HG stars is therefore approximated by fixed values of ζ_{ad} based on the results of Ge et al. (2015) and are $\zeta_{\text{ad}} = 2.0$ and $\zeta_{\text{ad}} = 6.5$ respectively. Meanwhile the recipe for stars with fully convective envelopes of Soberman et al. (1997) is applied for more evolved stars, e.g. core-helium-burning (CHeB) stars.

According to our single stellar models, stars with initial masses above $M \gtrsim 12M_{\odot}$ ignite helium before ascending their giant branch. When this situation occurs, to estimate the ζ_{ad} of a CHeB star, we currently apply the prescription by Soberman et al. (1997) (as the star is more evolved than an HG star), even though a deep convective envelope may not have yet been developed. For these stars we should instead adopt a ζ_{ad} more similar to the one for HG stars. For comparison, if the core of a CHeB star is half its total mass at the onset of mass transfer, then the recipe by (Soberman et al., 1997) estimates $\zeta_{\text{ad}} \approx 0.5$ instead of our $\zeta_{\text{ad}} = 6.5$. For

a fully non-conservative mass-transfer episode, this would correspond to a critical mass ratio ($q_{\text{crit}} = M_{\text{D}}/M_{\text{A}}$) for dynamically-stable mass transfer of 1.5, instead of our 4.5.

Other population-synthesis codes, which rely on the same analytic fits, already have different stability criteria for hotter CHeB stars and those which are cool enough to have deep convective envelopes (Belczynski et al., 2008; Toonen et al., 2012). They base the state of the envelope on the effective surface temperature T_{eff} of a star, which they compare to a temperature threshold T_{conv} . Belczynski et al. (2008) determine that stars with surface temperatures below $\log_{10}(T_{\text{conv}}/\text{K}) = 3.73 \pm 0.02$ have deep convective envelopes based on models by Ivanova and Taam (2004). Klencki et al. (2020) show with detailed single stellar models that the size of a convective envelope depends, amongst others, on the metallicity of the star and the numerical routines used to calculate convective overshooting. Hence, the uncertainty quoted by Belczynski et al. (2008) does not reflect the full range of uncertainties coming from single stellar evolution. We adopt $\log_{10}(T_{\text{conv}}/\text{K}) = 3.73$. If $T_{\text{eff}} < T_{\text{conv}}$, the star is considered to have a deeply convective envelope and ζ_{ad} is determined by the prescription of (Soberman et al., 1997). If $T_{\text{eff}} > T_{\text{conv}}$, the star is assumed to not yet have a deeply convective envelope. The prescription of ζ_{ad} for these stars is described in the next section.

5.3.2 Adiabatic response to mass loss of stars without deep convective envelopes

Our values of $\zeta_{\text{ad}} = 2.0$ for MS and $\zeta_{\text{ad}} = 6.5$ for HG stars are a single-value summary of the detailed calculations of Ge et al. (2015). Instead Ge et al. (2015) show that these values could be estimated as a function of the initial mass and the expansion of the donor star at the onset of a mass-transfer episode and calculate their values for stars with initial metallicity of $Z = 0.02$. The exact value of ζ_{ad} depends on the mass-loss rate and orbital properties. Ge et al. (2015) provide an effective ζ_{ad} such that there is no dynamical instability (delayed or prompt) during the entire mass-

transfer phase. Therefore, we use the entire range of values of ζ_{ad} as an alternative model to our single value approximation. However, Ge et al. (2015) only provide tabulated results and we have not yet found a robust method to interpolate their results. Instead, we determine ζ_{ad} by determining which of the tabulated values of initial masses and radii are closest to the ones of the considered star. In appendix 5.A we provide some additional information on the applicability of the results of Ge et al. (2015) to our single stellar models. In the results section we compare this approach against our previous single-value assumption for MS and HG stars.

5.4 Results

We present our results in three steps. First, we show the difference between our default model, which assumes any post-HG star has a deep convective envelope, and the model of Belczynski et al. (2008), where stars have deep convective envelopes if $T_{\text{eff}} < T_{\text{conv}}$. Second, we vary both the temperature threshold, T_{conv} , and the single value of ζ_{ad} for stars that do not have deeply convective envelopes. Third, we combined the temperature-threshold approach of Belczynski et al. (2008) with a ζ_{ad} prescription based on the result of Ge et al. (2015), which estimates the ζ_{ad} of stars without deep convective envelopes, depending on their mass and radius. In all cases our results focus on estimates of the rate and mass distribution of merging DCOs.

To estimate the properties of the merging DCO population detected by current gravitational-wave detectors we need to simulate systems for a range of metallicities and assume a model for both the star formation rate and selection effects (Dominik et al., 2013; Chruslinska and Nelemans, 2019; Neijssel et al., 2019; Spera et al., 2019). Here we focus our efforts on a single metallicity to explore a large range of stability criteria and the rate of merging DCOs per unit solar mass evolved in all stars (see Sec. 4.3.1 for further details on our methods of sampling and calculating the mass evolved in all stars). The stars are simulated with an initial metallicity of $Z = 0.0045$ because this is the dominant metallicity for the detectable DCOs mergers according to Neijssel et al. (2019) and Stevenson et al. (2019).

5.4.1 Convective envelopes: Stellar type vs. effective temperature threshold

We performed a simulation of 2×10^5 binaries using model assumptions similar to the default assumptions of Neijssel et al. (2019), except for the inclusion of pair-instability supernovae, as implemented in Stevenson et al. (2019) and mentioned in section 3. We apply the “pessimistic” CE assumption where we assume dynamically-unstable mass transfer started by a HG star always results in a stellar merger. Figure 5.3 depicts the luminosities and effective temperatures of donor stars at the onset of the mass-transfer phase which reduces the orbital separation the most, determining whether the binary system is able to merge as DCO within a Hubble time (see also the double asterisk (**)) symbol in Fig. 5.1).

The impact of our assumptions on ζ_{ad} for stars with initial masses of $M_{\text{ZAMS}} \geq 10M_{\odot}$ immediately becomes apparent in Fig. 5.3. Massive stars that start mass transfer during the HG rarely form merging BBHs: if the mass-transfer episode is dynamically unstable, then the system will merge (before the formation of a BBH); if the mass-transfer episode is dynamically stable then the system remains too wide, unless its separation is short enough to initiate a mass-transfer phase early on the HG. Mass transfer started by stars during the first giant branch or after the ignition of helium in the core is less dynamically stable and therefore more likely to evolve through a CE. Hence, the symbols depicting merging BBHs sharply follow the boundary between the HG and the CHeB phase. The same is true for BHNS and BNS progenitors, however a mass-transfer phase onto a NS companion is more likely to have an extreme mass ratio which shrinks the orbit during dynamically-stable mass transfer enough to produce merging DCOs. Furthermore, a supernova kick could potentially aid the formation of a merging DCO.

The vertical-dashed line in Fig. 5.3 is the temperature threshold for deep convective envelopes of Belczynski et al. (2008). This figure shows that most of the CHeB donor stars, stars in the progenitor systems of merging DCOs, have been falsely treated as having deep convective envelopes in previous COMPAS studies. Correcting

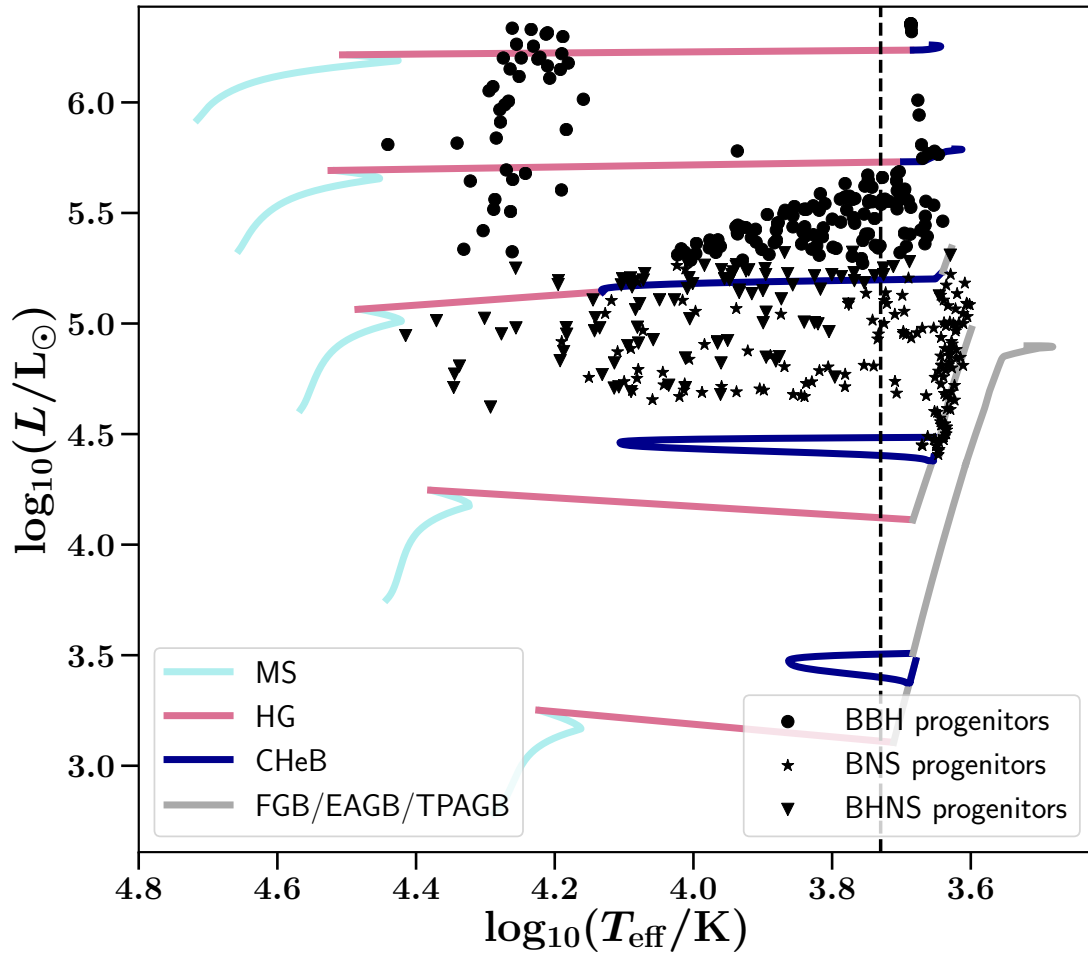


Figure 5.3: The Hertzsprung-Russell (HR)-diagram of stellar tracks with an initial metallicity of $\log_{10}(Z/Z_{\odot}) = -0.5$, which is the dominant metallicity for the detectable DCOs mergers in Neijssel et al. (2019) and Stevenson et al. (2019), and initial masses of $5 M_{\odot}$, $10 M_{\odot}$, $20 M_{\odot}$, $40 M_{\odot}$ and $80 M_{\odot}$. The different colours in the stellar tracks highlight different evolutionary stages. In particular the grey lines depict the different giant phases; first giant branch (FGB), early asymptotic giant branch (EAGB) and thermally-pulsating asymptotic giant branch (TPAGB) as defined in Hurley et al. (2000). The simulation follow the default model where ζ_{ad} is based on the stellar type of the donor and includes pessimistic CE evolution, where dynamically-unstable mass transfer started by a HG always results in a stellar merger. The black circles, stars and triangles depict the temperature and luminosity of the donor star at the onset of the mass-transfer phase which shrinks the orbital separation the most (see the double asterisk symbol in in Fig. 5.1) during the formation of merging DCOs, identified by different symbol. The agglomeration of circles at effective temperatures of $\log_{10}(T_{\text{eff}}/\text{K}) = 4.2$ and luminosities of $\log_{10}(L/L_{\odot}) = 6.0$ is due to merging BBHs which did not experience a CE phase.

for this, i.e. adopting the temperature threshold to determine which ζ_{ad} prescription to use, does not affect the BNS progenitors or BHNS progenitors, where the NS forms first. This is because of the high mass ratio at the onset of the mass transfer onto the NS. Indeed the average mass of a neutron star is about $\sim 1.3 M_{\odot}$, while for the companion to form a compact object its mass needs to be greater than $\sim 8 M_{\odot}$. Thus a $\zeta_{\text{ad}} = 6.5$ is often not sufficient to avoid dynamical instability during this mass-transfer episode. Only BNSs forming through channel III, which have almost equal mass ratios at the onset of the CE event, could avoid a CE if $\zeta_{\text{ad}} = 6.5$. However, in our models, the majority of BNSs formed through channel III experience mass transfer when both stars are on the giant branch (Vigna-Gómez et al., 2020) and hence they remain unaffected by the switch to a temperature threshold.

The mass ratios at the onset of the last mass-transfer phase are less extreme in BBH progenitors compared to those of BNS progenitors. During the collapse of the first BH progenitor the remnant retains more of the mass due to fallback (Fryer et al., 2012). Therefore, most merging BBH progenitors in Fig. 5.3 with initial masses $\sim 15 M_{\odot} < M_{\text{ZAMS}} < 40 M_{\odot}$ would have no longer experienced a CE during the final mass-transfer episode initiated by a CHeB star, if we had used $\zeta_{\text{ad}} = 6.5$ for CHeB donors with $T_{\text{eff}} > T_{\text{conv}}$. Instead, this mass-transfer phase would have been determined as dynamically stable. Dynamically-stable mass transfer would have left these systems too wide to merge in a Hubble time. The same would have been true for BHNS progenitors where the BH formed first.

In summary, the results of Neijssel et al. (2019) and Stevenson et al. (2019) for the rate and mass distribution of merging BBHs would have been very different, if they had adopted the temperature threshold by Belczynski et al. (2008) to determine ζ_{ad} for CHeB stars. The rate of mergers would have dropped and the mean total mass of the BBH mergers would have increased, since the less-massive BBHs are too wide to merge after dynamically-stable mass transfer. The change in rate and mass distribution would have also propagated into the log-likelihood calculations performed in Neijssel et al. (2019) and therefore the values for their model of the

metallicity-specific star formation rate.

5.4.2 Varying the single values of ζ_{ad} and T_{conv}

We previously showed that both the choices of ζ_{ad} and a temperature threshold T_{conv} considerably affect our results. Here we vary the values of T_{conv} and ζ_{ad} for post-MS stars with radiative envelopes. The prescriptions to estimate the mass-transfer rate from a donor star remain unchanged and follow the description given in chapter 3.3.2.1.

5.4.2.1 Varying the single value of ζ_{ad}

Figure 5.4 shows the rate of merging DCOs estimated per unit solar mass evolved in all stars in our simulation (see Sec. 4.3.1) and the fraction of systems which evolve through channel I. An increase in ζ_{ad} results in more binary systems experiencing a dynamically-stable mass-transfer phase. The fraction of systems evolving according to channel I out of the population of merging DCOs can indeed vary from zero if, in the absence of a deep convective envelope, ζ_{ad} is assumed to be $\lesssim 3$, to ~ 1 for ζ_{ad} values above ~ 8 , ~ 14 and ~ 10 for BBHs, BNSs and BHNSs, respectively. For merging BBHs, an increase in the ζ_{ad} , assigned to stars with radiative envelopes, raises the number of binary systems evolving through channel I, leaving the number of binary systems evolving through channel II and III roughly constant. This is because the progenitors of the merging DCOs, forming through these two channels (II and III), contain donor stars which are characterised by deep convective envelopes, at the moment of the (***) mass-transfer phase (see Fig. 5.1). The value of ζ_{ad} at the onset of the mass-transfer phase is therefore evaluated via the prescription proposed by Soberman et al. (1997) and is only sensitive to changes in T_{conv} .

The rate of merging BNSs is quite insensitive to the choice of ζ_{ad} . The average mass ratio at the onset of mass transfer from a massive star onto a NS companion is above 15. Therefore the mass transfer does not become dynamically stable for the choices of ζ_{ad} considered here. For merging BHNS the impact of a change in ζ_{ad} is

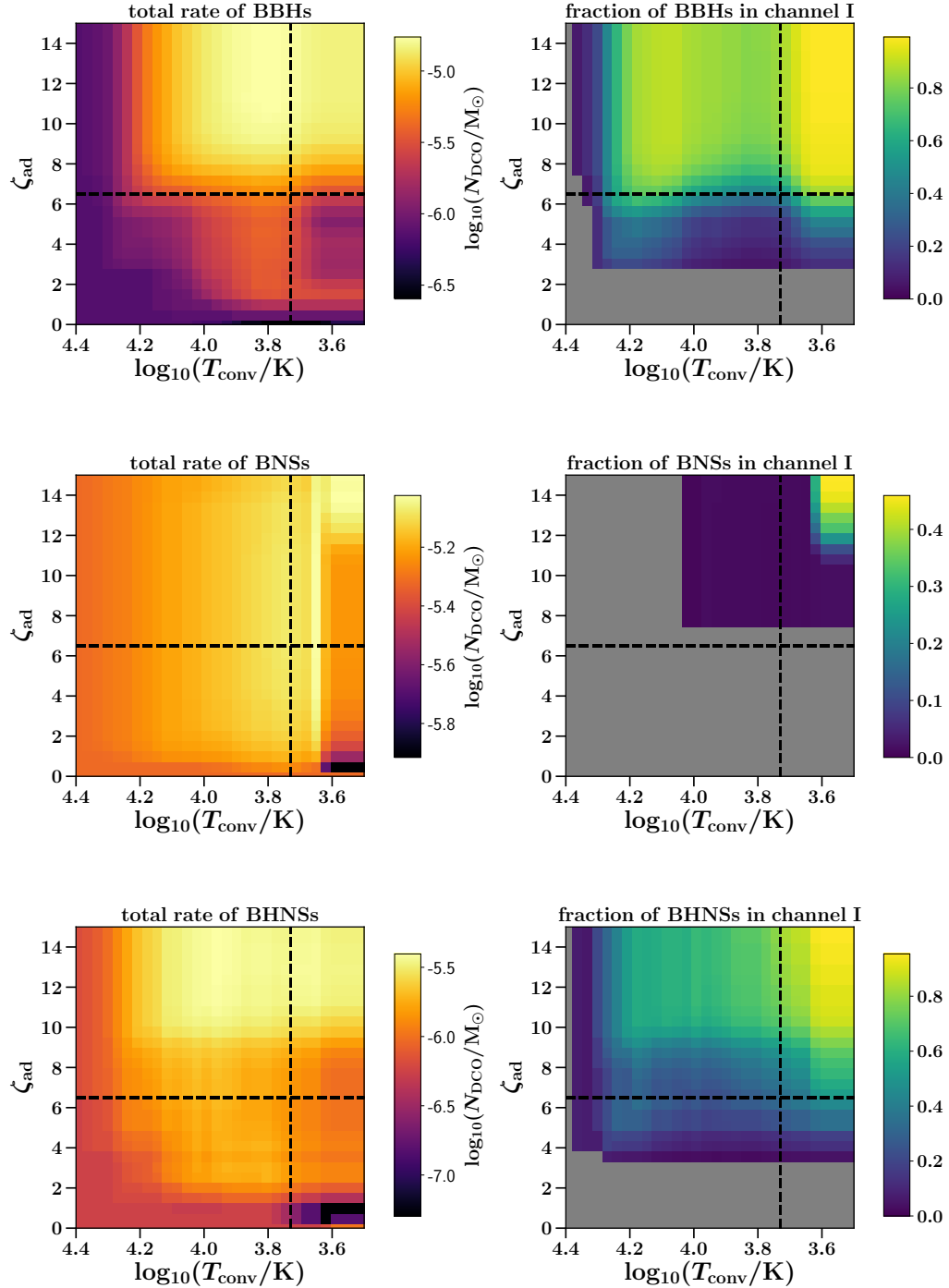


Figure 5.4: Left column depicts the number of merging DCO per unit solar mass evolved in all stars in our simulation (N_{DCO}/M_{\odot}), whilst assuming single ζ_{ad} values (y-axis) for post-MS stars with radiative envelopes and single T_{conv} values (x-axis), to determine if a star has a deep convective envelope. The right column shows the fraction of the merging DCOs that form through channel I. The black cross is the location of our default assumptions of $\zeta_{\text{ad}} = 6.5$ and $\log_{10}(T_{\text{conv}}/\text{K}) = 3.73$. Every row represents the contribution of DCOs of different nature; from top to bottom: BBHs, BNSs or BHNSs. These results are based on a simulation of 2×10^5 binaries at each grid point and the stars have an initial metallicity of $Z = 0.0045$. For this simulation, we follow the default model of Neijssel et al. (2019), with the additional implementation of pair-instability supernovae. Zero values are shown in grey.

less straight-forward since it depends on which type of compact object formed first.

5.4.2.2 Varying the single value of T_{conv}

When increasing T_{conv} from our default value of $\log_{10}(T_{\text{conv}}/\text{K}) = 3.73$, the number of stars determined to have deep convective envelopes increases and the rate of merging DCOs per unit solar mass evolved which form through channel II increases too. When $\log_{10}(T_{\text{conv}}/\text{K}) \geq 3.9$, the rate of binary systems evolving through channel II drops because the first mass-transfer phase from a post-MS star onto MS companion results in more stellar mergers.

The number of merging DCOs per unit solar mass evolved drops if T_{conv} is reduced from $\log_{10}(T_{\text{conv}}/\text{K}) = 3.73$. Here, stars on the giant branch are assumed to not have deep convective envelopes. The binary system would previously evolve through a CE phase and form a merging DCO according to channel II or channel III. However, by lowering the threshold to $\log_{10}(T_{\text{conv}}/\text{K}) = 3.6$, most giant donors are modelled as having radiative envelopes. Therefore, the binary system no longer experiences a CE and, because the mass transfer proceeds at large orbital separations, the system is not able to merge through stable mass transfer. The relative rate of mergers forming through channel II and channel III drops, resulting in an increased fraction of mergers forming through channel I.

5.4.2.3 Comparison of values for ζ_{ad} between studies

Other population-synthesis codes, such as **STARTRACK** (Belczynski et al., 2002b, 2008), **SeBa** (Portegies Zwart and Verbunt, 1996; Nelemans and van den Heuvel, 2001; Toonen et al., 2012), **binary_c** (Izzard et al., 2004b, 2006, 2009) and **MOBSE** (Giacobbo et al., 2018), rely on the same analytic fits to stellar tracks as the **COMPAS** code. Different codes use various recipes for ζ_{ad} to determine the dynamical stability of mass transfer. In some cases a critical mass ratio is used, here defined as $q_{\text{crit}} = M_{\text{D}}/M_{\text{A}}$, such that a mass ratio $q \geq q_{\text{crit}}$ results in dynamically-unstable mass transfer. What follows is a brief summary of the different recipes for ζ_{ad} used

in the aforementioned population-synthesis codes.

The `STARTRACK` code, on which we base our approach and value of T_{conv} , uses a $q_{\text{crit}} = 3$ as a critical mass ratio to avoid delayed dynamical instability during mass transfer started by stars with hydrogen envelopes. However, they also adopt a diagnostic diagram to determine the stability of a mass-transfer episode. The latter makes direct comparison difficult. The `SeBa` code assumes a fixed value for $\zeta_{\text{ad}} = 4$ for post-MS stars with radiative envelopes. For stars on the giant branch, `SeBa` defines a critical radius to distinguish between stars with radiative or deep convective envelopes (Toonen et al., 2012, priv. comm. Toonen). The `binary_c` code adopts a $q_{\text{crit}} = M_{\text{D}}/M_{\text{A}} = 1/0.65$ for MS stars and $q_{\text{crit}} = M_{\text{D}}/M_{\text{A}} = 2.5$ for HG stars (de Mink et al., 2013) and otherwise follows (Hurley et al., 2002). The `MOBSE` code relies on assumptions for mass transfer initiated by HG and CHeB donors which are not specified and we therefore assume they also follow (Hurley et al., 2002). Hurley et al. (2002) use a value of $\zeta_{\text{ad}} = 6.85$ for HG stars.

Values of $\zeta_{\text{ad}} = 2.5$, $\zeta_{\text{ad}} = 6.5$ or $\zeta_{\text{ad}} = 10.0$ correspond to critical mass ratios q_{crit} of approximately 2.5, 4.5 and 6.2 respectively, assuming a mass-transfer efficiency of $\beta = 0$ and angular momentum loss through isotropic re-emission. Therefore, our choice of $\zeta_{\text{ad}} = 6.5$ for HG stars allows for greater dynamical stability than `binary_c`, `STARTRACK` or `SeBa` and is similar to `BSE` (Hurley et al., 2002).

Figure 5.5 shows the simulated properties of merging BBHs when adopting $\zeta_{\text{ad}} = 2.5$, $\zeta_{\text{ad}} = 6.5$ and $\zeta_{\text{ad}} = 10.0$. At total BBH masses of $M_{\text{tot}} \sim 15 M_{\odot}$ and mass ratios of $q \sim 0.3$ we cannot confidently differentiate between the models due to uncertainties coming from our small sample size. However, at $M_{\text{tot}} \sim 35 M_{\odot}$ and mass ratios of $q \sim 0.7$, an increase in the value of ζ_{ad} clearly results in more merging BBHs. Changing $\zeta_{\text{ad}} = 6.5$ to $\zeta_{\text{ad}} = 10.0$ approximately quadruples the rate of merging BBHs with total masses of $M_{\text{tot}} \sim 35 M_{\odot}$. As mentioned in section 5.2.3 and shown in figure 5.3, the additional merging BBHs, generated at higher values of ζ_{ad} , evolve through channel I and so increase the average total mass and shift the average mass ratio closer to unity.

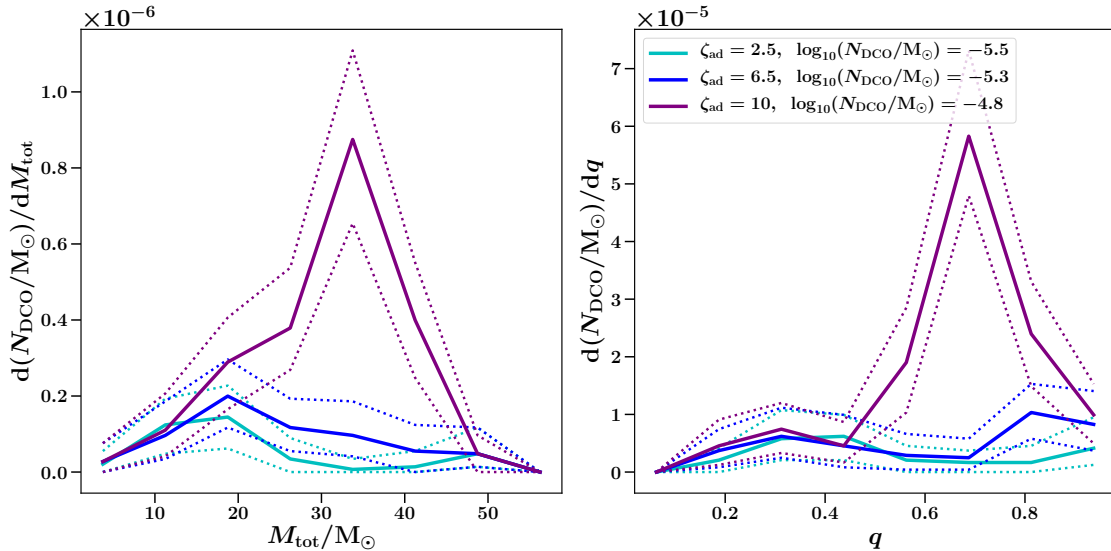


Figure 5.5: The merger rate and the distribution of the total mass M_{tot} and mass ratio q of merging BBHs at a metallicity $Z = 0.0045$. The simulations are done under the pessimistic CE assumption and with $\log_{10}(T_{\text{conv}}/\text{K}) = 3.73$. Here the mass ratio is $q = M_{\text{light}}/M_{\text{heavy}}$, where M_{light} is the least-massive BH and M_{heavy} the most massive BH of the merging binary. The area within the dotted lines indicates the 90 per cent confidence interval, estimated by bootstrapping the recovered population of merging BBHs 200 times.

The rate of formation, masses and mass ratios of merging BNSs do not differ appreciably when adopting $\zeta_{\text{ad}} = 2.5$, $\zeta_{\text{ad}} = 6.5$ or $\zeta_{\text{ad}} = 10.0$. This is consistent with the insensitivity seen also in Fig. 5.4 and explained previously. The different populations of merging BHNSs indicate an increased population of extreme mass-ratio systems ($q < 0.1$) at higher values of ζ_{ad} , however a larger sample size would be needed to confirm this trend.

In principle, the aforementioned population-synthesis codes are ideal tools to probe the impact of different assumptions for ζ_{ad} , q_{crit} on the formation of merging DCOs. However, aside from the stability of mass transfer, these codes also assume different binary-star physics; they differ, for example, in the calculation of crucial parameters such as: the natal kicks from SNe, the efficiency of mass transfer and the values for α and λ , describing CE events. A more detailed comparison study of the evolution of massive stars and the impact of different physics is needed, similar to the study by Toonen et al. (2014) for low mass stars. Therefore, caution must be taken when implementing the methods to estimate ζ_{ad} , as presented in this work,

into other population-synthesis codes. Each code should perform their own study into the effects of changing ζ_{ad} on the estimated rates and mass distributions of DCO mergers, given that differences in assumed binary-star physics might result in different outcomes.

5.4.2.4 Difference between q_{crit} and ζ_{ad}

Some codes rely on a q_{crit} to determine the dynamical stability of mass transfer, whereas others determine the stability based on ζ_{ad} . However, caution must be taken when directly comparing the two values. As shown by the solid black line in Fig. 5.2, the translation of ζ_{ad} to a q_{crit} depends on the efficiency of mass transfer β .

We compare our results against those of Giacobbo et al. (2018) to highlight the difference between requiring $\zeta_{\text{ad}} > \zeta_{\text{RL}}$ or $q < q_{\text{crit}}$ to classify a mass-transfer episode as stable. Giacobbo et al. (2018) also find that some of the BBHs merge through channel I (they refer to it as the zero common-envelope channel). At a metallicity of $Z = 0.004$, Giacobbo and Mapelli (2018) mention that 17 per cent of the BBH mergers form through this channel. According to our model at a metallicity of $Z = 0.0045$, assuming $\zeta_{\text{ad}} = 6.5$ and $\log_{10}(T_{\text{conv}}/\text{K}) = 3.73$, about 44 per cent of the merging BBHs form through channel I.

We assume they adopt $\zeta_{\text{ad}} = 6.85$ for HG stars based on Hurley et al. (2002). Although the difference could be due to other assumptions, we cannot exclude that it originated from their translation of $\zeta_{\text{ad}} = 6.85$ to a fixed critical mass-ratio q_{crit} applied for HG stars, as also done in Hurley et al. (2002). According to Hurley et al. (2000), a $\zeta_{\text{ad}} = 6.85$ corresponds to a critical mass ratio of 4, assuming fully conservative ($\beta = 1$) mass transfer. However, in our models we expect the mass transfer onto a NS or BH to be non-conservative $\beta \approx 0$, assuming the mass transfer is Eddington limited. In this case a $\zeta_{\text{ad}} = 6.85$ is closer to a critical mass ratio of ~ 5 (see also Fig. 5.2). If indeed we shifted our value of ζ_{ad} , we find that 17 per cent of merging BBHs form through channel I at this metallicity, similarly to Giacobbo et al. (2018). However as mentioned before, this is only a tentative comparison.

5.4.3 A mass- and radius-dependent value of ζ_{ad}

Ge et al. (2015) tabulate values of ζ_{ad} of stars with initial masses in the range $0.1 \leq M_{\text{ZAMS}}/M_{\odot} \leq 100$ at a metallicity of $Z = 0.02$, following their evolution up to the development of a deep convective envelope. Their values for the adiabatic response of the donor star to mass loss range between $-1 \lesssim \zeta_{\text{ad}} \lesssim 70$. In the absence of data for other different metallicities, we simply assume these ζ_{ad} values for all metallicities. In appendix 5.A we present our implementation of the ζ_{ad} values tabulated in Ge et al. (2015) and compare the values of ζ_{ad} to stellar tracks of COMPAS at different metallicities. Further studies are needed to discuss the impact of our assumptions.

Adopting both a mass- and radius-dependent value of ζ_{ad} and a temperature threshold of $\log_{10}(T_{\text{conv}}/\text{K}) = 3.73$ to determine the state of the envelope further increases the dynamical stability of mass transfer. Figure 5.6 shows the results of the three main models of stability criteria introduced in this paper:

- our default model;
- $\zeta_{\text{ad}} = 6.5$ for post-MS stars with radiative envelopes and ζ_{ad} of Soberman et al. (1997) for stars with deep convective envelopes; unlike from our default model, the state of the envelope is determined via a temperature threshold, where stars with $T_{\text{eff}} < T_{\text{conv}}$ are assumed to have developed a deep convective envelope;
- again using the temperature threshold criteria, we define ζ_{ad} according to Soberman et al. (1997) if $T_{\text{eff}} < T_{\text{conv}}$, while we follow the tabulated values of Ge et al. (2015) to estimate ζ_{ad} if $T_{\text{eff}} > T_{\text{conv}}$.

Compared to our default model the introduction of a temperature-dependent threshold for radiative and convective envelopes results in an increased dynamical stability of mass-transfer episodes started by CHeB stars with $T_{\text{eff}} > T_{\text{conv}}$. Therefore, about two thirds of the lower-mass BBH ($M_{\text{tot}} \sim 15 M_{\odot}$) progenitors no longer form through channel II and are left too wide to merge within a Hubble time (see

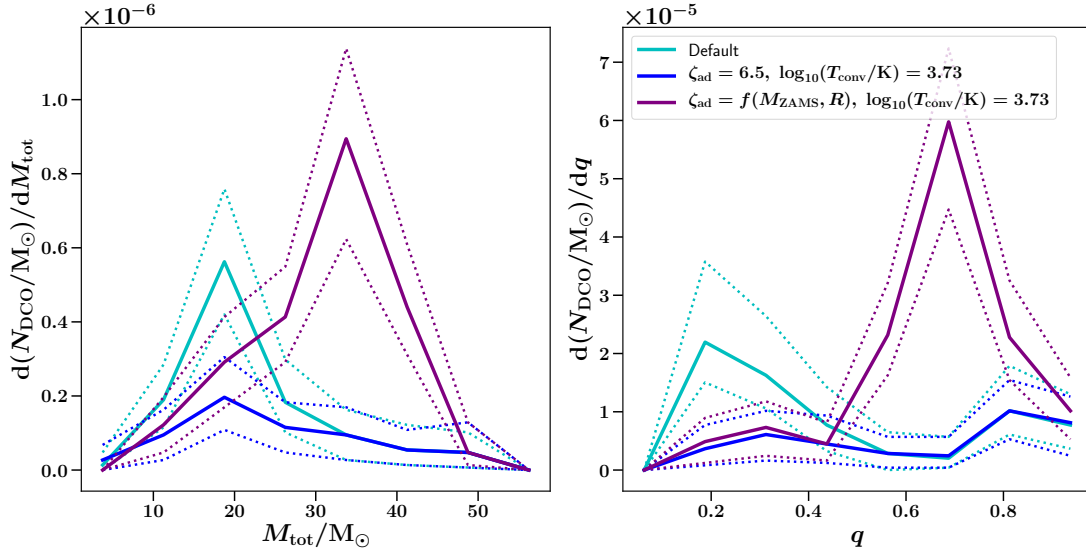


Figure 5.6: The merger rate and the distribution of the total mass M_{tot} and mass ratio q of merging BBHs at a metallicity $Z = 0.0045$. The simulations are done under the pessimistic CE assumption and with $\log_{10}(T_{\text{conv}}/\text{K}) = 3.73$. Here the mass ratio is $q = M_{\text{light}}/M_{\text{heavy}}$, where M_{light} is the least massive BH and M_{heavy} the most massive BH of the merging binary. The area within the dotted lines indicates the 90 per cent confidence interval, estimated by bootstrapping the recovered population of merging BBHs 200 times. The default model (cyan line) assumes that all post-HG stars have a ζ_{ad} according to Soberman et al. (1997). The second model (blue line) assumes that all stars with surface temperatures $T_{\text{eff}} < T_{\text{conv}}$ have deeply convective envelopes and that therefore their ζ_{ad} should follow the prescription of Soberman et al. (1997). HG stars and CHeB stars with hotter surface temperatures have a ζ_{ad} of fixed to 6.5. The third model (purple line) assumes the same temperature threshold as the second model (blue line) to distinguish between radiative and convective envelopes. In this last case, however, the value of ζ_{ad} for stars with radiative envelopes is based on the work by Ge et al. (2015), which has been calculated from the stars’ initial mass and radius at the onset of mass transfer.

also Sec.5.4.1). Further increasing the dynamical stability of mass-transfer episodes started by the Roche-lobe overflow (RLOF) of radiative post-MS stars, by adopting a mass- and radius-dependent value of ζ_{ad} , results in $\zeta_{\text{ad}} > 6.5$ for post-MS massive stars with radiative envelopes. The merger rate of BBHs increases by a factor of five compared to our default. Almost all BBHs forming through channel I with more than half of the BBHs having total masses above $30 M_{\odot}$ and mass ratios above 0.6 (see also Fig. 5.6).

5.5 Discussion

To recapitulate, Neijssel et al. (2019) find that at metallicities of ~ 0.0142 about a third of the merging BBHs form through channel I. Neijssel et al. (2019) falsely assumed that all post-HG stars have deep convective envelopes. This especially underestimates the mass transfer stability of CHeB stars (see Sec. 5.4.1). By applying a threshold for the effective surface below which stars are assumed to be deeply convective ($\log_{10}(T_{\text{conv}}/\text{K}) = 3.73$ based on Belczynski et al. 2008), the increased stability of CHeB donors results in a drop of systems forming through channel II with final total BBH masses of $\sim 15 M_{\text{odot}}$. Further increasing the stability of massive stars with radiative envelopes, by applying a mass and radius dependent prescription based on Ge et al. (2015), increases the number of BBHs merging through channel I. So far we have only considered the adiabatic response of the star to mass loss. In the outer parts of the envelope of extended massive stars the thermal timescale is sometimes shorter than the adiabatic timescale. Such super-adiabatic layers in the outer part of the envelope of massive stars yield even higher value of ζ (Woods and Ivanova, 2011; Passy et al., 2012; Ge et al., 2015; Pavlovskii et al., 2017). Ge et al. (2015) report an increase in ζ by a factor of ~ 1.5 for stars with masses above $50 M_{\odot}$.

The increased dynamical stability of mass transfer increases the rate of merging BBHs with total masses of $\sim 35 M_{\text{odot}}$ by almost an order of magnitude (see Fig. 5.6). During the mass-transfer phase from a massive star onto a NS the mass ratios are too extreme to be stabilised by the values of ζ_{ad} for radiative stars reported in Ge et al. (2015). Therefore, the rates and formation channels of merging BHNSs and merging BNSs remain mostly unaffected, except for BHNSs where the BH forms first.

5.5.1 Quasi-chemically-homogeneous evolution

Most of our BBH mergers no longer evolve through CE events after having adopted a mass- and radius-dependent value of ζ_{ad} and a temperature threshold of $\log_{10}(T_{\text{conv}}/\text{K}) =$

3.73 to determine the state of the envelope. We explored the effects of ζ_{ad} , but have ignored other potential physics which would affect our results. The BBHs forming through channel I start their last mass-transfer phase early on the HG, such that the orbital separation of the systems is tight enough to form a merging BBH through dynamically-stable mass transfer. If the companion star is spun up by accretion (Packet, 1981) or in the presence of tidal locking the companion star could evolve through quasi-chemically-homogeneous evolution instead (see e.g. Mandel and de Mink, 2016; Marchant et al., 2016). The stellar companion of the BH would no longer expand on the HG and avoid a mass-transfer phase onto the BH. Newer versions of COMPAS contain recipes to approximate the physics of quasi-chemically-homogeneous evolution in the rapid population-synthesis framework (Riley et al., 2021). Future studies should determine if systems evolve through channel I as presented here or instead evolve through quasi-chemically-homogeneous evolution.

5.5.2 Avoiding contact

In Sec.5.4.2.4 we showed that the translation of ζ_{ad} to q_{crit} depends on the mass-accretion efficiency during a mass-transfer phase. In our results we only considered ζ_{ad} for the dynamical stability of mass transfer. There are both advantages and disadvantages to using either a q_{crit} or ζ_{ad} to determine the dynamical stability of mass transfer. A single critical mass ratio q_{crit} does not account for the dependence of ζ_{RL} on the mass-transfer efficiency β . During non-conservative mass transfer, where mass leaves isotropically from the surface of the accretor, the mass lost from the system has a stabilising effect. By comparing ζ_{ad} to ζ_{RL} this stabilising effect is automatically taken into account. However, mass transfer does not only become dynamically unstable due to the response of the donor radius to mass loss.

A high mass-transfer rate could result in the accreting companion filling its Roche lobe, because accretion either increases the radius of the accreting companion or leads to the formation of a disk around it. For MS accretors, mass transfer could already result in contact systems when the timescale of mass transfer is comparable

to the thermal timescale of the accretor when filling its Roche lobe (see e.g. Web-
bink, 1976; Ulrich and Burger, 1976; Neo et al., 1977; Flannery and Ulrich, 1977;
Kippenhahn and Meyer-Hofmeister, 1977). In this case the mass-transfer episode
could become dynamically unstable due to the formation of a contact system and
subsequent formation of a common envelope, despite $\zeta_{\text{ad}} < \zeta_{\text{RL}}$. A similar argument
is possible for BH and NS accretors and the formation of an accretion disk. Cur-
rently we assumed that a BH accretes at the Eddington limit and the remainder of
the mass instantaneously leaves the system. If instead, similar to the MS accretor,
the material does not leave the binary system, a contact phase could result in a CE.
Our results in Sec.5.4.2.4 show that the fraction of binary systems evolving through
channel I drops below 20 per cent if we assume the mass ratio at the onset of mass
transfer needs to be below $q_{\text{crit}} \approx 4$ to avoid contact. If $q_{\text{crit}} \approx 2$ then none of our
binaries evolve through channel I.

5.5.3 ζ_{ad} and gravitational-wave detections

Let us assume that our models of binary star physics and our new choices of ζ_{ad}
do reflect the true nature of the stability and physics mass transfer. The results
presented here, based on stars with initial metallicities of $Z = 0.0045$, indicate that
most of the massive BBH mergers, with total masses above $30 M_{\odot}$, form without
experiencing a CE or a natal kick. This is different compared to BNSs which are
expected to experience CE events and receive natal kicks. Chruslinska et al. (2018)
mention that the only way to simultaneously reconcile the predicted merger rates of
BBHs and BNSs is by assuming the physics of CEs differs between the two progeni-
tors. Here we offer the possibility that most of the merging BBHs do not experience
a CE at all even if we allow for the survival of CE events from HG donors under the
optimistic CE assumption (see also Fig. 5.7). Klencki et al. (2020) performed a range
of detailed simulations to show that the optimistic CE assumption is likely not valid
for massive stars and only mass transfer from red super giants is capable of surviving
a CE phase. Furthermore, if it is true that stars with masses above $\sim 40M_{\odot}$ never

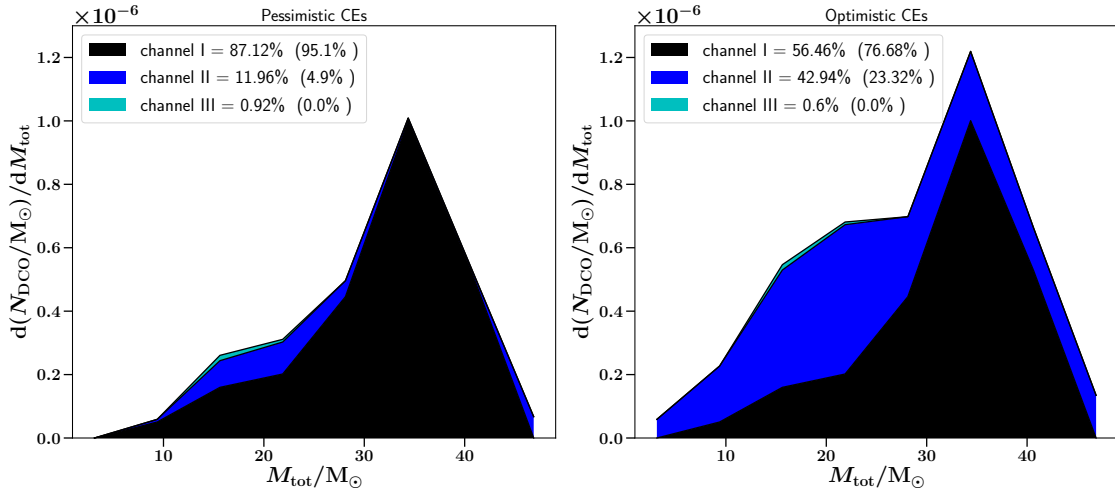


Figure 5.7: The total mass distribution of merging BBHs. The simulation assumes $\log_{10}(T_{\text{conv}}/\text{K}) = 3.73$ based on Belczynski et al. (2008) and a mass and radius dependent value of ζ_{ad} for radiative stars based on Ge et al. (2015). LLeft: the pessimistic CE assumption; right: the optimistic CE assumption (CE phases with HG donors always end in a merger or may lead to CE ejection, respectively). The colours indicate the formation channel of the binary system. The percentage indicates the fraction of binary systems evolving through each channel. The percentage in parentheses is the fraction of binary systems with total masses above $30 M_{\odot}$ evolving through each channel.

reach a red-supergiant phase, then it is unlikely that channel II or channel III is responsible for merging BBHs with total masses above $\sim 50 M_{\odot}$ (Klencki et al., 2020). Our simulations assume stars with initial metallicities of $Z = 0.0045$, a simulation at $Z = 0.001$ would result in more massive remnants with total masses above $\sim 50 M_{\odot}$ forming through channel I. Channel I would not require the detection of red supergiants since the stars are stripped of their envelopes through dynamically-stable mass transfer before they reach the giant branch.

Although tentative, our results indicate that estimates of the detection rate of DCO mergers are sensitive to the value of ζ_{ad} . It is however unlikely that observations of the mergers of DCOs provide a unique possibility to confirm the choices of ζ_{ad} and the possibility to have dynamically-stable mass transfer from post-MS which are more than 4 times as massive as the accreting NS or BH. For example, here we report that an increase from $\zeta_{\text{ad}} = 6.5$ to a $\zeta_{\text{ad}} = 10.0$ increases the mean total mass of merging BBHs. In Neijssel et al. (2019) a similar change is found by altering the metallicity-specific star formation rate in the early universe. This is just one of

many parameters, such as the natal kicks or the value of α for CEs, that affect the rate and mass distributions of BBH mergers.

5.5.4 Constraints from other observations

Ultra-luminous X-ray binaries (ULXs) provide additional constraints on the stability of mass transfer from massive stars. Ultra-luminous X-ray binaries are systems where the accretion rate onto the compact exceeds 10^{39} erg/s. A possible explanation of this source is a high-mass X-ray binary (HMXB) which experiences thermal timescale mass transfer from a massive star onto a BH or NS where the accretion rate exceeds the Eddington limit (see e.g. King et al., 2001; Rappaport et al., 2005; Pavlovskii et al., 2017, and references therein). The increased stability of mass-transfer episodes during the RLOF of post-MS stars as presented here would naturally result in an increased rate of ULXBs. Pavlovskii et al. (2017) report that within their models dynamically-stable mass transfer started by massive giants is capable of explaining both the rate of merging BBHs as well as the number of ULXBs. Other potential constraints come from the small population of short period Wolf-Rayet X-ray binaries (WXBs). van den Heuvel et al. (2017) show that WXBs could form through dynamically-stable mass transfer. Furthermore, they find that the number of predicted WXBs is very sensitive to their choice of q_{crit} for dynamically-stable mass transfer. A comprehensive study of the rate of formation of ULXBs and WXBs is needed to assess if the COMPAS models currently overestimate the stability of mass transfer.

5.6 Conclusion

The detailed models of (Ge et al., 2015) show that the value of the adiabatic response of the stellar radius to mass loss, ζ_{ad} , for stars with radiative envelopes is larger than the values commonly assumed in rapid population-synthesis codes. Where population-synthesis codes commonly assume $\zeta_{\text{ad}} \leq 7$, the values reported by (Ge

et al., 2015) range between 10 and 70 for massive stars, depending on the initial mass and the radius at the onset of mass transfer. In this study we show that an increased value of ζ_{ad} results in more binary systems evolving through channel I, which does not include a CE phase. This formation channel is not new and has already been reported in multiple studies such as van den Heuvel et al. (2017); Pavlovskii et al. (2017) and Giacobbo and Mapelli (2018). Our tentative results indicate this channel could be responsible for almost all of the detected gravitational-wave events coming from the mergers of BBHs. Using tabulated values of ζ_{ad} from Ge et al. (2015) for our models at a metallicity of $Z = 0.0045$ more than doubles the rate of BBH mergers. The rate of BBH mergers with total masses above $30 M_{\odot}$ quadruples and 95 per cent of these binary systems evolve through only dynamically-stable mass transfer. Detections of gravitational waves alone are unlikely to provide stringent constraints and comparison to other observations such as ULXs and WRXs are needed.

Acknowledgements

C. J. N. thanks the University of Birmingham for financial support. A.V-G. acknowledges funding support by the Danish National Research Foundation (DNRF132). The authors are supported by the Australian Research Council Centre of Excellence for Gravitational Wave Discovery (OzGrav), through project number CE170100004. We would like to thank Ge et al. (2015) for publishing their data in machine readable form (Ge et al., 2016). This paper used the Python (Oliphant, 2007; Perez et al., 2011), Numpy (Oliphant, 2006), Matplotlib (Hunter, 2007).

5.A Implementation Models and Illustrations

Here we provide a visual comparison (Fig. 5.8) of the values of the temperature threshold for deep convective envelopes by Belczynski et al. (2008), the values of ζ_{ad} by Ge et al. (2015) and their applicability to our adopted single stellar models (Hurley et al., 2000). The left column of Fig. 5.8 shows the single stellar tracks of COMPAS in the HR-diagram. The middle column of Fig. 5.8 shows the radial expansion of the stars, colour coded by stellar type. For clarity we omit the blue-loops and stars that are close to self-stripping. Mass transfer is unlikely to happen during these phases unless there is a fortuitous SN of the companion. Furthermore we colour-coded all the giant-branch phases with the same colour for clarity.

The simulations by Ge et al. (2015) assume a metallicity of $Z = 0.02$. The top panel in Fig.5.8 is at a metallicity of $Z = 0.0142$. The bullet points show the resolution in initial mass and radial expansion for ζ_{ad} by Ge et al. (2015). Their maximum expansion for stars with non fully convective envelopes coincides reasonably well with our stellar models. The stellar tracks in COMPAS are based on the stellar models by (Pols et al., 1998), which uses the detailed code by Eggleton (1971, 1972). The stellar models by Ge et al. (2015) are made using STARS (Eggleton et al., 2011), a later version of the detailed code by Eggleton (1971), which could explain the similarities between the stellar tracks. The threshold for fully convective envelopes of $\log_{10}(T_{\text{conv}}/\text{K}) = 3.73$ by Belczynski et al. (2008) is not that dissimilar to the transition to fully convective envelopes as found by Ge et al. (2015) for intermediate mass stars. However, in our single stellar models, stars with initial masses above $30 M_{\odot}$ ascend the giant branch with surface temperatures below $\log_{10}(T_{\text{eff}}/\text{K}) = 3.6$. Hence the temperature threshold of Belczynski et al. (2008) potentially still overestimates the temperatures at which massive stars develop deep convective envelopes. Klencki et al. (2020) provide an alternative fit for T_{conv} , however our stellar models do not reach such cool temperatures and therefore the fit is not applicable.

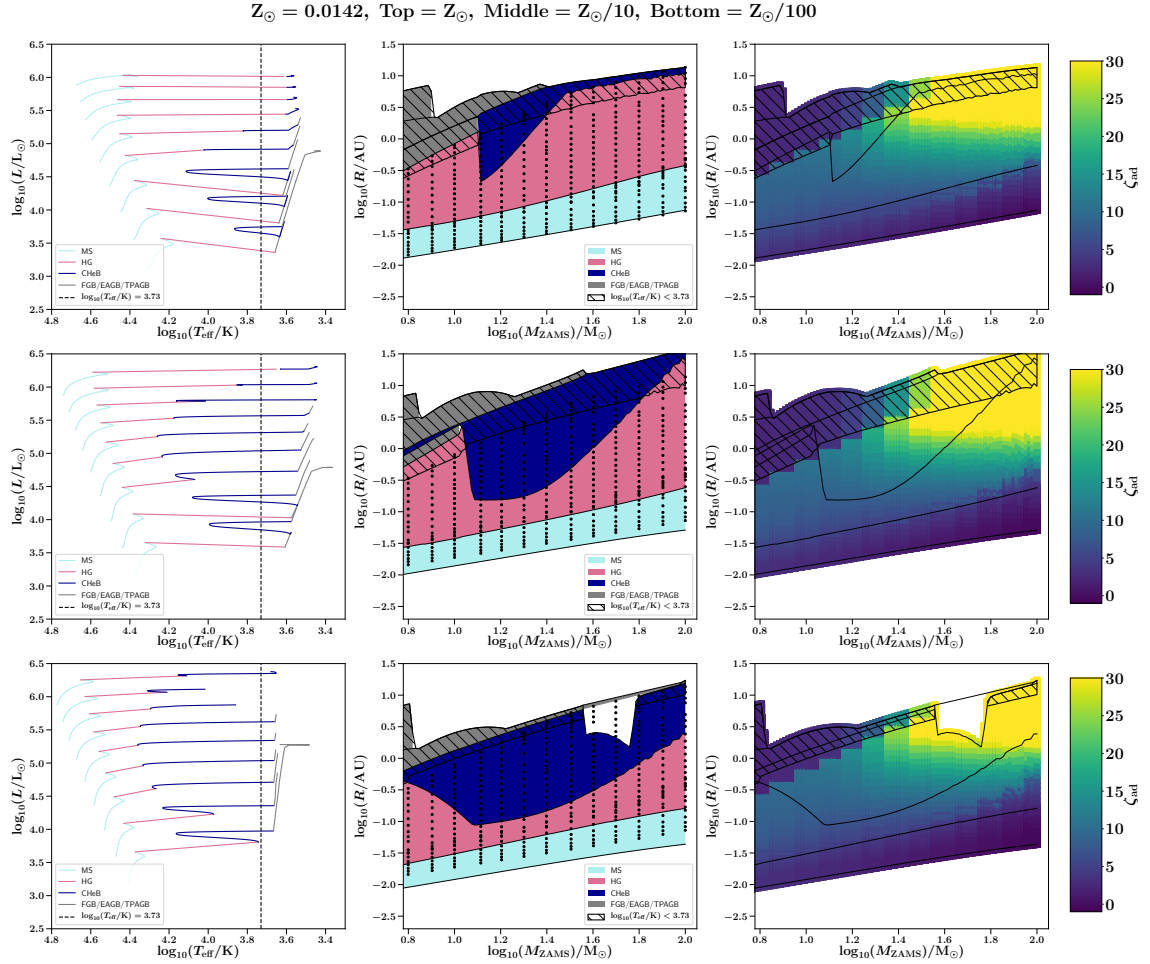


Figure 5.8: A comparison between the fits to single stellar models of Hurley et al. (2000), as implemented in the alpha-version of COMPAS, and the values of T_{conv} and ζ_{ad} . The left column shows the single stellar tracks in the HR-diagram colour-coded by the stellar type following the terminology of Hurley et al. (2002): MS, HG, first giant branch (FGB), CHEB, early asymptotic giant branch (EAGB) and thermally pulsing asymptotic giant branch (TPAGB). The dashed vertical line indicates the threshold for T_{conv} based on Belczynski et al. (2008). The middle column shows the expansion of the star as a function of its initial ZAMS mass. The colour depicts the stellar type of the star. The bullet points in the centre column depict the resolution of the values ζ_{ad} of Ge et al. (2015). The hatched region indicates where stars are determined to have deep convective envelopes when applying $\log_{10}(T_{\text{conv}}/\text{K}) = 3.73$. The right column shows the values of ζ_{ad} determined by the nearest value in M_{ZAMS} , R of Ge et al. (2015). The maximum value of ζ_{ad} is ~ 70 , but the scale of the colourbar is limited for clarity. The right panel shows ζ_{ad} even for fully convective stars to indicate the behaviour when we extrapolate the results by Ge et al. (2015) based on the nearest value. The drop in radii in models at $Z = 0.000142$ is an due to an incorrect implementation of the fits of Hurley et al. (2000) stellar radii of CHEB and is resolved in the beta-version of COMPAS.

Chapter 6

Wind mass-loss rates of stripped stars inferred from Cygnus X-1

Coenraad J. Neijssel, Serena Vinciguerra, Alejandro Vigna-Gómez, Ryosuke Hirai, James C. A. Miller-Jones, Arash Bahramian, Thomas J. Maccarone, and Ilya Mandel

Abstract Recent observations of the high-mass X-ray binary Cygnus X-1 have shown that both the companion star (41 solar masses) and the black hole (21 solar masses) are more massive than previously estimated. Furthermore, the black hole appears to be nearly maximally spinning. Here we present a possible formation channel for the Cygnus X-1 system that matches the observed system properties. In this formation channel, we find that the orbital parameters of Cygnus X-1, combined with the observed metallicity of the companion, imply a significant reduction in mass loss through winds relative to commonly used prescriptions for stripped stars.

Contents

6.1	Introduction	175
6.2	Cygnus X-1: Observations and assumed channel	176
6.2.1	Eccentricity, peculiar velocity and fallback	176
6.2.2	Black-hole progenitor mass	177
6.2.3	Black-hole spin & progenitor spin	178
6.2.4	Companion mass & abundance	181
6.3	Cygnus X-1: Maximum wind mass-loss rate	183
6.4	Cygnus X-1: Future evolution	187
6.5	Cygnus X-1: Caveats and conundrums	191
6.A	Wind mass-loss rate for stripped stars	197
6.B	Cygnus X-1 : Constraints on wind mass-loss rates assuming single stellar evolution	198
6.B.1	Uncertainties in f_{WR} and f_{LBV}	199
6.B.2	Effect on the entire remnant mass distribution	201
6.B.3	Additional variations	202
6.B.4	Constraints on winds from single stellar evolution	203

6.1 Introduction

Cygnus X-1 is a high-mass X-ray binary (HMXB) in the Cygnus OB3 association, which hosts a star in orbit with a black hole (BH) (e.g. Webster and Murdin, 1972; Bolton, 1972, 1975; Hutchings et al., 1973). The BH accretes matter from the stellar wind; this accretion powers X-ray radiation (e.g. Davidson and Ostriker, 1973; van den Heuvel, 1975; Conti, 1978; Petterson, 1978) and a jet (e.g. Bisiacchi et al., 1974; Marti et al., 1996; Stirling et al., 2001). Orosz et al. (2011) inferred the BH and stellar companion masses of Cygnus X-1 to be $14.8 \pm 1.0 M_{\odot}$ and $19.2 \pm 1.9 M_{\odot}$, respectively. Revised measurements of the distance to Cygnus X-1 (Miller-Jones et al., 2021) indicate that both objects are significantly more massive. The temperature and luminosity of the optical companion are estimated to be $T_{\text{eff}} = 31.1 \pm 0.7$ kK and $\log(L/L_{\odot}) = 5.63 \pm 0.07$ with a mass of $M_{\text{opt}} = 40.6_{-7.1}^{+7.7} M_{\odot}$, where we quote the median value and the 68 per cent confidence interval boundaries (Miller-Jones et al., 2021). The mass of the BH is estimated as $M_{\text{BH}} = 21.2_{-2.3}^{+2.2} M_{\odot}$. The binary has an almost circular orbit with a semi-major axis $a = 0.244_{-0.013}^{+0.012}$ AU and eccentricity $e = 0.0189_{-0.0026}^{+0.0028}$ (Miller-Jones et al., 2021). The BH is inferred to be nearly maximally spinning with a dimensionless spin of at least 0.95 according to both disk continuum and reflection line fitting studies (Gou et al., 2011; Fabian et al., 2012; Miller-Jones et al., 2021; Zhao et al., 2020). Via optical spectroscopy, it has been found that the ratios of the surface abundances of both helium and iron to hydrogen are about twice the respective values for the Sun (Shimanskii et al., 2012). As we discuss below, these observations taken together present a challenge for models of massive stellar binary evolution.

In this paper we describe the constraints that these observations place on the Cygnus X-1 formation channel (Sec. 6.2). We explore how the helium main sequence (HeMS) phase of this channel provides a constraint on the wind mass-loss rates of massive stars (Sec. 6.3). We present the likely future of the system and its implications for gravitational-wave detections (Sec. 6.4). Finally we discuss some caveats and questions raised by the observations of Cygnus X-1 (Sec. 6.5).

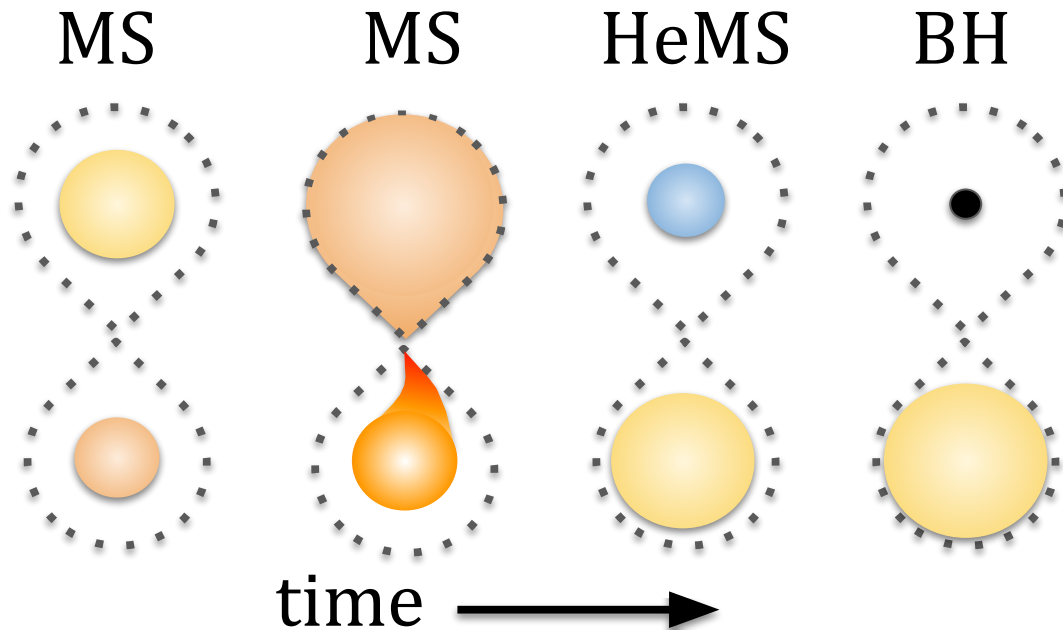


Figure 6.1: Assumed formation channel for Cygnus X-1. 1: Two stars (primary top, secondary bottom) are born in a binary. 2: The primary star is more massive and evolves faster, expands and starts a mass-transfer episode onto the secondary. 3: The primary is left as a hot stripped HeMS star with a companion which could have accreted a significant amount. 4: The primary star collapses and leaves behind a BH orbiting the secondary MS star.

6.2 Cygnus X-1: Observations and assumed channel

We assume the following formation channel for Cygnus X-1 (see Fig.6.1 for illustration). Two stars are born in a binary. The more massive star (the primary) evolves more quickly and expands first. The companion (the secondary) is close enough for the late main-sequence primary to commence mass transfer. The primary is stripped of its envelope, leaving an exposed helium core. The core continues nuclear fusion until it collapses and forms a BH in orbit with the still core-hydrogen-burning main sequence (MS) companion. In the sections below, we describe the observations and theoretical analyses that support this channel.

6.2.1 Eccentricity, peculiar velocity and fallback

The collapse of a star into a compact object can impart both a natal kick from an asymmetric explosion (see e.g. Fryer 2004 and references therein) and a kick from

rapid symmetric mass loss to the system (Blaauw, 1961). The low eccentricity of the Cygnus X-1 binary (Orosz et al., 2011; Miller-Jones et al., 2021) seems to disfavour a significant natal kick. However, tidal forces could have circularised the system since the collapse: for the inferred stellar and binary properties, the circularisation timescale for dynamical tides (applicable for radiative-envelope stars, Zahn, 1977) is only $\sim 10^5$ years (estimated using equations (41) and (43) of Hurley et al., 2002).

On the other hand, the system’s small peculiar velocity strongly indicates that the BH experienced nearly complete collapse with little mass ejection during its formation (Mirabel and Rodrigues, 2003). The peculiar velocity is 10.7 ± 2.7 km s⁻¹ relative to its host association (Rao et al., 2019), which limits the amount of instantaneous symmetric mass loss (Blaauw, 1961; Nelemans et al., 1999; Wong et al., 2012) to $\lesssim 2 M_{\odot}$, unless the kick from symmetric mass ejection is fortuitously cancelled by an oppositely directed natal kick. Further indirect evidence for the low natal kick lies in the absence of Type C quasi periodic oscillations, which may indicate Lense-Thirring precession due to spin-orbital misalignment as a result of a natal kick (Stella and Vietri, 1998) and are observed in most known black hole X-ray binaries (Ingram et al., 2016), the majority of which are believed to have received strong (~ 100 km s⁻¹) natal kicks (Atri et al., 2019). The low amount of ejected mass is also consistent with the current eccentricity in the absence of significant tidal circularisation, and suggests nearly complete fallback onto the black hole except for a small amount of neutrino mass loss (e.g. Nadezhin, 1980; Lovegrove and Woosley, 2013; Fernández et al., 2018). Nearly complete collapse matches the theoretical models simulating the fall-back onto black holes of similar masses (Fryer et al., 2012) and observational evidence for massive stars disappearing without supernovae (Adams et al., 2017).

6.2.2 Black-hole progenitor mass

The Eddington-limited mass-accretion rate for a BH of this mass is $\lesssim 2 \times 10^{-7} M_{\odot}$ yr⁻¹. Under the assumption of Eddington-limited accretion (but see, e.g., Fragos

and McClintock 2015; Eldridge et al. 2017; van Son et al. 2020, who relax this assumption), only a negligible amount of mass could have been accreted onto the BH since it formed (King and Kolb, 1999). The companion lifetime sets the accretion duration to no more than a few Myr, meaning that at most $\lesssim \text{few} \times 10^{-1} M_{\odot}$ could have been accreted. Assuming that the jet turned on promptly after the formation of the black hole, the $\text{few} \times 10^4$ yr estimate of the age of the jet (Russell et al., 2007) places an even stronger constraint on the amount of accreted mass, $\lesssim 10^{-2} M_{\odot}$ (see also Sell et al. 2015, who consider other models for the nebula origin but reach similar conclusions about its age). Therefore, the current black-hole mass $M_{\text{BH}} = 21.2_{-2.3}^{+2.2} M_{\odot}$ is a good estimate for the progenitor mass just before the collapse.

6.2.3 Black-hole spin & progenitor spin

The BH has a dimensionless spin χ close to unity, $\chi \geq 0.95$ (Gou et al., 2011; Fabian et al., 2012; Miller-Jones et al., 2021), although spin measurements may have large systematic errors because of modelling assumptions (Miller and Miller, 2015; Kawano et al., 2017; Zhao et al., 2020). A spin close to unity, coupled with negligible mass loss during collapse, suggests that if the pre-collapse progenitor had excess angular momentum, $\chi > 1$, it must have been carried away by a small amount of mass with high specific angular momentum (cf. Janka, 2013, 2017; Batta and Ramirez-Ruiz, 2019; Murguia-Berthier et al., 2020).

The rotational angular momentum of the BH was either present in the progenitor, or was gained during or after its collapse. Here we briefly summarise why we assume that the angular momentum comes from the progenitor and why this implies that the progenitor must have been stripped early in its evolution (see Mandel and Fragos 2020 for a longer discussion).

A BH needs to roughly double its mass through accretion in order to go from zero to maximal spin (Bardeen et al., 1973; Thorne, 1974). This is not possible for Cygnus X-1 under the assumption of Eddington-limited accretion. The spin could

have been acquired during the collapse, e.g., if the companion torques some of the ejecta which then fall back onto the BH (Batta et al., 2017; Schröder et al., 2018), but this requires some fine-tuning: for example, the ejecta must have sufficient velocities to be torqued by the companion, but without a significant tail of escaping ejecta to match formation through nearly complete fallback as discussed above. Therefore we assume that the angular momentum was present in the progenitor at the moment of the collapse.

Observations suggest that stars might be born as rapid rotators (Fukuda, 1982; Rosen et al., 2012; Ramírez-Agudelo et al., 2013, 2015), although these observations could be affected by binary interactions (Langer et al., 2008; de Mink et al., 2013). Even if stars are born as rapid rotators, they spin down through wind-driven mass loss and are unlikely to retain enough angular momentum to form rapidly spinning BHs.

The black hole’s dimensionless spin is determined by the ratio of its total angular momentum to the square of its mass. At lowest order, it is therefore insensitive to the redistribution of angular momentum through the progenitor star. However, if the bulk of the angular momentum moves into the envelope as the star expands, and the envelope is subsequently removed by winds or mass transfer, the remaining core is likely left with too little angular momentum to produce a rapidly spinning BH (Petrovic et al., 2005b; Belczynski et al., 2017; Fuller and Ma, 2019; Bavera et al., 2020; Mandel and Fragos, 2020). On the other hand, the core could retain sufficient angular momentum to form a rapidly spinning BH if there is a large amount of differential rotation between the layers of the star (Hirschi et al., 2005). Therefore, the efficiency of angular momentum transport in the star plays a key role, yet both the mechanism and degree of core-envelope coupling remain uncertain. Theory (Tayler, 1973; Spruit, 2002; Fuller et al., 2019; Takahashi and Langer, 2020) and observations, such as rotation rates of low-mass giant stars (Cantiello et al., 2014), suggest that there may be efficient angular momentum transport and the envelope is coupled to the core. If so, the observed rapid spin of the Cygnus X-1 black hole in a

close binary, in which the progenitor must have lost its envelope, appears to require pre-collapse interaction with the companion to spin up the stellar core.

Tidal locking of the period of the stellar rotation to the period of the binary provides the most likely mechanism for producing a rapidly rotating BH progenitor (Izzard et al., 2004a; Kushnir et al., 2016; Zaldarriaga et al., 2018; Belczynski et al., 2017; Bavera et al., 2020). Chemically homogeneous evolution could yield rapidly rotating black holes (Mandel and de Mink, 2016; Marchant et al., 2016), but is not expected to operate at such high metallicities and is not consistent with the observed expansion of the companion.

Instead, the following evolutionary sequence, proposed by Valsecchi et al. (2010) for M33 X-7, a similar high-mass X-ray binary with a rapidly spinning BH, and investigated in detail by Qin et al. (2019), appears to be the most likely formation mechanism for Cygnus X-1. The binary starts out with a period somewhat shorter than the current observed one. The more massive primary – the BH progenitor – commences mass transfer while still on the main sequence. This mass-transfer episode is likely to be largely non-conservative if limited by the spin-up of the accretor according to (Qin et al., 2019); this is favoured both by the observed evolutionary state of the secondary (conservative mass transfer would imply an initially lower-mass primary, and hence an older binary, placing an upper limit on the BH progenitor mass that would make it unlikely to form such a massive BH) and the observed period. The mass transfer removes the donor’s envelope, preventing subsequent re-expansion and angular momentum loss. Meanwhile, the core remains tidally locked to the MS companion. After hydrogen is exhausted in the core at the end of the MS, the star contracts into a rapidly spinning HeMS star. While this HeMS star is no longer tidally locked, it can still collapse into a rapidly spinning BH. Qin et al. (2019) find that the efficiency of angular momentum transport does not play a significant role for the evolution of the black hole progenitor during the main sequence, where tidal locking keeps its core rapidly spinning, but could be a key factor in determining the ultimate black hole spin through its impact on the angular

momentum lost through winds in later evolutionary stages. The Qin et al. (2019) models successfully reproduce systems with the orbital parameters of Cygnus X-1. In fact, the match appreciably improves with the upward revision in the BH and optical companion masses, as the observed masses in the bottom left panel of figure 3 of Qin et al. (2019) shift toward the locus of their model evolutionary trajectories (though their evolutionary trajectories are only shown for an initial mass ratio of 0.4, while the latest observations support more comparable masses). Given the number of uncertainties relating to this first mass transfer episode, in what follows we focus on the subsequent evolution of the binary under the assumption of this formation channel for Cygnus X-1.

6.2.4 Companion mass & abundance

We compare the observed mass, luminosity and temperature of the optical companion against analytic fits to stellar tracks of Hurley et al. (2000) as implemented in the COMPAS rapid population-synthesis code (Stevenson et al., 2017; Vigna-Gómez et al., 2018). The observations are consistent with a MS star that is about 70 to 80 per cent through its core-hydrogen-burning phase, ignoring the impact of rotation.

These stellar tracks are for stars with regular hydrogen-rich atmospheres. Using them ignores the possible impact of non-standard surface abundances, and so corresponds to the assumption that only a thin surface layer has a significant over-abundance of helium, rather than a uniform distribution of enriched material throughout the star. Stars in later stages of the MS with the relevant mass and metallicity should have at most a very thin convective layer at the surface (e.g., Maeder et al., 2008; Kippenhahn et al., 2012). Therefore, mixing is expected to be relatively inefficient: in the absence of large-scale convection, the Rayleigh-Taylor instability is likely to be suppressed by temperature inversion in the accreted material (Kippenhahn et al., 1980; Braun and Langer, 1995). The resulting thermohaline mixing will mix the helium-rich material through the companion only on timescales longer than the expected $\text{few} \times 10^4$ years since the formation of the BH if the bulk

of the enriched material was accreted at or shortly before the BH formation.

The evolutionary channel shown in figure 6.1, assuming that the optical companion has not overflowed its Roche lobe. While previous studies explored this possibility, perhaps with intermittent Roche-lobe overflow followed by longer periods when the binary is detached as in the present state, these models are typically based on assumptions that the companion is less massive than the BH (Podsiadlowski et al., 2003), which is inconsistent with present observations. Indeed, if we assume that mass transfer onto a black hole is almost entirely non-conservative because of the Eddington limit, the binary’s semi-major axis a evolves as

$$\frac{\dot{a}}{a} = -2 \frac{\dot{M}_{\text{opt}}}{M_{\text{opt}}} \left[1 - \left(\gamma + \frac{1}{2} \right) \frac{M_{\text{opt}}}{M_{\text{opt}} + M_{\text{BH}}} \right], \quad (6.1)$$

where γ is the specific angular momentum of the ejected material in units of the binary’s specific orbital angular momentum $J/(M_{\text{opt}} + M_{\text{BH}})$. The binary can widen as a result of such mass transfer only if $\gamma \lesssim 1$ for the observed component masses. However, in the common assumption of isotropic re-emission from the accretor, $\gamma = M_{\text{opt}}/M_{\text{BH}} \approx 2$. The ejected material would have to carry much lower specific angular momentum in order for the binary to detach once Roche-lobe overflow from the companion commences, which seems unlikely, lending support to our proposed channel.

The estimated mass and lifetime of the companion already enable us to roughly infer the initial mass of the BH progenitor. We assume that both stars are born and start fusion at the same time and use a fit (Farr and Mandel, 2018) to the Brott et al. (2011); Köhler et al. (2015) stellar models for the MS lifetime of non-rotating massive stars. For this simple estimate, we ignore the impact of binary interactions, consistent with the assumption of largely non-conservative mass transfer. The BH progenitor should have had an initial mass of $\sim 55 - 75 M_{\odot}$ in order to complete its evolution while leaving behind a MS companion of mass M_{opt} at $\sim 70\% - 80\%$ of its MS lifetime.

The surface abundances of the companion are non-standard for massive MS stars

and a challenge to explain even in the context of binary interaction. We discuss the abundances in more detail in Section 6.5. Here, we focus on the iron abundance, as this is key to the analysis of line-driven winds in the following section. Shimanskii et al. (2012) find that the iron abundance of the companion is 2.2 times the solar iron abundance, although precise measurements are challenging due to the complexity of the system. Assuming $Z_{\odot} = 0.014$ for solar metallicity (Asplund et al., 2009), this corresponds to an effective metallicity of $Z \approx 0.03$. On the other hand, Daffon et al. (2001) find a slightly sub-solar iron abundance of $\log \epsilon(\text{Fe}) = 7.33 \pm 0.12$ in HD 227460, which is a B0.5V star in the same Cygnus OB3 association as Cygnus X-1. This could indicate that $Z \approx 0.01$ is a better estimate of the initial iron abundance, and the iron abundance of the companion in Cygnus X-1 has been enhanced during the collapse of the primary to a BH. Therefore, we explore an initial metallicity range $0.01 \leq Z \leq 0.03$ in the following section.

6.3 Cygnus X-1: Maximum wind mass-loss rate

Hereafter we assume that, after the mass-transfer episode induced by the BH progenitor, the primary is left with no hydrogen layer on top of the He core. This assumption is consistent with the channel proposed by Qin et al. (2019), in which the rapidly spinning BH is ultimately formed through the collapse of a Wolf-Rayet star (see however discussion in Section 6.5).

In order for Cygnus X-1 to form through the channel depicted in Fig. 6.1, two things must be true. Firstly, the HeMS star must be born with sufficient mass to give rise to the observed BH mass even after losing mass through Wolf-Rayet winds during the HeMS. However, at a given metallicity, there is a maximum to the He core mass that can be formed at the end of the MS: as more massive stars have higher wind mass-loss rates, terminal-age MS He core masses asymptotically approach a maximum as a function of zero-age MS. This maximum He core mass is plotted in figure 6.2. Because the BH progenitor is stripped of its hydrogen envelope at the end of the MS for the binary evolutionary channel we assume, we can directly

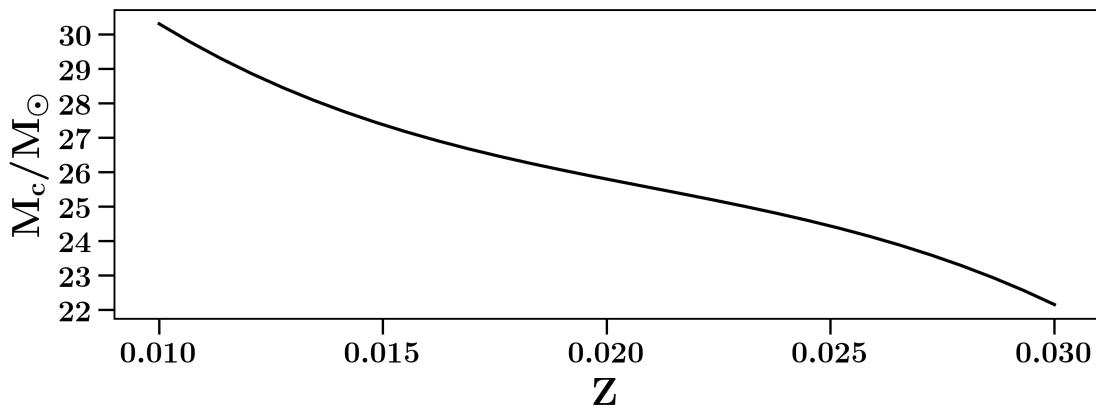


Figure 6.2: Maximum helium core mass at terminal-age MS as a function of metallicity, maximized over zero-age MS masses, based on the stellar tracks of Hurley et al. (2000) as implemented in COMPAS (Stevenson et al., 2017; Vigna-Gómez et al., 2018).

constrain the amount of mass loss during the HeMS phase. The Wolf-Rayet winds must then not remove more than the difference between this maximum mass and the final BH mass. We refer to this as the “ $M_{\text{HeMS}} \leq M_{\text{HeMS,max}}$ ” condition.

The maximum He core mass plotted in figure 6.2 is very sensitive to the MS wind prescriptions (see discussion in Renzo et al. 2017; Neijssel et al. 2019; Miller-Jones et al. 2021). The analysis of the remnant mass from massive single stars is particularly sensitive to luminous blue variable winds (Belczynski et al., 2010; Miller-Jones et al., 2021), which can remove the hydrogen envelope of the star and hasten the onset of the Wolf-Rayet phase (Conti, 1975); therefore, increasing the potential remnant mass can be achieved by decreasing either luminous blue variable winds or Wolf-Rayet winds. The plot in figure 6.2 assumes the default COMPAS luminous-blue-variable mass-loss rate of $1.5 \times 10^{-4} M_\odot \text{ yr}^{-1}$ (Belczynski et al., 2010) for stars approaching the Humphreys-Davidson limit (Humphreys and Davidson, 1994). The convective overshooting parameter employed in stellar evolution calculations is another source of uncertainty, with greater overshooting leading to larger cores (Brott et al., 2011). To explore the impact of convective overshooting, we simulated the He core mass at terminal-age MS for stars with different metallicities starting from a zero-age MS mass of $150 M_\odot$ using the stellar evolution code MESA (v12115, Paxton et al. 2011). We find that varying the overshooting parameter by an order of

magnitude between $f = 0.02$ and $f = 0.2$ (Qin et al. 2019 used $f = 0.11$) with the step overshoot scheme changes the He core mass at terminal-age MS by between 1% and 13% for the range of metallicities in figure 6.2. Finally, the COMPAS single stellar evolution models are based on the fitting formulae of Hurley et al. (2000) to the evolutionary tracks of Pols et al. (1998) which involve extrapolations to higher masses than those covered by the initial range of models, and may under-estimate the He core masses of massive stars. We therefore use the following additional constraint, which bypasses these sources of uncertainty in the maximum He core mass.

In our assumed channel the secondary MS companion must not overflow its Roche lobe onto the HeMS primary. We write this constraint as (Eggleton, 1983)

$$R_2(t) \leq a(t) \frac{0.49q^{2/3}(t)}{0.6q^{2/3}(t) + \ln(1 + q^{1/3}(t))}, \quad (6.2)$$

where $m_2(t)$ and $R_2(t)$ are the mass and radius of the companion as a function of time, $m_1(t)$ the mass of the BH or its progenitor, $q(t) = \frac{m_2(t)}{m_1(t)}$, is the mass ratio, and $a(t)$ the orbital separation of the binary.

The orbital separation widens due to wind mass loss. In the limit of fast, non-interacting winds, the widening is described by

$$\frac{\dot{a}}{a} = -\frac{\dot{M}_{\text{tot}}}{M_{\text{tot}}}, \quad (6.3)$$

where $M_{\text{tot}} = m_1 + m_2$ is the total mass of the system. Because winds widen the binary and remove mass from the HeMS primary faster than from its MS companion, they increase the size of the secondary’s Roche lobe over time. Thus, even though the secondary is not overflowing its Roche lobe now, it may have done so in the past if the mass-loss rate was high. If we evolve the system back in time, the requirement that the secondary never overflows its Roche lobe imposes an alternative upper limit (Axelsson et al., 2011) on the maximum Wolf-Rayet wind mass-loss rate. We refer to this as the “*no Roche-lobe overflow (RLOF)*” condition. Although the non-interacting wind assumption, describing the widening of the binary (Equation

6.3), may be an over-simplification for such short-period systems (MacLeod and Loeb, 2020), it allows us to conservatively estimate the constraints imposed by the existence of Cygnus X-1 and presented below.

We parametrise the mass-loss rate through Wolf-Rayet winds, modelled with the prescription proposed by Belczynski et al. (2010) and based on (Hamann et al., 1995; Hamann and Koesterke, 1998; Belczynski et al., 2010), with a multiplicative parameter f_{WR} , following Barrett et al. (2018b) (see Appendix 6.A for a definition and discussion). We constrain the allowed parameter space of the wind strength by rewinding the evolution of the binary from the current state. Because the BH formed recently in our model, we set the luminosity and temperature of the MS companion at the end of the HeMS phase of the primary equal to the current inferred luminosity and temperature of the observed MS secondary. The mass and age of the secondary inferred from temperature and luminosity vary slightly for different metallicities. As we argued earlier, the BH is expected to lose negligible mass during collapse, so we set the mass of the HeMS primary at the end of that phase equal to the inferred BH mass. We assume that the secondary was 99.7% Roche-lobe filling at the end of the primary’s HeMS phase (Miller-Jones et al., 2021)¹.

The reverse evolution of the MS and HeMS stars is followed using the analytic fits to the stellar tracks of Pols et al. (1998) as presented in Hurley et al. (2000). The winds of the MS star are given by Vink et al. (2001). The HeMS winds are parametrised with the multiplicative factor f_{WR} as described above and in Appendix 6.A. The orbital response to mass loss is given by Eq. (6.3). We go back in the evolution for a HeMS lifetime (note that the HeMS lifetime depends on how massive the HeMS star initially was, which depends on the wind strength we assume) and check that the $M_{\text{HeMS}} \leq M_{\text{HeMS,max}}$ condition is satisfied at the start of the HeMS

¹In Miller-Jones et al. (2021) the Roche-lobe filling factor is defined as the ratio between the distance from the center of the star to the point where the equipotential surface enclosing the volume of the star crosses the axis connecting the star to its BH companion, and the distance from the center of the star to the L1 Lagrange point. In this paper, we define the Roche-lobe filling factor as the ratio between the radius of the star and the volume-equivalent Roche-Lobe radius of Eggleton (1983). We therefore convert the median and one- σ lower bounds of 0.96 and 0.93 reported in table 1 of Miller-Jones et al. (2021) to values of 0.997 and 0.99, respectively, that we use here.

phase and the *no RLOF* condition is satisfied throughout this phase.

Figure 6.3 shows the upper limits on the wind strength, parametrized as f_{WR} , imposed by these two conditions as a function of metallicity. Both conditions show that the wind strength has to be reduced from the nominal value $f_{\text{WR}} = 1$ throughout the range of metallicities we have explored. The strongest constraint is placed by the $M_{\text{HeMS}} \leq M_{\text{HeMS,max}}$ condition, which is subject to uncertainties in the MS wind strengths, overshooting, and the single stellar evolution fits of Hurley et al. (2000). This yields an upper limit $f_{\text{WR}} \lesssim 0.4$ at $Z = 0.01$ and $\lesssim 0.05$ at $Z = 0.03$. However, even if we lift this constraint, the *no RLOF* condition still places a strong constraint on the allowed mass loss rate: $f_{\text{WR}} \lesssim 0.45$ at $Z = 0.01$ and $\lesssim 0.15$ at $Z = 0.03$. We also explore the impact of BH mass and Roche-lobe filling factor measurement uncertainties and find that the constraints on f_{WR} change by $\lesssim 0.1$ over the range consistent with observations (Miller-Jones et al., 2021).

6.4 Cygnus X-1: Future evolution

The revised mass of the companion star in Cygnus X-1 makes it a potential candidate for a future BH and raises the intriguing prospect that this system could form a merging binary BH, connecting HMXBs with gravitational-wave sources. We model the future evolution of the system and find that it is unlikely to form a merging binary BH.

Belczynski et al. (2011) used earlier, lower estimates of the mass of the BH and companion in Cygnus X-1 in order to analyse the future evolution of this system. They predicted that imminent mass transfer from the nearly Roche-lobe filling companion will significantly reduce the companion mass, leaving behind a core that could only form a neutron star, not a BH. They further estimated that the natal kick has a 30% probability of unbinding the binary, and there was only a $\sim 1\%$ probability that the ensuing neutron star – black hole binary would merge within 14 Gyr through gravitational-wave emission.

Here we update their predictions based on revised observations, using the COMPAS

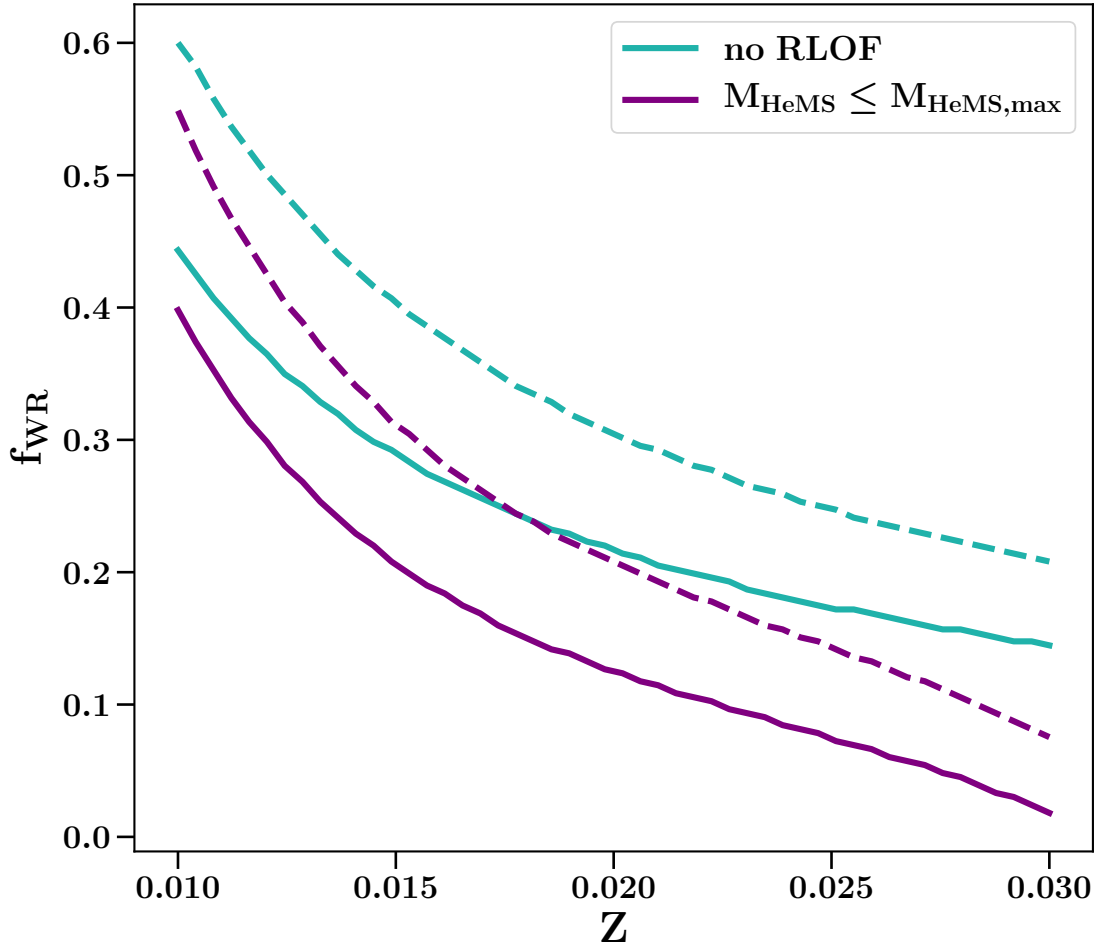


Figure 6.3: Upper limits on the parametrised Wolf-Rayet wind mass-loss rate from HeMS stars. The $M_{\text{HeMS}} \leq M_{\text{HeMS,max}}$ (purple) and *no RLOF* (teal) conditions only allow f_{WR} values below the curves at metallicity Z . The dashed curves correspond to assuming $M_{\text{BH}} = 19.2M_{\odot}$ and the current companion Roche-filling factor of 0.990 rather than the default values of $21.2M_{\odot}$ and 0.997 (solid curves), and indicate the impact of observational uncertainty.

population-synthesis code (Stevenson et al., 2017; Vigna-Gómez et al., 2018) for binary evolution calculations. We estimate the initial masses and orbital separation as in Section 6.3. We assume a Roche lobe filling factor of 0.997 and a metallicity of $Z = 0.02$. The median values for the BH mass and the luminosity and temperature of the MS companion from Miller-Jones et al. (2021) then yield $M_{\text{BH}} = 21.2 M_{\odot}$, $M_{\text{opt}} = 38.9 M_{\odot}$, $a = 51.3 R_{\odot}$, and $\tau_{\text{MS}} = 0.81$, i.e., the MS companion is 81 per cent through its core-hydrogen-burning phase by time. Once the MS companion overflows its Roche lobe, the mass-transfer phase could brighten Cygnus X-1 up to close to its Eddington luminosity of a few $\times 10^{39}$ erg s $^{-1}$. Once the envelope is removed, the companion will appear as a Wolf-Rayet (WR) star in an HMXB in a phase lasting for $\sim 3 \times 10^5$ years. In the default model described below, we apply WR mass loss with $f_{\text{WR}} = 1$ to such a star.

If we follow a treatment similar to Belczynski et al. (2011), in which the He core mass is determined by the mass of the star at the end of MS (after stripping in this case), we find the companion will collapse into a neutron star. Even if the binary survives the neutron star natal kick, which happens in 7% of all binaries in our models, it will generally be too wide to merge through gravitational-wave emission, with only a 0.12% probability that it will merge in 14 Gyr, similar to the findings of Belczynski et al. (2011). During this time, it may be detectable in radio pulsar surveys as a neutron-star – black-hole binary, although the non-recycled pulsar will likely only be observable as a radio source for a few tens of Myr. However, this treatment may significantly under-predict the core masses of stars that donated mass on the MS.

In our revised model, we address the potentially under-estimated core mass of stripped MS donors under the assumption that this core mass is determined only by the mass of the star at the end of the MS. We account for the substantial amount of helium synthesized by the companion before interaction with the following crude approximation. We consider a constant rate of helium production during the MS, so the mass of helium produced is $M_{\text{He,MS}} = \tau_{\text{MS}} M_{\text{c,final}}$, where $M_{\text{c,final}}$ is the final

helium core mass that would be achieved at the end of the MS phase for the given stellar mass, in the absence of mass transfer. Keeping track of the helium mass synthesized before stripping, $M_{\text{He,MS}}$, leads to higher core masses at the end of the MS phase.

With this correction, we predict that in the absence of BH natal kicks, Cygnus X-1 will become a bound binary BH, but one that is too wide to merge within 14 Gyr. If we incorporate the COMPAS prescription for BH kicks based on the “delayed” model of Fryer et al. (2012), this changes to a 38% probability of surviving the kick and forming a bound binary BH, with a 4% probability that this binary will merge within 14 Gyr through gravitational-wave emission due to a fortuitous kick. However, the kick prescription for low-mass black holes that do not undergo complete fallback (Fryer et al., 2012) is rather uncertain, with conflicting evidence on the natal kick magnitudes of low-mass BHs (Repetto et al., 2017; Mandel, 2016; Mirabel, 2017; Wyrzykowski and Mandel, 2019; Atri et al., 2019).

We also consider the impact of varying WR mass loss. Motivated by the results reported in figure 6.3 for $Z = 0.02$, we reduce f_{WR} to 0.2 from the value of 1 considered above. This increases the remnant mass of the current optical companion from $\sim 2.9 M_{\odot}$ to $\sim 5.7 M_{\odot}$, and the binary’s probability of remaining bound after the supernova from 38% to 62%. With our adjusted prescription for the helium core mass of the stripped companion and $f_{\text{WR}} = 0.2$, Cygnus X-1 has a 5% probability to merge within 14 Gyr as a binary BH.

We thus find that it is possible that a small fraction of HMXBs like Cygnus X-1 could form merging binary BHs, although this conclusion is sensitive to the treatment of mass transfer from MS donors in population-synthesis models and to the natal kick distribution of relatively low-mass BHs. If systems like Cygnus X-1 do become progenitors of gravitational-wave events, this would impact the modelled spin distribution of merging binary black holes, which predict that binary black hole mergers most likely have low effective spins (Kushnir et al., 2016; Zaldarriaga et al., 2018; Belczynski et al., 2017; Fuller and Ma, 2019; Bavera et al.,

2020). Gravitational-wave observations could ultimately address this possibility by resolving the spin distribution with more events (e.g., Farr et al., 2017). Meanwhile, wide, non-merging binary BHs could potentially be observable through microlensing (Eilbott et al., 2017).

6.5 Cygnus X-1: Caveats and conundrums

We show that the current properties of the Cygnus X-1 system imply a reduction in Wolf-Rayet wind mass-loss rates for exposed HeMS stars. These results depend on several key assumptions.

We assumed that the optical companion did not experience Roche lobe overflow in its past. This assumption is consistent with the challenge of detaching from mass transfer once it commences given that the companion has roughly twice the mass of the BH, as explained in section 6.2.4. However, it is somewhat surprising that several HMXBs with well measured properties – Cygnus X-1, LMC X-1 and M33 X-7 – share not only a high BH spin, but also a similar evolutionary state. Selection effects favour observing bright, long-lived systems, i.e., those with massive main-sequence donors that are close to Roche lobe filling (enabling more efficient accretion). There may also be an evolutionary stalling point, increasing the number of systems in this phase.

The latter scenario could indicate that the systems do manage to detach and resume mass transfer multiple times. While this would negate our wind mass-loss rate conclusions, it would imply that much less angular momentum is carried away during non-conservative mass transfer onto a BH than we expected. Assuming non-conservative mass transfer (valid if accretion onto a BH is Eddington-limited) from a donor that is twice as massive as the accretor, the specific angular momentum of the material ejected from the binary in units of the binary’s specific orbital angular momentum must be $\gamma < 0.85$ in order to avoid a decrease in the size of the Roche lobe (see Eq. 6.1 for the change in orbital separation). For comparison, isotropic re-emission from the BH corresponds to $\gamma = 2$. Conversely, if $\gamma = 2$, the companion

could still disengage from mass transfer if its radius shrinks faster than the size of the Roche lobe in response to mass loss. This would require the adiabatic logarithmic derivative of radius with respect to mass to exceed $\zeta \equiv d \log R / d \log M > 1.54$, which may be possible for stars in the late phase of their MS evolution that have already lost some mass.

It is also possible that the primary is not fully stripped during the mass transfer episode, but retains about $\sim 0.1 M_{\odot}$ of its hydrogen envelope (e.g. Yoon et al., 2010; Yoon, 2017; Bersten et al., 2014; Götberg et al., 2017, 2018; Laplace et al., 2020). The changed surface abundance could lead to reduced mass-loss rates until the remaining hydrogen is completely removed. However, it is not clear whether retaining an envelope of a fraction of a solar mass could be sufficient to prevent Wolf-Rayet-like winds. In any case, whether Wolf-Rayet wind mass-loss rates must be lower than anticipated or whether stars that experience mass transfer in binaries are only partially stripped, the impact on binary evolution is similar: there is less mass loss than previously assumed. In fact, our Wolf-Rayet wind reduction factors can be broadly interpreted as constraints on winds from stripped stars, whether they are naked helium stars or retain a small hydrogen-rich envelope.

Naked helium cores can expand significantly in the last stages of their lives, potentially leading to another mass-transfer episode from the BH progenitor late in the evolution. However, the degree of expansion is very mild for stars with initial masses $\gtrsim 20 M_{\odot}$ at near-solar metallicities (Yoon et al., 2010; Hirai, 2017; Laplace et al., 2020), so Cygnus X-1 is unlikely to have experienced such a mass-transfer episode.

As a consequence of its mass-accretion history, the secondary may be over-luminous relative to single stars of the same total mass (Dray and Tout, 2007, but see Hellings 1983, who concludes that they MS accretors quickly return to single-star models, and Braun and Langer 1995, who reach the opposite conclusion and find that accretors are under-luminous). Since we use single star evolutionary tracks to estimate the properties of the secondary star, this can affect our wind constraint

from the no-RLOF condition. However, since we choose a stellar model that matches the observed radius of the secondary at the present day, we do not anticipate the impact to be significant.

Finally, as figure 6.3 shows, the level of reduction in the winds is sensitive to the assumed metallicity of Cygnus X-1. We now discuss this in more detail.

Shimanskii et al. (2012) report that helium, carbon, oxygen, aluminium, sulfur and iron are overabundant by $[X/H]=0.23\text{--}0.43$ dex compared to the solar values (Anders and Grevesse, 1989). Nitrogen, neon, and silicon have an even higher overabundance of $[X/H]=0.69\text{--}0.94$ dex. These values appear robust against variations due to orbital motion and Roche-lobe filling factors, although some hydrogen and helium lines are sensitive to variations in the wind (Shimanskii et al., 2012). As mentioned above, the observations of Shimanskii et al. (2012) suggest that the system formed at initial metallicity of $Z \approx 0.03$, although this differs from the inferred metallicity of $Z \approx 0.01$ based on observations of HD 227460 by Daflon et al. (2001).

Previous accretion from the BH progenitor could significantly alter the chemical profile on the surface of the companion. For example, the detailed models of Qin et al. (2019) predict the observed enhancement of companion nitrogen abundances as a consequence of late main-sequence mass transfer from the BH progenitor. In addition to direct accretion, which is expected to enhance helium and nitrogen abundances, the deposited angular momentum can lead to a dramatic spin-up of the MS star (e.g. Packet, 1981), although spin-up to near break-up frequencies may suppress subsequent accretion. The surface could then be enhanced by helium and CNO-elements due to rotational mixing (Meynet and Maeder, 2000; Heger and Langer, 2000; Przybilla et al., 2010). The rotational mixing might also make the star over-luminous compared to a non-rotating model (Langer, 1992). The optical companion is observed to be tidally locked at present, with an inferred ratio of the rotational to orbital frequency of 1.05 ± 0.10 Miller-Jones et al. (2021). Assuming a present-day rotational period of 5.6 days, the rotational frequency is a third of the Keplerian (break-up) frequency at the stellar equator. Alternatively, as discussed above and

contrary to the channel assumed in this work, the MS companion may have been partially stripped by mass transfer onto the BH or its progenitor after the initial mass transfer phase from the primary, revealing deeper layers of the star.

Although these mechanisms could be responsible for the overabundance of some of the elements, they have difficulty in explaining the overabundance of late stage burning elements such as silicon and iron. This implies that these elements were primordially enhanced or were deposited from the progenitor of the BH in the final stages of its evolution.

High primordial abundances imply that both stars in the binary had a high metallicity at birth, which therefore requires a very strong reduction in the mass-loss rate (a factor of ~ 10) following the constraints described in section 6.3. On the other hand, a weak explosion induced by the collapse of the core can lead to an ejection of a small fraction of the outer part of the envelope at very low velocities. Because most of the envelope is assumed to fall back into the BH, the ejected material will be barely above the escape velocity, and could be efficiently accreted by the companion in a RLOF-like manner. If the heavy elements synthesized at the centre are efficiently mixed up to the outer regions before the inner slower material starts falling back, these elements can accrete onto the surface of the secondary. Such efficient mixing of heavy elements has been observed in supernovae such as SN1987A and Cassiopeia A (e.g. Utrobin et al., 1995; Fesen et al., 2006), and has been reproduced in 3D supernova explosion simulations (e.g. Hammer et al., 2010; Wongwathanarat et al., 2015, 2017), while Liu et al. (2015); Hirai et al. (2018) explore the contamination of a MS companion by supernova ejecta. However, it is not clear whether similar degrees of mixing can be induced in failed supernovae that form BHs rather than neutron stars, and the abundance pattern of the Cygnus X-1 companion merits further investigation.

Regardless of whether we assume that the observed companion metallicity of $Z = 0.03$ (Shimanskii et al., 2012) is primordial, or use the lower metallicity of $Z = 0.01$ based on HD 227460 (Daflon et al., 2001), we conclude that the observed

properties of Cygnus X-1 require a reduction in Wolf-Rayet winds to $\sim 5\text{--}40\%$ of their previously assumed values in the context of our assumed evolutionary channel.

Recent theoretical modelling of mass loss from stripped stars (Vink, 2017; Sander et al., 2020; Sander and Vink, 2020) points to reduced mass-loss rates compared to earlier literature. Moreover, these models suggest a steep dependence on the Eddington factor, which can change significantly during the lifetime of the stripped star. This indicates that extrapolating the empirical Wolf-Rayet mass-loss rates to the entire duration of the stripped star life is misleading. Our results are qualitatively consistent with these findings. The reduced mass-loss rates could also be attributed to strong wind clumping, which is expected to occur in line-driven winds due to radiative instabilities (Owocki et al., 1988; Sundqvist et al., 2018). Clumping of winds has been indirectly observed for massive MS stars in X-ray binaries (El Mellah et al., 2018; Lomaeva et al., 2020) and stripped stars may also experience high degrees of clumping.

We further find that HMXBs like Cygnus X-1 form through a different evolutionary channel than the bulk of merging binary black holes (see, e.g., Mandel and Farmer, 2018, for a review). However, a fortuitous natal kick accompanying the birth of the secondary BH could lead Cygnus X-1 to merge as a BH binary within 14 Gyr. Gravitational-wave observations may be able to constrain the contribution of this channel to the formation of merging binary BHs through spin measurements.

Acknowledgements

Simulations in this paper made use of the COMPAS rapid binary population-synthesis code, which is freely available at <http://github.com/TeamCOMPAS/COMPAS>. We thank Alexander Heger, Hagai Perets, Jerry Orosz, Stephen Justham, Selma de Mink and Jakub Klencki for discussions, and Robert Izzard and Silvia Toonen for comments on a preliminary draft of the manuscript. C. J. N. thanks the University of Birmingham for financial support. JCAM-J and IM are recipients of Australian Research Council Future Fellowships (FT140101082 and FT190100574, respectively).

AVG acknowledges funding support by the Danish National Research Foundation (DNRF132).

6.A Wind mass-loss rate for stripped stars

In this appendix, we describe the particular parametrized formalism we used to model wind-driven mass loss from stripped stars. While more recent theoretical models are available (e.g., Vink, 2017; Sander et al., 2020), this provides us with a convenient framework for investigating the empirical constraints placed by Cygnus X-1.

Hamann et al. (1995) formulated a prescription for the wind mass-loss rate for stripped or Wolf-Rayet stars as a function of the mass and luminosity of the stripped star. Hamann and Koesterke (1998) expanded on this work by reducing winds by a factor of \sqrt{D} where D is the wind clumping factor (Moffat et al., 1988; Nugis et al., 1998). Vink and de Koter (2005) further introduced a metallicity dependence to the winds. Combining the effects of clumping and metallicity leads to the prescription

$$(dM/dt)_{\text{WR}} = \underbrace{\frac{1}{\sqrt{D}} 10^{-11.95}}_1 \underbrace{\frac{L}{L_{\odot}}^{1.5} \frac{Z}{Z_{\odot}}^{0.86}}_2 \text{M}_{\odot} \text{yr}^{-1}, \quad (6.4)$$

where term 1 is the result of Hamann et al. (1995); Hamann and Koesterke (1998) and term 2 is from Vink and de Koter (2005). Setting $D = 100$, i.e., reducing wind mass-loss rates by a factor of 10, recovers Eq.(9) of Belczynski et al. (2010) and is consistent with the winds of Yoon et al. (2010).

We follow Barrett et al. (2018b) in scaling the prescription of Belczynski et al. (2010) by a multiplicative factor f_{WR} in order to parametrise the uncertainty in the wind mass-loss rates:

$$(dM/dt)_{\text{WR}} = f_{\text{WR}} \times 10^{-13} \frac{L}{L_{\odot}}^{1.5} \frac{Z}{Z_{\odot}}^{0.86} \text{M}_{\odot} \text{yr}^{-1}. \quad (6.5)$$

Note that this is not the same f_{WR} as used in Yoon et al. (2010) because ours already assumes a reduction of the original wind prescription of Hamann et al. (1995). The default assumption of $f_{\text{WR}} = 1$ corresponds to the default models of Belczynski et al. (2010); Yoon et al. (2010); Stevenson et al. (2017); Qin et al. (2019).

It is challenging to interpret our constraints on f_{WR} in terms of a wind clumping factor D . A direct interpretation of $f_{\text{WR}} = 0.2$ would imply a clumping factor of $D = 2500$ in the model of Eq. (6.4). Nugis et al. (1998); Nugis and Lamers (2000) used a clumping factor ranging from 10 to 30; D could be as high as 16 according to Hamann and Koesterke (1998). More recent theoretical models by Sander et al. (2017) use depth-dependent clumping factors and suggest a maximum value at infinity of $D_{\infty} = 10$ to be consistent with observations of electron-scattering wings. In later works however, Sander et al. (2020) and Sander and Vink (2020) propose 50 as a maximum upper limit for D_{∞} , by comparison with previous theoretical works (Gräfener and Hamann, 2005) and O/B star analyses (e.g. Bouret et al., 2012; Mahy et al., 2015). A clumping factor of 2500 seems extra-ordinary compared to previous models. As mentioned in the Section 6.5, additional constraints on the clumpiness of stellar winds from massive stars can be obtained from X-ray binaries (e.g. Lomaeva et al., 2020; El Mellah et al., 2018; Grinberg et al., 2017).

In light of the above, our reduction of f_{WR} is probably best interpreted as an overall constraint on mass loss from massive stripped stars (Vink, 2017), perhaps indicating a different dependence on metallicity or luminosity (cf. Sander et al., 2020; Sander and Vink, 2020), rather than a specific change in the clumping.

6.B Cygnus X-1 : Constraints on wind mass-loss rates assuming single stellar evolution

The BH-mass in of Cygnus X-1 can be used to constrain the wind mass-loss rates of massive stars using a set of assumptions. The main assumptions are; i) the remnant mass is solely determined by single stellar evolution; ii) our stellar evolutionary tracks are correct (Pols et al., 1998; Hurley et al., 2000); iii) the BH-mass is the maximum possible mass at the observed metallicity; iv) our remnant mass prescription is correct (Fryer et al., 2012).

We use the COMPAS population-synthesis code (Stevenson et al., 2017) to evolve

a population of single stars based on the analytic fits of Hurley et al. (2000). For the remnant mass distribution we adopt the “delayed” prescription by Fryer et al. (2012), although at high initial stellar masses there is no difference with the “rapid” mechanism of Fryer et al. (2012). Given the aim and the similarity of our prescriptions we are reproducing/updating the work done in Belczynski et al. (2010), on which our current wind mass-loss prescriptions are based.

For stars above $\approx 40 M_{\odot}$ the most dominant wind mass-loss rates are the luminous blue variable (LBV)-winds and the WR-winds. The wind mass-loss rates are defined as (Belczynski et al., 2010):

$$(dM/dt)_{\text{LBV}} = f_{\text{LBV}} \times 10^{-4} M_{\odot} \text{ yr}^{-1} \quad (6.6)$$

and

$$(dM/dt)_{\text{WR}} = f_{\text{WR}} \times 10^{-13} L^{1.5} \frac{Z}{Z_{\odot}}^{0.86} M_{\odot} \text{ yr}^{-1}. \quad (6.7)$$

Belczynski et al. (2010) show that both a change in f_{LBV} or WR-wind prescription (using a reduced mass-loss rate $(dM/dt)_{\text{WR}}$ by Nugis and Lamers (2000)) can increase the BH mass. Instead of changing between different prescriptions for $(dM/dt)_{\text{WR}}$ we opt to scale our prescription by f_{LBV} . Using this we run a two-dimensional grid of single stars to look at the combined parameter-space of f_{LBV} and f_{WR} and the resulting remnant masses (see Fig. 6.4). We do this for a star with a zero-age main sequence (ZAMS) mass of $150 M_{\odot}$. We corroborate the findings of Belczynski et al. (2010) and show the degenerate parameter space of f_{LBV} and f_{WR} that can reproduce a BH mass of $20.32^{+2.36}_{-2.41} M_{\odot}$.

6.B.1 Uncertainties in f_{WR} and f_{LBV}

Figure 6.4 takes an agnostic approach to the uncertainty in wind mass-loss rates. As mentioned by Belczynski et al. (2010), the uncertainty in the LBV winds on which these prescriptions are based (Vink and de Koter, 2002) span an order of a magnitude

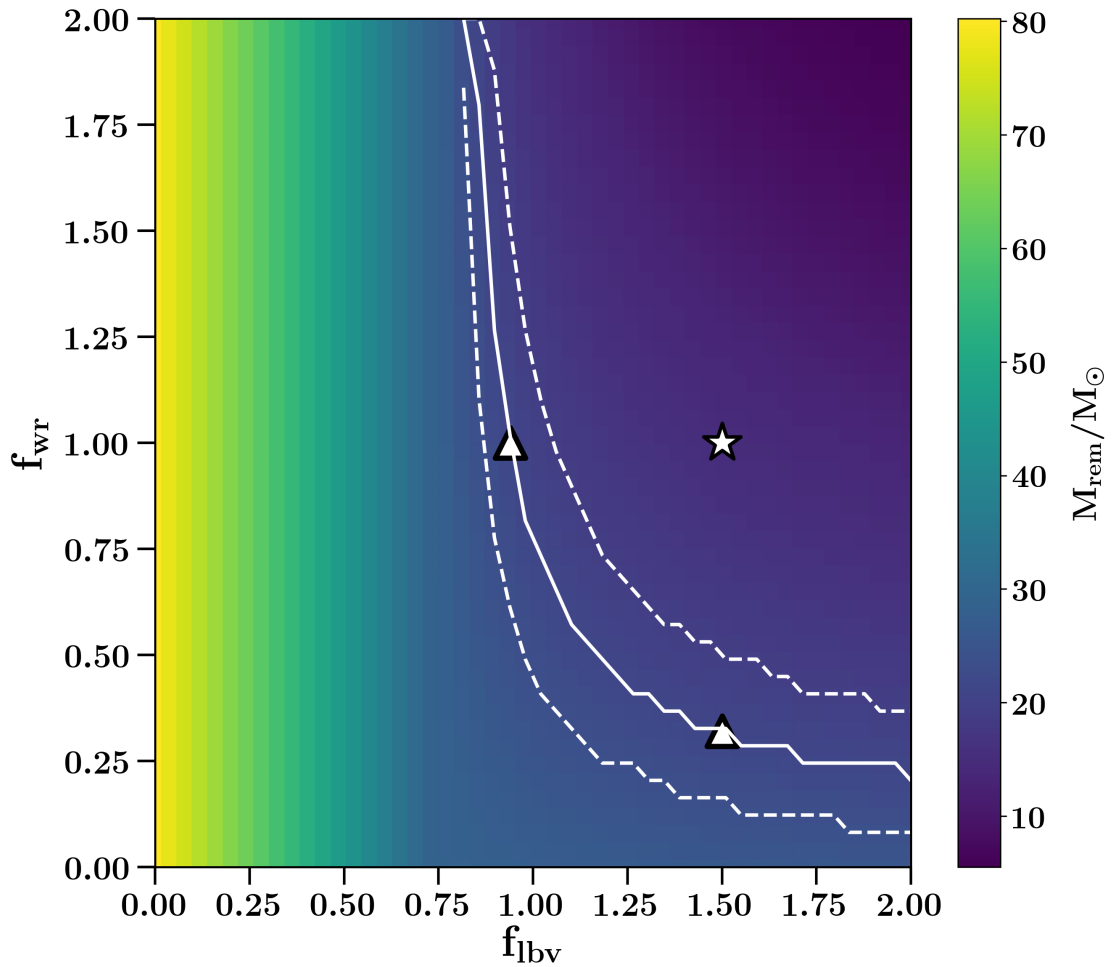


Figure 6.4: The remnant mass of a star born with $M = 150 M_{\odot}$ given a combination of f_{LBV} and f_{WR} . The solid and dashed line shows the BH-mass and its upper and lower limits of $20.32^{+2.36}_{-2.41} M_{\odot}$ as estimated by Miller-Jones et al. (2021). The star is our default assumption. The triangles show the combinations of f_{LBV} or f_{WR} (changing one parameter at a time relative to the default) which recover the observed BH mass.

($10^{-5} - 10^{-4}M_{\odot} \text{ yr}^{-1}$), where our default values are close to the upper limit. The WR-winds are partially based on the work by Hamann and Koesterke (1998), which includes the effects of clumping in the WR-winds. However the determination of, for example, the clump density enhancement, D , depends on the type of WR-star and is easily changed using other modeling parameters (Hamann and Koesterke, 1998). Our prescription is based on a clumping factor $D = 4$, but could be as high as 10 (Hamann and Koesterke, 1998; Crowther, 2007). This would drop the empirical established mass-loss rates by an additional factor $\sqrt{(10)}/\sqrt{(4)} = 1.5$ compared to our current values (Hamann and Koesterke, 1998). Hence our estimates for f_{LBV} and f_{WR} (see the triangles in Fig. 6.4) are still roughly consistent within the uncertainties of the prescription on which they are based and the same holds true for the degenerate parameter space between the triangles.

6.B.2 Effect on the entire remnant mass distribution

Even though f_{LBV} and f_{WR} can have a similar effect on the maximum BH mass for single stars, their effect on the entire remnant mass distribution differs. Figure 6.5 shows the remnant mass as a function of ZAMS mass for our default model and two variations (the triangles in Fig. 6.4). LBV-winds increases the maximum mass of the most massive stars ($M \gtrsim 50 M_{\odot}$). Self-stripping through wind mass loss happens already at lower masses and the effect of lowering the WR-winds affects stars as low as $30 M_{\odot}$. Therefore lowering the WR-winds might be more efficient in increasing the average BH mass at high metallicities. At lower metallicities the effects of winds are reduced. The WR-winds depends on metallicity whereas the LBV-wind does not (see eqs. 6.6 and 6.7). The WR-winds are reduced more and the LBV-winds are more efficient in increasing the BH mass for all stars.

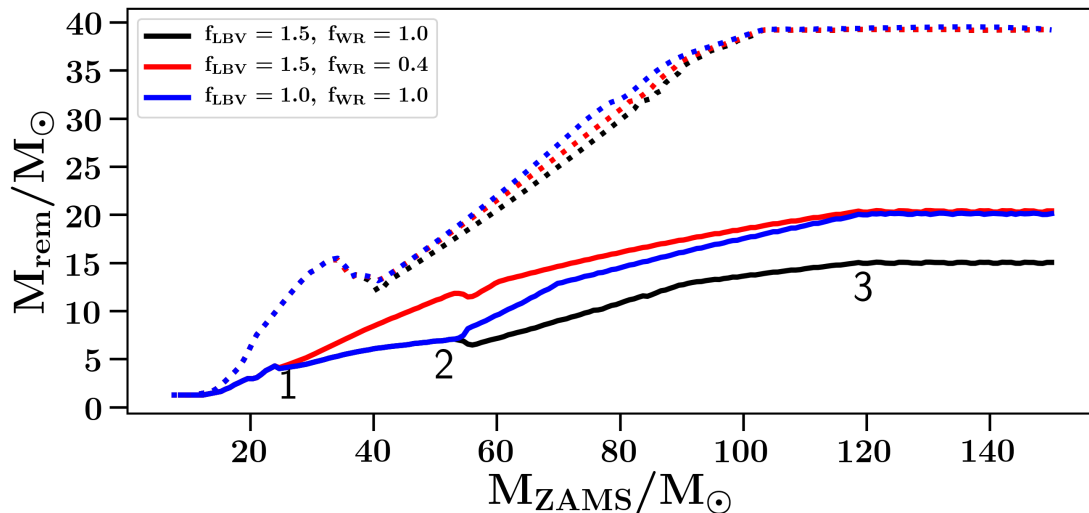


Figure 6.5: The remnant mass as a function of ZAMS mass for our default and two triangles in Fig. 6.4. The solid/dashed lines are for $Z = 0.02$ and $Z = 0.002$ respectively. The numbers indicates various masses from which the wind mass-loss prescriptions start to contribute. 1: Single stars are massive enough to ‘self-strip’ their envelopes through wind mass-loss becoming stripped stars with WR-winds. 2: Stars are massive enough to reach the Humphrey-Davidson post-MS. 3: Stars are massive enough to reach the Humphrey-Davidson during the MS limiting the maximum post-MS mass.

6.B.3 Additional variations

“LBV” winds on the MS

The flattening of the remnant mass spectrum at high initial masses is due to our application of LBV-winds on the MS (see Neijssel et al. (2019)). Their effect on the stellar cores is possibly artificial. Given the remnant mass distributions of Belczynski et al. (2010, 2019) we suspect they have a similar implementation. Without LBV-winds on the MS we have a continuous increase of remnant masses and could form BHs similar to Cygnus X-1 even at our current settings. For a more detailed investigation into LBV-winds and remnant masses see Giacobbo et al. (2018). At lower metallicities the remnant masses, in the absence of LBV-winds, are then quickly limited by (pulsational-)pair-instability-supernova (for our implementation see Stevenson et al. (2019)).

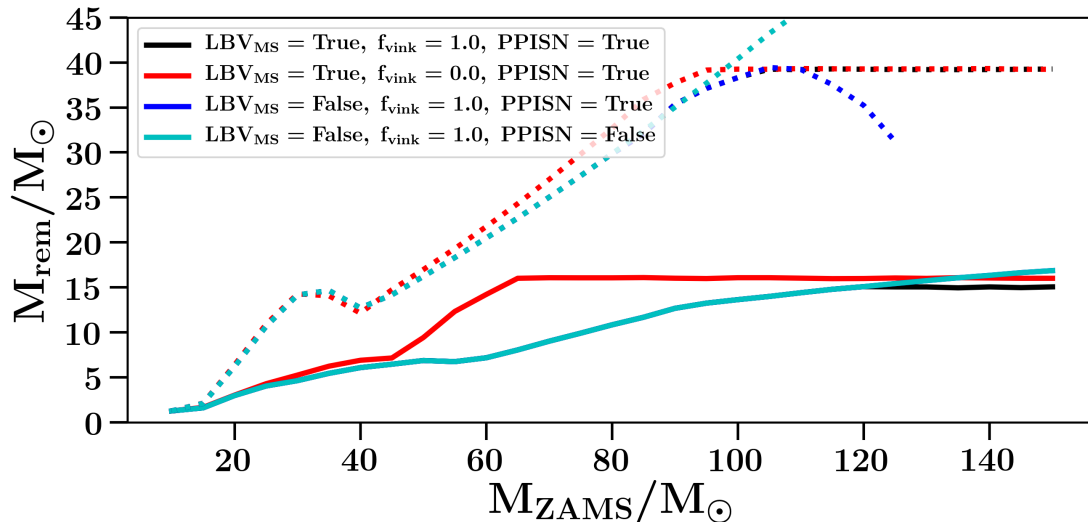


Figure 6.6: The remnant mass as a function of ZAMS mass for our default and different alternative variations. The solid/dashed lines are for $Z = 0.02$ and $Z = 0.002$ respectively. The turn-over for low metallicities is due to pulsational-pair-instability supernova which shed an increasing amount of mass at higher masses.

6.B.3.1 “Vink” winds

In principle one could also reduce all the wind mass-loss contributions including the MS-winds for hot stars by Vink and de Koter (2002). Belczynski et al. (2019) show the overall effect of reducing the combined winds in an attempt to recover a BH-mass of $70 M_{\odot}$. If we set the wind mass-loss rates of the MS winds from Vink and de Koter (2002) to zero, while keeping $f_{\text{LBV}} = 1.5$ and $f_{\text{WR}} = 1$, we can only raise the final BH-mass of a $150 M_{\odot}$ star to $\sim 18 M_{\odot}$. Therefore, an increase in remnant masses by reducing the combined winds is mostly due to f_{WR} and f_{LBV} and therefore LBV winds and WR winds remain the only winds we take into consideration.

6.B.4 Constraints on winds from single stellar evolution

We corroborate the findings on the effects of winds on remnant mass distributions such as presented in Belczynski et al. (2010); Giacobbo et al. (2018). We highlight that, within our models, the observed BH mass of Cygnus X-1 pushes for a reduction in winds. Both a lowering in Wolf-Rayet and the LBV winds can significantly increase our remnant masses at high metallicities, but they span a degenerate

parameter space. Furthermore, the findings are dependent on implementations especially those of the LBV-winds. Each choice of wind models at high metallicities has a distinct effect on the remnant mass distribution. These choices could propagate into remnant masses at lower metallicities and significantly affect predictions for gravitational-wave events for current and future detectors.

Chapter 7

Summary and Conclusion

In this dissertation we investigated the rates and property distributions of black hole binaries which merge within a Hubble time and are formed through isolated binary evolution. The rapid population-synthesis code `COMPAS` was used to simulate the evolution of large populations of massive stellar binaries under various assumptions. The general goal was to assess the impact of various uncertainties in the physics of massive stellar binaries on the rates and properties of double compact object (DCO) mergers and determine whether detections of gravitational waves, coming from merging DCO can provide significant constraints on the poorly constrained binary-star physics. What follows is a brief summary to the research presented in this dissertation. I end the dissertation with a personal view on the future of population synthesis.

Gravitational-wave mergers that are detected today could have originated from the very early universe. The results of chapter 4 show that the uncertainty in the metallicity-specific star formation rate over cosmological timescales affect our estimates on the rates and mass distributions DCO mergers. Rates vary by an order of magnitude between different model assumptions and even commonly used assumptions for the solar metallicity affect the rate by a factor ~ 3 . These uncertainties are of similar levels as those from binary-star physics such as natal kicks and common-envelop evolution (see amongs others Marassi et al., 2011; Dominik et al., 2012; Eldridge and Stanway, 2016; Kruckow et al., 2018; Chruslinska et al., 2018;

Vigna-Gómez et al., 2018). Therefore, to constrain binary-star physics one should simultaneously constrain the metallicity-specific star formation rate.

In order to aid future studies, a scaleable model for the metallicity-specific star formation rate is presented. This prescription is able to recover the various distinct models considered in chapter 4. Such a model might help future Bayesian approaches (similar to Barrett et al., 2017) to simultaneously constrain model parameters governing uncertainties in binary-star physics and metallicity-specific star formation rates.

In chapter 5 we discussed the impact of different prescriptions of the adiabatic response of stars to mass loss on rates of DCO mergers. Detailed stellar models (such as Ge et al., 2015; Pavlovskii et al., 2017) suggest that post-main sequence (MS) stars, with radiative envelopes, respond quicker to mass loss than previously expected. This increases the dynamical stability of mass transfer. The results of chapter 5 indicate that an increased dynamical stability of mass transfer started by post-MS stars, assuming the results of Ge et al. (2015), increases the merger rate of binary black holes by a factor of 3–4 (at a metallicity of $Z = 0.0045$). Furthermore, these merging binary black holes no longer experience a common-envelope evolution, which is a significant shift from the commonly assumed formation channel. However, the results presented in chapter 5 are only tentative. Larger simulations, including a wider range of metallicities, are needed. Furthermore, we only considered common envelopes due to dynamically-unstable mass transfer from the donor. A critical assessment needs to be done into common envelopes that come from contact binaries.

In chapter 6 the evolution of the X-ray binary Cygnus X-1 was discussed. Observations by Miller-Jones et al. (2021) estimate that the mass of the black hole (BH) in Cygnus X-1 is $21.2 M_{\odot}$, which is about $6 M_{\odot}$ more massive than previously assumed. Previously the mass of the BH was used to constrain wind mass-loss rates from Wolf-Rayet stars (Belczynski et al., 2010). Based on the formation channel by Qin et al. (2019), which could explain the high spin of the BH, we find that the Wolf-Rayet winds have to be reduced by a factor of 10 compared to Belczynski et al.

(2010), assuming the system formed at $Z = 0.02$. However, prior binary interactions could have resulted in a misinterpretation of the mass and metallicity of the companion and it remains uncertain if the formation channel adopted in chapter 6 is correct. This system will remain an interesting object for theorists, given the various peculiar properties of Cygnus X-1 such as the BH mass, the abundances of the companion and the tight orbital separation. The future evolution of Cygnus X-1 is also explored. The MS companion will start an episode of mass transfer onto the BH. The system has a low probability of forming a binary black hole merger. However, the estimates critically depend on the way in which mass transfer from massive main-sequence donors is treated.

Altogether this dissertation shows that uncertainties in almost every aspect of binary-star physics, including the initial distributions, vary the rate estimates of DCOs mergers by a factor of few or a lot more. It is unlikely that solely the detections of DCOs mergers through gravitational-waves will provide strong constraints on binary-star physics. However, it is certain that they add another interesting piece to the complex puzzle.

Personal view of the future

Rapid population-synthesis codes still offer a powerful platform to highlight areas of uncertainties in binary-star physics. Although some assumptions are simplistic, they provide an intuitive feel to the physics involved in massive stellar binaries. The simplistic analytic fits in population-synthesis codes could provide novel ways to backwards model systems without too many simplifying assumptions on the stellar physics, something which is currently substantially harder for detailed stellar evolution codes. Furthermore, the models remain relevant due to researchers making an extra effort to provide simple analytic recipes that approximate the results of their detailed models such as fits for the binding energies of the envelope (Xu and Li, 2010b; Loveridge et al., 2011), the adiabatic response of stars to mass loss (Ge et al., 2015) and temperature thresholds for convective envelopes (Klencki et al.,

2020).

At the same time care must be taken. There is a clear scientific bias towards innovation and implementation of new physics to explain recent observations. Such a bias is understandable since such theories and observations are directly challenging our understanding. Inspired by the results of population-synthesis codes, a lot of effort has gone into understanding the evolution of giants and stripped helium stars or peculiar supernova types. However, codes, like COMPAS, that rely on the stellar fits of Hurley et al. (2000) and Hurley et al. (2002) are already extrapolating beyond the range of the original stellar models by Pols et al. (1998). In chapter 4 and chapter 6 we show how the analytic fits of single stars without a distinct core, create possibly artificial results for mass-transferring systems. This could affect science cases such as, the maximum possible mass of black-holes, the formation of tight high-mass X-ray binaries and the formation of neutron star - black hole binaries. More effort must go into quantifying the impact of these features on previous results given the number of rapid population-synthesis codes that use similar stellar models. Solutions are being developed, with hybrid pipelines such as METISSE (Agrawal et al., 2020) enabling the rapid population-synthesis codes to implement new single stellar models based on detailed calculations.

In summary, I provide no fundamental proof for the physics involved with the evolution of massive stars in binary systems. However, I hope that my efforts helped in creating interesting methods and ideas for future studies.

Co-authorships

The work during my thesis resulted in me being a co-author on the following works: Stevenson et al. (2017); Barrett et al. (2018a,b); Vigna-Gómez et al. (2018); Bavera et al. (2019); Broekgaarden et al. (2019); Stevenson et al. (2019); Vinciguerra et al. (2019); Howitt et al. (2020); Vigna-Gómez et al. (2020); Lau et al. (2020); Vinciguerra et al. (2020); Miller-Jones et al. (2021). I am grateful to the authors for allowing me to be involved in their studies.

Bibliography

- Aasi, J., Abadie, J., Abbott, B., Abbott, R., Abbott, T., Abernathy, M., Accadia, T., Acernese, F., Adams, C., Adams, T., et al. (2016). Prospects for observing and localizing gravitational-wave transients with advanced ligo and advanced virgo. Living Reviews in Relativity, 19.
- Abate, C. (2019). What is the role of wind mass transfer in the progenitor evolution of Type Ia Supernovae? In Supernova Remnants: An Odyssey in Space after Stellar Death II, page 11.
- Abate, C., Pols, O. R., Izzard, R. G., Mohamed, S. S., and de Mink, S. E. (2013). Wind Roche-lobe overflow: Application to carbon-enhanced metal-poor stars. A&A, 552:A26.
- Abbott, B., Abbott, R., Abbott, T., Abernathy, M., Acernese, F., Ackley, K., Adams, C., Adams, T., Addesso, P., Adhikari, R., et al. (2016). Binary black hole mergers in the first advanced ligo observing run. Physical Review X, 6(4):041015.
- Abbott, B. P., Abbott, R., Abbott, T., Acernese, F., Ackley, K., Adams, C., Adams, T., Addesso, P., Adhikari, R., Adya, V., et al. (2017). Gw170817: observation of gravitational waves from a binary neutron star inspiral. Physical Review Letters, 119(16):161101.
- Abbott, B. P., Abbott, R., Abbott, T. D., Abernathy, M. R., Acernese, LIGO Scientific Collaboration, and Virgo Collaboration (2016a). GW151226: Observation of Gravitational Waves from a 22-Solar-Mass Binary Black Hole Coalescence. Phys. Rev. Lett., 116(24):241103.
- Abbott, B. P., Abbott, R., Abbott, T. D., Abernathy, M. R., Acernese, F., LIGO Scientific Collaboration, and Virgo Collaboration (2016b). Properties of the Binary Black Hole Merger GW150914. Phys. Rev. Lett., 116(24):241102.
- Abbott, B. P., Abbott, R., Abbott, T. D., Abraham, S., Acernese, F., Ackley, K., Adams, C., Adhikari, R. X., Adya, V. B., Affeldt, C., Agathos, M., Agatsuma, K., , LIGO Scientific Collaboration, and Virgo Collaboration (2020a). GW190425: Observation of a compact binary coalescence with total mass $\sim 3.4 m_{\odot}$. The Astrophysical Journal Letters, 892(1):L3.
- Abbott, B. P., Abbott, R., Abbott, T. D., Abraham, S., Acernese, F., Ackley, K., Adams, C., Adhikari, R. X., Adya, V. B., Affeldt, C., Agathos, M., Agatsuma, K., LIGO Scientific Collaboration, and Virgo Collaboration (2019). GWTC-1: A Gravitational-Wave Transient Catalog of Compact Binary Mergers Observed by LIGO and Virgo during the First and Second Observing Runs. Physical Review X, 9(3):031040.
- Abbott, B. P., Abbott, R., Abbott, T. D., Abraham, S., Acernese, F., Ackley, K., Adams, C., Adhikari, R. X., and et al. (2018a). Binary Black Hole Population Properties Inferred from the First and Second Observing Runs of Advanced LIGO and Advanced Virgo. ArXiv e-prints.
- Abbott, B. P., Abbott, R., Abbott, T. D., Abraham, S., Acernese, F., Ackley, K., Adams, C., Adhikari, R. X., and et al. (2018b). GWTC-1: A Gravitational-Wave Transient Catalog of Compact Binary Mergers Observed by LIGO and Virgo during the First and Second Observing Runs. ArXiv e-prints.
- Abbott, D. C. and Conti, P. S. (1987). Wolf-rayet stars. ARA&A, 25:113–150.

-
- Abbott, R., Abbott, T., Abraham, S., Acernese, F., Ackley, K., Adams, A., Adams, C., Adhikari, R., Adya, V., Affeldt, C., et al. (2021). Gwtc-2: compact binary coalescences observed by ligo and virgo during the first half of the third observing run. *Physical Review X*, 11(2):021053.
- Abbott, R., Abbott, T. D., Abraham, S., Acernese, F., Ackley, K., Adams, C., Adhikari, R. X., Adya, V. B., Affeldt, C., Agathos, M., Agatsuma, K., , LIGO Scientific Collaboration, and Virgo Collaboration (2020b). GW190814: Gravitational waves from the coalescence of a 23 solar mass black hole with a 2.6 solar mass compact object. *The Astrophysical Journal Letters*, 896(2):L44.
- Adams, S. M., Kochanek, C. S., Gerke, J. R., Stanek, K. Z., and Dai, X. (2017). The search for failed supernovae with the Large Binocular Telescope: confirmation of a disappearing star. *MNRAS*, 468(4):4968–4981.
- Ade, P. A., Aghanim, N., Arnaud, M., Ashdown, M., Aumont, J., Baccigalupi, C., Banday, A., Barreiro, R., Bartlett, J., Bartolo, N., et al. (2016). Planck 2015 results-xiii. cosmological parameters. *Astronomy & Astrophysics*, 594:A13.
- Agrawal, P., Hurley, J., Stevenson, S., Szécsi, D., and Flynn, C. (2020). The fates of massive stars: exploring uncertainties in stellar evolution with metisse. *Monthly Notices of the Royal Astronomical Society*, 497(4):4549–4564.
- Allan, A. P., Groh, J. H., Mehner, A., Smith, N., Boian, I., Farrell, E. J., and Andrews, J. E. (2020). The possible disappearance of a massive star in the low-metallicity galaxy PHL 293B. *Monthly Notices of the Royal Astronomical Society*, 496(2):1902–1908.
- Anders, E. and Grevesse, N. (1989). Abundances of the elements: Meteoritic and solar. *Geochim. Cosmochim. Acta*, 53(1):197–214.
- Arcavi, I., Howell, D. A., Kasen, D., Bildsten, L., Hosseinzadeh, G., McCully, C., Wong, Z. C., Katz, S. R., Gal-Yam, A., Sollerman, J., Taddia, F., Leloudas, G., Fremling, C., Nugent, P. E., Horesh, A., Mooley, K., Rumsey, C., Cenko, S. B., Graham, M. L., Perley, D. A., Nakar, E., Shaviv, N. J., Bromberg, O., Shen, K. J., Ofek, E. O., Cao, Y., Wang, X., Huang, F., Rui, L., Zhang, T., Li, W., Li, Z., Zhang, J., Valenti, S., Guevel, D., Shappee, B., Kochanek, C. S., Holoien, T. W. S., Filippenko, A. V., Fender, R., Nyholm, A., Yaron, O., Kasliwal, M. M., Sullivan, M., Blagorodnova, N., Walters, R. S., Lunnan, R., Khazov, D., Andreoni, I., Laher, R. R., Konidaris, N., Wozniak, P., and Bue, B. (2017). Energetic eruptions leading to a peculiar hydrogen-rich explosion of a massive star. *Nature*, 551(7679):210–213.
- Asplund, M., Grevesse, N., Sauval, A. J., and Scott, P. (2009). The Chemical Composition of the Sun. *ARA&A*, 47:481–522.
- Astropy Collaboration, Price-Whelan, A. M., Sipőcz, B. M., Günther, H. M., Lim, P. L., Crawford, S. M., Conseil, S., Shupe, D. L., Craig, M. W., Dencheva, N., Ginsburg, A., VanderPlas, J. T., Bradley, L. D., Pérez-Suárez, D., de Val-Borro, M., Aldcroft, T. L., Cruz, K. L., Robitaille, T. P., Tollerud, E. J., Ardelean, C., Babej, T., Bach, Y. P., Bachetti, M., Bakanov, A. V., Bamford, S. P., Barentsen, G., Barmby, P., Baumbach, A., Berry, K. L., Biscani, F., Boquien, M., Bostroem, K. A., Bouma, L. G., Brammer, G. B., Bray, E. M., Breytenbach, H., Buddelmeijer, H., Burke, D. J., Calderone, G., Cano Rodríguez, J. L., Cara, M., Cardoso, J. V. M., Cheedella, S., Copin, Y., Corrales, L., Crichton, D., D’Avella, D., Deil, C., Depagne, É., Dietrich, J. P., Donath, A., Droettboom, M., Earl, N., Erben,

-
- T., Fabbro, S., Ferreira, L. A., Finethy, T., Fox, R. T., Garrison, L. H., Gibbons, S. L. J., Goldstein, D. A., Gommers, R., Greco, J. P., Greenfield, P., Groener, A. M., Grollier, F., Hagen, A., Hirst, P., Homeier, D., Horton, A. J., Hosseinzadeh, G., Hu, L., Hunkeler, J. S., Ivezić, Ž., Jain, A., Jenness, T., Kanarek, G., Kendrew, S., Kern, N. S., Kerzendorf, W. E., Khvalko, A., King, J., Kirkby, D., Kulkarni, A. M., Kumar, A., Lee, A., Lenz, D., Littlefair, S. P., Ma, Z., Macleod, D. M., Mastropietro, M., McCully, C., Montagnac, S., Morris, B. M., Mueller, M., Mumford, S. J., Muna, D., Murphy, N. A., Nelson, S., Nguyen, G. H., Ninan, J. P., Nöthe, M., Ogaz, S., Oh, S., Parejko, J. K., Parley, N., Pascual, S., Patil, R., Patil, A. A., Plunkett, A. L., Prochaska, J. X., Rastogi, T., Reddy Janga, V., Sabater, J., Sakurikar, P., Seifert, M., Sherbert, L. E., Sherwood-Taylor, H., Shih, A. Y., Sick, J., Silbiger, M. T., Singanamalla, S., Singer, L. P., Sladen, P. H., Sooley, K. A., Sornarajah, S., Streicher, O., Teuben, P., Thomas, S. W., Tremblay, G. R., Turner, J. E. H., Terrón, V., van Kerkwijk, M. H., de la Vega, A., Watkins, L. L., Weaver, B. A., Whitmore, J. B., Woillez, J., Zabalza, V., and Astropy Contributors (2018). The Astropy Project: Building an Open-science Project and Status of the v2.0 Core Package. *AJ*, 156:123.
- Astropy Collaboration, Robitaille, T. P., Tollerud, E. J., Greenfield, P., Droettboom, M., Bray, E., Aldcroft, T., Davis, M., Ginsburg, A., Price-Whelan, A. M., Kerzendorf, W. E., Conley, A., Crighton, N., Barbary, K., Muna, D., Ferguson, H., Grollier, F., Parikh, M. M., Nair, P. H., Unther, H. M., Deil, C., Woillez, J., Conseil, S., Kramer, R., Turner, J. E. H., Singer, L., Fox, R., Weaver, B. A., Zabalza, V., Edwards, Z. I., Azalee Bostroem, K., Burke, D. J., Casey, A. R., Crawford, S. M., Dencheva, N., Ely, J., Jenness, T., Labrie, K., Lim, P. L., Pierfederici, F., Pontzen, A., Ptak, A., Refsdal, B., Servillat, M., and Streicher, O. (2013). Astropy: A community Python package for astronomy. *A&A*, 558:A33.
- Atri, P., Miller-Jones, J. C. A., Bahramian, A., Plotkin, R. M., Jonker, P. G., Nelemans, G., Maccarone, T. J., Sivakoff, G. R., Deller, A. T., Chaty, S., Torres, M. A. P., Horiuchi, S., McCallum, J., Natusch, T., Phillips, C. J., Stevens, J., and Weston, S. (2019). Potential kick velocity distribution of black hole X-ray binaries and implications for natal kicks. *MNRAS*, 489(3):3116–3134.
- Axelsson, M., Church, R. P., Davies, M. B., Levan, A. J., and Ryde, F. (2011). On the origin of black hole spin in high-mass black hole binaries: Cygnus X-1. *MNRAS*, 412(4):2260–2264.
- Babak, S., Taracchini, A., and Buonanno, A. (2017). Validating the effective-one-body model of spinning, precessing binary black holes against numerical relativity. *Phys. Rev. D*, 95(2):024010.
- Baldry, I., Glazebrook, K., and Driver, S. (2008). On the galaxy stellar mass function, the mass–metallicity relation and the implied baryonic mass function. *Monthly Notices of the Royal Astronomical Society*, 388(3):945–959.
- Bardeen, J. M., Carter, B., and Hawking, S. W. (1973). The four laws of black hole mechanics. *Communications in Mathematical Physics*, 31(2):161–170.
- Barrett, J. W., Gaebel, S. M., Neijssel, C. J., Vigna-Gómez, A., Stevenson, S., Berry, C. P. L., Farr, W. M., and Mandel, I. (2018a). Accuracy of inference on the physics of binary evolution from gravitational-wave observations. *MNRAS*, 477:4685–4695.
- Barrett, J. W., Gaebel, S. M., Neijssel, C. J., Vigna-Gómez, A., Stevenson, S., Berry, C. P. L., Farr, W. M., and Mandel, I. (2018b). Accuracy of inference on

-
- the physics of binary evolution from gravitational-wave observations. *MNRAS*, 477:4685–4695.
- Barrett, J. W., Mandel, I., Neijssel, C. J., Stevenson, S., and Vigna-Gómez, A. (2017). Exploring the Parameter Space of Compact Binary Population Synthesis. In Brescia, M., Djorgovski, S. G., Feigelson, E. D., Longo, G., and Cavuoti, S., editors, *Astroinformatics*, volume 325, pages 46–50.
- Baschek, B., Scholz, M., and Wehrse, R. (1991). The parameters r and t_{eff} in stellar models and observations. *Astronomy and Astrophysics*, 246:374–382.
- Batta, A. and Ramirez-Ruiz, E. (2019). Accretion Feedback from newly-formed black holes and its implications for LIGO Sources. *arXiv e-prints*, page arXiv:1904.04835.
- Batta, A., Ramirez-Ruiz, E., and Fryer, C. (2017). The Formation of Rapidly Rotating Black Holes in High-mass X-Ray Binaries. *ApJ*, 846(2):L15.
- Bavera, S. S., Fragos, T., Qin, Y., Zapartas, E., Neijssel, C. J., Mandel, I., Batta, A., Gaebel, S. M., Kimball, C., and Stevenson, S. (2020). The origin of spin in binary black holes. Predicting the distributions of the main observables of Advanced LIGO. *A&A*, 635:A97.
- Bavera, S. S., Fragos, T., Qin, Y., Zapartas, M., Neijssel, C. J., Mandel, I., Batta, A., Gaebel, S. M., Kimball, C., and Stevenson, S. (2019). The origin of the spin in binary black holes. *in prep*.
- Belczynski, K., Bulik, T., and Bailyn, C. (2011). The Fate of Cyg X-1: An Empirical Lower Limit on Black-hole-Neutron-star Merger Rate. *ApJ*, 742(1):L2.
- Belczynski, K., Bulik, T., Fryer, C. L., Ruiter, A., Valsecchi, F., Vink, J. S., and Hurley, J. R. (2010). On the Maximum Mass of Stellar Black Holes. *ApJ*, 714(2):1217–1226.
- Belczynski, K., Bulik, T., and Kalogera, V. (2002a). Merger Sites of Double Neutron Stars and Their Host Galaxies. *ApJ*, 571(2):L147–L150.
- Belczynski, K., Heger, A., Gladysz, W., Ruiter, A. J., Woosley, S., Wiktorowicz, G., Chen, H.-Y., Bulik, T., O’Shaughnessy, R., Holz, D. E., Fryer, C. L., and Berti, E. (2016). The effect of pair-instability mass loss on black-hole mergers. *A&A*, 594:A97.
- Belczynski, K., Hirschi, R., Kaiser, E. A., Liu, J., Casares, J., Lu, Y., O’Shaughnessy, R., Heger, A., and Justham, S. (2019). The Formation of a 70 Msun Black Hole at High Metallicity. *arXiv e-prints*, page arXiv:1911.12357.
- Belczynski, K., Holz, D. E., Bulik, T., and O’Shaughnessy, R. (2016). The first gravitational-wave source from the isolated evolution of two stars in the 40–100 solar mass range. *Nature*, 534(7608):512.
- Belczynski, K., Kalogera, V., and Bulik, T. (2002b). A Comprehensive Study of Binary Compact Objects as Gravitational Wave Sources: Evolutionary Channels, Rates, and Physical Properties. *ApJ*, 572(1):407–431.
- Belczynski, K., Kalogera, V., Rasio, F. A., Taam, R. E., Zezas, A., Bulik, T., Maccarone, T. J., and Ivanova, N. (2008). Compact Object Modeling with the StarTrack Population Synthesis Code. *ApJS*, 174(1):223–260.

-
- Belczynski, K., Klencki, J., Fields, C. E., Olejak, A., Berti, E., Meynet, G., Fryer, C. L., Holz, D. E., O’Shaughnessy, R., Brown, D. A., Bulik, T., Leung, S. C., Nomoto, K., Madau, P., Hirschi, R., Jones, S., Mondal, S., Chruslinska, M., Drozda, P., Gerosa, D., Doctor, Z., Giersz, M., Ekstrom, S., Georgy, C., Askar, A., Wysocki, D., Natan, T., Farr, W. M., Wiktorowicz, G., Miller, M. C., Farr, B., and Lasota, J. P. (2017). The evolutionary roads leading to low effective spins, high black hole masses, and O1/O2 rates of LIGO/Virgo binary black holes. arXiv e-prints, page arXiv:1706.07053.
- Belczynski, K., Perna, R., Bulik, T., Kalogera, V., Ivanova, N., and Lamb, D. Q. (2006). A Study of Compact Object Mergers as Short Gamma-Ray Burst Progenitors. ApJ, 648(2):1110–1116.
- Belczynski, K., Taam, R. E., Kalogera, V., Rasio, F. A., and Bulik, T. (2007). On the Rarity of Double Black Hole Binaries: Consequences for Gravitational Wave Detection. ApJ, 662(1):504–511.
- Belczynski, K., Taam, R. E., Kalogera, V., Rasio, F. A., and Bulik, T. (2007). On the rarity of double black hole binaries: Consequences for gravitational wave detection. The Astrophysical Journal, 662(1):504.
- Bersten, M. C., Benvenuto, O. G., Folatelli, G., Nomoto, K., Kuncarayakti, H., Srivastav, S., Anupama, G. C., Quimby, R., and Sahu, D. K. (2014). iPTF13bvn: The First Evidence of a Binary Progenitor for a Type Ib Supernova. AJ, 148(4):68.
- Bestenlehner, J. M., Gräfener, G., Vink, J. S., Najarro, F., de Koter, A., Sana, H., Evans, C. J., Crowther, P. A., Hénault-Brunet, V., Herrero, A., Langer, N., Schneider, F. R. N., Simón-Díaz, S., Taylor, W. D., and Walborn, N. R. (2014). The VLT-FLAMES Tarantula Survey. XVII. Physical and wind properties of massive stars at the top of the main sequence. A&A, 570:A38.
- Bethe, H. A. (1939). Energy Production in Stars. Physical Review, 55(5):434–456.
- Bethe, H. A. and Brown, G. (1998). Evolution of binary compact objects that merge. The Astrophysical Journal, 506(2):780.
- Bethe, H. A. and Critchfield, C. L. (1938). The Formation of Deuterons by Proton Combination. Physical Review, 54(4):248–254.
- Bisiaacchi, G. F., Dultzin, D., Firmani, C., and Hacyan, S. (1974). On the Interpretation of the he II λ 4686 Emission Line in HDE 226868 (cygnus X-1). ApJ, 190:L59.
- Blaauw, A. (1961). On the origin of the O- and B-type stars with high velocities (the “run-away” stars), and some related problems. Bull. Astron. Inst. Netherlands, 15:265.
- Blaauw, A. (1993). Massive Runaway Stars. In Cassinelli, J. P. and Churchwell, E. B., editors, Massive Stars: Their Lives in the Interstellar Medium, volume 35 of Astronomical Society of the Pacific Conference Series, page 207.
- Boco, L., Lapi, A., Goswami, S., Perrotta, F., Baccigalupi, C., and Danese, L. (2019). Merging Rates of Compact Binaries in Galaxies: Perspectives for Gravitational Wave Detections. ApJ, 881(2):157.
- Bolton, C. T. (1972). Identification of Cygnus X-1 with HDE 226868. Nature, 235(5336):271–273.

-
- Bolton, C. T. (1975). Orbital elements and an analysis of models for HDE 226868 = Cygnus X-1. *ApJ*, 200:269–277.
- Bondi, H. and Hoyle, F. (1944). On the mechanism of accretion by stars. *MNRAS*, 104:273.
- Bouret, J. C., Hillier, D. J., Lanz, T., and Fullerton, A. W. (2012). Properties of Galactic early-type O-supergiants. A combined FUV-UV and optical analysis. *A&A*, 544:A67.
- Bouwens, R. J., Illingworth, G. D., Franx, M., Chary, R. R., Meurer, G. R., Conselice, C. J., Ford, H., Giavalisco, M., and van Dokkum, P. (2009). UV Continuum Slope and Dust Obscuration from $z \sim 6$ to $z \sim 2$: The Star Formation Rate Density at High Redshift. *ApJ*, 705(1):936–961.
- Braun, H. and Langer, N. (1995). Effects of accretion onto massive main sequence stars. *A&A*, 297:483.
- Bressan, A., Marigo, P., Girardi, L., Salasnich, B., Dal Cero, C., Rubele, S., and Nanni, A. (2012). PARSEC: stellar tracks and isochrones with the PAdova and TRieste Stellar Evolution Code. *MNRAS*, 427(1):127–145.
- Broekgaarden, F. S., Berger, E., Neijssel, C. J., Vigna-Gómez, A., Chattopadhyay, D., Stevenson, S., Chruslinska, M., Justham, S., de Mink, S. E., and Mandel, I. (2021). Impact of Massive Binary Star and Cosmic Evolution on Gravitational Wave Observations I: Black Hole - Neutron Star Mergers. *arXiv e-prints*, page arXiv:2103.02608.
- Broekgaarden, F. S., Justham, S., de Mink, S. E., Gair, J., Mandel, I., Stevenson, S., Barrett, J. W., Vigna-Gómez, A., and Neijssel, C. J. (2019). STROOP-WAFEL: simulating rare outcomes from astrophysical populations, with application to gravitational-wave sources. *MNRAS*, 490(4):5228–5248.
- Brott, I., de Mink, S. E., Cantiello, M., Langer, N., de Koter, A., Evans, C. J., Hunter, I., Trundle, C., and Vink, J. S. (2011). Rotating massive main-sequence stars. I. Grids of evolutionary models and isochrones. *A&A*, 530:A115.
- Brown, G. E. (1995). Neutron star accretion and binary pulsar formation. *ApJ*, 440:270–279.
- Burrows, A. (2013). Colloquium: Perspectives on core-collapse supernova theory. *Reviews of Modern Physics*, 85(1):245–261.
- Cantiello, M., Mankovich, C., Bildsten, L., Christensen-Dalsgaard, J., and Paxton, B. (2014). Angular Momentum Transport within Evolved Low-mass Stars. *ApJ*, 788(1):93.
- Castor, J. I., Abbott, D. C., and Klein, R. I. (1975). Radiation-driven winds in Of stars. *ApJ*, 195:157–174.
- Chandrasekhar, S. (1939). *An introduction to the study of stellar structure*. The University of Chicago press.
- Chen, W.-C., Li, X.-D., and Qian, S.-B. (2006). Orbital evolution of algol binaries with a circumbinary disk. *The Astrophysical Journal*, 649(2):973–978.
- Chen, Z., Ivanova, N., and Carroll-Nellenback, J. (2020). A 3D Radiation Hydrodynamic AGB Binary Model. *ApJ*, 892(2):110.

-
- Chini, R., Barr, A., Buda, L. S., Dembsky, T., Drass, H., Nasser, A., Hoffmeister, V. H., and Fuhrmann, K. (2013). The Multiplicity of High-mass Stars. Central European Astrophysical Bulletin, 37:295–310.
- Chiosi, C. (1986). Effects of convective overshooting, mass loss (and chemical composition) across the HR diagram. In De Loore, C. W. H., Willis, A. J., and Laskarides, P., editors, Luminous Stars and Associations in Galaxies, volume 116, pages 317–338.
- Chruslinska, M., Belczynski, K., Klencki, J., and Benacquista, M. (2018). Double neutron stars: merger rates revisited. MNRAS, 474(3):2937–2958.
- Chruslinska, M. and Nelemans, G. (2019). Metallicity of stars formed throughout the cosmic history based on the observational properties of star-forming galaxies. MNRAS, 488(4):5300–5326.
- Chruslinska, M., Nelemans, G., and Belczynski, K. (2018). The influence of the distribution of cosmic star formation at different metallicities on the properties of merging double compact objects. Monthly Notices of the Royal Astronomical Society.
- Conti, P. S. (1975). On the relationship between Of and WR stars. Memoires of the Societe Royale des Sciences de Liege, 9:193–212.
- Conti, P. S. (1978). Stellar parameters of five early type companions of X-ray sources. A&A, 63:225–235.
- Crawford, J. A. (1955). On the Subgiant Components of Eclipsing Binary Systems. ApJ, 121:71.
- Crowther, P. A. (2007). Physical Properties of Wolf-Rayet Stars. ARA&A, 45(1):177–219.
- Daflon, S., Cunha, K., Becker, S. R., and Smith, V. V. (2001). Chemical Abundances of OB Stars in Five OB Associations. ApJ, 552(1):309–320.
- Darwin, G. H. (1879). On the Bodily Tides of Viscous and Semi-Elastic Spheroids, and on the Ocean Tides upon a Yielding Nucleus. Philosophical Transactions of the Royal Society of London Series I, 170:1–35.
- Davidson, K. and Ostriker, J. P. (1973). Neutron-Star Accretion in a Stellar Wind: Model for a Pulsed X-Ray Source. ApJ, 179:585–598.
- De Donder, E. and Vanbeveren, D. (1999). The effect of close binary evolution on the chemical enrichment of galaxies. In van der Hucht, K. A., Koenigsberger, G., and Eenens, P. R. J., editors, Wolf-Rayet Phenomena in Massive Stars and Starburst Galaxies, volume 193, page 738.
- de Kool, M. (1990). Common envelope evolution and double cores of planetary nebulae. ApJ, 358:189–195.
- De Loore, C., De Greve, J. P., and de Cuyper, J. P. (1975). Evolution of massive close binaries. II - The POST X-ray binary stage: Origin of run-away and binary pulsars. Ap&SS, 36:219–225.
- De Marco, O. (2009). The origin and shaping of planetary nebulae: putting the binary hypothesis to the test. Publications of the Astronomical Society of the Pacific, 121(878):316.

-
- De Marco, O., Passy, J.-C., Moe, M., Herwig, F., Mac Low, M.-M., and Paxton, B. (2011). On the α formalism for the common envelope interaction. Monthly Notices of the Royal Astronomical Society, 411(4):2277–2292.
- de Mink, S. E. and Belczynski, K. (2015). Merger rates of double neutron stars and stellar origin black holes: The impact of initial conditions on binary evolution predictions. The Astrophysical Journal, 814(1):58.
- de Mink, S. E., Langer, N., Izzard, R. G., Sana, H., and de Koter, A. (2013). The Rotation Rates of Massive Stars: The Role of Binary Interaction through Tides, Mass Transfer, and Mergers. ApJ, 764(2):166.
- de Mink, S. E., Pols, O. R., and Hilditch, R. W. (2007). Efficiency of mass transfer in massive close binaries. Tests from double-lined eclipsing binaries in the SMC. A&A, 467(3):1181–1196.
- de Mink, S. E., Pols, O. R., Langer, N., and Izzard, R. G. (2009). Massive binaries and the enrichment of the interstellar medium in globular clusters. Proceedings of the International Astronomical Union, 5(S266):169–174.
- de Mink, S. E., Sana, H., Langer, N., Izzard, R. G., and Schneider, F. R. N. (2014). The Incidence of Stellar Mergers and Mass Gainers among Massive Stars. ApJ, 782:7.
- Dewi, J. D. and Tauris, T. M. (2000). On the energy equation and efficiency parameter of the common envelope evolution. arXiv preprint astro-ph/0007034.
- Dewi, J. D. M., Podsiadlowski, P., and Pols, O. R. (2005). The spin period-eccentricity relation of double neutron stars: evidence for weak supernova kicks? MNRAS, 363(1):L71–L75.
- Dewi, J. D. M., Podsiadlowski, P., and Sena, A. (2006). Double-core evolution and the formation of neutron-star binaries with compact companions. Mon. Not. Roy. Astron. Soc., 368:1742–1748.
- Dominik, M., Belczynski, K., Fryer, C., Holz, D. E., Berti, E., Bulik, T., Mandel, I., and O’Shaughnessy, R. (2013). Double Compact Objects. II. Cosmological Merger Rates. ApJ, 779(1):72.
- Dominik, M., Belczynski, K., Fryer, C., Holz, D. E., Berti, E., Bulik, T., Mandel, I., and O’Shaughnessy, R. (2012). Double Compact Objects. I. The Significance of the Common Envelope on Merger Rates. ApJ, 759:52.
- Dominik, M., Berti, E., O’Shaughnessy, R., Mandel, I., Belczynski, K., Fryer, C., Holz, D. E., Bulik, T., and Pannarale, F. (2015). Double Compact Objects III: Gravitational-wave Detection Rates. ApJ, 806:263.
- Dray, L. M. and Tout, C. A. (2007). On rejuvenation in massive binary systems. MNRAS, 376(1):61–70.
- D’Souza, M. C. R., Motl, P. M., Tohline, J. E., and Frank, J. (2006). Numerical Simulations of the Onset and Stability of Dynamical Mass Transfer in Binaries. ApJ, 643(1):381–401.
- Duchêne, G. and Kraus, A. (2013). Stellar Multiplicity. ARA&A, 51:269–310.

-
- Duncan, K., Conselice, C. J., Mortlock, A., Hartley, W. G., Guo, Y., Ferguson, H. C., Davé, R., Lu, Y., Ownsworth, J., Ashby, M. L., et al. (2014). The mass evolution of the first galaxies: stellar mass functions and star formation rates at $4 < z < 7$ in the candels goods-south field. Monthly Notices of the Royal Astronomical Society, 444(3):2960–2984.
- Dunstall, P. R., Dufton, P. L., Sana, H., Evans, C. J., Howarth, I. D., Simón-Díaz, S., de Mink, S. E., Langer, N., Maíz Apellániz, J., and Taylor, W. D. (2015). The VLT-FLAMES Tarantula Survey. XXII. Multiplicity properties of the B-type stars. A&A, 580:A93.
- Eddington, A. S. (1926). The Internal Constitution of the Stars. Cambridge University Press.
- Eggenberger, P., Meynet, G., Maeder, A., Hirschi, R., Charbonnel, C., Talon, S., and Ekström, S. (2008). The Geneva stellar evolution code. Ap&SS, 316(1-4):43–54.
- Eggleton, P. P. (1971). The evolution of low mass stars. MNRAS, 151:351.
- Eggleton, P. P. (1972). Composition changes during stellar evolution. MNRAS, 156:361.
- Eggleton, P. P. (1983). Approximations to the radii of Roche lobes. ApJ, 268:368.
- Eggleton, P. P., Kiseleva, L. G., and Hut, P. (1998). The Equilibrium Tide Model for Tidal Friction. ApJ, 499(2):853–870.
- Eggleton, P. P., Tout, C., Pols, O., Izzard, R., Eldridge, J., Lesaffre, P., Stancliffe, R., Church, R., and Lau, H. (2011). STARS: A Stellar Evolution Code.
- Eilbott, D. H., Riley, A. H., Cohn, J. H., Kesden, M., and King, L. J. (2017). Detecting binarity of GW150914-like lenses in gravitational microlensing events. MNRAS, 467(1):L100–L104.
- Ekström, S., Meynet, G., Georgy, C., Hirschi, R., Maeder, A., Groh, J., Eggenberger, P., and Buldgen, G. (2020). Open problems in high-mass stellar evolution. Stars and their Variability Observed from Space.
- El Mellah, I., Sundqvist, J. O., and Keppens, R. (2018). Accretion from a clumpy massive-star wind in supergiant X-ray binaries. MNRAS, 475(3):3240–3252.
- El Mellah, I., Sundqvist, J. O., and Keppens, R. (2019). Wind Roche lobe overflow in high-mass X-ray binaries. A possible mass-transfer mechanism for ultraluminous X-ray sources. A&A, 622:L3.
- Eldridge, J. J. (2017). Population Synthesis of Massive Close Binary Evolution, page 671. Springer.
- Eldridge, J. J. and Stanway, E. R. (2016). BPASS predictions for binary black hole mergers. MNRAS, 462:3302–3313.
- Eldridge, J. J., Stanway, E. R., and Tang, P. N. (2019). A consistent estimate for gravitational wave and electromagnetic transient rates. MNRAS, 482(1):870–880.
- Eldridge, J. J., Stanway, E. R., Xiao, L., McClelland, L. A. S., Taylor, G., Ng, M., Greis, S. M. L., and Bray, J. C. (2017). Binary Population and Spectral Synthesis Version 2.1: Construction, Observational Verification, and New Results. PASA, 34:e058.

-
- Fabian, A. C., Wilkins, D. R., Miller, J. M., Reis, R. C., Reynolds, C. S., Cackett, E. M., Nowak, M. A., Pooley, G. G., Pottschmidt, K., Sanders, J. S., Ross, R. R., and Wilms, J. (2012). On the determination of the spin of the black hole in Cyg X-1 from X-ray reflection spectra. *MNRAS*, 424(1):217–223.
- Farr, W. M. and Mandel, I. (2018). Comment on “An excess of massive stars in the local 30 Doradus starburst”. *Science*, 361(6400):aat6506.
- Farr, W. M., Stevenson, S., Miller, M. C., Mandel, I., Farr, B., and Vecchio, A. (2017). Distinguishing spin-aligned and isotropic black hole populations with gravitational waves. *Nature*, 548:426–429.
- Farrow, N., Zhu, X.-J., and Thrane, E. (2019). The mass distribution of Galactic double neutron stars. *Astrophys. J.*, 876(1):18.
- Fernández, R., Quataert, E., Kashiyama, K., and Coughlin, E. R. (2018). Mass ejection in failed supernovae: variation with stellar progenitor. *MNRAS*, 476(2):2366–2383.
- Fesen, R. A., Hammell, M. C., Morse, J., Chevalier, R. A., Borkowski, K. J., Dopita, M. A., Gerardy, C. L., Lawrence, S. S., Raymond, J. C., and van den Bergh, S. (2006). Discovery of Outlying High-Velocity Oxygen-Rich Ejecta in Cassiopeia A. *ApJ*, 636(2):859–872.
- Finn, L. S. and Chernoff, D. F. (1993). Observing binary inspiral in gravitational radiation: One interferometer. *Phys. Rev. D*, 47:2198–2219.
- Fishbach, M., Holz, D. E., and Farr, W. M. (2018). Does the Black Hole Merger Rate Evolve with Redshift? *ApJ*, 863:L41.
- Flannery, B. P. and Ulrich, R. K. (1977). On the origin of Centaurus X-3 and related binary X-ray sources. *ApJ*, 212:533–540.
- Fragos, T. and McClintock, J. E. (2015). The Origin of Black Hole Spin in Galactic Low-mass X-Ray Binaries. *ApJ*, 800(1):17.
- Fryer, C. L. (2004). Neutron Star Kicks from Asymmetric Collapse. *ApJ*, 601(2):L175–L178.
- Fryer, C. L., Belczynski, K., Wiktorowicz, G., Dominik, M., Kalogera, V., and Holz, D. E. (2012). Compact Remnant Mass Function: Dependence on the Explosion Mechanism and Metallicity. *ApJ*, 749:91.
- Fukuda, I. (1982). A statistical study of rotational velocities of the stars. *PASP*, 94:271–284.
- Fuller, J. and Ma, L. (2019). Most Black Holes Are Born Very Slowly Rotating. *ApJ*, 881(1):L1.
- Fuller, J., Piro, A. L., and Jermyn, A. S. (2019). Slowing the spins of stellar cores. *MNRAS*, 485(3):3661–3680.
- Furlong, M., Bower, R., Theuns, T., Schaye, J., Crain, R., Schaller, M., Dalla Vecchia, C., Frenk, C., McCarthy, I., Helly, J., et al. (2015). Evolution of galaxy stellar masses and star formation rates in the eagle simulations. *Monthly Notices of the Royal Astronomical Society*, 450(4):4486–4504.

-
- Gamow, G. (1928). Zur Quantentheorie des Atomkernes. *Zeitschrift für Physik*, 51(3-4):204–212.
- Ge, H., Webbink, R. F., Chen, X., and Han, Z. (2015). Adiabatic Mass Loss in Binary Stars. II. From Zero-age Main Sequence to the Base of the Giant Branch. *ApJ*, 812(1):40.
- Ge, H., Webbink, R. F., Chen, X., and Han, Z. (2016). VizieR Online Data Catalog: Adiabatic mass loss in binary stars. II. (Ge+, 2015). *VizieR Online Data Catalog*, page J/ApJ/812/40.
- Giacobbo, N. and Mapelli, M. (2018). The progenitors of compact-object binaries: impact of metallicity, common envelope and natal kicks. *MNRAS*, 480(2):2011–2030.
- Giacobbo, N. and Mapelli, M. (2019). The impact of electron-capture supernovae on merging double neutron stars. *Mon. Not. Roy. Astron. Soc.*, 482(2):2234–2243.
- Giacobbo, N., Mapelli, M., and Spera, M. (2018). Merging black hole binaries: the effects of progenitor’s metallicity, mass-loss rate and Eddington factor. *MNRAS*, 474:2959–2974.
- Götberg, Y., de Mink, S. E., and Groh, J. H. (2017). Ionizing spectra of stars that lose their envelope through interaction with a binary companion: role of metallicity. *A&A*, 608:A11.
- Götberg, Y., de Mink, S. E., Groh, J. H., Kupfer, T., Crowther, P. A., Zapartas, E., and Renzo, M. (2018). Spectral models for binary products: Unifying subdwarfs and Wolf-Rayet stars as a sequence of stripped-envelope stars. *A&A*, 615:A78.
- Gou, L., McClintock, J. E., Reid, M. J., Orosz, J. A., Steiner, J. F., Narayan, R., Xiang, J., Remillard, R. A., Arnaud, K. A., and Davis, S. W. (2011). The Extreme Spin of the Black Hole in Cygnus X-1. *ApJ*, 742(2):85.
- Gräfener, G. and Hamann, W. R. (2005). Hydrodynamic model atmospheres for WR stars. Self-consistent modeling of a WC star wind. *A&A*, 432(2):633–645.
- Grinberg, V., Hell, N., El Mellah, I., Neilsen, J., Sander, A. A. C., Leutenegger, M., Fürst, F., Huenemoerder, D. P., Kretschmar, P., Kühnel, M., Martínez-Núñez, S., Niu, S., Pottschmidt, K., Schulz, N. S., Wilms, J., and Nowak, M. A. (2017). The clumpy absorber in the high-mass X-ray binary Vela X-1. *A&A*, 608:A143.
- Hamann, W. R. and Koesterke, L. (1998). Spectrum formation in clumped stellar winds: consequences for the analyses of Wolf-Rayet spectra. *A&A*, 335:1003–1008.
- Hamann, W. R., Koesterke, L., and Wessolowski, U. (1995). Spectral analyses of the Galactic Wolf-Rayet stars: hydrogen-helium abundances and improved stellar parameters for the WN class. *A&A*, 299:151.
- Hammer, N. J., Janka, H. T., and Müller, E. (2010). Three-dimensional Simulations of Mixing Instabilities in Supernova Explosions. *ApJ*, 714(2):1371–1385.
- Han, Z.-W., Ge, H.-W., Chen, X.-F., and Chen, H.-L. (2020). Binary Population Synthesis. *Research in Astronomy and Astrophysics*, 20(10):161.
- Hannam, M., Schmidt, P., Bohé, A., Haegel, L., Husa, S., Ohme, F., Pratten, G., and Pürrer, M. (2014). Simple Model of Complete Precessing Black-Hole-Binary Gravitational Waveforms. *Phys. Rev. Lett.*, 113(15):151101.

-
- Hansen, C. J., Kawaler, S. D., and Trimble, V. (2012). Stellar interiors: physical principles, structure, and evolution. Springer Science & Business Media.
- Hayashi, C. and Hoshi, R. (1961). The Outer Envelope of Giant Stars with Surface Convection Zone. PASJ, 13:442–449.
- Heger, A. and Langer, N. (2000). Presupernova Evolution of Rotating Massive Stars. II. Evolution of the Surface Properties. ApJ, 544(2):1016–1035.
- Heger, A. and Woosley, S. E. (2002). The Nucleosynthetic Signature of Population III. ApJ, 567(1):532–543.
- Hellings, P. (1983). Phenomenological Study of Massive Accretion Stars. Ap&SS, 96(1):37–54.
- Hillebrandt, W. and Niemeyer, J. C. (2000). Type IA Supernova Explosion Models. ARA&A, 38:191–230.
- Hillwig, T. C., Jones, D., Marco, O. D., Bond, H. E., Margheim, S., and Frew, D. (2016). OBSERVATIONAL CONFIRMATION OF a LINK BETWEEN COMMON ENVELOPE BINARY INTERACTION AND PLANETARY NEBULA SHAPING. The Astrophysical Journal, 832(2):125.
- Hirai, R. (2017). Formation scenario of the progenitor of iPTF13bvn revisited. MNRAS, 466(4):3775–3783.
- Hirai, R., Podsiadlowski, P., and Yamada, S. (2018). Comprehensive Study of Ejecta-companion Interaction for Core-collapse Supernovae in Massive Binaries. ApJ, 864(2):119.
- Hirschi, R., Meynet, G., and Maeder, A. (2005). Stellar evolution with rotation. XIII. Predicted GRB rates at various Z . A&A, 443(2):581–591.
- Hjellming, M. S. (1989). ALGOLS as Limits on Binary Evolution Scenarios. Space Sci. Rev., 50(1-2):155–164.
- Hjellming, M. S. and Webbink, R. F. (1987). Thresholds for rapid mass transfer in binary systems. I - Polytropic models. ApJ, 318:794–808.
- Hobbs, G., Lorimer, D. R., Lyne, A. G., and Kramer, M. (2005). A statistical study of 233 pulsar proper motions. MNRAS, 360:974–992.
- Höfner, S. and Olofsson, H. (2018). Mass loss of stars on the asymptotic giant branch. Mechanisms, models and measurements. A&A Rev., 26(1):1.
- Hogg, D. W. (1999). Distance measures in cosmology. arXiv Astrophysics e-prints.
- Hopkins, A. M. and Beacom, J. F. (2006). On the Normalization of the Cosmic Star Formation History. ApJ, 651(1):142–154.
- Howitt, G., Stevenson, S., Vigna-Gómez, A., Justham, S., Ivanova, N., Woods, T. E., Neijssel, C. J., and Mandel, I. (2020). Luminous red novae: population models and future prospects. Monthly Notices of the Royal Astronomical Society, 492(3):3229–3240.
- Hoyle, F. and Lyttleton, R. A. (1939). The effect of interstellar matter on climatic variation. Proceedings of the Cambridge Philosophical Society, 35(3):405.

-
- Huang, S. (1963). Modes of mass ejection by binary stars and the effect on their orbital periods. Publications of Goddard Space Flight Center, page 63.
- Hulse, R. A. and Taylor, J. H. (1975). Discovery of a pulsar in a binary system. ApJ, 195:L51–L53.
- Humphreys, R. M. and Davidson, K. (1994). The luminous blue variables: Astrophysical geysers. PASP, 106:1025–1051.
- Hunter, J. D. (2007). Matplotlib: A 2d graphics environment. Computing In Science & Engineering, 9(3):90–95.
- Hurley, J. R., Pols, O. R., and Tout, C. A. (2000). Comprehensive analytic formulae for stellar evolution as a function of mass and metallicity. MNRAS, 315(3):543–569.
- Hurley, J. R., Tout, C. A., and Pols, O. R. (2002). Evolution of binary stars and the effect of tides on binary populations. MNRAS, 329(4):897–928.
- Husa, S., Khan, S., Hannam, M., Pürrer, M., Ohme, F., Forteza, X. J., and Bohé, A. (2016). Frequency-domain gravitational waves from nonprecessing black-hole binaries. I. New numerical waveforms and anatomy of the signal. Phys. Rev. D, 93(4):044006.
- Hut, P. (1980). Stability of tidal equilibrium. A&A, 92(1-2):167–170.
- Hut, P. (1981). Tidal evolution in close binary systems. A&A, 99:126–140.
- Hutchings, J. B., Crampton, D., Glaspey, J., and Walker, G. A. H. (1973). Optical observations and model for Cygnus X-1. ApJ, 182:549.
- Ibanoğlu, C., Soyduğan, F., Soyduğan, E., and Dervişoğlu, A. (2006). Angular momentum evolution of Algol binaries. MNRAS, 373(1):435–448.
- Iben, I., J. (1974). Post main sequence evolution of single stars. ARA&A, 12:215–256.
- Iben, Icko, J. and Livio, M. (1993). Common Envelopes in Binary Star Evolution. PASP, 105:1373.
- Ingram, A., van der Klis, M., Middleton, M., Done, C., Altamirano, D., Heil, L., Uttley, P., and Axelsson, M. (2016). A quasi-periodic modulation of the iron line centroid energy in the black hole binary H1743-322. MNRAS, 461(2):1967–1980.
- Ivanova, N. (2018). On the Use of Hydrogen Recombination Energy during Common Envelope Events. ApJ, 858(2):L24.
- Ivanova, N., Justham, S., Chen, X., De Marco, O., Fryer, C., Gaburov, E., Ge, H., Glebbeek, E., Han, Z., Li, X.-D., et al. (2013a). Common envelope evolution: where we stand and how we can move forward. The Astronomy and Astrophysics Review, 21(1):59.
- Ivanova, N., Justham, S., Nandez, J. L. A., and Lombardi, J. C. (2013b). Identification of the long-sought common-envelope events. Science, 339(6118):433–435.
- Ivanova, N. and Taam, R. E. (2003). Magnetic Braking Revisited. ApJ, 599(1):516–521.

-
- Ivanova, N. and Taam, R. E. (2004). Thermal Timescale Mass Transfer and the Evolution of White Dwarf Binaries. ApJ, 601(2):1058–1066.
- Izzard, R. G., de Mink, S. E., Pols, O. R., Langer, N., Sana, H., and de Koter, A. (2013). Massive binary stars and self-enrichment of globular clusters. Mem. Soc. Astron. Italiana, 84:171.
- Izzard, R. G., Dermine, T., and Church, R. P. (2010). White-dwarf kicks and implications for barium stars. A&A, 523:A10.
- Izzard, R. G., Dray, L. M., Karakas, A. I., Lugaro, M., and Tout, C. A. (2006). Population nucleosynthesis in single and binary stars. I. Model. A&A, 460(2):565–572.
- Izzard, R. G., Glebbeek, E., Stancliffe, R. J., and Pols, O. R. (2009). Population synthesis of binary carbon-enhanced metal-poor stars. A&A, 508(3):1359–1374.
- Izzard, R. G., Hall, P. D., Tauris, T. M., and Tout, C. A. (2011). Common envelope evolution. Proceedings of the International Astronomical Union, 7(S283):95–102.
- Izzard, R. G., Preece, H., Jofre, P., Halabi, G. M., Masseron, T., and Tout, C. A. (2017). Binary stars in the Galactic thick disc. Monthly Notices of the Royal Astronomical Society, 473(3):2984–2999.
- Izzard, R. G., Ramirez-Ruiz, E., and Tout, C. A. (2004a). Formation rates of core-collapse supernovae and gamma-ray bursts. MNRAS, 348(4):1215–1228.
- Izzard, R. G., Tout, C. A., Karakas, A. I., and Pols, O. R. (2004b). A new synthetic model for asymptotic giant branch stars. MNRAS, 350(2):407–426.
- Janka, H.-T. (2013). Natal kicks of stellar mass black holes by asymmetric mass ejection in fallback supernovae. MNRAS, 434(2):1355–1361.
- Janka, H.-T. (2017). Neutron Star Kicks by the Gravitational Tug-boat Mechanism in Asymmetric Supernova Explosions: Progenitor and Explosion Dependence. ApJ, 837(1):84.
- Janka, H. T., Langanke, K., Marek, A., Martínez-Pinedo, G., and Müller, B. (2007). Theory of core-collapse supernovae. Phys. Rep., 442(1-6):38–74.
- Jones, D. and Boffin, H. M. (2017). Binary stars as the key to understanding planetary nebulae. Nature Astronomy, 1(5):1–6.
- Justham, S., Rappaport, S., and Podsiadlowski, P. (2006). Magnetic braking of Ap/Bp stars: application to compact black-hole X-ray binaries. MNRAS, 366(4):1415–1423.
- Kaiser, E. A., Hirschi, R., Arnett, W. D., Georgy, C., Scott, L. J. A., and Cristini, A. (2020). Relative importance of convective uncertainties in massive stars. Monthly Notices of the Royal Astronomical Society, 496(2):1967–1989.
- Karakas, A. I. and Lattanzio, J. C. (2014). The Dawes Review 2: Nucleosynthesis and Stellar Yields of Low- and Intermediate-Mass Single Stars. PASA, 31:e030.
- Kawano, T., Done, C., Yamada, S., Takahashi, H., Axelsson, M., and Fukazawa, Y. (2017). Black hole spin of Cygnus X-1 determined from the softest state ever observed. PASJ, 69:36.

-
- Kewley, L. J. and Ellison, S. L. (2008). Metallicity Calibrations and the Mass-Metallicity Relation for Star-forming Galaxies. *ApJ*, 681:1183–1204.
- Khan, S., Husa, S., Hannam, M., Ohme, F., Pürrer, M., Forteza, X. J., and Bohé, A. (2016). Frequency-domain gravitational waves from nonprecessing black-hole binaries. II. A phenomenological model for the advanced detector era. *Phys. Rev. D*, 93(4):044007.
- Kiminki, D. C. and Kobulnicky, H. A. (2012). An Updated Look at Binary Characteristics of Massive Stars in the Cygnus OB2 Association. *ApJ*, 751:4.
- King, A. R., Davies, M. B., Ward, M. J., Fabbiano, G., and Elvis, M. (2001). Ultraluminous x-ray sources in external galaxies. *The Astrophysical Journal*, 552(2):L109–L112.
- King, A. R. and Kolb, U. (1999). The evolution of black hole mass and angular momentum. *MNRAS*, 305:654–660.
- Kippenhahn, R., Kohl, K., and Weigert, A. (1967). Entwicklung in engen Doppelsystemen II. *ZAp*, 66:58.
- Kippenhahn, R. and Meyer-Hofmeister, E. (1977). On the radii of accreting main sequence stars. *A&A*, 54:539–542.
- Kippenhahn, R., Ruschenplatt, G., and Thomas, H. C. (1980). The time scale of thermohaline mixing in stars. *A&A*, 91(1-2):175–180.
- Kippenhahn, R. and Weigert, A. (1967). Entwicklung in engen Doppelsystemen I. Massenaustausch vor und nach Beendigung des zentralen Wasserstoff-Brennens. *ZAp*, 65:251.
- Kippenhahn, R., Weigert, A., and Weiss, A. (2012). *Stellar Structure and Evolution*. Springer.
- Klencki, J., Moe, M., Gladysz, W., Chruslinska, M., Holz, D. E., and Belczynski, K. (2018). Impact of inter-correlated initial binary parameters on double black hole and neutron star mergers. *A&A*, 619:A77.
- Klencki, J., Nelemans, G., Istrate, A. G., and Pols, O. (2020). Massive donors in interacting binaries: effect of metallicity. *arXiv e-prints*, page arXiv:2004.00628.
- Kobulnicky, H. A., Kiminki, D. C., Lundquist, M. J., Burke, J., Chapman, J., Keller, E., Lester, K., Rolan, E. K., Topel, E., Bhattacharjee, A., Smullen, R. A., Vargas Álvarez, C. A., Runnoe, J. C., Dale, D. A., and Brotherton, M. M. (2014). Toward Complete Statistics of Massive Binary Stars: Penultimate Results from the Cygnus OB2 Radial Velocity Survey. *ApJS*, 213:34.
- Kochanek, C. S., Beacom, J. F., Kistler, M. D., Prieto, J. L., Stanek, K. Z., Thompson, T. A., and Yüksel, H. (2008). A Survey About Nothing: Monitoring a Million Supergiants for Failed Supernovae. *ApJ*, 684(2):1336–1342.
- Köhler, K., Langer, N., de Koter, A., de Mink, S. E., Crowther, P. A., Evans, C. J., Gräfener, G., Sana, H., Sanyal, D., Schneider, F. R. N., and Vink, J. S. (2015). The evolution of rotating very massive stars with LMC composition. *A&A*, 573:A71.
- Kopal, Z. (1954). A study of the roche model. *Jodrell Bank Ann*, 1:37–57.

-
- Kozyreva, A., Blinnikov, S., Langer, N., and Yoon, S. C. (2014). Observational properties of low-redshift pair instability supernovae. *A&A*, 565:A70.
- Kroupa, P. (2001). On the variation of the initial mass function. *Monthly Notices of the Royal Astronomical Society*, 322:231–246.
- Kruckow, M. U., Neunteufel, P. G., Di Stefano, R., Gao, Y., and Kobayashi, C. (2021). A catalog of potential post-common envelope binaries. *The Astrophysical Journal*, 920(2):86.
- Kruckow, M. U., Tauris, T. M., Langer, N., Kramer, M., and Izzard, R. G. (2018). Progenitors of gravitational wave mergers: binary evolution with the stellar grid-based code COMBINE. *MNRAS*, 481(2):1908–1949.
- Kudritzki, R.-P. and Puls, J. (2000). Winds from Hot Stars. *ARA&A*, 38:613–666.
- Kushnir, D., Zaldarriaga, M., Kollmeier, J. A., and Waldman, R. (2016). GW150914: spin-based constraints on the merger time of the progenitor system. *MNRAS*, 462:844–849.
- Lai, D. (1997). Dynamical Tides in Rotating Binary Stars. *ApJ*, 490(2):847–862.
- Lajoie, C.-P. and Sills, A. (2010). MASS TRANSFER IN BINARY STARS USING SMOOTHED PARTICLE HYDRODYNAMICS. i. NUMERICAL METHOD. *The Astrophysical Journal*, 726(2):66.
- Lamberts, A., Garrison-Kimmel, S., Clausen, D., and Hopkins, P. (2016). When and where did gw150914 form? *Monthly Notices of the Royal Astronomical Society: Letters*, 463(1):L31–L35.
- Lamers, H. J. G. L. M. and Cassinelli, J. P. (1999). *Introduction to Stellar Winds*. Cambridge University Press.
- Lamers, H. J. G. L. M., Snow, T. P., and Lindholm, D. M. (1995). Terminal Velocities and the Bistability of Stellar Winds. *ApJ*, 455:269.
- Langer, N. (1992). Helium enrichment in massive early type stars. *A&A*, 265:L17–L20.
- Langer, N., Cantiello, M., Yoon, S.-C., Hunter, I., Brott, I., Lennon, D., de Mink, S., and Verheijdt, M. (2008). Rotation and Massive Close Binary Evolution. In Bresolin, F., Crowther, P. A., and Puls, J., editors, *Massive Stars as Cosmic Engines*, volume 250 of *IAU Symposium*, pages 167–178.
- Langer, N. and Norman, C. (2006). On the collapsar model of long gamma-ray bursts: constraints from cosmic metallicity evolution. *The Astrophysical Journal Letters*, 638(2):L63.
- Laplace, E., Götberg, Y., de Mink, S. E., Justham, S., and Farmer, R. (2020). The expansion of stripped-envelope stars: Consequences for supernovae and gravitational-wave progenitors. *A&A*, 637:A6.
- Lau, M. Y. M., Mandel, I., Vigna-Gómez, A., Neijssel, C. J., Stevenson, S., and Sesana, A. (2020). Detecting double neutron stars with LISA. *MNRAS*, 492(3):3061–3072.
- Lauterborn, D. (1970). Evolution with mass exchange of case C for a binary system of total mass 7 M sun. *A&A*, 7:150.

-
- Leitherer, C., Schaerer, D., Goldader, J. D., Delgado, R. M. G., Robert, C., Kune, D. F., de Mello, D. F., Devost, D., and Heckman, T. M. (1999). Starburst99: Synthesis Models for Galaxies with Active Star Formation. *ApJS*, 123:3–40.
- Lipunov, V. M., Postnov, K. A., and Prokhorov, M. E. (1997). Formation and coalescence of relativistic binary stars: the effect of kick velocity. *MNRAS*, 288:245–259.
- Liu, Z.-W., Tauris, T. M., Röpke, F. K., Moriya, T. J., Kruckow, M., Stancliffe, R. J., and Izzard, R. G. (2015). The interaction of core-collapse supernova ejecta with a companion star. *A&A*, 584:A11.
- Livio, M. (1989). Common Envelope Evolution of Binary Stars. *Space Sci. Rev.*, 50(1-2):299–310.
- Livio, M. and Soker, N. (1988). The common envelope phase in the evolution of binary stars. *ApJ*, 329:764–779.
- Lomaeva, M., Grinberg, V., Guainazzi, M., Hell, N., Bianchi, S., Bissinger né Kühnel, M., Fürst, F., Kretschmar, P., Martínez-Chicharro, M., Martínez-Núñez, S., and Torrejón, J. M. (2020). High-resolution X-ray spectroscopy of the stellar wind in Vela X-1 during a flare. *A&A*, 641:A144.
- Lovegrove, E. and Woosley, S. E. (2013). Very Low Energy Supernovae from Neutrino Mass Loss. *ApJ*, 769(2):109.
- Loveridge, A. J., van der Sluys, M. V., and Kalogera, V. (2011). ANALYTICAL EXPRESSIONS FOR THE ENVELOPE BINDING ENERGY OF GIANTS AS A FUNCTION OF BASIC STELLAR PARAMETERS. *The Astrophysical Journal*, 743(1):49.
- Lucy, L. B. (1967). Gravity-Darkening for Stars with Convective Envelopes. *ZAp*, 65:89.
- Lucy, L. B. (1968). The Structure of Contact Binaries. *ApJ*, 151:1123.
- Lucy, L. B. and Solomon, P. M. (1970). Mass Loss by Hot Stars. *ApJ*, 159:879.
- Ma, X., Hopkins, P. F., Faucher-Giguère, C.-A., Zolman, N., Muratov, A. L., Kereš, D., and Quataert, E. (2015). The origin and evolution of the galaxy mass-metallicity relation. *Monthly Notices of the Royal Astronomical Society*, 456(2):2140–2156.
- MacLeod, M. and Loeb, A. (2020). Hydrodynamic Winds From Twin-Star Binaries. *arXiv e-prints*, page arXiv:2007.07252.
- Madau, P. and Dickinson, M. (2014). Cosmic star-formation history. *Annual Review of Astronomy and Astrophysics*, 52:415–486.
- Madau, P. and Fragos, T. (2017). Radiation Backgrounds at Cosmic Dawn: X-Rays from Compact Binaries. *ApJ*, 840:39.
- Maeder, A. (1987). Evidences for a bifurcation in massive star evolution. The ON-blue stragglers. *A&A*, 178:159–169.
- Maeder, A. (2009). *Physics, Formation and Evolution of Rotating Stars*. Springer.
- Maeder, A., Georgy, C., and Meynet, G. (2008). Convective envelopes in rotating OB stars. *A&A*, 479(2):L37–L40.

-
- Maeder, A. and Meynet, G. (2000). The evolution of rotating stars. Annual Review of Astronomy and Astrophysics, 38(1):143–190.
- Maeder, A. and Meynet, G. (2010). Evolution of massive stars with mass loss and rotation. New A Rev., 54(3-6):32–38.
- Mahy, L., Rauw, G., De Becker, M., Eenens, P., and Flores, C. A. (2015). A spectroscopic investigation of the O-type star population in four Cygnus OB associations. II. Determination of the fundamental parameters. A&A, 577:A23.
- Mandel, I. (2016). Estimates of black hole natal kick velocities from observations of low-mass X-ray binaries. MNRAS, 456:578–581.
- Mandel, I. and de Mink, S. E. (2016). Merging binary black holes formed through chemically homogeneous evolution in short-period stellar binaries. MNRAS, 458(3):2634–2647.
- Mandel, I. and Farmer, A. (2018). Merging stellar-mass binary black holes. arXiv e-prints, page arXiv:1806.05820.
- Mandel, I., Farr, W. M., and Gair, J. R. (2019). Extracting distribution parameters from multiple uncertain observations with selection biases. MNRAS.
- Mandel, I. and Fragos, T. (2020). An alternative interpretation of GW190412 as a binary black hole merger with a rapidly spinning secondary. arXiv e-prints, page arXiv:2004.09288.
- Mandel, I. and Müller, B. (2020). Simple recipes for compact remnant masses and natal kicks. MNRAS, 499(3):3214–3221.
- Mapelli, M., Giacobbo, N., Ripamonti, E., and Spera, M. (2017). The cosmic merger rate of stellar black hole binaries from the Illustris simulation. MNRAS, 472:2422–2435.
- Marassi, S., Schneider, R., Corvino, G., Ferrari, V., and Portegies Zwart, S. (2011). Imprint of the merger and ring-down on the gravitational wave background from black hole binaries coalescence. Phys. Rev. D, 84(12):124037.
- Marchant, P., Langer, N., Podsiadlowski, P., Tauris, T. M., and Moriya, T. J. (2016). A new route towards merging massive black holes. A&A, 588:A50.
- Marchant, P., Renzo, M., Farmer, R., Pappas, K. M. W., Taam, R. E., de Mink, S. E., and Kalogera, V. (2019). Pulsational Pair-instability Supernovae in Very Close Binaries. ApJ, 882(1):36.
- Marti, J., Rodriguez, L. F., Mirabel, I. F., and Paredes, J. M. (1996). A search for arcminute-scale radio jets in Cygnus X-1. A&A, 306:449.
- Mazeh, T. (2008). Observational Evidence for Tidal Interaction in Close Binary Systems. In Goupil, M. J. and Zahn, J. P., editors, EAS Publications Series, volume 29 of EAS Publications Series, pages 1–65.
- McCracken, G. and Stott, P. (2013). Fusion: the Energy of the Universe. Academic Press.
- McCrea, W. H. (1964). Extended main-sequence of some stellar clusters. MNRAS, 128:147.

-
- Mennekens, N. and Vanbeveren, D. (2014). Massive double compact object mergers: gravitational wave sources and r-process element production sites. A&A, 564:A134.
- Meyer, F. and Meyer-Hofmeister, E. (1979). Formation of cataclysmic binaries through common envelope evolution. A&A, 78:167–176.
- Meynet, G. and Maeder, A. (2000). Stellar evolution with rotation. V. Changes in all the outputs of massive star models. A&A, 361:101–120.
- Miller, M. C. (2016). Implications of the gravitational wave event GW150914. General Relativity and Gravitation, 48:95.
- Miller, M. C. and Miller, J. M. (2015). The masses and spins of neutron stars and stellar-mass black holes. Phys. Rep., 548:1–34.
- Miller-Jones, J. C. A., Bahramian, A., Orosz, J. A., Mandel, I., Gou, L., Maccarone, T. J., Neijssel, C. J., Zhao, X., Ziółkowski, J., Reid, M. J., Uttley, P., Zheng, X., Byun, D.-Y., Dodson, R., Grinberg, V., Jung, T., Kim, J.-S., Marcote, B., Markoff, S., Rioja, M. J., Rushton, A. P., Russell, D. M., Sivakoff, G. R., Tetarenko, A. J., Tudose, V., and Wilms, J. (2021). Cygnus x-1 contains a $21\text{ }_{\text{solar}}$ mass black hole; implications for massive star winds. Science, 371(6533):1046–1049.
- Mirabel, F. (2017). The formation of stellar black holes. New Astronomy Reviews, 78:1–15.
- Mirabel, I. F. and Rodrigues, I. (2003). Formation of a Black Hole in the Dark. Science, 300(5622):1119–1121.
- Miyaji, S., Nomoto, K., Yokoi, K., and Sugimoto, D. (1980). Supernova triggered by electron captures. PASJ, 32:303–329.
- Moe, M. and Di Stefano, R. (2017). Mind Your Ps and Qs: The Interrelation between Period (P) and Mass-ratio (Q) Distributions of Binary Stars. ApJS, 230:15.
- Moffat, A. F. J., Drissen, L., Lamontagne, R., and Robert, C. (1988). Spectroscopic Evidence for Rapid Blob Ejection in Wolf-Rayet Stars. ApJ, 334:1038.
- Mohamed, S. and Podsiadlowski, P. (2007). Wind Roche-Lobe Overflow: a New Mass-Transfer Mode for Wide Binaries. In Napiwotzki, R. and Burleigh, M. R., editors, 15th European Workshop on White Dwarfs, volume 372 of Astronomical Society of the Pacific Conference Series, page 397.
- Mokiem, M. R., de Koter, A., Evans, C. J., Puls, J., Smartt, S. J., Crowther, P. A., Herrero, A., Langer, N., Lennon, D. J., Najarro, F., Villamariz, M. R., and Vink, J. S. (2007). The VLT-FLAMES survey of massive stars: wind properties and evolution of hot massive stars in the Large Magellanic Cloud. A&A, 465(3):1003–1019.
- Morton, D. C. (1960). Evolutionary Mass Exchange in Close Binary Systems. ApJ, 132:146.
- Müller, B., Heger, A., Liptai, D., and Cameron, J. B. (2016). A simple approach to the supernova progenitor-explosion connection. MNRAS, 460(1):742–764.

-
- Murguia-Berthier, A., Batta, A., Janiuk, A., Ramirez-Ruiz, E., Mandel, I., Noble, S. C., and Everson, R. W. (2020). On the maximum stellar rotation to form a black hole without an accompanying luminous transient. arXiv e-prints, page arXiv:2005.10212.
- Nadezhin, D. K. (1980). Some Secondary Indications of Gravitational Collapse. Ap&SS, 69(1):115–125.
- Neijssel, C. (2022). In preperation.
- Neijssel, C. J., Vigna-Gómez, A., Stevenson, S., Barrett, J. W., Gaebel, S. M., Broekgaarden, F. S., de Mink, S. E., Szécsi, D., Vinciguerra, S., and Mandel, I. (2019). The effect of the metallicity-specific star formation history on double compact object mergers. MNRAS, 490(3):3740–3759.
- Nelemans, G., Tauris, T. M., and van den Heuvel, E. P. J. (1999). Constraints on mass ejection in black hole formation derived from black hole X-ray binaries. A&A, 352:L87–L90.
- Nelemans, G. and van den Heuvel, E. P. J. (2001). The formation of black hole low-mass X-ray binaries: Through case B or case C mass transfer? A&A, 376:950–954.
- Nelemans, G., Verbunt, F., Yungelson, L. R., and Portegies Zwart, S. F. (2000). Reconstructing the evolution of double helium white dwarfs: envelope loss without spiral-in. A&A, 360:1011–1018.
- Nelson, C. A. and Eggleton, P. P. (2001). A Complete Survey of Case A Binary Evolution with Comparison to Observed Algol-type Systems. ApJ, 552(2):664–678.
- Neo, S., Miyaji, S., Nomoto, K., and Sugimoto, D. (1977). Effect of Rapid Mass Accretion onto the Main-Sequence Stars. PASJ, 29:249–262.
- Nieuwenhuijzen, H. and de Jager, C. (1990). Parametrization of stellar rates of mass loss as functions of the fundamental stellar parameters M , L , and R . A&A, 231:134–136.
- Nomoto, K. (1984). Evolution of 8-10 solar mass stars toward electron capture supernovae. I - Formation of electron-degenerate O + NE + MG cores. ApJ, 277:791–805.
- Nomoto, K. (1987). Evolution of 8–10 M_{sun} Stars toward Electron Capture Supernovae. II. Collapse of an O + NE + MG Core. ApJ, 322:206.
- Nugis, T., Crowther, P. A., and Willis, A. J. (1998). Clumping-corrected mass-loss rates of Wolf-Rayet stars. A&A, 333:956–969.
- Nugis, T. and Lamers, H. J. G. L. M. (2000). Mass-loss rates of Wolf-Rayet stars as a function of stellar parameters. A&A, 360:227–244.
- Oliphant, T. (2006). NumPy: A guide to NumPy. USA: Trelgol Publishing. [Online; accessed <today>].
- Oliphant, T. E. (2007). Python for scientific computing. Computing in Science & Engineering, 9(3).

-
- Öpik, E. (1924). Statistical studies of double stars: On the distribution of relative luminosities and distances of double stars in the harvard revised photometry north of declination-31. Publications of the Tartu Astrofizica Observatory, 25(1).
- Orosz, J. A., McClintock, J. E., Aufdenberg, J. P., Remillard, R. A., Reid, M. J., Narayan, R., and Gou, L. (2011). The Mass of the Black Hole in Cygnus X-1. ApJ, 742(2):84.
- Owocki, S. and Shaviv, N. (2012). Instability & mass loss near the eddington limit. In Eta Carinae and the Supernova Impostors, pages 275–297. Springer.
- Owocki, S. P., Castor, J. I., and Rybicki, G. B. (1988). Time-dependent Models of Radiatively Driven Stellar Winds. I. Nonlinear Evolution of Instabilities for a Pure Absorption Model. ApJ, 335:914.
- Packet, W. (1981). On the spin-up of the mass accreting component in a close binary system. A&A, 102:17–19.
- Paczynski, B. (1966). Evolution of Close Binaries. I. Acta Astron., 16:231.
- Paczynski, B. (1967a). Evolution of Close Binaries. V. The Evolution of Massive Binaries and the Formation of the Wolf-Rayet Stars. Acta Astron., 17:355.
- Paczynski, B. (1967b). Gravitational Waves and the Evolution of Close Binaries. Acta Astron., 17:287.
- Paczynski, B. (1976). Common Envelope Binaries. In Eggleton, P., Mitton, S., and Whelan, J., editors, Structure and Evolution of Close Binary Systems, volume 73 of IAU Symposium, page 75.
- Paczynski, B. and Sienkiewicz, R. (1972). Evolution of Close Binaries VIII. Mass Exchange on the Dynamical Time Scale. Acta Astron., 22:73–91.
- Pan, Y., Buonanno, A., Taracchini, A., Kidder, L. E., Mroué, A. H., Pfeiffer, H. P., Scheel, M. A., and Szilágyi, B. (2014). Inspiral-merger-ringdown waveforms of spinning, precessing black-hole binaries in the effective-one-body formalism. Phys. Rev. D, 89(8):084006.
- Panther, B., Heavens, A. F., and Jimenez, R. (2004). The mass function of the stellar component of galaxies in the sloan digital sky survey. Monthly Notices of the Royal Astronomical Society, 355(3):764–768.
- Passy, J.-C., Herwig, F., and Paxton, B. (2012). The Response of Giant Stars to Dynamical-timescale Mass Loss. ApJ, 760(1):90.
- Passy, J.-C., Marco, O. D., Fryer, C. L., Herwig, F., Diehl, S., Oishi, J. S., Low, M.-M. M., Bryan, G. L., and Rockefeller, G. (2011). SIMULATING THE COMMON ENVELOPE PHASE OF a RED GIANT USING SMOOTHED-PARTICLE HYDRODYNAMICS AND UNIFORM-GRID CODES. The Astrophysical Journal, 744(1):52.
- Pastorello, A., Mason, E., Taubenberger, S., Fraser, M., Cortini, G., Tomasella, L., Botticella, M. T., Elias-Rosa, N., Kotak, R., Smartt, S., et al. (2019). Luminous red novae: Stellar mergers or giant eruptions? Astronomy & Astrophysics, 630:A75.
- Pavlovskii, K. and Ivanova, N. (2015). Mass transfer from giant donors. MNRAS, 449(4):4415–4427.

-
- Pavlovskii, K., Ivanova, N., Belczynski, K., and Van, K. X. (2017). Stability of mass transfer from massive giants: double black hole binary formation and ultraluminous X-ray sources. *MNRAS*, 465:2092–2100.
- Paxton, B., Bildsten, L., Dotter, A., Herwig, F., Lesaffre, P., and Timmes, F. (2011). Modules for Experiments in Stellar Astrophysics (MESA). *ApJS*, 192:3.
- Paxton, B., Marchant, P., Schwab, J., Bauer, E. B., Bildsten, L., Cantiello, M., Dessart, L., Farmer, R., Hu, H., Langer, N., Townsend, R. H. D., Townsley, D. M., and Timmes, F. X. (2015). Modules for Experiments in Stellar Astrophysics (MESA): Binaries, Pulsations, and Explosions. *ApJS*, 220(1):15.
- Perez, F., Granger, B. E., and Hunter, J. D. (2011). Python: an ecosystem for scientific computing. *Computing in Science & Engineering*, 13(2):13–21.
- Peters, P. C. (1964). Gravitational radiation and the motion of two point masses. *Physical Review*, 136(4B):B1224.
- Petrovic, J., Langer, N., and van der Hucht, K. A. (2005a). Constraining the mass transfer in massive binaries through progenitor evolution models of Wolf-Rayet+O binaries. *A&A*, 435(3):1013–1030.
- Petrovic, J., Langer, N., Yoon, S. C., and Heger, A. (2005b). Which massive stars are gamma-ray burst progenitors? *A&A*, 435(1):247–259.
- Petterson, J. A. (1978). On the occurrence of streams and disks in massive X-ray binary systems. *ApJ*, 224:625–630.
- Pfahl, E., Podsiadlowski, P., and Rappaport, S. (2005). Relativistic binary pulsars with black hole companions. *The Astrophysical Journal*, 628(1):343.
- Pfahl, E., Rappaport, S., Podsiadlowski, P., and Spruit, H. (2002). A New Class of High-Mass X-Ray Binaries: Implications for Core Collapse and Neutron Star Recoil. *ApJ*, 574(1):364–376.
- Plavec, M. and Kratochvil, P. (1964). Tables for the Roche model of close binaries. *Bulletin of the Astronomical Institutes of Czechoslovakia*, 15:165.
- Podsiadlowski, P., Ivanova, N., Justham, S., and Rappaport, S. (2010). Explosive common-envelope ejection: implications for gamma-ray bursts and low-mass black-hole binaries. *MNRAS*, 406(2):840–847.
- Podsiadlowski, P., Langer, N., Poelarends, A. J. T., Rappaport, S., Heger, A., and Pfahl, E. (2004). The Effects of Binary Evolution on the Dynamics of Core Collapse and Neutron Star Kicks. *ApJ*, 612(2):1044–1051.
- Podsiadlowski, P., Rappaport, S., and Han, Z. (2003). On the formation and evolution of black hole binaries. *MNRAS*, 341(2):385–404.
- Pols, O. R. (2012). Stellar Structure and Evolution. https://www.astro.ru.nl/~onnop/education/stev_utrecht_notes/.
- Pols, O. R., Karakas, A. I., Lattanzio, J. C., and Tout, C. A. (2003). Can Standard Evolution Models Explain the Properties of Barium Stars? In Corradi, R. L. M., Mikolajewska, J., and Mahoney, T. J., editors, *Symbiotic Stars Probing Stellar Evolution*, volume 303 of *Astronomical Society of the Pacific Conference Series*, page 290.

-
- Pols, O. R. and Marinus, M. (1994). Monte-Carlo simulations of binary stellar evolution in young open clusters. *A&A*, 288:475–501.
- Pols, O. R., Schröder, K.-P., Hurley, J. R., Tout, C. A., and Eggleton, P. P. (1998). Stellar evolution models for $Z = 0.0001$ to 0.03 . *MNRAS*, 298:525–536.
- Pols, O. R., Tout, C. A., Eggleton, P. P., and Han, Z. (1995). Approximate input physics for stellar modelling. *MNRAS*, 274(3):964–974.
- Popham, R. and Narayan, R. (1991). Does Accretion Cease When a Star Approaches Breakup? *ApJ*, 370:604.
- Portegies Zwart, S. F. and Verbunt, F. (1996). Population synthesis of high-mass binaries. *A&A*, 309:179–196.
- Portegies Zwart, S. F. and Yungelson, L. R. (1998a). Formation and evolution of binary neutron stars. *A&A*, 332:173–188.
- Portegies Zwart, S. F. and Yungelson, L. R. (1998b). Formation and evolution of binary neutron stars. *A&A*, 332:173–188.
- Prandtl, L. (1925). 7. Bericht über Untersuchungen zur ausgebildeten Turbulenz. *Zeitschrift Angewandte Mathematik und Mechanik*, 5(2):136–139.
- Preibisch, T., Balega, Y., Hofmann, K.-H., Weigelt, G., and Zinnecker, H. (1999). Multiplicity of the massive stars in the Orion Nebula cluster. *New A*, 4:531–542.
- Przybilla, N., Firnstein, M., Nieva, M. F., Meynet, G., and Maeder, A. (2010). Mixing of CNO-cycled matter in massive stars. *A&A*, 517:A38.
- Puls, J., Vink, J. S., and Najarro, F. (2008). Mass loss from hot massive stars. *A&A Rev.*, 16(3-4):209–325.
- Pustyl'nik, I. (1998). The Early History of Resolving the Algol Paradox. *Astronomical and Astrophysical Transactions*, 15:357.
- Qin, Y., Marchant, P., Fragos, T., Meynet, G., and Kalogera, V. (2019). On the Origin of Black Hole Spin in High-mass X-Ray Binaries. *ApJ*, 870(2):L18.
- Rafelski, M., Wolfe, A. M., Prochaska, J. X., Neeleman, M., and Mendez, A. J. (2012). Metallicity Evolution of Damped Ly α Systems Out to $z \sim 5$. *ApJ*, 755:89.
- Ramírez-Agudelo, O. H., Sana, H., de Mink, S. E., Hénault-Brunet, V., de Koter, A., Langer, N., Tramper, F., Gräfener, G., Evans, C. J., Vink, J. S., Dufton, P. L., and Taylor, W. D. (2015). The VLT-FLAMES Tarantula Survey. XXI. Stellar spin rates of O-type spectroscopic binaries. *A&A*, 580:A92.
- Ramírez-Agudelo, O. H., Simón-Díaz, S., Sana, H., de Koter, A., Sabín-Sanjulían, C., de Mink, S. E., Dufton, P. L., Gräfener, G., Evans, C. J., Herrero, A., Langer, N., Lennon, D. J., Maíz Apellániz, J., Markova, N., Najarro, F., Puls, J., Taylor, W. D., and Vink, J. S. (2013). The VLT-FLAMES Tarantula Survey. XII. Rotational velocities of the single O-type stars. *A&A*, 560:A29.
- Rao, A., Gandhi, P., Knigge, C., Paice, J. A., Leigh, N. W. C., and Boubert, D. (2019). Kinematic study of the association Cyg OB3 with Gaia DR2. *arXiv e-prints*, page arXiv:1908.00810.

-
- Rappaport, S., Podsiadlowski, P., and Pfahl, E. (2005). Stellar-mass black hole binaries as ultraluminous x-ray sources. Monthly Notices of the Royal Astronomical Society, 356(2):401–414.
- Rasio, F. A. and Shapiro, S. L. (1995). Hydrodynamics of Binary Coalescence. II. Polytropes with $\Gamma = 5/3$. ApJ, 438:887.
- Ratti, E. M., van Grunsven, T. F. J., Torres, M. A. P., Jonker, P. G., Miller-Jones, J. C. A., Hessels, J. W. T., Van Winckel, H., van der Sluys, M., and Nelemans, G. (2013). IGR J19308+0530: Roche lobe overflow on to a compact object from a donor 1.8 times as massive. MNRAS, 431(1):L10–L14.
- Regós, E., Bailey, V. C., and Mardling, R. (2005). Mass transfer in eccentric binary stars. Monthly Notices of the Royal Astronomical Society, 358(2):544–550.
- Reiter, J., Walsh, L., and Weiss, A. (1995). Solar models: a comparative study of two stellar evolution codes. MNRAS, 274(3):899–908.
- Renzo, M., Ott, C. D., Shore, S. N., and de Mink, S. E. (2017). Systematic survey of the effects of wind mass loss algorithms on the evolution of single massive stars. A&A, 603:A118.
- Repetto, S., Igoshev, A. P., and Nelemans, G. (2017). The Galactic distribution of X-ray binaries and its implications for compact object formation and natal kicks. MNRAS, 467:298–310.
- Riley, J., Mandel, I., Marchant, P., Butler, E., Nathaniel, K., Neijssel, C., Shortt, S., and Vigna-Gómez, A. (2021). Chemically homogeneous evolution: a rapid population synthesis approach. Monthly Notices of the Royal Astronomical Society, 505(1):663–676.
- Rosen, A. L., Krumholz, M. R., and Ramirez-Ruiz, E. (2012). What Sets the Initial Rotation Rates of Massive Stars? ApJ, 748(2):97.
- Roxburgh, I. W. (1965). A note on the boundary of convective zones in stars. MNRAS, 130:223.
- Russell, D. M., Fender, R. P., Gallo, E., and Kaiser, C. R. (2007). The jet-powered optical nebula of Cygnus X-1. MNRAS, 376(3):1341–1349.
- Saladino, M. I., Pols, O. R., van der Helm, E., Pelupessy, I., and Portegies Zwart, S. (2018). Gone with the wind: the impact of wind mass transfer on the orbital evolution of AGB binary systems. A&A, 618:A50.
- Salpeter, E. E. (1955). The Luminosity Function and Stellar Evolution. ApJ, 121:161.
- Sana, H. (2017). The multiplicity of massive stars: a 2016 view. In Eldridge, J. J., Bray, J. C., McClelland, L. A. S., and Xiao, L., editors, The Lives and Death-Throes of Massive Stars, volume 329 of IAU Symposium, pages 110–117.
- Sana, H., de Koter, A., de Mink, S. E., Dunstall, P. R., Evans, C. J., Hénault-Brunet, V., Maíz Apellániz, J., Ramírez-Agudelo, O. H., Taylor, W. D., Walborn, N. R., Clark, J. S., Crowther, P. A., Herrero, A., Gieles, M., Langer, N., Lennon, D. J., and Vink, J. S. (2013). The VLT-FLAMES Tarantula Survey. VIII. Multiplicity properties of the O-type star population. A&A, 550:A107.

-
- Sana, H., de Mink, S. E., de Koter, A., Langer, N., Evans, C. J., Gieles, M., Gosset, E., Izzard, R. G., Le Bouquin, J.-B., and Schneider, F. R. N. (2012). Binary Interaction Dominates the Evolution of Massive Stars. Science, 337:444.
- Sander, A. A. C., Hamann, W. R., Todt, H., Hainich, R., and Shenar, T. (2017). Coupling hydrodynamics with comoving frame radiative transfer. I. A unified approach for OB and WR stars. A&A, 603:A86.
- Sander, A. A. C. and Vink, J. S. (2020). On the nature of massive helium star winds and Wolf-Rayet-type mass-loss. MNRAS, 499(1):873–892.
- Sander, A. A. C., Vink, J. S., and Hamann, W. R. (2020). Driving classical Wolf-Rayet winds: a Γ - and Z-dependent mass-loss. MNRAS, 491(3):4406–4425.
- Savaglio, S., Glazebrook, K., Le Borgne, D., Juneau, S., Abraham, R., Chen, H.-W., Crampton, D., McCarthy, P., Carlberg, R., Marzke, R., et al. (2005). The gemini deep deep survey. vii. the redshift evolution of the mass-metallicity relation. The Astrophysical Journal, 635(1):260.
- Schechter, P. (1976). An analytic expression for the luminosity function for galaxies. The Astrophysical Journal, 203:297–306.
- Schneider, F. R. N., Izzard, R. G., Langer, N., and de Mink, S. E. (2015). Evolution of Mass Functions of Coeval Stars through Wind Mass Loss and Binary Interactions. ApJ, 805(1):20.
- Schneider, F. R. N., Podsiadlowski, P., Langer, N., Castro, N., and Fossati, L. (2016). Rejuvenation of stellar mergers and the origin of magnetic fields in massive stars. MNRAS, 457(3):2355–2365.
- Schönberg, M. and Chandrasekhar, S. (1942). On the Evolution of the Main-Sequence Stars. ApJ, 96:161.
- Schröder, S. L., Batta, A., and Ramirez-Ruiz, E. (2018). Black Hole Formation in Fallback Supernova and the Spins of LIGO Sources. ApJ, 862(1):L3.
- Schröder, S. L., MacLeod, M., Ramirez-Ruiz, E., Mandel, I., Fragos, T., Loeb, A., and Everson, R. W. (2021). The Evolution of Binaries under the Influence of Radiation-Driven Winds from a Stellar Companion. arXiv e-prints, page arXiv:2107.09675.
- Scott, D. W. (2015). Multivariate density estimation: theory, practice, and visualization. John Wiley & Sons.
- Sell, P. H., Heinz, S., Richards, E., Maccarone, T. J., Russell, D. M., Gallo, E., Fender, R., Markoff, S., and Nowak, M. (2015). Shell-shocked: the interstellar medium near Cygnus X-1. MNRAS, 446(4):3579–3592.
- Sepinsky, J. F., B. Willems, V. K., and Rasio, F. A. (2007). Interacting binaries with eccentric orbits: Secular orbital evolution due to conservative mass transfer. The Astrophysical Journal, 667(2):1170–1184.
- Shao, Y. and Li, X.-D. (2014). On the Formation of Be Stars through Binary Interaction. ApJ, 796(1):37.
- Shao, Y. and Li, X.-D. (2016). non conservative mass transfer in massive binaries and the formation of wolf-rayet stars + o binaries. The Astrophysical Journal, 833(1):108.

-
- Shaviv, G. and Salpeter, E. E. (1973). Convective overshooting in stellar interior models. *The Astrophysical Journal*, 184:191–200.
- Shigeyama, T., Nomoto, K., and Hashimoto, M. (1988). Hydrodynamical models and the light curve of Supernova 1987A in the Large Magellanic Cloud. *A&A*, 196:141–151.
- Shimanskii, V. V., Karitskaya, E. A., Bochkarev, N. G., Galazutdinov, G. A., Lyuty, V. M., and Shimanskaya, N. N. (2012). Analysis of optical spectra of V1357 Cyg≡Cyg X-1. *Astronomy Reports*, 56(10):741–760.
- Skowron, D. M., Kourniotis, M., Prieto, J. L., Castro, N., Bonanos, A. Z., and Pieńkowski, D. (2017). OGLE-LMC-ECL-09937: The Most Massive Algol-Type Binary System with a Mass Measurement Accurate to 2%. *Acta Astron.*, 67(4):329–344.
- Smarr, L. L. and Blandford, R. (1976). The binary pulsar: physical processes, possible companions, and evolutionary histories. *ApJ*, 207:574–588.
- Smartt, S. J. (2009). Progenitors of Core-Collapse Supernovae. *ARA&A*, 47(1):63–106.
- Smith, N. (2014). Mass Loss: Its Effect on the Evolution and Fate of High-Mass Stars. *ARA&A*, 52:487–528.
- Soberman, G. E., Phinney, E. S., and van den Heuvel, E. P. J. (1997). Stability criteria for mass transfer in binary stellar evolution. *A&A*, 327:620–635.
- Sota, A., Maíz Apellániz, J., Morrell, N. I., Barbá, R. H., Walborn, N. R., Gamen, R. C., Arias, J. I., and Alfaro, E. J. (2014). The Galactic O-Star Spectroscopic Survey (GOSSS). II. Bright Southern Stars. *ApJS*, 211:10.
- Spera, M. and Mapelli, M. (2017). Very massive stars, pair-instability supernovae and intermediate-mass black holes with the sevn code. *MNRAS*, 470:4739–4749.
- Spera, M., Mapelli, M., and Bressan, A. (2015). The mass spectrum of compact remnants from the PARSEC stellar evolution tracks. *MNRAS*, 451(4):4086–4103.
- Spera, M., Mapelli, M., Giacobbo, N., Trani, A. A., Bressan, A., and Costa, G. (2019). Merging black hole binaries with the SEVN code. *MNRAS*, 485(1):889–907.
- Spruit, H. C. (2002). Dynamo action by differential rotation in a stably stratified stellar interior. *A&A*, 381:923–932.
- Stancliffe, R. J. (2006). Does simultaneous solution matter for stellar evolution codes? *MNRAS*, 370(4):1817–1822.
- Stanway, E. R., Eldridge, J. J., and Becker, G. D. (2016). Stellar population effects on the inferred photon density at reionization. *MNRAS*, 456:485–499.
- Stella, L. and Vietri, M. (1998). Lense-Thirring Precession and Quasi-periodic Oscillations in Low-Mass X-Ray Binaries. *ApJ*, 492(1):L59–L62.
- Stevenson, S., Sampson, M., Powell, J., Vigna-Gómez, A., Neijssel, C. J., Szécsi, D., and Mandel, I. (2019). The Impact of Pair-instability Mass Loss on the Binary Black Hole Mass Distribution. *ApJ*, 882(2):121.

-
- Stevenson, S., Vigna-Gómez, A., Mandel, I., Barrett, J. W., Neijssel, C. J., Perkins, D., and de Mink, S. E. (2017). Formation of the first three gravitational-wave observations through isolated binary evolution. *Nature Communications*, 8:14906.
- Stirling, A. M., Spencer, R. E., de la Force, C. J., Garrett, M. A., Fender, R. P., and Ogley, R. N. (2001). A relativistic jet from Cygnus X-1 in the low/hard X-ray state. *MNRAS*, 327(4):1273–1278.
- Strolger, L.-G., Riess, A. G., Dahlen, T., Livio, M., Panagia, N., Challis, P., Tonry, J. L., Filippenko, A. V., Chornock, R., Ferguson, H., et al. (2004). The hubble higher z supernova search: supernovae to $z=1.6$ and constraints on type ia progenitor models. *The Astrophysical Journal*, 613(1):200.
- Stryker, L. L. (1993). Blue Stragglers. *PASP*, 105:1081.
- Sundqvist, J. O., Owocki, S. P., and Puls, J. (2018). 2D wind clumping in hot, massive stars from hydrodynamical line-driven instability simulations using a pseudo-planar approach. *A&A*, 611:A17.
- Taam, R. E., Bodenheimer, P., and Ostriker, J. P. (1978). Double core evolution. I. A 16 M sun star with a 1 M sun neutron-star companion. *ApJ*, 222:269–280.
- Taam, R. E. and Ricker, P. M. (2006). Common Envelope Evolution. *arXiv e-prints*, pages astro-ph/0611043.
- Takahashi, K. and Langer, N. (2020). Modeling of Magneto-Rotational Stellar Evolution I. Method and first applications. *arXiv e-prints*, page arXiv:2010.13909.
- Takahashi, K., Yoshida, T., and Umeda, H. (2013). Evolution of Progenitors for Electron Capture Supernovae. *ApJ*, 771(1):28.
- Tauris, T. M. and Dewi, J. D. M. (2001). Research Note On the binding energy parameter of common envelope evolution. Dependency on the definition of the stellar core boundary during spiral-in. *A&A*, 369:170–173.
- Tauris, T. M., Kramer, M., Freire, P. C. C., Wex, N., Janka, H. T., Langer, N., Podsiadlowski, P., Bozzo, E., Chaty, S., Kruckow, M. U., van den Heuvel, E. P. J., Antoniadis, J., Breton, R. P., and Champion, D. J. (2017). Formation of Double Neutron Star Systems. *ApJ*, 846(2):170.
- Tauris, T. M., Langer, N., and Podsiadlowski, P. (2015). Ultra-stripped supernovae: progenitors and fate. *MNRAS*, 451:2123–2144.
- Tayler, R. J. (1973). The adiabatic stability of stars containing magnetic fields. I. Toroidal fields. *MNRAS*, 161:365.
- Taylor, P. and Kobayashi, C. (2015). The effects of AGN feedback on present-day galaxy properties in cosmological simulations. *MNRAS*, 448:1835–1846.
- Team COMPAS: J. Riley, Riley, J., Agrawal, P., Barrett, J. W., Boyett, K. N. K., Broekgaarden, F. S., Chattopadhyay, D., Gaebel, S. M., Gittins, F., Hirai, R., Howitt, G., Justham, S., Khandelwal, L., Kummer, F., Lau, M. Y. M., Mandel, I., de Mink, S. E., Neijssel, C., Riley, T., van Son, L., Stevenson, S., Vigna-Gomez, A., Vinciguerra, S., Wagg, T., and Willcox, R. (2021). Rapid stellar and binary population synthesis with COMPAS. *arXiv e-prints*.
- Theuns, T., Boffin, H. M. J., and Jorissen, A. (1996). Wind accretion in binary stars - II. Accretion rates. *MNRAS*, 280(4):1264–1276.

-
- Thorne, K. S. (1974). Disk-Accretion onto a Black Hole. II. Evolution of the Hole. *ApJ*, 191:507–520.
- Toonen, S., Claeys, J. S. W., Mennekens, N., and Ruiter, A. J. (2014). PopCORN: Hunting down the differences between binary population synthesis codes. *A&A*, 562:A14.
- Toonen, S. and Nelemans, G. (2013). The effect of common-envelope evolution on the visible population of post-common-envelope binaries. *A&A*, 557:A87.
- Toonen, S., Nelemans, G., and Portegies Zwart, S. (2012). Supernova Type Ia progenitors from merging double white dwarfs. Using a new population synthesis model. *A&A*, 546:A70.
- Tout, C. A., Aarseth, S. J., Pols, O. R., and Eggleton, P. P. (1997). Rapid binary star evolution for N-body simulations and population synthesis. *MNRAS*, 291(4):732–748.
- Tout, C. A., Pols, O. R., Eggleton, P. P., and Han, Z. (1996). Zero-age main-sequence radii and luminosities as analytic functions of mass and metallicity. *MNRAS*, 281(1):257–262.
- Tremonti, C. A., Heckman, T. M., Kauffmann, G., Brinchmann, J., Charlot, S., White, S. D., Seibert, M., Peng, E. W., Schlegel, D. J., Uomoto, A., et al. (2004). The origin of the mass-metallicity relation: insights from 53,000 star-forming galaxies in the sloan digital sky survey. *The Astrophysical Journal*, 613(2):898.
- Tuchman, Y. and Wheeler, J. C. (1990). Large Magellanic Cloud Helium-rich Peculiar Blue Supergiants and SN 1987A. *ApJ*, 363:255.
- Tutukov, A. and Yungelson, L. (1973). Evolution of massive close binaries. *Nauchnye Informatsii*, 27:70.
- Tutukov, A. V. and Yungelson, L. R. (1993). The merger rate of neutron star and black hole binaries. *MNRAS*, 260:675–678.
- Ulrich, R. K. and Burger, H. L. (1976). The accreting component of mass-exchange binaries. *ApJ*, 206:509–514.
- Utrobin, V. P., Chugai, N. N., and Andronova, A. A. (1995). Asymmetry of SN 1987A: fast ^{56}Ni clump. *A&A*, 295:129–135.
- Valsecchi, F., Glebbeek, E., Farr, W. M., Fragos, T., Willems, B., Orosz, J. A., Liu, J., and Kalogera, V. (2010). Formation of the black-hole binary M33 X-7 through mass exchange in a tight massive system. *Nature*, 468(7320):77–79.
- van den Heuvel, E. P. J. (1967). The origin of blue stragglers and peculiar and metallic-line stars. *The Observatory*, 87:68–72.
- van den Heuvel, E. P. J. (1975). Modes of mass transfer and classes of binary X-ray sources. *ApJ*, 198:L109–L112.
- van den Heuvel, E. P. J. and De Loore, C. (1973). The nature of X-ray binaries III. Evolution of massive close binaries with one collapsed component - with a possible application to Cygnus X-3. *A&A*, 25:387.

-
- van den Heuvel, E. P. J. and Heise, J. (1972). Centaurus X-3, Possible Reactivation of an Old Neutron Star by Mass Exchange in a Close Binary. Nature Physical Science, 239(92):67–69.
- van den Heuvel, E. P. J., Portegies Zwart, S. F., and de Mink, S. E. (2017). Forming short-period Wolf-Rayet X-ray binaries and double black holes through stable mass transfer. MNRAS, 471(4):4256–4264.
- van den Heuvel, E. P. J., Portegies Zwart, S. F., and de Mink, S. E. (2017). Forming short-period Wolf-Rayet X-ray binaries and double black holes through stable mass transfer. Mon. Not. Roy. Astron. Soc., 471(4):4256–4264.
- van der Sluys, M. (2019). Binary evolution in a nutshell. https://astro.ru.nl/~sluys/Binaries/files/BinaryEvolutionNutshell_letter.pdf.
- van Rensbergen, W., de Greve, J. P., Mennekens, N., Jansen, K., and de Loore, C. (2011). Mass loss out of close binaries. The formation of Algol-type systems, completed with case B RLOF. A&A, 528:A16.
- van Rensbergen, W., Vanbeveren, D., and De Loore, C. (1996). OB-runaways as a result of massive star evolution. A&A, 305:825.
- van Son, L. A. C., De Mink, S. E., Broekgaarden, F. S., Renzo, M., Justham, S., Laplace, E., Morán-Fraile, J., Hendriks, D. D., and Farmer, R. (2020). Polluting the Pair-instability Mass Gap for Binary Black Holes through Super-Eddington Accretion in Isolated Binaries. ApJ, 897(1):100.
- Vassiliadis, E. and Wood, P. R. (1993). Evolution of Low- and Intermediate-Mass Stars to the End of the Asymptotic Giant Branch with Mass Loss. ApJ, 413:641.
- Venumadhav, T., Zackay, B., Roulet, J., Dai, L., and Zaldarriaga, M. (2019). New Binary Black Hole Mergers in the Second Observing Run of Advanced LIGO and Advanced Virgo. ArXiv e-prints.
- Verbunt, F., Igoshev, A., and Cator, E. (2017). The observed velocity distribution of young pulsars. A&A, 608:A57.
- Verbunt, F. and Phinney, E. S. (1995). Tidal circularization and the eccentricity of binaries containing giant stars. A&A, 296:709.
- Verbunt, F. and Zwaan, C. (1981). Magnetic braking in low-mass X-ray binaries. A&A, 100:L7–L9.
- Vigna-Gómez, A., MacLeod, M., Neijssel, C. J., Broekgaarden, F. S., Justham, S., Howitt, G., de Mink, S. E., Vinciguerra, S., and Mandel, I. (2020). Common envelope episodes that lead to double neutron star formation. PASA, 37:e038.
- Vigna-Gómez, A., Neijssel, C. J., Stevenson, S., Barrett, J. W., Belczynski, K., Justham, S., de Mink, S. E., Müller, B., Podsiadlowski, P., Renzo, M., Szécsi, D., and Mandel, I. (2018). On the formation history of Galactic double neutron stars. MNRAS, 481(3):4009–4029.
- Vinciguerra, S., Branchesi, M., Ciolfi, R., Mandel, I., Neijssel, C. J., and Stratta, G. (2019). SAPREMO: a simplified algorithm for predicting detections of electromagnetic transients in surveys. MNRAS, 484(1):332–344.

-
- Vinciguerra, S., Neijssel, C. J., Vigna-Gómez, A., Mandel, I., Podsiadlowski, P., Maccarone, T. J., Nicholl, M., Kingdon, S., Perry, A., and Salemi, F. (2020). Be X-ray binaries in the SMC as (I) indicators of mass transfer efficiency. arXiv e-prints, page arXiv:2003.00195.
- Vink, J. S. (2017). Winds from stripped low-mass helium stars and Wolf-Rayet stars. A&A, 607:L8.
- Vink, J. S. and de Koter, A. (2002). Predictions of variable mass loss for Luminous Blue Variables. A&A, 393:543–553.
- Vink, J. S. and de Koter, A. (2005). On the metallicity dependence of Wolf-Rayet winds. A&A, 442(2):587–596.
- Vink, J. S., de Koter, A., and Lamers, H. J. G. L. M. (1999). On the nature of the bi-stability jump in the winds of early-type supergiants. A&A, 350:181–196.
- Vink, J. S., de Koter, A., and Lamers, H. J. G. L. M. (2001). Mass-loss predictions for O and B stars as a function of metallicity. A&A, 369:574–588.
- Vitale, S. and Farr, W. M. (2018). Measuring the star formation rate with gravitational waves from binary black holes. ArXiv e-prints.
- von Zeipel, H. (1924). The radiative equilibrium of a slightly oblate rotating star. MNRAS, 84:684–701.
- Voss, R. and Tauris, T. M. (2003). Galactic distribution of merging neutron stars and black holes - Prospects for short gamma-ray burst progenitors and LIGO/VIRGO. Mon. Not. Roy. Astron. Soc., 342:1169.
- Weaver, T. A., Woosley, S. E., and Fuller, G. M. (1985). Electron Capture and the Final Evolution of Massive Stars. In Numerical Astrophysics, page 374.
- Weaver, T. A., Zimmerman, G. B., and Woosley, S. E. (1978). Presupernova evolution of massive stars. ApJ, 225:1021–1029.
- Webbink, R. F. (1976). The Evolution of Low-Mass Close Binary Systems. II. $1.50 M_{sun} + 0.75 M_{sun}$: Evolution Into Contact. ApJS, 32:583.
- Webbink, R. F. (1984). Double white dwarfs as progenitors of R Coronae Borealis stars and type I supernovae. ApJ, 277:355–360.
- Webster, B. L. and Murdin, P. (1972). Cygnus X-1-a Spectroscopic Binary with a Heavy Companion ? Nature, 235(5332):37–38.
- Weisberg, J. M. and Taylor, J. H. (2005). The Relativistic Binary Pulsar B1913+16: Thirty Years of Observations and Analysis. In Rasio, F. A. and Stairs, I. H., editors, Binary Radio Pulsars, volume 328 of Astronomical Society of the Pacific Conference Series, page 25.
- Weiss, A. (2002). Key problems in stellar evolution. In Stellar Structure and Habitable Planet Finding, volume 485, pages 57–64.
- Weizsäcker, C. v. (1937). Über elementumwandlungen im innern der sterne. i. Physikalische Zeitschrift, 38(6).
- Wellstein, S., Langer, N., and Braun, H. (2001). Formation of contact in massive close binaries. A&A, 369:939–959.

-
- Willson, L. A. (2000). Mass Loss From Cool Stars: Impact on the Evolution of Stars and Stellar Populations. *ARA&A*, 38:573–611.
- Wong, T.-W., Valsecchi, F., Fragos, T., and Kalogera, V. (2012). Understanding Compact Object Formation and Natal Kicks. III. The Case of Cygnus X-1. *ApJ*, 747(2):111.
- Wongwathanarat, A., Janka, H.-T., Müller, E., Pllumbi, E., and Wanajo, S. (2017). Production and Distribution of ^{44}Ti and ^{56}Ni in a Three-dimensional Supernova Model Resembling Cassiopeia A. *ApJ*, 842(1):13.
- Wongwathanarat, A., Müller, E., and Janka, H. T. (2015). Three-dimensional simulations of core-collapse supernovae: from shock revival to shock breakout. *A&A*, 577:A48.
- Wood, P. and Sebo, K. (1996). On the pulsation mode of mira variables: evidence from the large magellanic cloud. *Monthly Notices of the Royal Astronomical Society*, 282(3):958–964.
- Woods, T. E. and Ivanova, N. (2011). Can We Trust Models for Adiabatic Mass Loss? *ApJ*, 739:L48.
- Woosley, S. E. (1989). The great supernova of 1987. *Annals of the New York Academy of Sciences*, 571:397–413.
- Woosley, S. E. (2017). Pulsational Pair-instability Supernovae. *ApJ*, 836:244.
- Woosley, S. E. (2018). Models for the Unusual Supernova iPTF14hls. *ApJ*, 863(1):105.
- Woosley, S. E. and Weaver, T. A. (1988). Presupernova models: sensitivity to convective algorithm and Coulomb corrections. *Phys. Rep.*, 163(1):79–94.
- Wyrzykowski, Ł. and Mandel, I. (2019). Constraining the masses of microlensing black holes and the mass gap with Gaia DR2. *ArXiv e-prints*.
- Xu, X.-J. and Li, X.-D. (2010a). ERRATUM: “On the Binding Energy Parameter λ of Common Envelope Evolution” (2010, ApJ, 716, 114). *ApJ*, 722(2):1985–1988.
- Xu, X.-J. and Li, X.-D. (2010b). On the Binding Energy Parameter λ of Common Envelope Evolution. *ApJ*, 716:114–121.
- Yoon, S.-C. (2017). Towards a better understanding of the evolution of Wolf-Rayet stars and Type Ib/Ic supernova progenitors. *MNRAS*, 470(4):3970–3980.
- Yoon, S.-C. and Cantiello, M. (2010). EVOLUTION OF MASSIVE STARS WITH PULSATION-DRIVEN SUPERWINDS DURING THE RED SUPERGIANT PHASE. *The Astrophysical Journal*, 717(1):L62–L65.
- Yoon, S. C., Woosley, S. E., and Langer, N. (2010). Type Ib/c Supernovae in Binary Systems. I. Evolution and Properties of the Progenitor Stars. *ApJ*, 725(1):940–954.
- Yüksel, H., Kistler, M. D., Beacom, J. F., and Hopkins, A. M. (2008). Revealing the High-Redshift Star Formation Rate with Gamma-Ray Bursts. *ApJ*, 683(1):L5.

- Yungelson, L. R. (2005). Population synthesis for low and intermediate mass binaries. *AIP Conference Proceedings*, 797(1):1–10.
- Zahn, J.-P. (1977). Tidal friction in close binary stars. *A&A*, 57:383–394.
- Zaldarriaga, M., Kushnir, D., and Kollmeier, J. A. (2018). The expected spins of gravitational wave sources with isolated field binary progenitors. *MNRAS*, 473:4174–4178.
- Zhao, X.-S., Dong, Y.-T., Gou, L.-J., Feng, Y., Jia, N., Li, Y.-F., Liao, Z.-X., Liu, J.-R., Zheng, X.-Y., Zhang, S.-N., Qu, J.-L., Song, L.-M., Zhang, S., Bu, Q.-C., Cai, C., Cao, X.-L., Chang, Z., Chen, G., Chen, L., Chen, T.-X., Chen, Y.-B., Chen, Y., Chen, Y.-P., Cui, W., Cui, W.-W., Deng, J.-K., Dong, Y.-W., Du, Y.-Y., Fu, M.-X., Gao, G.-H., Gao, H., Gao, M., Ge, M.-Y., Gu, Y.-D., Guan, J., Guo, C.-C., Han, D.-W., Huang, Y., Huo, J., Jia, S.-M., Jiang, L.-H., Jiang, W.-C., Jin, J., Jin, Y.-J., Kong, L.-D., Li, B., Li, C.-K., Li, G., Li, M.-S., Li, T.-P., Li, W., Li, X., Li, X.-B., Li, X.-F., Li, Y.-G., Li, Z.-W., Liang, X.-H., Liao, J.-Y., Liu, B.-S., Liu, C.-Z., Liu, G.-Q., Liu, H.-X., Liu, H.-W., Liu, X.-J., Liu, Y.-N., Lu, B., Lu, F.-J., Lu, X.-F., Luo, Q., Luo, T., Ma, X., Meng, B., Nang, Y., Nie, J.-Y., Ou, G., Sai, N., Shang, R.-C., Song, X.-Y., Sun, L., Tan, Y., Tao, L., Tuo, Y.-L., Wang, C., Wang, G.-F., Wang, J., Wang, W.-S., Wang, Y.-S., Wen, X.-Y., Wu, B.-Y., Wu, B.-B., Wu, M., Xiao, G.-C., Xiao, S., Xiong, S.-L., Xu, Y.-P., Yang, J.-W., Yang, S., Yang, Y.-J., Yang, Y.-R., Yi, Q.-B., Yin, Q.-Q., You, Y., Zhang, A.-M., Zhang, C.-M., Zhang, F., Zhang, H.-M., Zhang, J., Zhang, T., Zhang, W.-C., Zhang, W., Zhang, W.-Z., Zhang, Y., Zhang, Y.-F., Zhang, Y.-J., Zhang, Y., Zhang, Z., Zhang, Z., Zhang, Z.-L., Zhao, H.-S., Zhao, X.-F., Zheng, S.-J., Zhou, D.-K., Zhou, J.-F., Zhu, Y.-X., Yue-Zhu, and Zhuang, R.-L. (2020). Confirming the spin parameter of the black hole in cygnus x-1 using the insight-hxmt. *Journal of High Energy Astrophysics*, 27:53–63.
- Zorotovic, M., Schreiber, M. R., Gänsicke, B. T., and Nebot Gómez-Morán, A. (2010). Post-common-envelope binaries from SDSS. IX: Constraining the common-envelope efficiency. *A&A*, 520:A86.